Università degli Studi di Napoli *Federico* II

PhD thesis in

PHYSICS

XXXV cycle

Coordinator: prof. Vincenzo Canale

Intrinsic feedback effect optical trapping

Academic discipline FIS/03

Candidate
Antonio Ciarlo

Tutor
Prof. Antonio Sasso

Years: 2019/2023

Contents

Introduction

Light interacts with matter producing mechanical optical forces. Kepler conjectured this for the first time observing how the tails of comets were always directed in the opposite direction to their motion towards the Sun [1]. However, the theoretical description of the momentum transfer that produces optical forces was formulated only in the late nineteenth century within Maxwell's theory of electromagnetism [2]. Then, in 1901, Lebedev [3], Nichols and Hull [4] gave a first experimental proof of this phenomenon by illuminating microscopic objects in vacuum. These experiments, however, produced very small effects and, for this reason, were strongly questioned.

Only in 1970, thanks to the advent of laser sources, Arthur Ashkin demonstrated that laser light could affect the motion of illuminated micrometric particles by optical levitation [5]. Few years later, Ashkin succeeded in the realisation of a tridimensional trapping system by using highly focused laser beams. This system is known as *optical tweezers* (OT) because it can manipulate micrometric particles without any mechanical contact. After the pioneering work of Ashkin, OTs have become a useful tool in many fields of scientific research, such as in biology, medicine, chemistry, and physics. Indeed, OT generate forces of magnitude ranging from few femtonewtons to tens of piconewton extending the range of applicability of already existing techniques like Atomic Force Microscopes, which produce only forces with magnitude larger than few tens of piconewtons. For example, OT allow to manipulate bacteria [6] and even single molecules [7, 8], to study in a new way statistical mechanics phenomena such as colloidal crystals [9, 10] or Kramers' transitions [11], and to study quantum mechanics phenomena [12, 13]. In addition, optical tweezers are also force transducers since, to a first approximation, its force is proportional to the displacement from the trapping position like for a spring. In this way, the trapped object can be used as a probe to measure external forces acting on it. This technique is called photonic force microscopy [14, 15].

From Ashkin's seminal work to the present day, OTs have been improved and made more versatile for instance by using advanced beam-shaping techniques [16], spectroscopic techniques [17, 18], and evanescent waves [19, 20]. Particularly interesting are the experiments aimed at stabilising the position of the trapped particle using techniques based on feedback [21]. Indeed, feedback mechanisms are widely used in science and technology, for example in haptic optical tweezers [22], laser cooling of single atoms [23], cavity optomechanics [24], and laser cooling of particles in vacuum [25]. These feedback mechanisms are typically implemented by actively controlling the optical tweezers with external setups, such as acousto-optics or electro-optics devices, while trapping the particle outside the laser cavity. Therefore, the dynamics of the laser is independent from that of the Brownian motion of the particle.

In this thesis a novel optical tweezers is studied: unlike conventional OT the particle is trapped in an optical waist made inside the laser cavity itself. This kind of optical trapping, called *intracavity optical tweezers* (IOT) and proposed and realized by the group of G. Volpe [26], is the main object of this work. The basic idea of IOT is the following. When the particle is in the beam waist inside the laser cavity, it introduces additional losses caused by the particle scattering. This leads to a decrease of the laser power which tends to release the particle. As the particle moves away from the waist, the losses are reduced and the laser power tends to return to its maximum value bringing the particle back to the focal point. This mechanism represents an intrinsic feedback which, together with the optical gradient, contributes to enhance the trapping efficiency.

In this thesis work, new intracavity trapping configurations are explored using a ring fibre laser. Starting from the study of an IOT in which only one laser beam oscillates in the laser cavity (single-beam configuration), the system is modified to produce a two counter-propagating beams configuration [27]. In this configuration, the intrinsic feedback effect correlates the power of the two beams that oscillate simultaneously in the cavity. Then a particularly interesting case is studied where, by introducing a small misalignment of the two beams, two traps separated by a few micrometers are made. In this way, it is possible to study the transitions of the trapped particle between the two traps, due to their competition, in the presence of optical feedback.

An important aspect of cavity trapping concerns the Brownian motion which animates the trapped particle, which is typically immersed in water. In this case, the motion of the trapped particle is described by the Langevin equation of an overdamped harmonic oscillator characterised by a timescale of the displacement of the particle of some ms. This timescale is quite longer than the response time of the laser system, which is typically of few ns, guaranteeing that the laser system is always in its steady-state. In order to investigate the behaviour of the IOT when these two times are comparable, it would be necessary to trap in vacuum, which allows also to study quantum mechanics effects [12, 13]. In this thesis work, an intermediate step towards this direction is realised developing an IOT that traps particles in air. Compared to trapping in water, this has required a non-trivial system for loading particles into the intracavity trap based on piezoelectric crystals. When a piezoelectric crystal vibrates at the right frequency, the particles, which are stuck on their supporting surface because of the Van der Waals force, can be detached and loaded into the trap.

After introducing the theoretical basis of optical forces and the motion of a trapped particle in chapters 1 and 2, the IOT theory is described in chapter 3, in which a toy model is also studied that, in this work, is modified to overcome some of its limitations. In chapter 4 are described the experimental setups designed and realised for this thesis. After introducing the data analysis in chapter 5, the results for standard OT and IOT are presented in chapter 6.

Chapter 1

Optical forces

Optical forces, described by Maxwell's electromagnetic laws, stem from the light-matter interaction and, in particular, from conservation of electromagnetic and mechanical momentum. Considering the interaction between a particle and an optical field, the theoretical description of the optical forces depends on the ratio between the characteristic linear dimension of the particle a and the light wavelength λ. It is possible to distinguish three regimes: the *geometric optics or ray optics* regime, valid if $\lambda \ll a$; the *dipole* regime characterised by $\lambda \gg a$; the *intermediate* regime when $\lambda \sim a$. These three regimes are discussed in the first three sections of this chapter. The last section is a summary of the results obtained in order to highlight the differences between the three regimes.

1.1 Ray optics regime

The geometric optics regime is valid when the linear dimension of the particle is much larger than the wavelength of the light field, which can be consider as a set of *optical rays* because the volume occupied by the particle encloses many spatial periods of the optical field. In this picture, the light-matter interaction is described by optical rays impinging on the separation surface between the particle and the surrounding medium. According to Snell's law ([28]), part of each ray is reflected and part transmitted so that:

$$\theta_r = \theta_i \tag{1.1}$$

$$n_t \sin\theta_t = n_i \sin\theta_i \tag{1.2}$$

where n_i and n_t are the refractive indexes of the medium and of the particle, respectively. Instead, θ_i is the angle of incidence, θ_r the angle of reflection, and θ_t the angle of refraction as shown in Fig. 1.1. The intensity I_i of the incident ray is split into the reflected ray, with intensity I_r, and the transmitted ray, with intensity I_t, according to Fresnel's laws ([28]), that give the expression of reflectance $R = I_r/I_i$

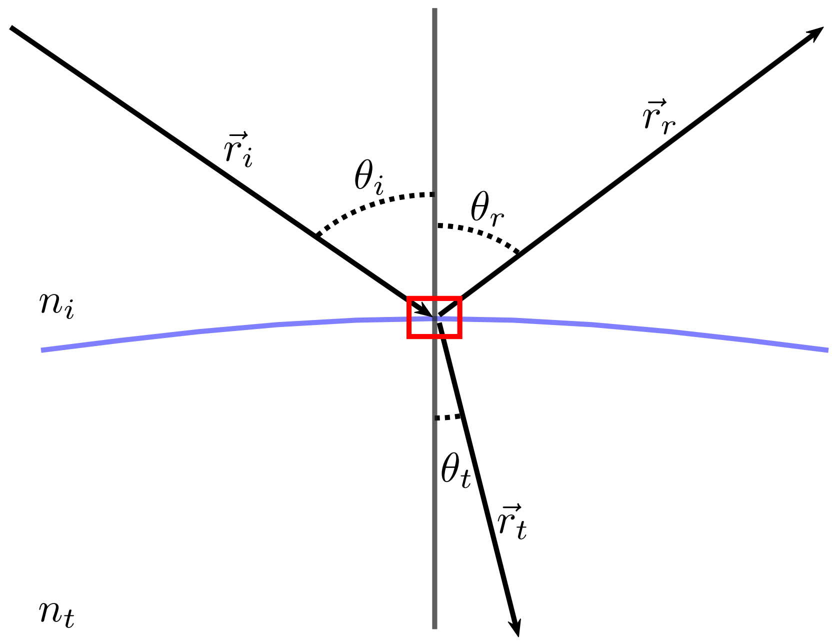

Figure 1.1: representation of an incidence ray impinging on a generic separation surface between two medium where $\vec{r}_i$, $\vec{r}_r$, and $\vec{r}_t$ indicate the direction of the incidence, reflected, and transmitted rays, respectively. The corresponding angles are indicated by θ_i, θ_r, and θ_t. The red square indicates the impinging region that is well approximated by a plane.

and transmittance $T = I_t/I_i$, i.e.

$$R_s = \left|\frac{n_i \cos\theta_i - n_t \cos\theta_t}{n_i \cos\theta_i + n_t \cos\theta_t}\right|^2 \quad T_s = \frac{4 n_i n_t \cos\theta_i \cos\theta_t}{|n_i \cos\theta_i + n_t \cos\theta_t|^2} \tag{1.3}$$

$$R_p = \left|\frac{n_i \cos\theta_t - n_t \cos\theta_i}{n_i \cos\theta_t + n_t \cos\theta_i}\right|^2 \quad T_p = \frac{4 n_i n_t \cos\theta_i \cos\theta_t}{|n_i \cos\theta_t + n_t \cos\theta_i|^2} \tag{1.4}$$

where the subscript s indicates a s-polarized wave (electric field orthogonal to incidence plane), and p a p-polarized wave (magnetic field orthogonal to the incidence plane).

In order to understand the origin of the optical forces, the simple situation of an optical ray of power P_i impinging perpendicularly ($\theta_i = 0$) on a mirror is considered. The incident ray is described as a flux of $N = P_i\lambda_0/(hc)$ photons carrying a momentum of

$$\vec{p}_i = (h/\lambda_0)\hat{u} \tag{1.5}$$

where h is the Planck constant, λ_0 the wavelength in vacuum of the light field, and c is the speed of light in vacuum. In this condition, a photon impinging on the mirror is completely reflected back and its momentum changes from $\vec{p}_i$ to $\vec{p}_r = -\vec{p}_i$ implying a momentum variation per unit time of $\Delta_t\vec{p} = -2\vec{p}_{\lambda_0}$. Consequently, the mirror undergoes to a momentum variation per unit time of $\Delta_t\vec{p}_m = -\Delta_t\vec{p} = 2\vec{p}_{\lambda_0}$

for each photon and the recoil force on the mirror is

$$\vec{F}_g = N\Delta_t \vec{p}_m = 2N\vec{p}_{\lambda_0} = \frac{2P_i}{c}\hat{u} \tag{1.6}$$

This force depends only on the power of the optical field and, as expected, does not depend on the wave nature of the light, i.e. the wavelength. Typically, the force of equation (1.6) is very weak even for high values of the power. For example, if the power is $P_i = 15.0\,\mathrm{mW}$, the force acting on the mirror is

$$\vec{F}_g = \frac{2P_i}{c} \simeq \frac{2\cdot 15.0\,\mathrm{W}}{3.00\cdot 10^8\,\mathrm{m}}\mathrm{s} \sim 10^{-10}\mathrm{N} \tag{1.7}$$

which would accelerate a reflecting disk of $1\,\mathrm{g}$ in vacuum by

$$|\vec{a}_g| = \frac{\left|\vec{F}_g\right|}{m} \sim 10^{-7}\frac{\mathrm{m}}{\mathrm{s}^2} \tag{1.8}$$

explaining why the first experiments about optical forces on macroscopic objects done by Lebedev, Nichols, and Hull were strongly questioned [3, 4]. Instead, the optical forces have non-negligible effects interacting with micrometric particles. Indeed, the same force of equation (1.7) accelerates a metallic micrometric particle of radius $10\,\mu\mathrm{m}$ of

$$|\vec{a}_g| = \frac{\left|\vec{F}_g\right|}{m} \sim 1\frac{\mathrm{m}}{\mathrm{s}^2} \tag{1.9}$$

Furthermore, this condition gives the maximum force that an optical ray can produce because, when an optical ray of power P_i impinges with non-normal incidence, the total force acting on the incidence point is given by the sum of the force produced by the reflected and transmitted rays. Thus, generalizing equation (1.6), the force is given by

$$\vec{F}_g = \frac{n_i P_i}{c}\frac{\vec{r}_i}{|\vec{r}_i|} - \frac{n_i P_r}{c}\frac{\vec{r}_r}{|\vec{r}_r|} - \frac{n_i P_t}{c}\frac{\vec{r}_t}{|\vec{r}_t|} \tag{1.10}$$

where the Minkowski's definition of light momentum is employed[1]. This relation, although more general than equation (1.6), does not take in account the finite size of the object interacting with the light field.

When an optical ray impinges on a finite size object, multiple reflections and transmissions can happen and the incidence angle depends on the position in which the ray impinges on the object itself, which is typically a micrometric sphere. The force can be calculated starting from the single ray interaction. Initially, the ray travels along the direction $\vec{r}_i$ with power P_i and, when the ray impinges on the sphere

[1]The momentum of the light in a medium (not in vacuum) can be defined in two ways: Abraham, observing that the photon momentum is proportional to its velocity, obtained $p = h/(n\lambda_0)$, because the photon velocity is reduced to $v = c/n$; Minkowski, starting from the photon momentum definition in vacuum $p = h/\lambda_0$ and because in a medium the wavelength becomes $\lambda = \lambda_0/n$, obtained $p = h/\lambda = hn/\lambda_0$. This is known as *Abraham-Minkowski dilemma*.

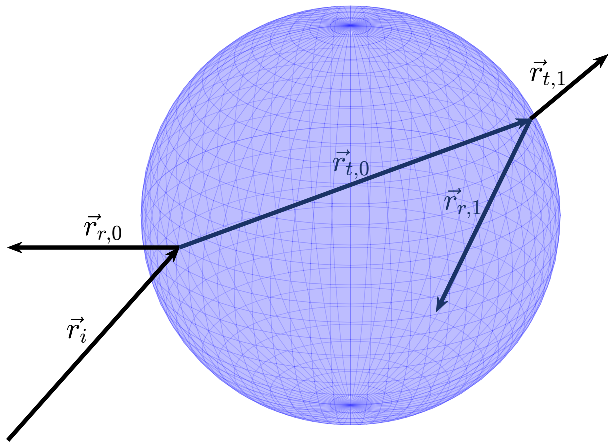

Figure 1.2: multiple reflections inside a sphere, where the incidence ray travels along $\vec{r}_i$, the first reflected ray along $\vec{r}_{r,0}$, the first transmitted ray inside the sphere along $\vec{r}_{t,0}$, the other rays travelling inside the sphere along $\vec{r}_{r,j}$ ($j = 1, 2$), and the ones travelling outside the sphere along $\vec{r}_{t,j}$.

(scattering event), its power is split between the reflected ray travelling along $\vec{r}_{r,0}$ and the transmitted ray travelling along $\vec{r}_{t,0}$ inside the sphere. The transmitted ray travels until it impinges on the surface of the sphere, producing again two rays: a reflected ray travelling along $\vec{r}_{r,1}$ inside the sphere and a transmitted ray travelling along $\vec{r}_{t,1}$ outside the sphere, like in figure 1.2. The ray travelling along $\vec{r}_{r,1}$ will impinge on the surface of the sphere producing two more rays, and this process continues until, after infinite iterations, all the light is transmitted outside the sphere. Thus, the total force is calculated applying equation (1.10) for each scattering event, giving

$$\vec{F}_g = \frac{n_i P_i}{c}\frac{\vec{r}_i}{|\vec{r}_i|} - \frac{n_i P_r}{c}\frac{\vec{r}_{r,0}}{|\vec{r}_{r,0}|} - \sum_{j=1}^{\infty}\frac{n_i P_{t,j}}{c}\frac{\vec{r}_{t,j}}{|\vec{r}_{t,j}|} \tag{1.11}$$

This force lies in the incidence plane because it is defined by a converging series[2] of vectors staying in the incidence plane. This allows to split the force along the direction of $\vec{r}_i$ and along its perpendicular direction $\vec{r}_\perp$, that is

$$\vec{F}_g = \left|\vec{F}_{g,\mathrm{scat}}\right|\frac{\vec{r}_i}{|\vec{r}_i|} + \left|\vec{F}_{g,\mathrm{grad}}\right|\frac{\vec{r}_\perp}{|\vec{r}_\perp|} \tag{1.12}$$

where the force along the incidence direction $\vec{F}_{g,\mathrm{scat}}$ is called *scattering force* and $\vec{F}_{g,\mathrm{grad}}$ is called *gradient force*. Therefore, the gradient force is the force that can trap stably the particle. The scattering and gradient forces of a circularly polarised

[2]The convergence of this series is assured by the energy conservation.

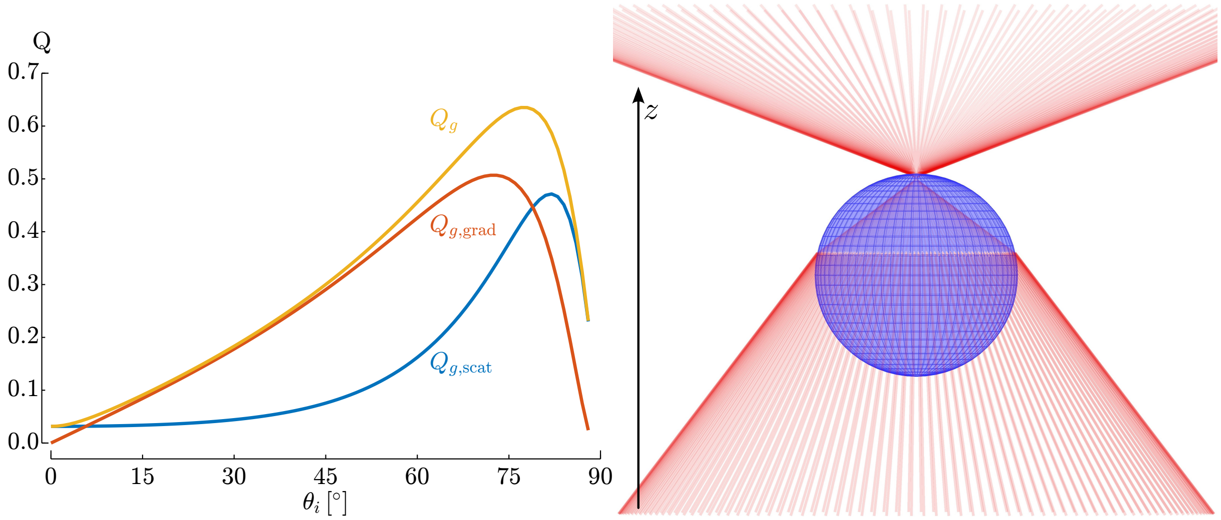

(a) (b)

Figure 1.3: (a) trapping efficiencies Q as function of the angle of incidence θ_i of the optical ray for a particle of refractive index $n_t = 1.59$ immersed in water, $n_i = 1.33$; (b) optical trap diagram in ray optics regime focusing a laser beam along the z axis (solid black arrow).

ray on a sphere were derived by Ashkin [29]:

$$F_{g,\text{scat}} = \frac{n_i P_i}{c}\left[1 + R\cos 2\theta_i - T^2\frac{\cos(2\theta_i - 2\theta_r) + R\cos 2\theta_i}{1 + R^2 + 2R\cos 2\theta_r}\right] \tag{1.13}$$

$$F_{g,\text{grad}} = \frac{n_i P_i}{c}\left[R\sin 2\theta_i - T^2\frac{\sin(2\theta_i - 2\theta_r) + R\sin 2\theta_i}{1 + R^2 + 2R\cos 2\theta_r}\right] \tag{1.14}$$

To better understand the physical conditions that allows to trap a particle, the *trapping efficiencies* are defined as

$$Q_{g,\text{scat}} = \frac{c}{n_i P_i} F_{g,\text{scat}} \tag{1.15}$$

$$Q_{g,\text{grad}} = \frac{c}{n_i P_i} F_{g,\text{grad}} \tag{1.16}$$

$$Q_g = \sqrt{Q_{g,\text{scat}}^2 + Q_{g,\text{grad}}^2} \tag{1.17}$$

that are dimensionless quantities describing the way in which the momentum is transferred from the optical ray to the particle. As shown in figure 1.3a, $Q_{g,\text{grad}}$ grows faster than $Q_{g,\text{scat}}$ as function of the incidence angle θ_i indicating that the trapping condition is due principally to the rays with high incidence angles.

Equation (1.11), as said, is relative to only one ray, but typically the particle interacts with all the rays exiting from the wavefront point-by-point along $\vec{r}_m$, as schematically shown in figure 1.3b. Each of these rays produce a force according to

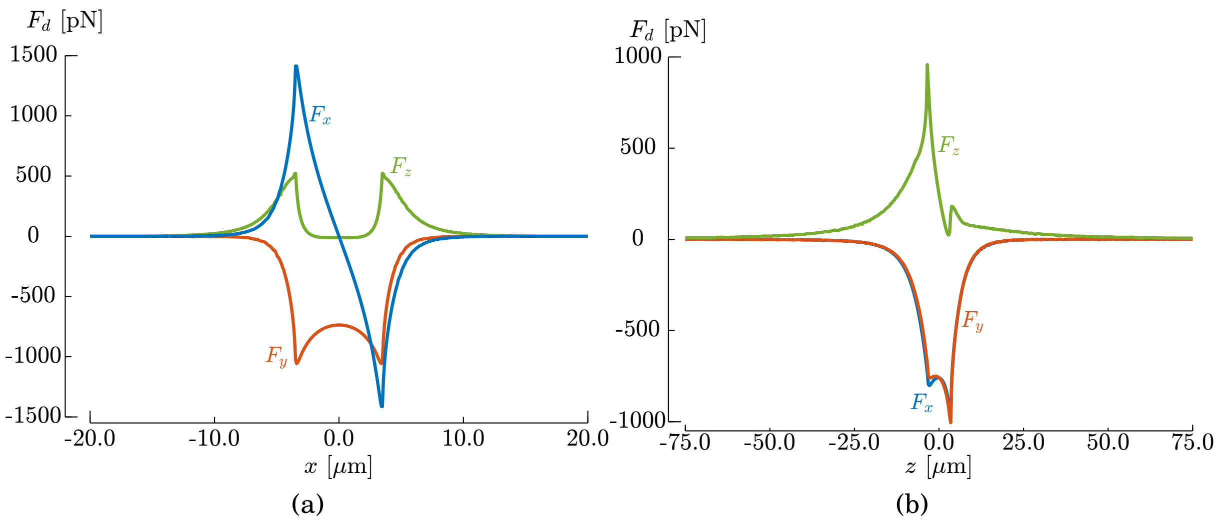

Figure 1.4: F_x (blue solid line), F_y (orange solid line), and F_z (green solid line) components of the trapping force $\vec{F}_d$ acting on a particle of radius $5\,\mu$m and refractive index $n_p = 1.59$ illuminated by a $1064\,$nm TEM$_{00}$ laser beam and trapped in water if (a) the particle is moving only along x with $y = z = 0.05\,\mu$m and (b) only along z and with $x = y = 0.05\,\mu$m. These plots are obtained numerically with the MATLAB tool *Optical Tweezers in Geometrical Optics* (OTGO) [30].

equation (1.11) and the total force acting on the mass centre of the particle is ([31], chapter 2.5)

$$\vec{F}_g = \sum_m \vec{F}_g^{(m)} = \sum_m \left(\frac{n_i P_i^{(m)}}{c} \frac{\vec{r}_i^{(m)}}{\left|\vec{r}_i^{(m)}\right|} - \frac{n_i P_r^{(m)}}{c} \frac{\vec{r}_{r,0}^{(m)}}{\left|\vec{r}_{r,0}^{(m)}\right|} - \sum_{j=1}^{\infty} \frac{n_i P_{t,j}^{(m)}}{c} \frac{\vec{r}_{t,j}^{(m)}}{\left|\vec{r}_{t,j}^{(m)}\right|} \right) \tag{1.18}$$

that can be again divided into scattering and gradient forces. When the particle interacts with a wavefront, therefore, its size is a fundamental parameter. Indeed, if the particle is larger than the wavefront spot size on the particle surface, all the rays have a small incidence angle and the gradient force is weaker than the scattering one as shown previously. Instead, if the wavefront spot on the particle is comparable with the particle size, the rays having a large incidence angle are sufficient to produce a gradient force that overcome the scattering one (trapping condition). The components of the trapping force acting on a particle of radius $5\,\mu$m and of refractive index $n_p = 1.59$ illuminated by a $1064\,$nm TEM$_{00}$ laser beam travelling along the z direction are shown in figure 1.4a as function of the x direction ($y = z = 0.05\,\mu$m) and in figure 1.4b as function of the z direction ($x = y = 0.05\,\mu$m).

If the incident rays converge to a point (strongly focused light beams) and the particle has a suitable refractive index, equation (1.18) ([31], chapter 2.5) has an equilibrium position (trapping position) and, for small displacement from the equilibrium position, the force is

$$\vec{F}_g = -\vec{k}_g \cdot (\vec{r} - \vec{r}_{eq})\hat{r} \tag{1.19}$$

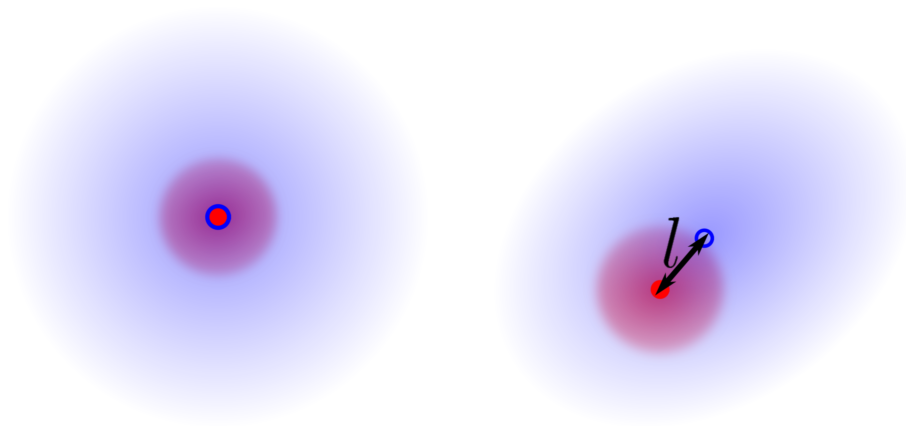

Figure 1.5: (a) illustration of a particle considered like a pair of charged clouds; (b) illustration of the same particle in the presence of an external electromagnetic field. The blue cloud represents the negative charges and the red one the positive charges, while the red circle represents the centre of the positive charges and the blue circle the centre of the negative charges.

where $\vec{k}_g = (k_{g,x}, k_{g,y}, k_{g,z})$ is the *trap stiffness* along the three axis and $\vec{r}_{eq}$ is the equilibrium position vector.

1.2 Dipole regime

The dipole regime occurs when the wavelength of the light field λ is much greater than the particle size and, therefore, its volume encloses small fractions of a spatial period of the light field. For this reason, the particle can be considered like a pair of charged clouds, schematically reported in Figure 1.5a, that interact with the optical field thorough the *induced dipole* phenomenon. Indeed, the electromagnetic field separates the centre of positive and negative charges deforming the clouds, like in figure 1.5b and, therefore, the particle behaves like a pair of point charges with equal magnitude q and opposite sign, separated by a distance l, i.e. like a *dipole*. If the electromagnetic fields $\vec{\mathscr{E}}_i(t,\vec{r})$ and $\vec{\mathscr{B}}_i(t,\vec{r})$ interact with the dipole, the total force acting on its centre of mass, indicated by the vector $\vec{r}_d$, is [31]

$$\vec{F}_d(t,\vec{r}_d) = \left(\vec{\mathfrak{d}} \cdot \vec{\nabla}\right) \vec{\mathscr{E}}_i(t,\vec{r}_d) + \frac{d\vec{\mathfrak{d}}}{dt} \wedge \vec{\mathscr{B}}_i(t,\vec{r}_d) + \frac{d\vec{r}_d}{dt} \wedge \left(\vec{\mathfrak{d}} \cdot \vec{\nabla}\right) \vec{\mathscr{B}}_i(t,\vec{r}_d) \tag{1.20}$$

where

$$\vec{\mathfrak{d}} = q\Delta\vec{r} \tag{1.21}$$

is the dipole moment, $\Delta\vec{r} \equiv \vec{r}_+ - \vec{r}_- = l$ with $\vec{r}_\pm$ the position of the two charged particles forming the dipole. Assuming to work in the non-relativistic regime, using the Maxwell equations, equation (1.20) becomes

$$\vec{F}_d(t,\vec{r}_d) = \left(\vec{\mathfrak{d}}\cdot\vec{\nabla}\right)\vec{\mathscr{E}}_i(t,\vec{r}_d) + \frac{d}{dt}\left(\vec{\mathfrak{d}}\wedge\vec{\mathscr{B}}_i(t,\vec{r}_d)\right) + \vec{\mathfrak{d}}\wedge\left(\vec{\nabla}\wedge\vec{\mathscr{E}}_i\right) \tag{1.22}$$

Experimentally, the time average of equation (1.22) is the measured physical quantity[3] and it is

$$\overline{\vec{F}_d(\vec{r}_d)} = \sum_{j=x,y,z}\left\langle \mathfrak{d}_j\vec{\nabla}\mathscr{E}_{i,j}(t,\vec{r}_d)\right\rangle \tag{1.23}$$

being $\left\langle \frac{d}{dt}\left(\vec{\mathfrak{d}}\wedge\vec{\mathscr{B}}_i(t,\vec{r}_d)\right)\right\rangle = 0.$[4]

In order to clarify the physical meaning of this equation, it useful to study the simple case of a monochromatic optical field of frequency ν propagating in vacuum, i.e.

$$\vec{\mathscr{E}}_i(t,\vec{r}) = \frac{1}{2}\left(\vec{E}_i(\vec{r})e^{i2\pi\nu t} + c.c.\right) \tag{1.24}$$

where $c.c.$ indicates the complex conjugate and $\vec{E}_i$ is the wave phasor, and of a spherical particle of radius a and volume V consisting of a homogeneous and uniform material of permittivity $\epsilon = \epsilon_r\epsilon_0$. In this case, the dipole moment is given by

$$\vec{\mathfrak{d}}(\vec{r}_d) = \alpha_d\vec{E}_i(\vec{r}_d) = \frac{\alpha_{CM}}{1-\frac{\epsilon_r-1}{\epsilon_r+2}\left[(k_0a)^2+\frac{2}{3}i(k_0a)^3\right]}\vec{E}_i(\vec{r}_d) = (\alpha'_d + i\alpha''_d)\vec{E}_i(\vec{r}_d) \tag{1.25}$$

where $k_0 = 2\pi/\lambda_0$ is the wavenumber, $\alpha_{CM} = 3V\epsilon_0\frac{\epsilon_r-1}{\epsilon_r+2}$ is the *Clausius-Mossotti relation*, α'_d and α''_d are the real and imaginary part of α_d respectively. All these simplifications allow, after some mathematical manipulations, to extrapolate the following force expression [31]

$$\overline{\vec{F}_d(\vec{r}_d)} = \frac{1}{4}\alpha'_d\vec{\nabla}\left|\vec{E}_i\right|^2 + \frac{\sigma_{ext,d}}{c}\vec{S}_i - \frac{1}{2}\sigma_{ext,d}\vec{\nabla}\wedge\vec{\mathfrak{z}} \tag{1.26}$$

where $\sigma_{ext,d} \equiv k_0\alpha''_d/\epsilon_0$ is the *extinction cross section* of the field describing the rate at which the energy of the electromagnetic wave is dissipated by absorption and scattering, $\vec{S}$ is the Poynting's vector, and $\vec{\mathfrak{z}}$ is the *spin density* defined as

$$\vec{\mathfrak{z}} = \int \epsilon_0\vec{\mathscr{E}}_\perp\wedge\vec{A}\,dV \xrightarrow{\text{monochromatic wave}} \vec{\mathfrak{z}} = i\frac{\epsilon_0}{2\omega}\vec{E}_i\wedge\vec{E}_i^* \tag{1.27}$$

with $\vec{A}$ the magnetic vector potential.

The first term of equation (1.26) is called *gradient force*, being related to the gradient of the square of the electric field magnitude, and it can be rewritten for a monochromatic field with intensity $I_i = \frac{c\epsilon_0}{2}\left|\vec{E}_i\right|$ as

$$\vec{F}_{d,grad}(\vec{r}_d) = \frac{\alpha'_d}{2c\epsilon_0}\vec{\nabla}\left[I_i(\vec{r}_d)\right]^2 \tag{1.28}$$

[3]The responsiveness of common instruments is not sufficient to measure at optical frequencies, typically between 10^{17} Hz and 10^{18} Hz, and therefore the measured quantities are time averaged.

[4]The time average of this total derivative is zero, because it is proportional to the difference between $\vec{\mathfrak{d}}\wedge\vec{\mathscr{B}}_i(t,\vec{r}_d)$ evaluated at t and at $t+T$. From the definition of time average, therefore, this term is zero.

This force is a conservative force since it is due to the potential energy of the dipole in the electric field and it can trap a particle if the optical field is strongly focused. In this condition, the optical field gradient is directed towards the focal point (*trapping position*) and produces a gradient force bigger than the other forces ensuring the confinement of the particle.

The second term of equation (1.26) is

$$\vec{F}_{d,scatt} = \frac{\sigma_{ext,d}}{c}\vec{S}_i \tag{1.29}$$

and it is called *scattering force*, being defined by the extinction cross section and the Poynting vector. This force has the same direction of the Poynting vector pushing the particle away along the beam direction and it is *non-conservative*, because it arises from the exchange of momentum due to scattering and absorption phenomena[5].

The last term of equation (1.26) is

$$\vec{F}_{d,s-r}(\vec{r}_d) = -\frac{1}{2}\sigma_{ext,d}\vec{\nabla} \wedge \vec{\jmath} \tag{1.30}$$

is called *spin-curl force* arising from the polarization of the electromagnetic field. Therefore, this force is present only if the field polarisation is non-homogeneous, as can be demonstrated by developing the curl of $\jmath$ defined by (1.27), and it is *non-conservative*.

Equation (1.26), obtained in vacuum, can be extended to the case of a particle immersed in a medium interacting with the electromagnetic field. Indeed, considering a monochromatic field in a homogeneous and isotropic medium of permittivity ϵ_m, equation (1.25) becomes

$$\vec{\mathfrak{d}}(\vec{r}_d) = \tilde{\alpha}_d\vec{E}_i(\vec{r}_d) = \frac{\tilde{\alpha}_{CM}}{1 - \frac{m^2-1}{m^2+2}\left[(k_0a)^2 + \frac{2}{3}i(k_0a)^3\right]}\vec{E}_i(\vec{r}_d) \equiv (\tilde{\alpha}'_d + i\tilde{\alpha}''_d)\vec{E}_i(\vec{r}_d) \tag{1.31}$$

with $\tilde{\alpha}_{CM} = 3V\epsilon_0\epsilon_m\frac{m^2-1}{m^2+2}$, $m^2 \equiv \epsilon_r/\epsilon_m$, and ([31], chapter 3.4)

$$\tilde{\alpha}'_d = \frac{\tilde{\alpha}_{CM}}{1 + \left(\dfrac{k_0^3\tilde{\alpha}_{CM}}{6\pi\epsilon_0}\right)^2} \sim \tilde{\alpha}_{CM} \tag{1.32}$$

$$\tilde{\alpha}''_d = \frac{k_0^3\tilde{\alpha}_{CM}^2}{6\pi\epsilon_0}\frac{1}{1 + \left(\dfrac{k_0^3\tilde{\alpha}_{CM}}{6\pi\epsilon_0}\right)^2} \sim \frac{k_0^3\tilde{\alpha}_{CM}^2}{6\pi\epsilon_0} \tag{1.33}$$

being $k_0a \ll 1$. These simplifications allow to deploy the dependence of the gradient force on m, being

$$\vec{F}_{d,grad}(\vec{r}_d) \sim \frac{1}{4}\tilde{\alpha}_{CM}\vec{\nabla}\left|\vec{E}_i(\vec{r}_d)\right|^2 = \pi a^3\epsilon_0\epsilon_m\frac{m^2-1}{m^2+2}\vec{\nabla}\left|\vec{E}_i(\vec{r}_d)\right|^2 \tag{1.34}$$

[5]To demonstrate that the scattering force is non-conservative, one can prove that its circulation is non-zero.

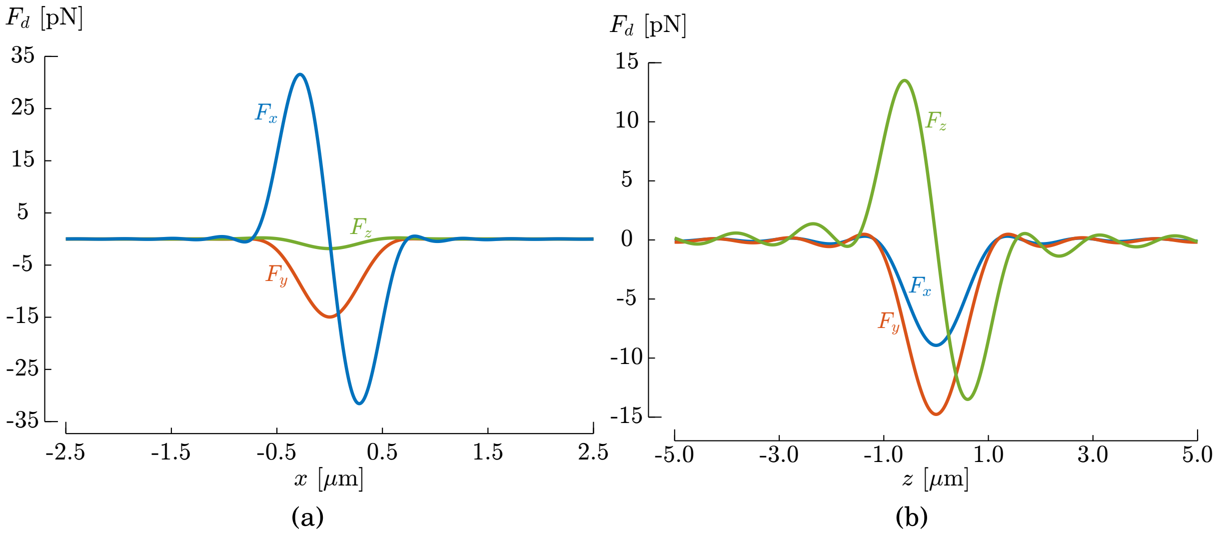

Figure 1.6: F_x (blue solid line), F_y (orange solid line), and F_z (green solid line) components of the trapping force $\vec{F}_d$ acting on a particle of radius $0.1\,\mu\mathrm{m}$ and of refractive index $n_p = 1.59$ illuminated by a $1064\,\mathrm{nm}$ TEM_{00} laser beam and trapped in water if (a) the particle is moving only along x with $y = z = 0.05\,\mu\mathrm{m}$ and (b) only along z and with $x = y = 0.05\,\mu\mathrm{m}$. This plot are obtained with numerical evaluation performed with *Optical Tweezers Software* (OTS) [31].

and of the scattering force, being

$$\vec{F}_{d,scatt} \sim \frac{k_0^4 \tilde{\alpha}_{CM}^2 \sqrt{\epsilon_m}}{6\pi\epsilon_0^2 c}\vec{S}_i = \frac{8}{3}\pi\frac{\sqrt{\epsilon_m}}{c}(k_0\sqrt{\epsilon_m})^4 a^6 \left(\frac{m^2-1}{m^2-2}\right)^2 \vec{S}_i \tag{1.35}$$

Immersion media and particle material are, hence, extremely important in the light-matter interaction and can completely change the equations of motion. Indeed, the gradient force changes its direction depending on the value of m, while the scattering force does not. In particular, the gradient force attracts the particles in the focal point of the light field if $m > 1$ and pushing the particle away if $m < 1$.

To conclude, the total optical force for monochromatic field with linear polarization is

$$\vec{F}_d = \pi a^3 \epsilon_0 \epsilon_m \frac{m^2-1}{m^2+2}\vec{\nabla}\left|\vec{E}_i(\vec{r}_d)\right|^2 + \frac{8}{3}\pi\frac{\sqrt{\epsilon_m}}{c}(k_0\sqrt{\epsilon_m})^4 a^6 \left(\frac{m^2-1}{m^2-2}\right)^2 \vec{S}_i \tag{1.36}$$

being the spin-curl force zero in this case. This expression clarifies the role of the particle dimensions in the dipole regime being the scattering force proportional to a^6 while the gradient one to a^3. This means that, if the trapped sphere is small enough, the scattering force will be much smaller than the gradient force and, therefore, the trap is more stable.

The components of the trapping force acting on a particle of radius $0.1\,\mu\mathrm{m}$ and of refractive index $n_p = 1.59$ immersed in water and illuminated by a $1064\,\mathrm{nm}$ TEM_{00}

laser beam are shown in figure 1.6a as function of x and in 1.6b as function of z. Also in the dipole regime, it is possible to demonstrate that equation (1.26) has, under the right conditions, an equilibrium point and that, for small displacement around it, the force can be written as the restoring force of a three-dimensional spring, i.e.

$$\vec{F}_d = -\vec{k}_d \cdot (\vec{r} - \vec{r}_{eq})\hat{r} \tag{1.37}$$

where $\vec{k}_d = (k_{d,x}, k_{d,y}, k_{d,z})$ is the *trap stiffness* along the three axis and $\vec{r}_{eq}$ is the equilibrium position vector.

1.3 Intermediate regime

The intermediate regime occurs when the wavelength of the light field λ is comparable to the linear dimension of the interacting object. In this case, the use of the rigorous electrodynamic tensor theory can not be omitted because neither can the object be consider a dipole nor can the wave nature of the electromagnetic field be ignored.

A particle, from the point of view of the electromagnetic field, appears as a distribution of charge density $\rho = \rho(t, \vec{r})$ and of current $\vec{j} = \vec{j}(t, \vec{r})$ contained in a volume V with border $S = \partial V$. The generalised Lorentz force allows to obtain the force on the particle and it is equal to [32]

$$\frac{d\vec{P}_m}{dt} = \int_V \left[\rho\vec{\mathscr{E}} + \vec{j} \wedge \vec{\mathscr{B}}\right] dV \tag{1.38}$$

where $\vec{P}_m$ is the mechanical momentum of the particle, $\vec{\mathscr{E}} = \vec{\mathscr{E}}(t, \vec{r})$ the electric field, and $\vec{\mathscr{B}} = \vec{\mathscr{B}}(t, \vec{r})$ the magnetic field. Using the Maxwell's equations in vacuum and making the expression symmetric with some mathematical calculations, the force is ([31], chapter 5.1)

$$\frac{d\vec{P}_m}{dt} = \int_V \epsilon_0 \left[(\vec{\nabla} \cdot \vec{\mathscr{E}})\vec{\mathscr{E}} - \vec{\mathscr{E}} \wedge \left(\vec{\nabla} \wedge \vec{\mathscr{E}}\right) - c^2\vec{\nabla}(\vec{\mathscr{B}} \cdot \vec{\mathscr{B}}) - \frac{\partial\vec{\mathscr{E}} \wedge \vec{\mathscr{B}}}{\partial t}\right] dV \tag{1.39}$$

The importance of having the symmetric equation (1.39) is to relate it to the Maxwell stress tensor $\boldsymbol{T}_M$. Remembering the following relations

$$\begin{cases} \vec{f}_{rad} = \frac{d}{dt}\left(\vec{P}_m + \vec{P}_c\right) = \int_V \vec{\nabla} \cdot \boldsymbol{T}_M dV \\ \int \epsilon_0 \frac{\partial\vec{\mathscr{E}} \wedge \vec{\mathscr{B}}}{\partial t} dV = \frac{d}{dt}\int_V \frac{\vec{S}}{c^2} dV = \frac{d\vec{P}_c}{dt} \end{cases} \tag{1.40}$$

it is natural to manipulate (1.39) as below

$$\frac{d\vec{P}_m}{dt} + \int_V \frac{\partial\vec{\mathscr{E}} \wedge \vec{\mathscr{B}}}{\partial t} dV = \int_V \epsilon_0 \left[(\vec{\nabla} \cdot \vec{\mathscr{E}})\vec{\mathscr{E}} - \vec{\mathscr{E}} \wedge \left(\vec{\nabla} \wedge \vec{\mathscr{E}}\right) - c^2\vec{\nabla}(\vec{\mathscr{B}} \cdot \vec{\mathscr{B}})\right] dV \tag{1.41}$$

In this way, the first term of this equation is the force acting on the particle, indicated as $\vec{f}_{rad} = \frac{d}{dt}\left(\vec{P}_m + \vec{P}_c\right)$ and, thus,

$$\vec{f}_{rad} = \frac{d}{dt}\left(\vec{P}_m + \vec{P}_c\right) = \int_V \vec{\nabla}\cdot\boldsymbol{T}_M dV = \int_V \epsilon_0 \left[(\vec{\nabla}\cdot\vec{\mathscr{E}})\vec{\mathscr{E}} - \vec{\mathscr{E}}\wedge\left(\vec{\nabla}\wedge\vec{\mathscr{E}}\right) - c^2\vec{\nabla}(\vec{\mathscr{B}}\cdot\vec{\mathscr{B}})\right] dV \quad (1.42)$$

Introducing the dyadic product as $\otimes$ and using the the vector identities, the force can be written as

$$\vec{f}_{rad} = \int_V \vec{\nabla}\cdot\boldsymbol{T}_M dV = \int_V \epsilon_0\vec{\nabla}\left[\vec{\mathscr{E}}\otimes\vec{\mathscr{E}} + c^2\vec{\mathscr{B}}\otimes\vec{\mathscr{B}} - \frac{1}{2}\left(\vec{\mathscr{E}}\cdot\vec{\mathscr{E}} + c^2\vec{\mathscr{B}}\cdot\vec{\mathscr{B}}\right)\mathbb{1}\right] dV$$

$$\Downarrow$$

$$\boldsymbol{T}_M = \epsilon_0\left[\vec{\mathscr{E}}\otimes\vec{\mathscr{E}} + c^2\vec{\mathscr{B}}\otimes\vec{\mathscr{B}} - \frac{1}{2}\left(\vec{\mathscr{E}}\cdot\vec{\mathscr{E}} + c^2\vec{\mathscr{B}}\cdot\vec{\mathscr{B}}\right)\mathbb{1}\right] \quad (1.43)$$

that, thanks to the Ostrogradskij's theorem and denoting by $d\vec{S}$ the vector with magnitude equal to the infinitesimal surface dS and direction orthogonal to the contour of V, can be written as

$$\vec{f}_{rad} = \oint_{\partial V} \boldsymbol{T}_M d\vec{S} \quad (1.44)$$

whose average over time returns the average force applied by the electromagnetic field on the particle, i.e.

$$\vec{F}_{rad} = \oint_{\partial V} \langle\boldsymbol{T}\rangle_M d\vec{S} \quad (1.45)$$

where $\langle\boldsymbol{T_M}\rangle$ denotes the time average of the Maxwell stress tensor.

Equation (1.45) is very general and, for this reason, difficult to apply, but it can be written in a simpler form for a sphere of radius r in a monochromatic field

$$\begin{cases} \vec{\mathscr{E}}_i(t,\vec{r}) = \frac{1}{2}\left(\vec{E}(\vec{r})e^{i\omega t} + c.c.\right) \\ \vec{\mathscr{B}}_i(t,\vec{r}) = \frac{1}{2}\left(\vec{B}(\vec{r})e^{i\omega t} + c.c.\right) \end{cases} \quad (1.46)$$

where $\vec{E}_i$ and $\vec{B}_i$ indicate the wave *phasors*. In this case, the time average of the Maxwell stress tensor is [31]

$$\langle\boldsymbol{T}_M\rangle = \frac{1}{2}\epsilon_i\,\Re\left[\vec{E}\otimes\vec{E}^* + \frac{c^2}{n_i^2}\vec{B}\otimes\vec{B}^* - \frac{1}{2}\left(\left|\vec{E}\right|^2 + \frac{c^2}{n_i^2}\left|\vec{B}\right|^2\right)\mathbb{1}\right] \quad (1.47)$$

and, therefore, the force of equation (1.45) becomes

$$\vec{F}_{rad} = \frac{1}{2}\epsilon r^2\,\Re\left\{\oint_{\partial V}\left[\vec{E}\otimes\vec{E}^* + \frac{c^2}{n_i^2}\vec{B}\otimes\vec{B}^* - \frac{1}{2}\left(\left|\vec{E}\right|^2 + \frac{c^2}{n_i^2}\left|\vec{B}\right|^2\right)\mathbb{1}\right]\cdot\vec{r}dS\right\} \quad (1.48)$$

where ϵ and n_i are the permittivity and the refractive index, respectively, of the medium in which the incident field propagates, and $\Re[\cdot]$ indicates the real part of its argument.

To give an explicit expression of the optical force, it is necessary to use the multipole expansion and the Mie theory, see appendix A, that returns an analytical expression of the field phasors when an electromagnetic wave interacts with a sphere or a cylinder. Therefore, equation (1.48) can be written as

$$\vec{F}_{rad} = -\frac{1}{4}\epsilon_i r^2 \oint_{\partial V} \left(\left|\vec{E}_s\right|^2 + \frac{c^2}{n_i^2}\left|\vec{B}_s\right|^2 + 2\Re\left[\vec{E}_i\vec{E}_s^* + \frac{c^2}{n_i^2}\vec{B}_i\vec{B}_s^*\right]\right)\vec{r}dS \tag{1.49}$$

where $\vec{E}_s$ are the phasors of the incident and the scattered electric field obtained in equation (A.10), and $\vec{B}_i$ and $\vec{B}_s$ are the phasors of the incident and the scattered magnetic field. Equation (1.49) tells us that the optical force acting is produced by the scattered electromagnetic field, due to the term $\left|\vec{E}_s\right|^2 + \frac{c^2}{n_i^2}\left|\vec{B}_s\right|^2$, and by the interference of the incident and scattered field, due to the term $2\Re\left[\vec{E}_i\vec{E}_s^* + \frac{c^2}{n_i^2}\vec{B}_i\vec{B}_s^*\right]$.

From the expressions of equation (A.12), which show the dependence of the diffuse field on the refractive index of the sphere and its radius a, it is clear that the optical force depends on both the geometrical-optical characteristics of the sphere and the wave nature of the field, unlike the other two regimes.

As with the two previous regimes, the optical force can be written, for small displacement from the equilibrium position, as

$$\vec{F}_{rad} = -\vec{k}_{rad}\cdot(\vec{r}-\vec{r}_{eq})\hat{r} \tag{1.50}$$

where $\vec{k}_{rad} = (k_{rad,x}, k_{rad,y}, k_{rad,z})$ is the *trap stiffness* along the three axis and $\vec{r}_{eq}$ is the equilibrium position vector.

1.4 Comparison of the three regimes

To summarise the results obtained in this chapter and highlights the differences of the three regimes, it is useful to compare the following expressions of the optical forces obtained previously:

$$\vec{F}_g = \sum_m \left(\frac{n_i P_i^{(m)}}{c}\frac{\vec{r}_i^{(m)}}{\left|\vec{r}_i^{(m)}\right|} - \frac{n_i P_r^{(m)}}{c}\frac{\vec{r}_{r,0}^{(m)}}{\left|\vec{r}_{r,0}^{(m)}\right|} - \sum_{j=1}^{\infty}\frac{n_i P_{t,j}^{(m)}}{c}\frac{\vec{r}_{t,j}^{(m)}}{\left|\vec{r}_{t,j}^{(m)}\right|}\right) \tag{1.51}$$

$$\vec{F}_d = \pi a^3\epsilon_0\epsilon_m\frac{m^2-1}{m^2+2}\vec{\nabla}\left|\vec{E}_i(\vec{r}_d)\right|^2 + \frac{8}{3}\pi\frac{\sqrt{\epsilon_m}}{c}(k_0\sqrt{\epsilon_m})^4 a^6\left(\frac{m^2-1}{m^2-2}\right)^2\vec{S}_i \tag{1.52}$$

$$\vec{F}_{rad} = -\frac{1}{4}\epsilon_i r^2 \oint_{\partial V} \left(\left|\vec{E}_s\right|^2 + \frac{c^2}{n_i^2}\left|\vec{B}_s\right|^2 + 2\Re\left[\vec{E}_i\vec{E}_s^* + \frac{c^2}{n_i^2}\vec{B}_i\vec{B}_s^*\right]\right)\vec{r}dS \tag{1.53}$$

This direct comparison between the forces shows some important differences:

- the optical force in the geometric regime is higher if the particle size is comparable to the light beam spot size on the particle. Therefore, it decreases

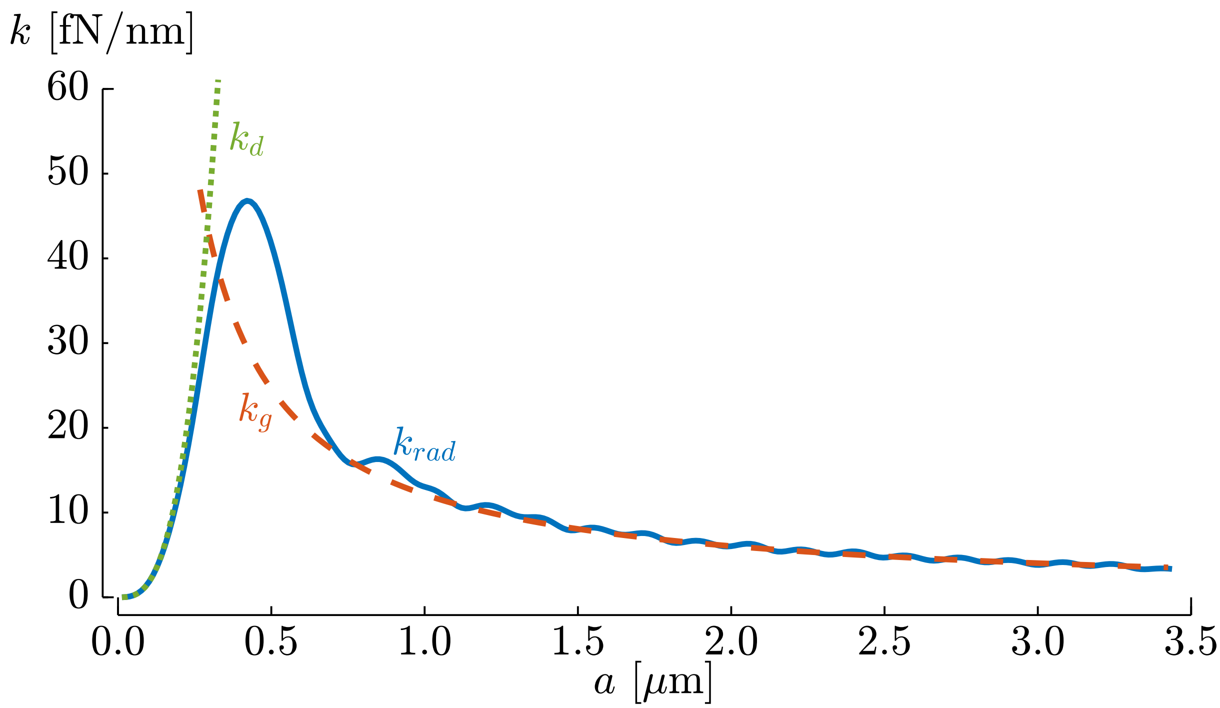

Figure 1.7: trap stiffness k as function of the particle radius a of a spherical particle trapped by a laser beam with power $10\,\mathrm{mW}$ and wavelength $\lambda_0 = 1064\,\mathrm{nm}$ focused by a lens with numerical aperture $\mathrm{NA} = 1.20$. The refractive index of the particle is $n_p = 1.50$ and it is trapped in water with refractive index $n_m = 1.33$. The blue solid line represents the intermediate regime solution, the dotted green line the ray optics regime solution and the dashed orange line the dipole regime solution. These calculations are performed with the *Optical Tweezers Software* (OTS) [31].

increasing the particle size because, as shown in chapter 1.1, the trapping condition is principally determined by the rays impinging on the sphere with high incidence angles;

- the optical force in the dipole regime, instead, is strongly dependent on the particle size and, being the scattering force proportional to particle volume to the square ($\propto a^6$ with a particle radius), the scattering force is very small compared to the gradient one (proportional to the particle volume) for small particles;

- the optical force in the intermediate regime is characterised by two contributions. The first is related to the scattered electromagnetic field only $\left(\left|\vec{E}_s\right|^2 + \frac{c^2}{n_i^2}\left|\vec{B}_s\right|^2\right)$ and the second on to the interference of the incident and scattered fields, because of the term $2\Re\left[\vec{E}_i\vec{E}_s^* + \frac{c^2}{n_i^2}\vec{B}_i\vec{B}_s^*\right]$.

Furthermore, the optical force, despite the regime in which it is calculated, can be written for small displacement around the equilibrium position as

$$\vec{F}_{rad} = -\vec{k}_{rad} \cdot (\vec{r} - \vec{r}_{eq})\hat{r} \tag{1.54}$$

where $\vec{k}_{rad} = (k_{rad,x}, k_{rad,y}, k_{rad,z})$ is the *trap stiffness* along the three axis and $\vec{r}_{eq}$ is the equilibrium position vector. Although it might appear from this analytical form that the forces of the three regimes are identical in this condition, the differences between the three regimes lie in the stiffnesses. Indeed, as can be seen from figure 1.7, the stiffness calculated for the three regimes as a function of the radius of the sphere a is very different depending on the approximation considered.

Chapter 2

Brownian motion of a trapped particle

A particle immersed in a fluid undergoes thermal collisions from the molecules of the fluid that lead to a random motion known as *Brownian motion*. Brownian motion was discovered by Robert Brown who studied the random movement of particles released by pollen grains in water. The theory of Brownian motion was developed by Bachelier in his doctoral thesis [33], by Einstein in his 1905 paper [34], by and Langevin in 1908 [35] and Smoluchowski in 1916 [36], but only in 1923 it was formulated as a stochastic process by Wiener [37]. Hence, when a particle is trapped with an optical tweezers, its motion is not only influenced by the optical forces, but also by a random force that makes it oscillate around the trapping position. The first section of this chapter deals with the Brownian motion of a free particle, while the second and third ones with the equation of motion of a trapped particle and of a particle in a double-well potential. In the last two sections, the case in which the particle inertia is non-negligible is discussed.

2.1 Brownian motion

Brownian motion (or *Brownian diffusion*) of a particle of mass m immersed in a homogeneous and isotropic fluid is caused by the multiple collisions of the particle with the $N-1$ constituents of the fluid, which are assumed to have size and mass much smaller than the particle. The equation of motion is obtained by solving the following Newton's equations

$$m_n \frac{d^2}{dt^2}\vec{r}_n = \vec{F}_n(\vec{r}_1, ..., \vec{r}_N) \tag{2.1}$$

where $n = 1, ..., N$ is an index specifying both the particle and the fluid constituents, $\vec{r}_n$ the position of all particles in the system, m_n their mass and $\vec{F}_n(\vec{r}_1, ..., \vec{r}_N)$ the overall force acting on the n-th particle.

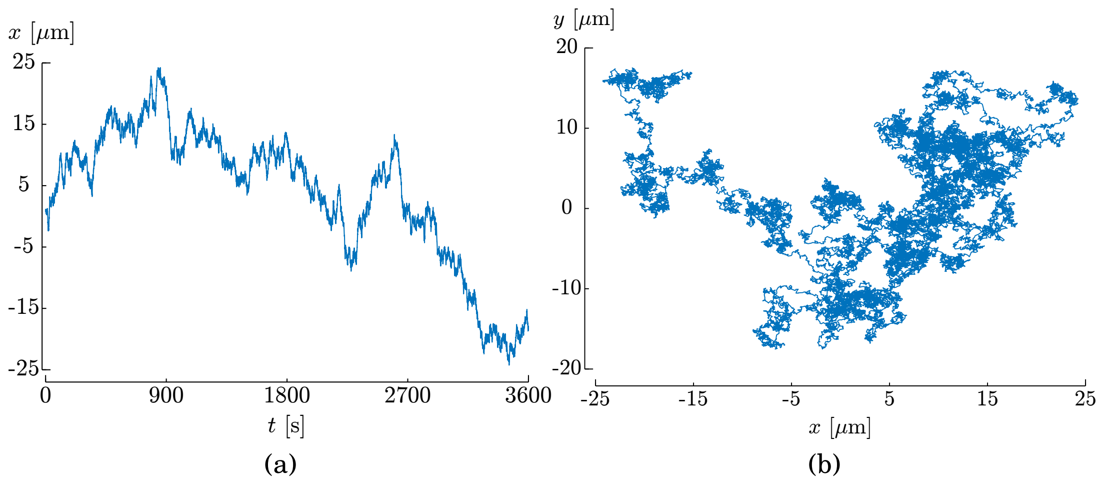

Figure 2.1: (a) x position as function of time t and (b) y position as function of x of an experimental trajectory of a silica particle of $3.16\,\mu\mathrm{m}$ diameter that is moving in water with Brownian motion.

Equation (2.1) is deterministic but, in practice, Brownian motion is unpredictable since N is of the order of magnitude of Avogadro's number. Therefore, it becomes necessary to study Brownian motion as a stochastic process observing that:

- the particle is on average stationary around its initial position, due to the isotropy and homogeneity of the fluid;
- the collisions at time t_1 are independent of those at time t_2, since the particle has a very large mass compared to that of the fluid constituents, i.e. there is a diffusion process without memory;
- the motion is continuous since the number of constituents is very high and the collisions very frequent, which makes it possible to state that the displacements distribution tends to be Gaussian according to the central limit theorem.

This stochastic process, indicated as W, is called *Wiener process* and it is defined by the properties:

- this process is zero for $t = 0$, i.e. $W(t = 0) = 0$;
- W has Gaussian increments: $W(t + u) - W(t),\ u \geq 0$ is normally distributed with zero mean and variance u;
- W has independent increments;
- W has only continuous path, i.e. $W(t)$ is continuous in t with probability 1.

A typical trajectory of a particle that undergoes Brownian motion is shown in figure 2.1a and 2.1b. Brownian motion can be studied using: the Langevin equation [35] that is based on considering in Newton's equation of motion a random force term, the free diffusion equation [34] that studies Brownian motion in its ensemble properties, or the Fokker-Planck equation [38] that generalise the free diffusion equation. Throughout this chapter, the one-dimensional case is considered being the n-dimensional generalisation straightforward.

2.1.1 Langevin equation

Langevin in 1908 [35] proposed a formalisation of the Brownian motion by introducing a random noise contribution into the Newton equation of motion of the particle. For a particle of mass m moving in a fluid with a viscosity coefficient η, the *Langevin equation* is given by

$$\begin{cases} \dfrac{dr(t)}{dt} = v(t) \\ \dfrac{dv(t)}{dt} = -\dfrac{\gamma}{m}v(t) + \dfrac{1}{m}\xi(t) \end{cases} \tag{2.2}$$

where $\xi(t)$ is the random force and $\gamma = 6\pi\eta a$ is the *particle friction coefficient* defined, for a sphere of radius a, by Stokes' law [39].

The random force $\xi(t)$ allows to explain the equilibrium properties of the system. Indeed, by exploiting the energy equipartition theorem, the expected value of v^2 is

$$E[v^2(t)]_{eq} = \frac{k_B T}{m} \tag{2.3}$$

which can not be obtained without the term $\xi(t)$, since the equation (2.2) with $\xi(t) = 0$ has the solution

$$v(t) = e^{-t/\tau_B}v(0) \Rightarrow E[v^2(t)]_{eq} = e^{-2t/\tau_B}E[v^2(0)]_{eq} \xrightarrow[t\to\infty]{} 0 \tag{2.4}$$

where $\tau_B = m/\gamma$. The random force $\xi(t)$ is a white noise and it has two important properties:

- the average value over all possible realisations of the noise, which is defined as $E[\xi(t)]_\xi$, is zero since the particle on average stays around the initial position due to the homogeneity and isotropy of the fluid;

- the motion has no memory effects, i.e. the autocorrelation of the motion is

  $$E[\xi(t_1)\xi(t_2)]_\xi = g\delta(t_1 - t_2) \tag{2.5}$$

  where g is called the correlation weight. As written above, the particle has a very large mass with respect to the mass of the fluid constituents and, therefore, the collisions at time t_1 are independent of those at time t_2.

These properties ensure that the Langevin equation describes a Wiener process satisfying all the definitions given previously.

As shown in appendix B, the correlation weight is

$$g = 2k_B T\gamma \tag{2.6}$$

and the random force $\xi(t)$ can be rewritten as

$$\xi(t) = \sqrt{2\gamma k_B T}\,\Xi(t) \tag{2.7}$$

where $\Xi(t)$ is a white noise random variable that satisfies the relations $E[\Xi(t)]_\Xi = 0$ and $E[\Xi(t_1)\Xi(t_2)]_\Xi = \delta(t_1 - t_2)$. Therefore, the Langevin equation can be rewritten as

$$\begin{cases} \dfrac{dr(t)}{dt} = v(t) \\ \dfrac{dv(t)}{dt} = -\dfrac{\gamma}{m}v(t) + \dfrac{\sqrt{2\gamma k_B T}}{m}\Xi(t) \end{cases} \tag{2.8}$$

Following the calculations done in appendix B, the solution of this equation with its derivative is given by:

$$\begin{cases} r(t) = r_0 + \dfrac{mv_0}{\gamma}\left(1 - e^{-\frac{\gamma}{m}t}\right) + \sqrt{\dfrac{2k_B T}{\gamma}}\left(\displaystyle\int_0^t \Xi(\tau)\,d\tau - \int_0^t \Xi(\tau)e^{\frac{\gamma}{m}\tau}\,d\tau e^{-\frac{\gamma}{m}t}\right) \\ v(t) = v_0 e^{-\frac{\gamma}{m}t} + \dfrac{\gamma}{m}\sqrt{\dfrac{2k_B T}{\gamma}}\displaystyle\int_0^t \Xi(\tau)e^{\frac{\gamma}{m}\tau}\,d\tau e^{-\frac{\gamma}{m}t} \end{cases} \tag{2.9}$$

where r_0 and v_0 are the initial conditions of the particle position and velocity. As shown in appendix B, equation (2.9) assures that $E[v^2(t)]_{eq}$ is

$$E[v(t)^2]_{eq} \xrightarrow[t\to\infty]{} \frac{k_B T}{m} \tag{2.10}$$

in agreement with the energy equipartition theorem.

Studying diffusion processes, it is useful to evaluate the expected value on all the realisations of the noise Ξ of the particle position $E[r(t)]_\Xi$ and the *mean squared displacement* $\mathrm{MSD}(\tau) = \mathrm{Var}[\Delta r(\tau)]$. Because in the experiments the initial position r_0 and the initial velocity v_0 are unknown and because of the properties of Brownian motion discussed before, r_0 and v_0 can be chosen as $r_0 = 0$ and $v_0 = \sqrt{k_B T/m}$. Therefore, the expected value of $r(t)$, following the calculation of appendix B, is

$$E[r(t)]_\Xi = \sqrt{\frac{k_B T}{m}}\frac{m}{\gamma}\left(1 - e^{-\frac{\gamma}{m}t}\right) \tag{2.11}$$

and the MSD is

$$\mathrm{MSD}(\tau) = \frac{2k_B T}{\gamma}\tau + \frac{2k_B T m}{\gamma^2}\left[e^{-\frac{\gamma}{m}\tau} - 1\right] \tag{2.12}$$

where τ is called *lag time*. Very often, the systems under analysis show a predominance of viscosity over inertia, i.e. $m\frac{dv(t)}{dt} \ll \gamma v(t)$ and, thus, the Langevin equation is

$$\gamma v(t) = \xi(t) \tag{2.13}$$

In this case, the MSD is

$$E[r^2(\tau)]_\Xi = \frac{2k_B T}{\gamma}\tau \tag{2.14}$$

and it increases linearly in time.

2.1.2 Free diffusion equation

The free diffusion equation arises when Brownian motion is studied in its ensemble properties. Assuming that the inertial effects are negligible, an ensemble of Brownian particles is characterised by the probability density function $\rho(t,r)$. To describe the time evolution of the ensemble it is necessary to study the distribution $\rho(t,r)$ when the time t increases by Δt, $\rho(t+\Delta t, r)$, and to define the probability $p_\xi(\xi)$ that a particle, during the time interval Δt, travels a distance ξ from the point $r-\xi$ to the point r . Once these concepts are introduced, the probability density distribution $p_\xi(\xi)$ for the ensemble is given by the relation [34]

$$\rho(t+\Delta t, r) = \int_{-\infty}^{+\infty} \rho(t, r-\xi) p_\xi(\xi) d\xi \tag{2.15}$$

Expanding in Taylor series at $\Delta t = 0$ and $\xi = 0$, this equation becomes (at the first non-zero order)

$$\frac{\partial \rho}{\partial t} = D\frac{\partial^2 \rho}{\partial r^2} \tag{2.16}$$

defined as *free diffusion equation*, where D, the *diffusion coefficient*, is

$$D = \int_{-\infty}^{+\infty} \xi^2 p_\xi(\xi) d\xi \tag{2.17}$$

It is easily demonstrated that if $\rho(r,0) = \delta(r)$, then

$$\rho(t,r) = \frac{1}{\sqrt{4\pi D t}} e^{-\frac{r^2}{4Dt}} \tag{2.18}$$

and that

$$\mathrm{MSD} = \int_{-\infty}^{\infty} r^2 \rho(t,r) dr = 2Dt \tag{2.19}$$

obtained using the properties of the Gamma function [40].

On average, Brownian particles tend to migrate to less populated regions causing a *particle current* $J_{diff}(t,r)$. Assuming that the number of particles is conserved, the following continuity relation is obtained

$$\frac{\partial \rho}{\partial t}(t,r) = -\frac{\partial J_{diff}}{\partial r}(t,r) \tag{2.20}$$

which once compared to the equation (2.16) gives the equation describing the link between J_{diff} and D, i.e.

$$J_{diff}(t,r) = -D\frac{\partial \rho}{\partial r}(t,r) \tag{2.21}$$

called *Fick's law*.

2.1.3 Fokker-Planck equation

The free diffusion equation describes the motion of an ensemble of free Brownian particles, but often these particles interacts with an external field. To take this into account, equation (2.16) is generalizable to the case where an external force $F(r) = -\frac{dU}{dr}(r)$ acts on the particles supposing that inertial effects are negligible. An external force produces a drift velocity $v_D(t,r) = F(t,r)/\gamma$ that changes the particle current

$$J_{\mathrm{diff}}(t,r) \to J(t,r) = J_{\mathrm{diff}}(t,r) + J_D(t,r) \tag{2.22}$$

where, by definition of current,

$$J_D(t,r) = v_D(t,r)\rho(t,r) \tag{2.23}$$

This leads to a modification of equation (2.20) using J instead of J_{diff}, i.e.

$$\frac{\partial \rho}{\partial t}(t,r) = -\frac{\partial J}{\partial r}(t,r) = D\frac{\partial^2 \rho}{\partial r^2}(t,r) - \frac{1}{\gamma}\frac{\partial [F(t,r)\rho(t,r)]}{\partial r} \tag{2.24}$$

called *Fokker-Planck equation*. In the case of a system at thermal equilibrium, the distribution $\rho(t,r)$ is given by the Maxwell-Boltzmann distribution,

$$\rho(r) = \rho_0 \exp\left[-\frac{U(r)}{k_B T}\right] \tag{2.25}$$

with ρ_0 a normalization factor, and the total diffusion is $J(t,r) = 0$, i.e.

$$J_{\mathrm{diff}}(t,r) = -J_D(t,r) \Rightarrow v_D(r)\rho(r) = D\frac{\partial \rho}{\partial r}(r) \tag{2.26}$$

Substituting into this equation the expression $v_D(r) = F(r)/\gamma$ and the derivative of the Maxwell-Boltzmann distribution $\frac{\partial \rho}{\partial r} = \frac{F(r)}{k_B T}\rho(r)$, the equation becomes

$$\frac{F(r)}{\gamma}\rho(r) = D\frac{F(r)}{k_B T}\rho(r) \tag{2.27}$$

giving

$$D = \frac{k_B T}{\gamma} \tag{2.28}$$

known as the *Stokes-Einstein* relation. Therefore the diffusion of a particle increases as the temperature of the thermal bath increases (the collisions between the particle and constituents of the fluid are more energetic) while decreases as the particle friction coefficient increases, which depends on the geometrical properties of the particle and the fluid viscosity.

The Fokker-Planck equation (2.24) is derived from the free diffusion equation obtained assuming that the inertial effects are negligible. To take into account the inertial effects and without going into the details of how to derive the Fokker-Planck equation for the general case, consider the n-dimensional stochastic process X that satisfies the stochastic differential equation

$$d\vec{X} = \vec{g}(t, \vec{X})dt + \hbar(t, \vec{X})d\vec{W} \tag{2.29}$$

where $\vec{W}$ is a m-dimensional Wiener process, $\vec{g}(t, \vec{X})$ is the n-dimensional drift vector, and $\hbar(t, \vec{X})$ is a $n \times m$ matrix that defines the diffusion coefficient matrix through the relation $\vec{D} = \frac{1}{2}\hbar \cdot \hbar^T$, in which $\cdot$ indicates the matrix multiplication and $\hbar^T$ is the transpose of $\hbar$. Under these assumptions, it is possible to demonstrate that the probability density function $\rho(t, \vec{x})$ of the stochastic process X satisfies the equation [38, 41, 42]

$$\frac{\partial \rho}{\partial t}(t, \vec{x}) = -\sum_{l=1}^{n} \frac{\partial}{\partial x_l}[g_l(t, \vec{x})\rho(t, \vec{x})] + \sum_{l=1}^{n}\sum_{j=1}^{n} \frac{\partial^2}{\partial x_l \partial x_j}[D_{i,j}(t, \vec{x})\rho(t, \vec{x})] \tag{2.30}$$

called *Fokker-Planck equation*, with $\vec{x} = (x_1, ..., x_n)$ the vector of the n independent variables. For Brownian motion, the stochastic differential equation is defined by the differential form of the Langevin equation (2.2), i.e.

$$dv = -\frac{\gamma}{m}v(t)dt + \frac{\sqrt{2\gamma k_B T}}{m}\xi(t)dt \tag{2.31}$$

which implies

$$\begin{cases} d\vec{X} = dv \\ g = -\dfrac{\gamma}{m}v(t) \\ \hbar = \dfrac{\sqrt{2\gamma k_B T}}{m} \\ d\vec{W} = \Xi dt \end{cases} \tag{2.32}$$

Therefore, the Fokker-Planck equation for Brownian motion is

$$\frac{\partial \rho}{\partial t} = \frac{\gamma}{m}\frac{\partial}{\partial v}(v\rho) + \frac{\gamma k_B T}{m^2}\frac{\partial^2 \rho}{\partial v^2} \tag{2.33}$$

Imposing the initial condition $\rho(t = 0) = \delta(v - v_0)$, which is valid because the particle at the initial time has velocity v_0, and performing the Fourier transform of (2.33), it is possible to demonstrate that the solution of the Fokker-Planck equation is [43, 44]

$$\rho(t, v) = \sqrt{\frac{m}{2\pi k_B T}} \frac{e^{-\frac{m}{2k_B T}\frac{\left(v - v_0 e^{-\frac{\gamma}{m}t}\right)^2}{1 - e^{-2\frac{\gamma}{m}t}}}}{\sqrt{1 - e^{-2\frac{\gamma}{m}t}}} \tag{2.34}$$

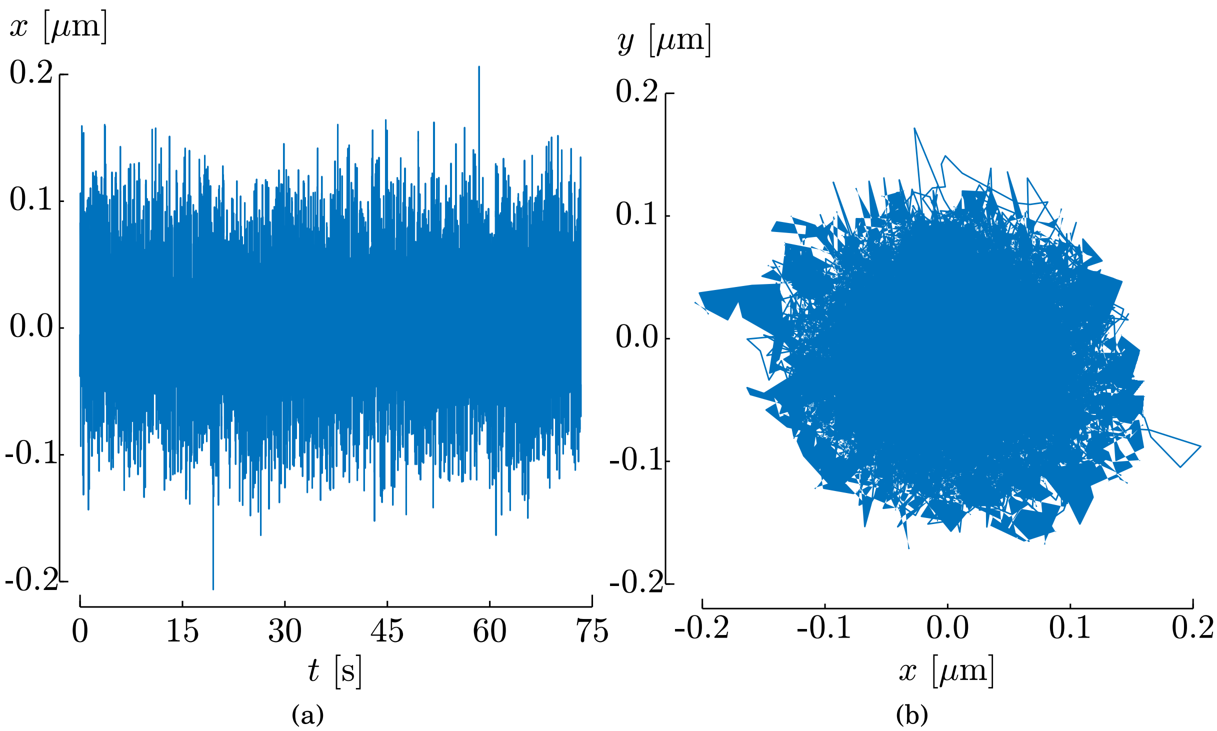

Figure 2.2: (a) x position as function of time t and (b) y position as function of x of an experimental trajectory of a silica particle of $3.16\,\mu\mathrm{m}$ diameter trapped in water.

that, when the particle reaches the equilibrium ($t \to \infty$), becomes the Maxwell-Boltzmann distribution, as it is easily demonstrated by direct calculation

$$\rho(v) = \lim_{t\to\infty} \rho(t, v) = \sqrt{\frac{m}{2\pi k_B T}} e^{-\frac{mv^2}{2k_B T}} \tag{2.35}$$

2.2 Trapped particle motion

An optically trapped particle in a fluid jiggles around its equilibrium position due to Brownian motion and, in order to describe its motion, it is necessary to add optical forces to the Langevin equation. The optical forces, therefore, confine the particle around the optical focus of the system, as shown in figure 2.2a and 2.2b. In chapter 1, the optical force is written, for small displacement around the equilibrium position, as a restoring force characterised by a spring constants called *trap stiffness*. The trap stiffness, the fluid viscosity, and the particle radius can be estimated from the particle trajectory using the following techniques: *power spectrum analysis*, *mean squared displacement analysis*, *autocorrelation function analysis*, *potential analysis*, and *equipartition method*.

To describe these techniques, the main step is to write the Langevin equation

$$\frac{d^2 r}{dt^2}(t) = -\frac{\gamma}{m}\frac{dr}{dt}(t) + \frac{F_{\text{trap}}}{m} + \frac{\sqrt{2\gamma k_B T}}{m}\Xi(t) \tag{2.36}$$

with the trap force $F_{\text{trap}}(t) = -kr(t)$ where k is the trap stiffness. This implies that the Langevin equation can be rewritten as

$$\frac{d^2r}{dt^2}(t) = -\frac{\gamma}{m}\frac{dr}{dt}(t) - \frac{k}{m}r(t) + \frac{\sqrt{2\gamma k_B T}}{m}\Xi(t) \tag{2.37}$$

where the reference frame has its origin in the equilibrium position. Under these assumptions, the particle motion has two characteristics times: the *relaxation time* $\tau_m = m/\gamma$, which indicates the time scale at which the inertial effects decay, and the *diffusion time* $\tau_D = a^2/D$, which is the time the particle have diffused its own radius. When the relaxation time τ_m is much smaller than the typical diffusion time τ_D, the inertial effects are negligible and $m\frac{dv(t)}{dt} \ll \gamma v(t)$ (overdamped conditions). For example, micrometric particles trapped in water are characterised by $\tau_m \sim 10^{-7}\,\mathrm{s}$ and $\tau_D \sim 1\,\mathrm{s}$ and inertial effects are negligible. In overdamped conditions, equation (2.37) becomes

$$\frac{dr}{dt}(t) = \sqrt{\frac{2k_B T}{\gamma}}\Xi(t) - \frac{k}{\gamma}r(t) \tag{2.38}$$

By mathematically manipulating these equations (2.36) and (2.38), it is possible to make predictions for measurable quantities of interest.

2.2.1 Power spectrum analysis

This technique is the most reliable for a spherical particle because, working in the frequency domain, it minimises some sources of noise such as slow mechanical drift. The first step is to evaluate the Fourier transform of equation (2.37) that is

$$-\omega^2\tilde{r} = -i\frac{\gamma}{m}\omega\tilde{r} - \frac{k}{m}\tilde{r} + \frac{\sqrt{2\gamma k_B T}}{m}\tilde{\Xi} \Rightarrow \tilde{r} = \frac{1}{m}\frac{\sqrt{2\gamma k_B T}\tilde{\Xi}}{\left(\frac{k}{m} - \omega^2\right) + i\frac{\gamma}{m}\omega} \tag{2.39}$$

where $\tilde{r} \equiv \tilde{r}(\omega) = \int_{-\infty}^{+\infty} r(t)e^{i\omega t}\,dt$ indicates the Fourier transform[1] of r and the differentiation theorem for the Fourier transform is used. The square modulus of $\tilde{r}(\omega)$ defines the *energy spectral density*, which in this case is

$$\mathcal{E}_{r,\Xi}(\omega) = |\tilde{r}|^2 = \frac{2\gamma k_B T}{m^2}\frac{\left|\tilde{\Xi}\right|^2}{\left(\frac{k}{m} - \omega^2\right)^2 + \frac{\gamma^2}{m^2}\omega^2} \tag{2.40}$$

To estiamte the Fourier transform of the white noise, $\tilde{\Xi}$, it is useful to evaluate the *power spectral density* (PSD) defined as

$$\mathcal{S}_r(\omega) = \lim_{t\to\infty}\frac{1}{t}\left|\tilde{r}_t(\omega)\right|^2 = \lim_{t\to\infty}\frac{1}{t}\left|\tilde{r}(\omega)\tilde{\mathbb{I}}_{t_0}(T)\right|^2 = |\tilde{r}|^2 \tag{2.41}$$

where t_0 is an arbitrary time and $\tilde{\mathbb{I}}_{t_0}(t)$ is the Fourier transform of the indicator function of the set $[t_0 - t/2, t_0 + t/2]$. Observing that $\lim_{T\to\infty}\frac{1}{T}\left|\tilde{\Xi}\right|^2 = 1$, the *power*

[1]The inverse Fourier transform is defined as $r(t) = \frac{1}{\sqrt{2\pi}}\int_{-\infty}^{+\infty}\tilde{r}(\omega)e^{-i\omega t}\,d\omega$.

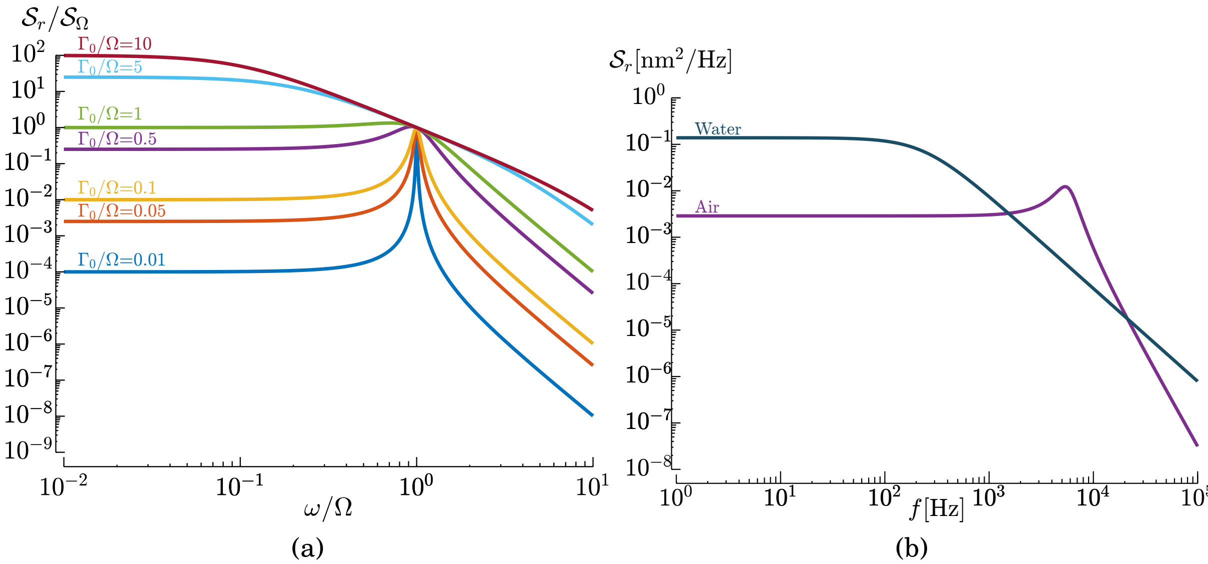

Figure 2.3: (a) PSD, $S_r(\omega)$, of equation (2.43) over $S_\Omega = S_r(\Omega)$ as function of ω/Ω for different values of the ratio Γ_0/Ω considering a silica particle of diameter $3.16\,\mu\mathrm{m}$ and density $1850\,\mathrm{kg/m^3}$ trapped in air; (b) comparison between the PSD of a particle trapped in air (violet line) and in water (blue line) as function of the frequency $f = \frac{\omega}{2\pi}$ for $\Gamma_0/\Omega = 0.5$. For this numerical evaluation, the temperature of the thermal bath is $298.15\,\mathrm{K}$, the air viscosity is $1.8 \cdot 10^{-5}\,\mathrm{Pa \cdot s}$, and the water viscosity is $8.9 \cdot 10^{-4}\,\mathrm{Pa \cdot s}$.

spectral density is

$$\mathcal{S}_r(\omega) = \frac{2\gamma k_B T}{m^2} \frac{1}{\left(\frac{k}{m} - \omega^2\right)^2 + \frac{\gamma^2}{m^2}\omega^2} \tag{2.42}$$

To explain the physical meaning of this equation, it is useful to define the frequencies $\Omega = \sqrt{k/m}$ and $\Gamma_0 = \gamma/m$ and to rewrite equation (2.42) as

$$\mathcal{S}_r(\omega) = \frac{2k_B T}{k} \frac{\Gamma_0 \Omega^2}{\left(\Omega^2 - \omega^2\right)^2 + \Gamma_0^2 \omega^2} \tag{2.43}$$

which gives the value $\mathcal{S}_r \rightarrow \frac{2k_B T \gamma}{k^2}$ for $\omega \rightarrow 0$. The PSD of experimental data, therefore, gives important information about the trap stiffness, the fluid viscosity, and the particle mass. The behaviour of equation (2.43) is shown in Figure 2.3a and is characterised by a peak for $\omega = \Omega$ representing a resonance condition.

Instead, in overdamped conditions, the power spectrum analysis is obtained by performing the Fourier transform of equation (2.38), i.e.

$$i\omega\tilde{r} = \sqrt{\frac{2k_B T}{\gamma}}\tilde{\Xi} - \frac{k}{\gamma}\tilde{r} \Rightarrow \tilde{r} = \sqrt{\frac{2k_B T}{\gamma}} \frac{\tilde{\Xi}}{i\omega + \frac{k}{\gamma}} \equiv \sqrt{\frac{2k_B T}{\gamma}} \frac{\tilde{\Xi}}{i\omega + \omega_c} \tag{2.44}$$

with $\omega_c = k/\gamma$ and, consequently, $f_c = k/(2\pi\gamma)$ called *corner frequency*. As before,

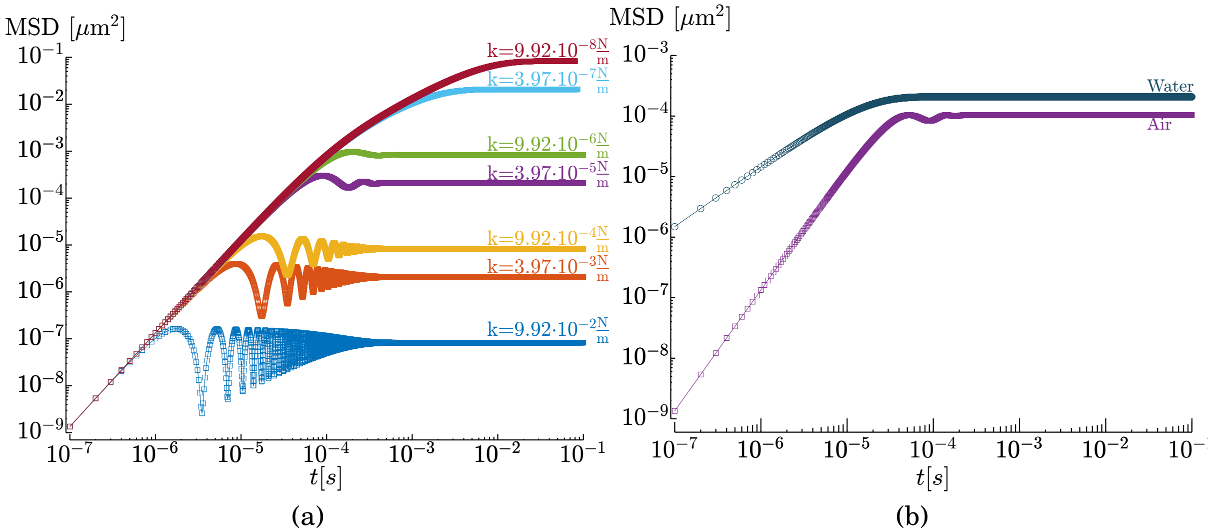

Figure 2.4: (a) MSD of equation (2.46) as function of the time t for different values of the trapping stiffness k considering a silica particle of diameter $3.16\,\mu\mathrm{m}$ and density $1850\,\mathrm{kg/m^3}$ trapped in air; (b) comparison between the MSD of the same particle trapped in air (violet line) and in water (blue line) as function of the time t for $k = 3.97 \cdot 10^{-5}\,\mathrm{N/m}$. For this numerical evaluation, the temperature of the thermal bath is $298.15\,\mathrm{K}$, the air viscosity is $1.8 \cdot 10^{-5}\,\mathrm{Pa \cdot s}$, and the water viscosity is $8.9 \cdot 10^{-4}\,\mathrm{Pa \cdot s}$.

this equation gives the PSD

$$\mathcal{S}_r(\omega) = \frac{2k_BT}{\gamma}\frac{1}{\omega^2 + \omega_c^2} \tag{2.45}$$

that is a Lorentzian curve with a maximum value of $\mathcal{S}_r(\omega_{\max} = 0) = 2k_BT\frac{\gamma}{k^2}$ from which it follows that f_c is the corner frequency because $\mathcal{S}_r(\omega_c) = \mathcal{S}_r(\omega_{\max})/2$ when $f = f_c$. By evaluating the corner frequency and assuming the fluid viscosity known the trap stiffness can be measured.

As displayed in figure 2.3b, the PSD has large values at low frequencies in overdamped conditions (equation (2.45)) and large values at the resonant frequency when inertial effects are not negligible (equation (2.42)). In addition, the inertia affects the PSD introducing a not-Lorentzian shape of the function characterised by the resonant frequency at Ω.

2.2.2 Mean squared displacement analysis

This technique is based on the evaluation of MSD, which quantifies the deviation of the position of the particle from its initial position. For example, the MSD is linear in time for Brownian motion (equation (2.19)), quadratic in time for ballistic motion[2], constant in time for a trapped particle. These behaviours are observable at different time scales and, therefore, can coexist and can be studied together with a single measurement. The MSD for a trapped particle, following the calculations of appendix C, is

$$\mathrm{MSD}(\tau) = \frac{2k_B T}{k} - \frac{2k_B T}{k}\left[\cosh\left(\frac{\Omega_1}{2}\tau\right) + \frac{\Gamma_0}{\Omega_1}\sinh\left(\frac{\Omega_1}{2}\tau\right)\right]e^{-\Gamma_0\tau/2} \tag{2.46}$$

where τ is called *lag time*. In this expression there are two angular frequencies contributions: $\Omega = \sqrt{k/m}$, that is the angular frequency of the trapped particle without damping; $\Omega_1 = \sqrt{\frac{\gamma^2}{m^2} - 4\frac{k}{m}} = \sqrt{\Gamma_0^2 - 4\Omega^2}$, that is the cyclic frequency of the damped oscillator in which $\Gamma_0 = \frac{\gamma}{m}$ is the damping coefficient. The MSD, for $\tau \to \infty$, has the limit value of

$$\lim_{\tau\to\infty} \mathrm{MSD}(\tau) = \frac{2k_B T}{k} \tag{2.47}$$

from which it is possible to evaluate the trap stiffness k assuming the temperature T known. Evaluated k, the particle mass can be obtained from Ω and the damping coefficient from Γ_0. The MSD behaviour of figure 2.4a clearly shows that, for high stiffnesses[3] ($k > 5 \cdot 10^{-4}\,\frac{\mathrm{N}}{\mathrm{m}}$), the MSD reaches the plateau $2\frac{k_B T}{k}$ quickly, but with very strong oscillations. Instead, for common stiffnesses obtained with laser powers between $10\,\mathrm{mW}$ and $1000\,\mathrm{mW}$ ($5 \cdot 10^{-7}\,\frac{\mathrm{N}}{\mathrm{m}} k < 5 \cdot 10^{-5}\,\frac{\mathrm{N}}{\mathrm{m}}$), the MSD reaches the plateau almost at the same time, but with less strong oscillations. For low stiffnesses ($k < 5 \cdot 10^{-7}\,\frac{\mathrm{N}}{\mathrm{m}}$), the oscillations totally disappear and the plateau is reached at a higher time.

In overdamped conditions, the MSD is

$$\mathrm{MSD}(\tau) = \frac{2k_B T}{k}\left(1 - e^{-\frac{k}{\gamma}\tau}\right) \tag{2.48}$$

obtained in a way similar to the previous one. Without inertial effects, the oscillations before the plateau at $\frac{2k_B T}{k}$ are totally absent for any stiffness value, as clearly visible in figure 2.4b. Assuming the temperature T is known, the stiffness k can be evaluated by the plateau and the viscosity γ by the characteristic time γ/k of the exponential.

2.2.3 Autocorrelation function analysis

The autocorrelation function analysis is based on the autocorrelation function (ACF) evaluation of the trajectory, $\mathcal{C}_r(\tau)$, defined as

$$\mathcal{C}_r(\tau) = E[r(t+\tau)r(t)] \tag{2.49}$$

[2]Ballistic motion of a trapped particle is observable when the acquisition frequency is high enough to distinguish individual collisions between the constituents and the particle.

[3]In this theoretical chapter, very high stiffnesses have been shown only to emphasise the theoretical properties, but optical tweezers can give stiffnesses only up to $10^{-5}\,\frac{\mathrm{N}}{\mathrm{m}} \div 10^{-4}\,\frac{\mathrm{N}}{\mathrm{m}}$.

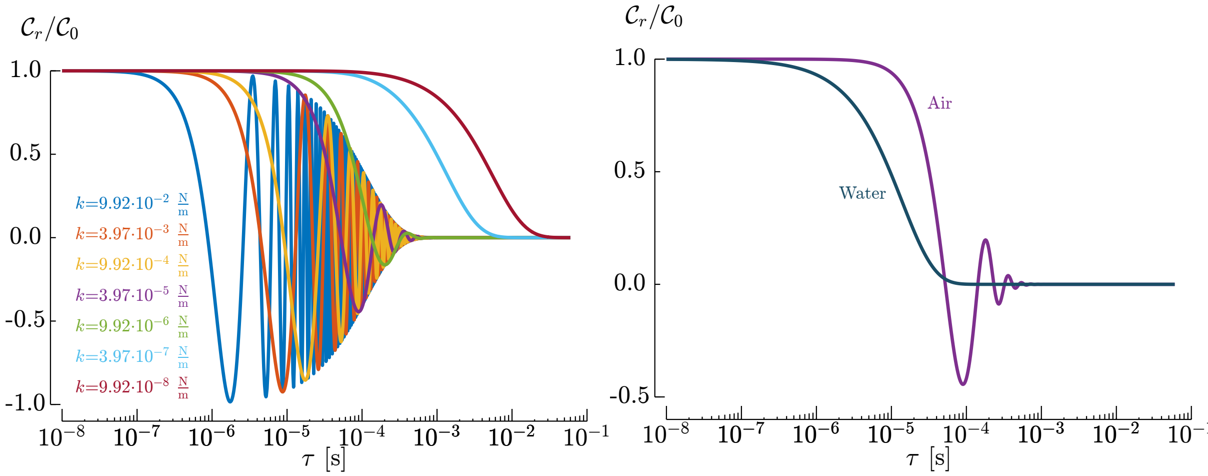

(a) (b)

Figure 2.5: (a) ACF, $\mathcal{C}_r$, of equation (2.51) over $\mathcal{C}_0 = \mathcal{C}_r(0)$ as function of τ for different values of the trapping stiffness k considering a silica particle of diameter $3.16\,\mu\mathrm{m}$ and density $1850\,\mathrm{kg/m^3}$ trapped in air; (b) comparison between the $\mathcal{C}_r/\mathcal{C}_0$ of the same particle trapped in air (violet line) and in water (blue line) as function of τ for $k = 3.97 \cdot 10^{-5}\,\mathrm{N/m}$. For this numerical evaluation, the temperature of the thermal bath is $298.15\,\mathrm{K}$, the air viscosity is $1.8 \cdot 10^{-5}\,\mathrm{Pa \cdot s}$, and the water viscosity is $8.9 \cdot 10^{-4}\,\mathrm{Pa \cdot s}$.

The evaluation of the ACF can be done by direct calculation from equation (C.12), but a simple way is to use the Wiener–Khinchin theorem that relates the ACF to the PSD via the Fourier transform. Observing that the PSD of equations (2.43) and (2.45) is an even function, the Wiener-Khinchin theorem can be written as

$$\mathcal{C}_r(\tau) = \frac{1}{2\pi}\int_{-\infty}^{+\infty} \mathcal{S}_r(\omega) e^{i\omega\tau}\, d\omega = \frac{1}{\pi}\int_{0}^{+\infty} \mathcal{S}_r(\omega) \cos\omega\tau \, d\omega \tag{2.50}$$

which gives for equation (2.43), i.e. when inertia is not negligible,

$$\begin{aligned} \mathcal{C}_r(\tau) &= \frac{k_BT}{k}\left[\cosh\left(\frac{\Omega_1}{2}\tau\right) + \frac{\Gamma_0}{\Omega_1}\sinh\left(\frac{\Omega_1}{2}\tau\right)\right] e^{-\frac{\Gamma_0}{2}\tau} = \\ &= \frac{k_BT}{k}\left[\cosh\left(\frac{\sqrt{\frac{\gamma^2}{m^2} - 4\frac{k}{m}}}{2}\tau\right) + \frac{\gamma/m}{\sqrt{\frac{\gamma^2}{m^2} - 4\frac{k}{m}}}\sinh\left(\frac{\sqrt{\frac{\gamma^2}{m^2} - 4\frac{k}{m}}}{2}\tau\right)\right] e^{-\frac{\gamma}{2m}\tau} \end{aligned} \tag{2.51}$$

The ACF behaviour of figure 2.5a has the same properties of the MSD of figure 2.4a. Indeed, for high stiffnesses ($k > 5 \cdot 10^{-4}\,\frac{\mathrm{N}}{\mathrm{m}}$), the ACF deviates from the initial value $\mathcal{C}_r(t=0) = \frac{k_BT}{k}$ quickly, but with very strong oscillations. For common stiffnesses ($k < 5 \cdot 10^{-5}\,\frac{\mathrm{N}}{\mathrm{m}}$), the ACF deviates from $\frac{k_BT}{k}$ the later the higher the value of the stiffness and it reaches zero ($\lim_{t\to\infty}\mathcal{C}_r(t) = 0$) oscillating at a lower frequency the higher the value of stiffness. In addition, before reaching the plateau value, the

ACF shows that the particle is anti-correlated with itself due to resonant effects. From the ACF as for the PSD, assuming the particle mass known, it is possible to evaluate from Ω the trap stiffness and from Γ_0 the fluid viscosity.

Following the same procedure, the ACF in overdamped conditions is

$$\mathcal{C}_r(\tau) = \frac{k_B T}{k} e^{-\frac{k}{\gamma}\tau} \tag{2.52}$$

whose initial value, $\frac{k_B T}{k}$, gives the stiffness of the trap knowing the temperature T, while the way it tends to zero gives the viscosity of the fluid because of the exponential term $e^{-\frac{k}{\gamma}\tau}$.

As for the MSD, the oscillations are totally absent in overdamped conditions, as can be clearly seen from equation (2.52) and figure 2.5b. In addition, the ACF deviates earlier from the initial value and reaches zero sooner than the ACF defined by equation (2.51).

2.2.4 Potential analysis and equipartition method

These two techniques are based on the possibility to extract information about the trapping force from the probability density function. The probability density function can be obtained from the Fokker-Planck equation, which, for a trapped particle, is defined by the stochastic differential equations

$$\begin{cases} dr = v dt \\ dv = -\frac{\gamma}{m} v dt - \frac{k}{m} r dt + \frac{\sqrt{2\gamma k_B T}}{m} \Xi dt \end{cases} \tag{2.53}$$

that give the following Fokker-Planck equation

$$\frac{\partial \rho}{\partial t} = -v\frac{\partial \rho}{\partial r} + \frac{\partial}{\partial v}\left[\left(\frac{\gamma}{m} v + \frac{k}{m} r\right)\rho\right] + \frac{k_B T \gamma}{m^2}\frac{\partial^2 \rho}{\partial v^2} \tag{2.54}$$

obtained using equations (2.29) and (2.30), where

$$\begin{cases} d\vec{X} = \begin{pmatrix} dr \\ dv \end{pmatrix} \\ \mathscr{g} = \begin{pmatrix} v \\ -\frac{\gamma}{m} v - \frac{k}{m} r \end{pmatrix} \\ \mathscr{h} = \begin{pmatrix} 0 & 0 \\ 0 & \frac{\sqrt{2\gamma k_B T}}{m} \end{pmatrix} \\ d\vec{W} = \begin{pmatrix} 0 \\ \Xi dt \end{pmatrix} \end{cases} \tag{2.55}$$

By introducing the following independent variables

$$z_1 = v + \varphi_1 r \qquad\qquad z_2 = v + \varphi_2 r \tag{2.56}$$

with $\varphi_1 = \frac{1}{2}\frac{\gamma}{m} - \frac{1}{2}\sqrt{\frac{\gamma^2}{m^2} - 4\frac{k}{m}}$ and $\varphi_2 = \frac{1}{2}\frac{\gamma}{m} + \frac{1}{2}\sqrt{\frac{\gamma^2}{m^2} - 4\frac{k}{m}}$, the Fokker-Planck equation (2.54) assumes the symmetrical expression [44]

$$\frac{\partial \rho}{\partial t} = \varphi_2 \frac{\partial}{\partial z_1}(z_1 \rho) + \varphi_1 \frac{\partial}{\partial z_2}(z_2 \rho) + \frac{k_B T \gamma}{m^2}\left(\frac{\partial}{\partial z_1} + \frac{\partial}{\partial z_2}\right)^2 \rho \tag{2.57}$$

that has as solution the inverse Fourier transform of the function

$$\begin{aligned} \mathrm{FT}[\rho(t,z_1,z_2)]_{\chi_1,\chi_2} = \exp\Bigg[& -iz_{10}e^{-\varphi_2 t}\chi_1 - iz_{20}e^{-\varphi_1 t}\chi_2 - \frac{1}{2}\frac{k_B T\gamma}{m^2}\frac{\chi_1^2}{\varphi_2}(1-e^{-2\varphi_2 t}) + \\ & -2\frac{k_B T\gamma}{m^2}\frac{\chi_1\chi_2}{\varphi_1-\varphi_2}(1-e^{-(\varphi_1+\varphi_2)t}) - \frac{1}{2}\frac{k_B T\gamma}{m^2}\frac{\chi_2^2}{\varphi_1}(1-e^{-2\varphi_1 t})\Bigg] \end{aligned} \tag{2.58}$$

where χ_1 and χ_2 are the variable of the Fourier space relative to z_1 and z_2. The inverse Fourier transform of this equation is a 2-D Gaussian function in the variable z_1 and z_2, in which the time variable t is only present in the terms $e^{-2\varphi_1 t}$, $e^{-2\varphi_2 t}$, and $e^{-(\varphi_1+\varphi_2)t}$. It is possible to demonstrate that, when the particle has reached the thermal equilibrium with the thermal bath ($t \to \infty$), the $\rho_{\mathrm{eq}}(t,r,v)$ is the following Maxwell-Boltzmann distribution

$$\rho_{\mathrm{eq}}(r,v) = \sqrt{\frac{k}{2\pi k_B T}}\sqrt{\frac{m}{2\pi k_B T}} e^{-\frac{\frac{1}{2}kr^2 + \frac{1}{2}mv^2}{k_B T}} = \rho_{r,\mathrm{eq}}(r)\rho_{v,\mathrm{eq}}(v) \tag{2.59}$$

so that, if the particle velocity is unknown, the distribution describing this system is, i.e.

$$\rho_{r,\mathrm{eq}}(r) = \sqrt{\frac{k}{2\pi k_B T}} e^{-\frac{\frac{1}{2}kr^2}{k_B T}} \equiv \rho_{r,\mathrm{eq}}(0) e^{-\frac{\frac{1}{2}kr^2}{k_B T}} \tag{2.60}$$

being $\int_{-\infty}^{\infty} \rho(v)_{\mathrm{eq}}\, dv = 1$. This result is generalisable to a conservative potential $U(r)$ for which

$$\rho_{r,\mathrm{eq}}(r) = \rho_{r,\mathrm{eq}}(0) e^{-\frac{U(r)}{k_B T}} \tag{2.61}$$

Potential analysis According to the major result of equation (2.61), the logarithm of (2.60) gives the potential, because

$$\ln\left[\frac{\rho_{r,\mathrm{eq}}(r)}{\rho_{r,\mathrm{eq}}(0)}\right] = -\frac{U(r)}{k_B T} \tag{2.62}$$

For small displacements of the particle from the trapping position, the force term is $F(r) = -kr$ and, consequently, the potential is

$$U(r) = \frac{k_B T}{2} k(r - r_0)^2 + C \tag{2.63}$$

with r_0 the equilibrium position and C arbitrary constant. Therefore, equation (2.62) gives the trap stiffness, i.e.

$$\ln\left[\frac{\rho_{r,\mathrm{eq}}(r)}{\rho_{r,\mathrm{eq}}(0)}\right] = -\frac{1}{2k_B T} k(r - r_0)^2 + C' \tag{2.64}$$

where $C' = C/(k_B T)$. Under these assumptions, the potential analysis does not differ between the general case and the low Reynolds number regime.

Equipartition method This method is based on the relation between the variance of the distribution and the trap stiffness. Assuming the particle in thermal equilibrium with the thermal bath and, thus, starting from equation (2.60), the variance of the particle position is

$$\mathrm{Var}[r] = \int_{-\infty}^{+\infty} (r - r_0)^2 \rho_{r,\mathrm{eq}}(r)\, dr = \frac{k_B T}{k} \tag{2.65}$$

and, therefore,

$$k = \frac{k_B T}{\mathrm{Var}[r]} \tag{2.66}$$

As for the potential analysis and under these assumptions, the equipartition method, as described so far, can be used indiscriminately both in the general case and for the low Reynolds number regime.

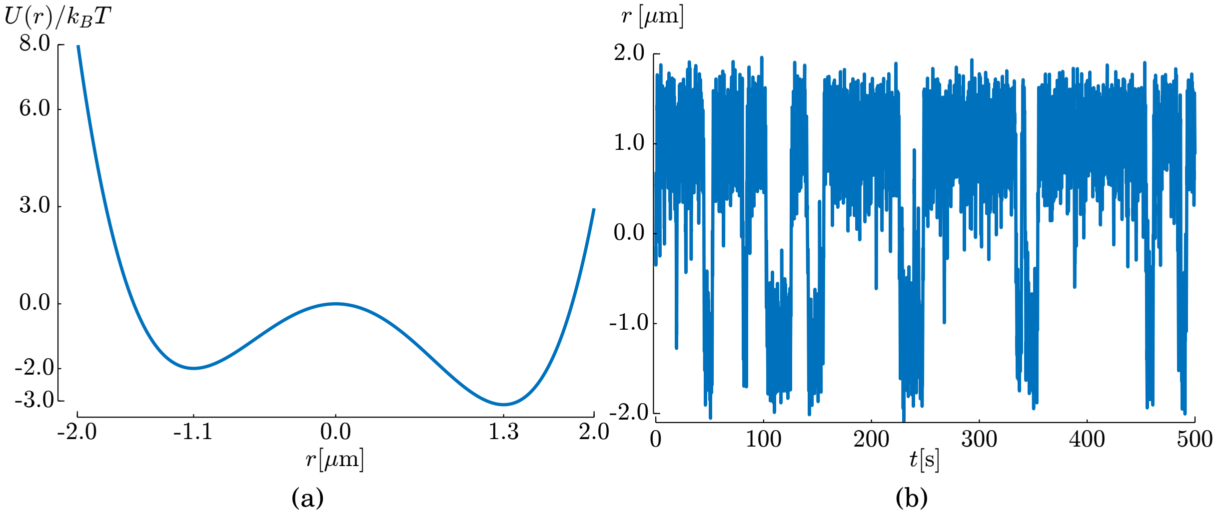

Figure 2.6: (a) double-well potential with $a = 2.0 \cdot 10^4$ J/m^4, $b = 4.0 \cdot 10^{-3}$ J/m^3, and $c = 2.9 \cdot 10^{-8}$ J/m^2 so that $r_+ = 1.3\,\mu$m and $r_- = -1.1\,\mu$m; (b) simulated trajectory of a silica particle of diameter $1.00\,\mu$m interacting with the double-well potential of (a).

2.3 Double-well potential

When a particle in a fluid interacts with a double-well potential, it is possible to study the statistical properties of the particle transitions between the two metastable states of the potential. These *thermal driven transitions* characterise many physical, biological, and chemical processes, such as diffusion in solids, switching in superconducting junctions, chemical reactions, and protein folding. In these conditions the overdamped Langevin equation[4] is

$$\frac{dr}{dt}(t) = -\frac{1}{\gamma}\frac{dU}{dr}(r) + \frac{\sqrt{2\gamma k_B T}}{\gamma}\Xi(t) \tag{2.67}$$

where $U(r)$, for the purposes of this thesis, is the double-well potential described in 1 dimension by

$$U(r) = \frac{a}{4}r^4 - \frac{b}{3}r^3 - \frac{c}{2}r^2 \tag{2.68}$$

with $a \geq 0$, $b \geq 0$, and $c \geq 0$. Its behaviour is shown in figure 2.6a. This potential is characterised by two stable position r_+ and r_- where the potential has two minima. Between the two stable position there is an intermediate unstable position r_s where the potential has a local maximum. For the potential (2.68), the two stable position are

$$r_\pm = \frac{b}{2a} \pm \frac{\sqrt{b^2 + 4ac}}{2a} \Rightarrow U(r_\pm) = -\frac{\left(b \pm \sqrt{4ac + b^2}\right)^2 \left(b^2 \pm b\sqrt{4ac + b^2} + 6ac\right)}{96a^3} \tag{2.69}$$

[4]For the purposes of this work, it is not of interest to study the general case where the term $\frac{d^2r}{dt^2}$ can not be neglected.

while the unstable position is $r_s = 0$ in which the potential is chosen to be zero. This potential is characterised by the potential barriers

$$\Delta U_\pm = U(r_s) - U(r_\pm) \tag{2.70}$$

and, assuming that $k_B T \ll \Delta U_\pm$, the transition rates $\psi_\pm$ from the equilibrium position are [45]

$$\psi_\pm = \frac{1}{T_\pm} = \frac{1}{2\pi\gamma}\sqrt{\left|\frac{d^2U}{dr^2}(r_\pm)\frac{d^2U}{dr^2}(r_s)\right|}e^{-\frac{\Delta U_\pm}{k_B T}} \tag{2.71}$$

where $T_\pm$ is defined as transition time. This indicates that the particle is confined around r_+ or r_-, but, due to the random force $\Xi[t]$, occasionally transits from r_+ to r_- or vice versa as shown in figure 2.6b. In these conditions, to evaluate the potential experimentally it is very useful to use the potential method of equation (2.62), i.e.

$$U(r) = -k_B T \ln\left[\frac{\rho_{r,\mathrm{eq}}(r)}{\rho_{r,\mathrm{eq}}(0)}\right] \tag{2.72}$$

2.3.1 Normalised autocorrelation function

The normalised autocorrelation function of a particle (or an ensemble of non-interacting particles) interacting with a double-well potential can be evaluated if the potential has a symmetrical form ($b = 0$ in equation (2.68)). Under these conditions, the Fokker-Planck equation can be manipulated such that the normalized auto-correlation function (NACF is characterised by $\bar{\mathcal{C}}(0)_r = 1$) is (equation (6.3.12) of [46])

$$\bar{\mathcal{C}}_r(\tau) \simeq \Delta_1 e^{-\lambda_1 \tau} + (1-\Delta_1)e^{-\frac{\tau}{\tau_W}} \tag{2.73}$$

In this equation, λ_1 is the characteristic frequency of the process defined as the smallest eigenvalue of the Fokker-Planck equation, that is (equation (6.3.3) of [46])

$$\frac{1}{\lambda_1(q)} = \tau_0 \frac{e^q}{1+\mathrm{erf}(\sqrt{q})} \iint_0^{+\infty} e^{-(s-\sqrt{q})^2-(t-\sqrt{q})^2}\,\frac{\mathrm{erf}(\sqrt{2st})}{\sqrt{st}}\,ds\,dt \tag{2.74}$$

where $q = c^2/(4k_B T\,a)$ and $\tau_0 = \gamma/\sqrt{2k_B T\,a}$. Instead, τ_W is the characteristic time of the fast relaxation processes in the well and Δ_1 the population fraction of the particles crossing over the well barrier ($1-\Delta_1$ is the population fraction of the particles in the deep well) [5], that are (equation (6.3.13) of [46])

$$\tau_W(q) = \frac{\lambda_1 T_c - 1}{\lambda_1 - 1/T_{\mathrm{ef}}} \qquad \Delta_1 = \frac{T_c/T_{\mathrm{ef}} - 1}{\lambda_1 T_c - 2 + 1/(\lambda_1 T_{\mathrm{ef}})} \tag{2.75}$$

[5] This definition is valid both for an ensemble of particles and for a single particle. Indeed, for a single particle, Δ_1 is the population fraction of the crossing events over the well barrier.

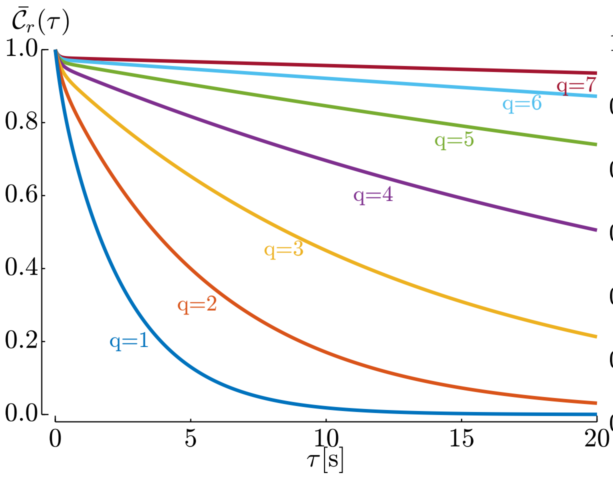

(a)

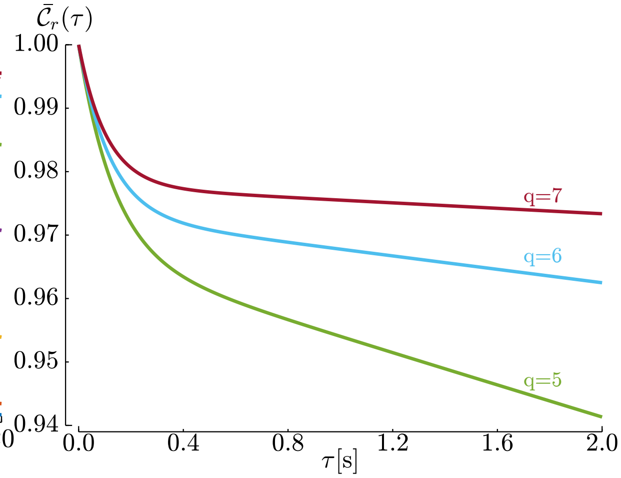

(b)

Figure 2.7: (a) normalized autocorrelation function $\bar{\mathcal{C}}_r(\tau)$ of equation (2.73) for different values of q and for $\tau_0 = 0.65\,\mathrm{s}$; (b) zoom of $\bar{\mathcal{C}}_r(\tau)$ to emphasise the presence of the two decay times λ_1^{-1} and τ_W with $\lambda_1^{-1} > \tau_W$.

where T_c is the correlation time given by (equation (6.2.37) of [46])

$$T_c(q) = \tau_0 \frac{2^{\frac{3}{4}} e^{\frac{3}{2}q}}{\mathcal{W}_{-\frac{3}{2}}(-\sqrt{2q})} \iint\limits_0^{+\infty} e^{-(s-\sqrt{q})^2-(t-\sqrt{q})^2} \, \frac{\mathrm{erf}(\sqrt{2st})}{\sqrt{s}} \, ds \, dt \tag{2.76}$$

and T_{ef} is the effective correlation time (equation (6.3.9) of [46])

$$T_{\text{ef}}(q) = \tau_0 \frac{\mathcal{W}_{-\frac{3}{2}}(-\sqrt{2q})}{\mathcal{W}_{-\frac{1}{2}}(-\sqrt{2q})} \tag{2.77}$$

In these expressions, $\mathcal{W}_\nu(x)$ are the Whittaker's parabolic cylinder functions, defined as

$$\mathcal{W}_\nu(x) = \frac{e^{-\frac{x^2}{4}}}{\Gamma(-\nu)} \int\limits_0^{\infty} e^{-xu-\frac{u^2}{2}} u^{-\nu-1} \, du \quad \text{if } \nu < 0 \tag{2.78}$$

where Γ is the Gamma function. Now being able to evaluate all terms of equation (2.73), the trend of the NACF can be studied. This function is a decreasing function characterised by two exponential decreases with characteristic times τ_W and λ_1^{-1}. Figure 2.7a shows the trend of equation (2.73) for different values of q, while figure 2.7b emphasises its double exponential behaviour.

From the NACF, it is possible to evaluate the characteristic time of the fast relaxation process τ_W, the characteristic frequency λ_1, and the population fraction Δ_1. Then, from these values and equations (2.75), the correlation time T_c and the effective correlation time T_{ef} can be evaluated.

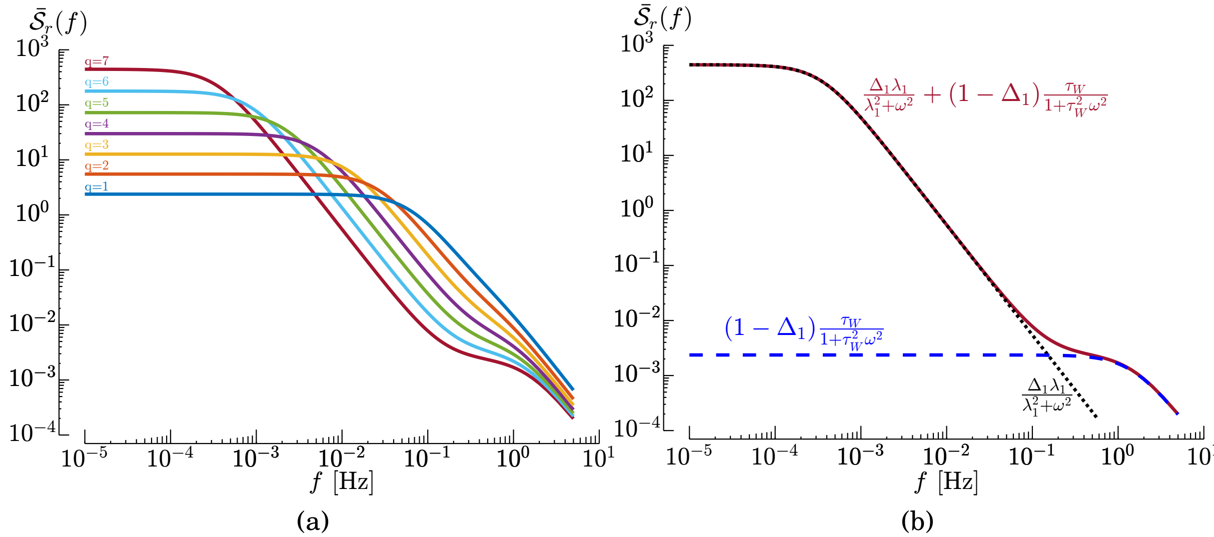

Figure 2.8: (a) normalized PSD function $\bar{\mathcal{S}}_r(\omega)$ of equation (2.79) for different values of q and for $\tau_0 = 0.65\,\mathrm{s}$; (b) $\bar{\mathcal{S}}_r(\omega)$ (red solid line) for $q = 7$ as function of f where the two Lorentzian behaviours are indicated with a dotted black line and a blue dashed line.

2.3.2 Power spectral density

The Wiener-Khinchin theorem gives the PSD knowing the NACF being the PSD the Fourier transform of the NACF, i.e.

$$\bar{\mathcal{S}}(\omega) = \int_0^{+\infty} \bar{\mathcal{C}}_r(\tau)\cos(\omega\tau)\,d\omega = \frac{\Delta_1\lambda_1}{\lambda_1^2+\omega^2} + (1-\Delta_1)\frac{\tau_W}{1+\tau_W^2\omega^2} \tag{2.79}$$

Therefore, the PSD is the sum of two Lorentzian curve with characteristic frequencies λ_1 and τ_W^{-1} and its behaviour for different values of q (Δ_1, λ_1, and τ_W depend on $q = c^2/(4k_BT\,a)$) is shown in figure 2.8a. Figure 2.8b explains the role of the two Lorentzian curve of equation (2.79). As for the NACF, the PSD is useful to evaluate the characteristic time of the fast relaxation process τ_W, the characteristic frequency λ_1, the population fraction Δ_1, the correlation time T_c, and the effective correlation time T_{ef}.

Chapter 3

Intracavity optical tweezers theory

In this chapter, the mechanisms that regulate the trapping of particles inside the ring fibre laser cavity realised for this work are discussed theoretically. When a particle is trapped inside a fibre laser cavity, i.e. by an *intracavity optical tweezers* (IOT), the particle becomes part of the laser system changing the cavity losses according to its position and, therefore, the laser power. Thus, this phenomenon is more complex that "standard" trapping being the trapping dependent on the particle position inside the cavity. Indeed, IOT combines three phenomena together: laser dynamics[1] depending on cavity losses, optical trapping due to optical forces, and Brownian motion of the trapped particle.

Therefore, the first section of this chapter focuses on the basic principles of a ring fibre laser. The second section describes the trapping dynamics of IOT for the laser used in this work, i.e. a ring fibre laser, illustrating a toy model [26] that, in this work, is modified to overcome some of its limitations.

3.1 Ring fibre laser dynamics

The laser used in this experiment is a diode-pumped Yb^{3+} ring fibre laser. This laser is pumped by injecting into a doped fibre (active medium) a diode laser light at $\lambda_p = 976\,\mathrm{nm}$ that is efficiently absorbed by the Yb^{3+} bands as shown in figure 3.1a. In this way, the active medium generates laser light with wavelength $1030\,\mathrm{nm}$ according to the band diagram of the Yb^{3+} shown in figure 3.1b.

Following the analytic work of A. Hardy about linear fibre laser [47, 48], this laser is described as a quasi-three level system. When the laser condition is satisfied, two laser beams travelling in opposite directions, called *signals*, are produced even if the system is pumped in only one direction. The signals are characterised by their power density per unit wavelength λ, indicated as $\mathcal{P}^{\pm}(t, r, \lambda)$, where $\pm$ indicate the two directions, t the time and r the position inside the fibre ring laser. To simplify the analytical model, the transition times of the non-radiative decays are

[1] Laser dynamics is the temporal evolution of quantities that characterise laser phenomena, such as laser power and losses.

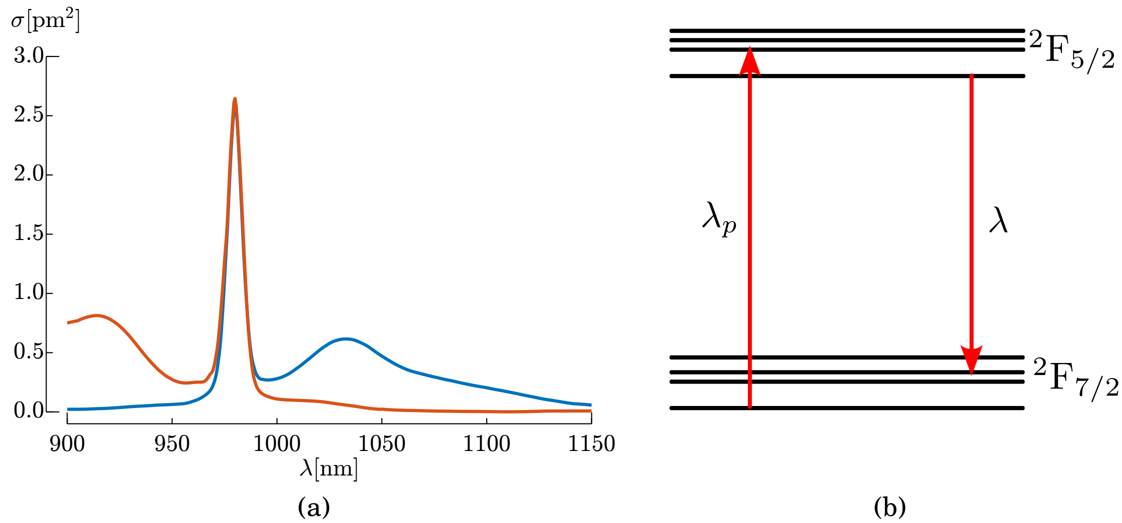

Figure 3.1: (a) emission (blue solid line) and absorption (orange solid line) cross sections of Yb^{3+} doped fibre as function of λ; (b) band diagram of Yb^{3+} where $\lambda_p = 976\,\mathrm{nm}$ is the pump wavelength and $\lambda = 1030\,\mathrm{nm}$ is the emission wavelength.

assumed to be negligible compared to the lifetime of the laser upper level τ. Denoting the power of the pump light at wavelength λ_p as $P_p(t,r)$ and the upper lasing level population density as $N_2(t,r)$, the time-dependent rate equations describing the laser dynamics are:

$$
\begin{aligned}
\frac{\partial N_2(t,r)}{\partial t} &= \frac{\lambda_p \Gamma_p}{Ahc}\left[\sigma_{ap}N - (\sigma_{ep}+\sigma_{ap})N_2(t,r)\right]P_p(t,r) - \frac{N_2(t,r)}{\tau} + \\
&+ \int \frac{\Gamma_s(\lambda)}{Ahc}\left\{\sigma_a(\lambda)N - \left[\sigma_e(\lambda)+\sigma_a(\lambda)\right]N_2(t,r)\right\}\left[\mathcal{P}^+(t,r,\lambda)+\mathcal{P}^-(t,r,\lambda)\right]\lambda d\lambda
\end{aligned}
\tag{3.1}
$$

$$
\begin{aligned}
\pm\frac{d\mathcal{P}^\pm(t,r,\lambda)}{dr} &= \Gamma_s\left\{\left[\sigma_e(\lambda)+\sigma_a(\lambda)\right]N_2(t,r) - \sigma_a(\lambda)N\right\}\mathcal{P}^\pm(t,r,\lambda) + \\
&+ \Gamma_\mathrm{s}\sigma_e(\lambda)N_2(r)\frac{2hc^2}{\lambda^3} - \alpha(r,\lambda)\mathcal{P}^\pm(t,r,\lambda)
\end{aligned}
\tag{3.2}
$$

$$
\frac{dP_p(t,r)}{dr} = -\Gamma_p\left[\sigma_{ap}N - (\sigma_{ep}+\sigma_{ap})N_2(t,r)\right]P_\mathrm{p}(t,r) - \alpha_p(r)P_p(t,r)
\tag{3.3}
$$

where the parameters Γ_p and Γ_s are the power filling factors for the pump and the signals, $\alpha(r,\lambda)$ represents the scattering loss, $\alpha_p(r) = \alpha(r,\lambda_p)$, c is the speed of light in vacuum, h is the Planck's constant, A is the area of the fibre core cross section, $\sigma_{a,e}(\lambda)$ is the absorption (emission) cross section, $\sigma_{ap,ep} = \sigma_{a,e}(\lambda_p)$ is the absorption (emission) cross section at the pump wavelength, and N the density of Yb^{3+} dopants in the fibre (atoms per volume, typically of the order of magnitude of $0.01\,\mathrm{nm}^{-3}$).

In these expressions, the total derivative respect to r can be expressed as partial derivates through the relation $\frac{d}{dr} = \frac{\partial}{\partial r} \pm \frac{n}{c}\frac{\partial}{\partial t}$ where the $\pm$ is defined by the direction of propagation of the beam.

Lasers are often used in steady-state conditions, for that the time derivative is zero. In this condition, the steady-state rate equations are

$$\frac{N_2(r)}{N} = \frac{\frac{\lambda_p \Gamma_p}{Ahc}\sigma_{ap} P_p(r) + \int \frac{\Gamma_s(\lambda)}{Ahc}\sigma_a(\lambda)\left[\mathcal{P}^+(r,\lambda) + \mathcal{P}^-(r,\lambda)\right]\lambda d\lambda}{\frac{1}{\tau} + \frac{\lambda_p \Gamma_p}{Ahc}(\sigma_{ep} + \sigma_{ap}) P_p(r) + \int \frac{\Gamma_s(\lambda)}{Ahc}\left[\sigma_e(\lambda) + \sigma_a(\lambda)\right]\left[\mathcal{P}^+(r,\lambda) + \mathcal{P}^-(r,\lambda)\right]\lambda d\lambda} \tag{3.4}$$

$$\begin{aligned} \pm\frac{d\mathcal{P}^\pm(r,\lambda)}{dr} &= \Gamma_s \left\{\left[\sigma_e(\lambda) + \sigma_a(\lambda)\right] N_2(r) - \sigma_a(\lambda) N\right\} \mathcal{P}^\pm(r,\lambda) + \\ &\quad + \Gamma_{\mathrm{s}}\sigma_e(\lambda) N_2(r)\frac{2hc^2}{\lambda^3} - \alpha(r,\lambda)\mathcal{P}^\pm(r,\lambda) \end{aligned} \tag{3.5}$$

$$\frac{dP_p(r)}{dr} = -\Gamma_p\left[\sigma_{ap}N - (\sigma_{ep} + \sigma_{ap})N_2(r)\right] P_{\mathrm{p}}(r) - \alpha_p P_p(r) \tag{3.6}$$

These differential equations system determines the quantities $N_2(r)$, $P_p(r)$, and $\mathcal{P}^\pm$ only with some *boundary conditions*. For the pump power $P_p(r)$, it is straightforward to choose $P_p(0) = P_0$, i.e. the amount of pump power entering the system. Instead, for the signals, it is important to figure out that, in a ring fibre laser, the laser signal in the position $r = 0$ must be equal to the laser signal at $r = L = 0$, where L is the length of the ring, minus an amount of power lost due to losses, i.e.

$$\begin{cases} \mathcal{P}^+(0,\lambda) = \mathcal{P}^+(L,\lambda)[1 - l^+(\lambda)] \\ \mathcal{P}^-(0,\lambda) = \mathcal{P}^+(L,\lambda)[1 - l^-(\lambda)] \end{cases} \tag{3.7}$$

To solve the rate equations of this system with these boundary conditions, numeric evaluation is needed and an analytical form cannot be obtained without approximations. For this reason, it is useful to describe the laser dynamics with the simplified model proposed by Haken [49], i.e.

$$\frac{dP}{dt}(t,r) = \left(N_0 W - \frac{l}{\tau_R}\right) P(t,r) - \frac{2N_0\tau W}{h\nu}P^2(t,r) \tag{3.8}$$

where N_0 is the population of excited atoms without laser action at a fixed pump power, W is the stimulated emission rate, τ_R the cavity round trip time, l the cavity losses, τ is the relaxation time, h the Planck's constant, and ν the optical frequency of the laser light. This model will be used later in this chapter to introduce the toy model.

3.2 Intracavity trapping of a particle

In an intracavity optical tweezers the trapped particle is part of the cavity itself. Hence, it introduces additional optical losses that change directly the laser mechanism by scattering laser light outside the cavity. These losses depend on the

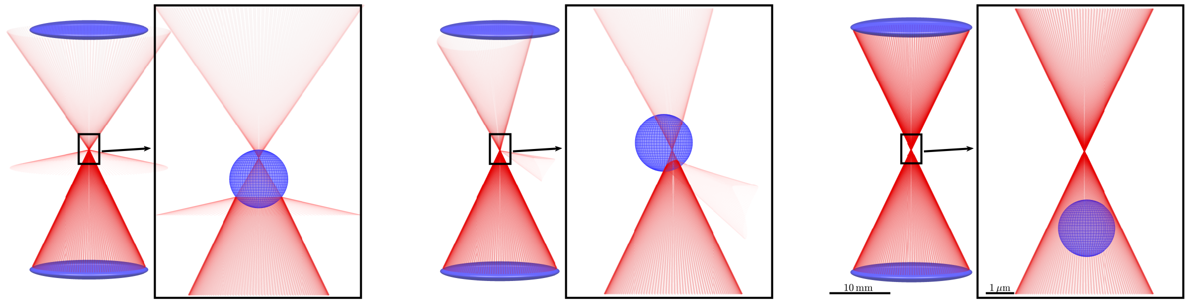

(a) (b) (c)

Figure 3.2: schematic representation of the scattering process of a particle trapped in a ring fibre laser, where the blue ellipsoids represent the trapping lenses and the inset shows a zoom in which the trapped particle is visible. (a) the particle is in the trapping region and scatters a substantial amount of light out of the cavity; (b) the particle is above the focus and shifted relative to the optical axis, scattering less laser light than in case (a); (c) the particle is far from the trapping position and scatters an insignificant amount of laser light.

particle position as described by figures 3.2a, 3.2b, and 3.2c. In IOT, the particle is trapped using a couple of confocal lenses (blue ellipsoids in figure 3.2) that, without any trapped particle, re-inject the laser light in the active medium with no additional losses. When a particle is close to the system focus, the laser beam is partially reflected back and partially deviated by the particle (figures 3.2a and 3.2b). Therefore, the laser beam is not completely re-injected in the active medium increasing the cavity losses, which reduces the stimulated emission phenomena decreasing the laser power of the trapping beam. In this condition, the laser beam power is insufficient for trapping and the particle undergoes free diffusion. When the particle moves away from the trapping position, the laser beam is gradually less influenced by the particle and, consequently, the laser power increases trapping again the particle, as shown in figure 3.2c. In this way, the laser increases its power only when the particle is not trapped generating an *intrinsic feedback effect*, which improves the trapping efficiency.

To quantitatively take into account the feedback effect, equation (3.2) needs to be modified in order to take into account the losses due to the particle, i.e.

$$\begin{aligned}\pm\frac{d\mathcal{P}^{\pm}(t,r,\lambda)}{dr} &= \Gamma_s\left\{\left[\sigma_e(\lambda)+\sigma_a(\lambda)\right]N_2(t,r)-\sigma_a(\lambda)N\right\}\mathcal{P}^{\pm}(t,r,\lambda)+ \\ &+\Gamma_{\mathrm{s}}\sigma_e(\lambda)N_2(r)\frac{2hc^2}{\lambda^3}-\alpha_{\mathrm{tot}}(r,\lambda)\mathcal{P}^{\pm}(t,r,\lambda)\end{aligned} \tag{3.9}$$

where $\alpha_{\mathrm{tot}}(r,\lambda)$ represents all the losses of the system including the ones introduced by the particle when located in r.

Then, to describe the particle motion, the Langevin equation (2.36) for a trapped particle needs to be written using the explicit expressions of the optical force obtained in chapter 1, in which the laser power changes according to the feedback effect described in equation (3.9). Therefore, the particle motion is described by the following system of equations

$$\begin{cases} \frac{d^2r}{dt^2}(t) = -\frac{\gamma}{m}\frac{dr}{dt}(t) + \frac{F_{\text{trap}}}{m}(t, r, P^+, P^-) + \frac{\sqrt{2\gamma k_B T}}{m}\Xi(t) \\ \pm\frac{d\mathcal{P}^{\pm}(t, r, \lambda)}{dr} = \Gamma_s \left\{\left[\sigma_e(\lambda) + \sigma_a(\lambda)\right] N_2(t, r) - \sigma_a(\lambda)N\right\} \mathcal{P}^{\pm}(t, r, \lambda) + \\ \qquad + \Gamma_{\text{s}}\sigma_e(\lambda)N_2(r)\frac{2hc^2}{\lambda^3} - \alpha_{\text{tot}}(r, \lambda)\mathcal{P}^{\pm}(t, r, \lambda) \end{cases} \tag{3.10}$$

where γ is the particle friction coefficient, F_{trap} the trapping force that depends on the laser power, T the temperature of the thermal bath, $\Xi(t)$ the random white noise. These equations can be solved only by numerical evaluations and, in order to study in a simple way what happens in IOT, the toy model, described in the next part of this section, is introduced.

3.2.1 Toy model

This system can be described by a toy model [26] that avoids dealing with the complex system of equations (3.10). This toy model is based on the assumption that the trap stiffness is proportional to the laser power $P(r)$ through the relation

$$k(r) = \bar{k}P(r) \tag{3.11}$$

where $\bar{k}$ is a constant that depends on the properties of the trapping system. Being the timescale for the displacement of the particle (milliseconds) much greater than the response time of the laser (nanoseconds), the laser is consider to be always at its steady state. Therefore, the laser dynamics can be described by the simplified model of equation (3.8)

$$\frac{dP}{dt}(t, r) = \left(N_0 W - \frac{l(r)}{\tau_R}\right) P(t, r) - \frac{2N_0\tau W}{h\nu}P^2(t, r) \tag{3.12}$$

where the losses of the cavity $l(r)$ now depends on the particle displacement r respect to the trapping position. This dependency is assumed to be [26]:

$$l(r) = l_0\left(1 - \frac{r^2}{r_{\text{los}}^2}\right) \tag{3.13}$$

with r_{los} a characteristic length depending on several parameters, such as the particle radius, the refractive indexes of the particle and of the surrounding medium, the losses due to absorption and scattering events. Therefore, the rate equation for the power $P(t, r)$ can be written as:

$$\frac{dP}{dt}(t, r) = \left[N_0 W - \frac{l_0}{\tau_R}\left(1 - \frac{r^2}{r_{\text{los}}^2}\right)\right] P(t, r) - \frac{2N_0\tau W}{h\nu}P^2(t, r) \tag{3.14}$$

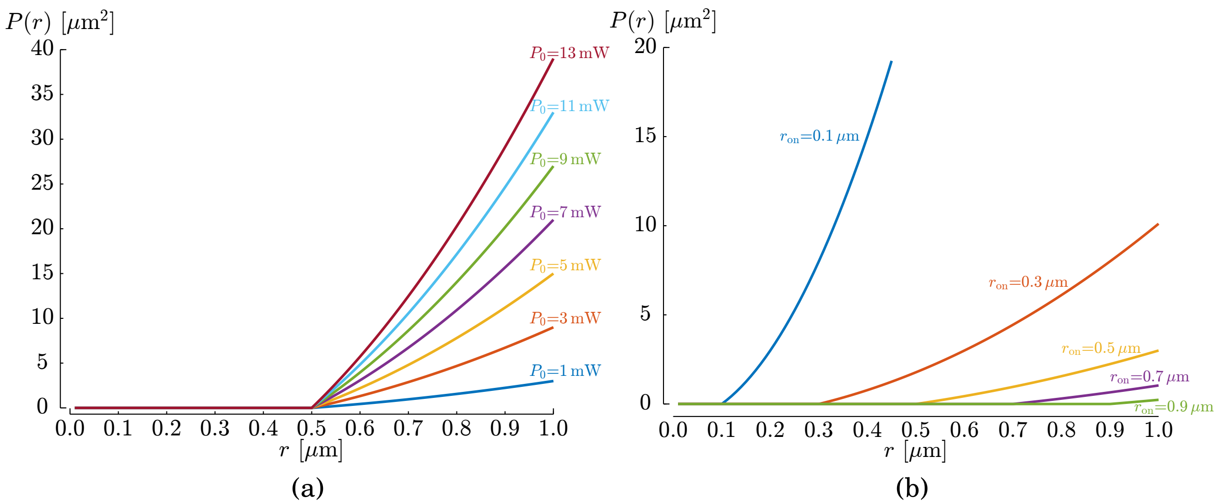

Figure 3.3: power of the toy model P as function of r for (a) different values of P_0 at $r_{\text{on}} = 0.5\,\mu\text{m}$ and (b) different values of r_{on} at $P_0 = 3\,\text{mW}$.

that is an ordinary differential equation of the form

$$\begin{cases} \dfrac{dP}{dt}(t,r) = \mathscr{C}_1(r)P(t,r) - \mathscr{C}_2 P^2(t,r) \\ \mathscr{C}_1(r) = N_0 W - \dfrac{l_0}{\tau_R}\left(1 - \dfrac{r^2}{r_{\text{los}}^2}\right) \end{cases} \tag{3.15}$$

with $\mathscr{C}_2 = \frac{2N_0\tau W}{h\nu}$. The system of equations (3.15) has the solution

$$P(t,r) = \frac{\mathscr{C}_1(r)}{\mathscr{C}_2 + e^{-\mathscr{C}_1(r)(t+c_0)}} \tag{3.16}$$

with c_0 defined by the initial power $P(0,r)$. The stationary value of the power is, consequently, given by the infinity time limit, i.e.

$$P(r) = \begin{cases} 0 & \mathscr{C}_1(r) \le 0 \\ \dfrac{\mathscr{C}_1(r)}{\mathscr{C}_2} & \mathscr{C}_1(r) > 0 \end{cases} \tag{3.17}$$

where the ratio $\mathscr{C}_1(r)/\mathscr{C}_2$ can be written as

$$\frac{\mathscr{C}_1(r)}{\mathscr{C}_2} = \frac{h\nu}{2N_0\tau W}\left[N_0 W - \frac{l_0}{\tau_R}\left(1 - \frac{r^2}{r_{\text{los}}^2}\right)\right] \equiv P_0\left(\frac{r^2}{r_{\text{on}}^2} - 1\right) \tag{3.18}$$

having introduced $r_{\text{on}} = r_{\text{los}}\sqrt{\frac{1}{\tau_R} - \frac{N_0 W}{l_0}}$ as the minimum displacement of the particle after that the laser turns on. Instead, the power $P_0 = \frac{h\nu}{2N_0\tau W}\left(\frac{l_0}{\tau_R} - N_0 W\right)$ is the laser

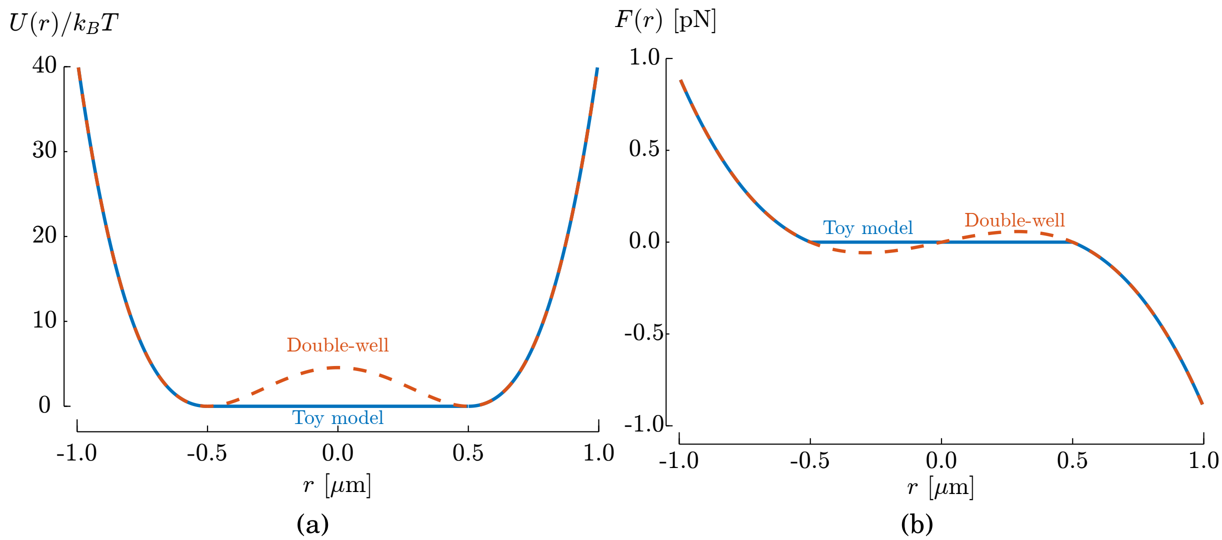

Figure 3.4: (a) toy model potential (blue solid line) of equation (3.21) and the corresponding double-well potential (orange dash line) as function of r, (b) corresponding force $F(r)$ as function of r for the toy model (blue solid line) and the corresponding double-well potential (blue dashed line). The parameters used to plot these curves are $P_0 = 3.0\,\text{mW}$, $r_{\text{on}} = 0.5\,\mu\text{m}$, $\bar{k} = 1 \cdot 10^{-4}\,\text{N}/(\text{m} \cdot \text{W})$, and the temperature of the thermal bath $T = 298.15\,\text{K}$.

power when the particle is far from the trapping position of $r = \sqrt{2} r_{\text{on}}$. Therefore, the toy model gives the following power for the trapping laser

$$P(r) = P_0 \left(\frac{r^2}{r_{\text{on}}^2} - 1 \right) \mathbb{I}_{|r|>r_{\text{on}}}(r) = \begin{cases} 0 & \text{if } |r| \leq r_{\text{on}} \\ P_0 \left(\frac{r^2}{r_{\text{on}}^2} - 1 \right) & \text{if } |r| > r_{\text{on}} \end{cases} \tag{3.19}$$

where $\mathbb{I}$ is the indicator function of the set $|r| > r_{\text{on}}$. Figures 3.3a and 3.3b show the behaviour of the laser power as function of r for different values of P_0 and r_{on}. From the laser power, it is possible to obtain the trap stiffness through equation (3.11) and the equations of motion become

$$\begin{cases} \frac{d^2 r}{dt^2}(t) = -\frac{\gamma}{m} \frac{dr}{dt}(t) - \frac{k(r)}{m} r(t) + \frac{\sqrt{2\gamma k_B T}}{m} \Xi(t) \\ \\ k(t, r) = \bar{k} P_0 \left(\frac{r(t)^2}{r_{\text{on}}^2} - 1 \right) \mathbb{I}_{|r(t)|>r_{\text{on}}}(r) \end{cases} \tag{3.20}$$

Even if the laser power corresponds to the stationary solution of equation (3.15), it still depends on time through the particle position. Nevertheless, the toy model equation is still valid because the laser dynamics (with characteristic time of $\sim$ ns) is much faster than the particle one (with characteristic time in liquid of $\sim$ ms, in gaseous media of $\sim 10\mu$s).

It is natural to compare the system of equations (3.20) with the Langevin equation for a particle in a double-well potential, because, except for the indicator function $\mathbb{I}_{|r(t)|>r_{\rm on}}(r)$, they have the same mathematical expression. However, it is the characteristic function itself that does not allow to apply the methods of section 2.3.1 to derive the ACF and thus the PSD. Instead, assuming the particle in thermal equilibrium with the thermal bath, equation (2.61) is still valid and can be used to evaluate experimentally the potential. In this toy model, the potential is related to the force through the relation

$$U(r) = -\int_0^r \left[-k(r')r'\right] dr' = \frac{\bar{k}P_0}{4r_{\rm on}^2}\left(r^2 - r_{\rm on}^2\right)^2 \mathbb{I}_{|r|>r_{\rm on}}(r) \tag{3.21}$$

and, as said, it differs from the double-well potential only in the presence of $\mathbb{I}_{|r|>r_{\rm on}}(r)$ that cuts the double-well behaviour as shown in figure 3.4a. Indeed, the centres of the two well of the corresponding double-well potential are $\pm r_{\rm on}$, as it is clear from the force behaviour of figure 3.4b.

Unlike trapping with standard optical tweezers, in IOT the force pushing the particle into the trapping position is non-linear also for small displacement and the trap stiffness can not be defined. A good indicator of the particle confinement is the trajectory variance, because it gives a measure of how far the particle deviates quadratically from the equilibrium position[2]. In order to determine the trajectory variance, the probability density function needs to be evaluated and, being the potential defined by equation (3.21), it is

$$\rho_r(r) = \rho_r(0)\exp\left[\left(-\frac{A}{4}r^4 + \frac{C}{2}r^2 - \frac{C_0}{4}\right)\mathbb{I}_{|r|>r_{\rm on}}(r)\right] \tag{3.22}$$

where $A = \frac{1}{k_BT}\frac{\bar{k}P_0}{r_{\rm on}^2}$, $C = \frac{1}{k_BT}\bar{k}P_0$, and $C_0 = \frac{1}{k_BT}\bar{k}P_0 r_{\rm on}^2$. From this follows that the expected value of r^j is

$$\begin{aligned}\int_{-\infty}^{+\infty} r^j \rho_r(r)\, dr &= \rho_r(0)\int_{-\infty}^{+\infty} r^j e^{\left(-\frac{A}{4}r^4+\frac{C}{2}r^2-\frac{C_0}{4}\right)\mathbb{I}_{|r|>r_{\rm on}}(r)}\, dr = \\ &= \rho_r(0)\left[1+(\text{-}1)^j\right]\int_0^{+\infty} r^j e^{\left(-\frac{A}{4}r^4+\frac{C}{2}r^2-\frac{C_0}{4}\right)\mathbb{I}_{|r|>r_{\rm on}}(r)}\, dr = \\ &= \rho_r(0)\left[1+(\text{-}1)^j\right]\left[\int_0^{r_{\rm on}} r^j\, dr + e^{-\frac{C_0}{4}}\int_{r_{\rm on}}^{+\infty} r^j e^{-\frac{A}{4}r^4+\frac{C}{2}r^2}\, dr\right]\end{aligned} \tag{3.23}$$

with $j > 0$. Therefore, the mean value of the particle position r is zero, because the expected value r^{2j+1} is zero for each value of j because of the term $[1 + (\text{-}1)^j]$ that is zero for $2j + 1$ being $\rho_r(r)$ an even function[3].

[2]For an harmonic potential (standard tweezers), this indicator (variance of the trajectory) is proportional to the trap stiffness as shown in equation (2.66)

[3]This is manifestly expressed in equation (3.23).

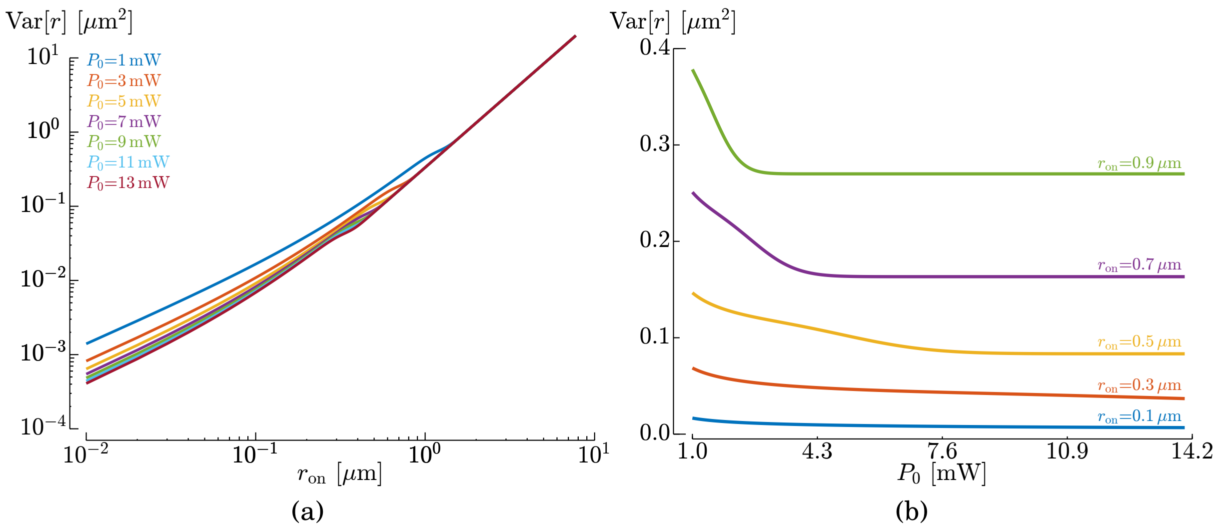

Figure 3.5: variance of intracavity trapped particle $\mathrm{Var}[r]$ as function of (a) r_{on} at different values of P_0 and (b) of P_0 at different values of r_{on}.

In this expression, the first integral is trivially $r_{\text{on}}^{j+1}/(j+1)$ and the second one, developing in Maclaurin series the exponential $\exp\left(\frac{C}{2}r^2\right)$ and using the integration theorem for the series, is

$$\begin{aligned}\int_{r_{\text{on}}}^{+\infty} r^j e^{-\frac{A}{4}r^4+\frac{C}{2}r^2}\,dr &= \sum_{n=0}^{+\infty}\frac{2^{-n}C^n}{n!}\int_{r_{\text{on}}}^{+\infty} r^{2n+j}e^{-\frac{A}{4}r^4}\,dr = \\ &= \sum_{n=0}^{+\infty}\frac{2^{-n}C^n}{n!\,A}\left(\frac{4}{A}\right)^{\frac{j+2n-3}{4}}\Gamma\left(\frac{j+2n+1}{4},\frac{Ar_{\text{on}}^4}{4}\right)\end{aligned} \tag{3.24}$$

where Γ indicates the incomplete Gamma function. Therefore, equation (3.23) becomes

$$\int_{-\infty}^{+\infty} r^{2j}\rho_r(r)\,dr = 2\rho_r(0)\left[\frac{r_{\text{on}}^{2j+1}}{2j+1}+e^{-\frac{C_0}{4}}\sum_{n=0}^{+\infty}\frac{2^{-n}C^n}{n!\,A}\left(\frac{4}{A}\right)^{\frac{2j+2n-3}{4}}\Gamma\left(\frac{2j+2n+1}{4},\frac{Ar_{\text{on}}^4}{4}\right)\right] \tag{3.25}$$

In order to have a useful form of these integrals, the $\rho_r(0)$ value needs to be evaluated using the normalization condition $\int_{-\infty}^{+\infty}\rho_r(r)\,dr = 1$ that implies

$$\rho_r(0) = \frac{1}{2}\left\{r_{\text{on}} + e^{-\frac{C_0}{4}}\sum_{n=0}^{+\infty}\frac{2^{-n}C^n}{n!\,A}\left(\frac{4}{A}\right)^{\frac{2n-3}{4}}\Gamma\left(\frac{2n+1}{4},\frac{Ar_{\text{on}}^4}{4}\right)\right\}^{-1} \tag{3.26}$$

From the general result (3.23), the variance of the intracavity trapped particle is

$$\mathrm{Var}[r] = \int_{-\infty}^{+\infty} r^2\rho_r(r)\,dr = \frac{\frac{r_{\text{on}}^3}{3}+e^{-\frac{C_0}{4}}\sum_{n=0}^{+\infty}\frac{2^{-n}C^n}{n!\,A}\left(\frac{4}{A}\right)^{\frac{2n-1}{4}}\Gamma\left(\frac{2n+3}{4},\frac{Ar_{\text{on}}^4}{4}\right)}{r_{\text{on}}+e^{-\frac{C_0}{4}}\sum_{n=0}^{+\infty}\frac{2^{-n}C^n}{n!\,A}\left(\frac{4}{A}\right)^{\frac{2n-3}{4}}\Gamma\left(\frac{2n+1}{4},\frac{Ar_{\text{on}}^4}{4}\right)} \tag{3.27}$$

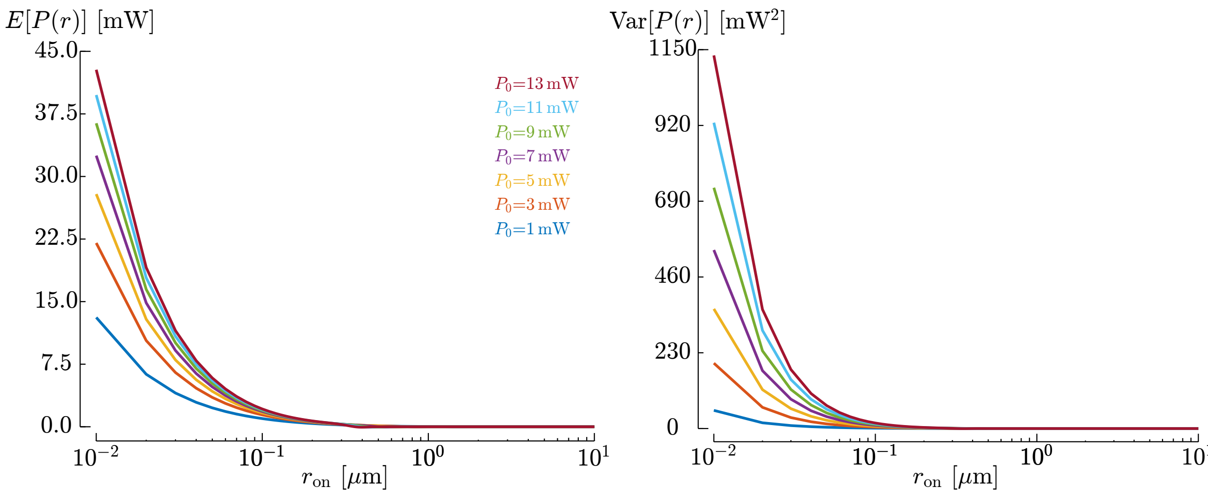

(a) (b)

Figure 3.6: mean (a) and variance (b) of the intracavity laser power $P(r)$ as function of r_{on} at different values of P_0.

that has a non linear and non trivial behaviour as function of r_{on}, while it is less complex in function of P_0, as figures 3.5a and 3.5b show.

As said, the peculiarity of intracavity optical tweezers is that the power of the optical trap changes as the particle moves from the trapping position and, therefore, also the power has statistical properties defined by the probability density function ρ_r. Therefore, the power defined by equation (3.19) has an average value that leads to an integral of the type of equation (3.24), being

$$
\begin{aligned}
E[P(r)] &= \int_{-\infty}^{+\infty} P(r)\rho_r(r)\,dr = 2P_0 \int_{r_{\text{on}}}^{+\infty} \left(\frac{r^2}{r_{\text{on}}^2} - 1\right)\rho_r(r)\,dr = \\
= P_0 &\frac{\sum_{n=0}^{+\infty} \frac{2^{-n}C^n}{r_{\text{on}}^2 n!\,A}\left(\frac{4}{A}\right)^{\frac{2n-1}{4}} \Gamma\left(\frac{2n+3}{4}, \frac{Ar_{\text{on}}^4}{4}\right) + \sum_{n=0}^{+\infty} \frac{2^{-n}C^n}{n!\,A}\left(\frac{4}{A}\right)^{\frac{2n-3}{4}} \Gamma\left(\frac{2n+1}{4}, \frac{Ar_{\text{on}}^4}{4}\right)}{e^{\frac{C_0}{4}} r_{\text{on}} + \sum_{n=0}^{+\infty} \frac{2^{-n}C^n}{n!A}\left(\frac{4}{A}\right)^{\frac{2n-3}{4}} \Gamma\left(\frac{2n+1}{4}, \frac{Ar_{\text{on}}^4}{4}\right)} = \\
= P_0 &\frac{\sum_{n=0}^{+\infty} \frac{2^{-n}C^n}{n!\,A}\left(\frac{4}{A}\right)^{\frac{2n-3}{4}} \left[\frac{1}{r_{\text{on}}^2}\sqrt{\frac{4}{A}}\Gamma\left(\frac{2n+3}{4}, \frac{Ar_{\text{on}}^4}{4}\right) + \Gamma\left(\frac{2n+1}{4}, \frac{Ar_{\text{on}}^4}{4}\right)\right]}{e^{\frac{C_0}{4}} r_{\text{on}} + \sum_{n=0}^{+\infty} \frac{2^{-n}C^n}{n!A}\left(\frac{4}{A}\right)^{\frac{2n-3}{4}} \Gamma\left(\frac{2n+1}{4}, \frac{Ar_{\text{on}}^4}{4}\right)}
\end{aligned}
\tag{3.28}
$$

These results allow to evaluate also the power variance, that is

$$
\begin{aligned}
\text{Var}[P(r)] = E\left[P^2(r) - E[P(r)]^2\right] = 2P_0^2 \int_{r_L}^{+\infty} \frac{r^4}{r_L^4}\rho_r(r)\,dr - 2P_0^2 \int_{r_L}^{+\infty} \rho_r(r)\,dr + \\
- 2P_0 E[P(r)] - 2\left(E[P(r)]\right)^2
\end{aligned}
\tag{3.29}
$$

These two quantities in function of r_{on} are plotted in figure 3.6a and 3.6b respectively. In order to well understand the laser power behaviour, the ratio ϱ between

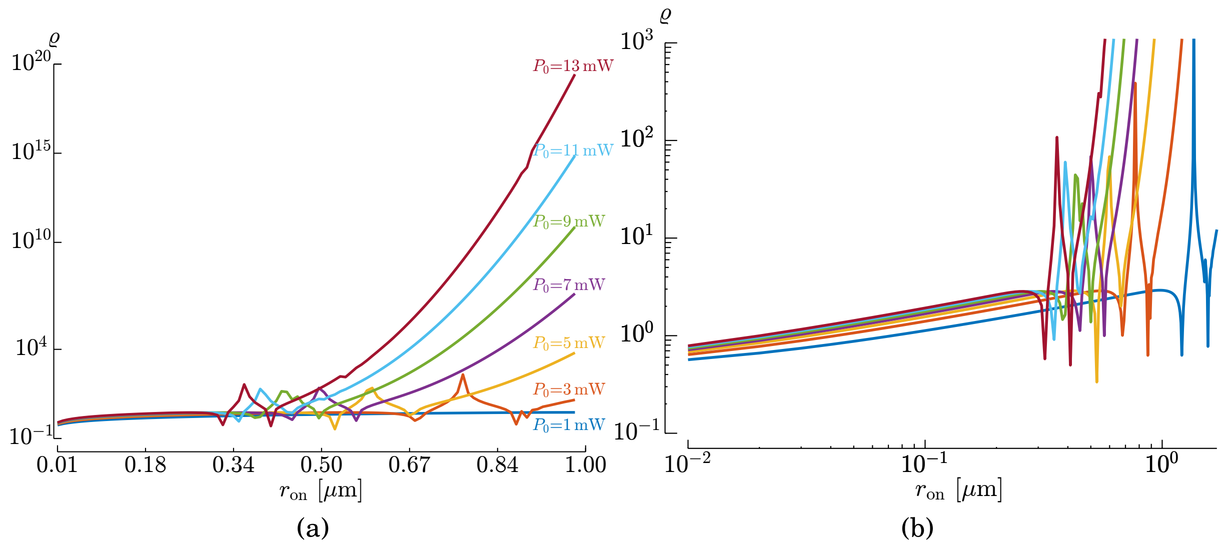

Figure 3.7: ratio ϱ between the standard deviation and mean value of the laser power as function of r_{on} at different values of P_0 in linear scale (a) and logarithmic scale (b).

the standard deviation of the laser power $\mathrm{Std}[P(r)] = \sqrt{\mathrm{Var}[P(r)]}$ and its average value is evaluated as function of r_{on}, as shown in figures 3.7a and 3.7a. The ratio ϱ indicates how and to what extent the trapped particle alters the cavity losses:

- if it is less than 1, the standard deviation of the power is small, the power fluctuates in a narrow range around the mean, and the feedback effect is weak because the losses introduced by the particle are low;
- if it is greater than 1, the standard deviation can be bigger than the mean value, the power fluctuates in a wide range, and the feedback effect is very strong (the particle is able to power off completely the laser).

The threshold value of r_{on} for that $\varrho > 1$ depends strongly on the power P_0 and there are different threshold values at the same laser power due to the fluctuations of ϱ shown in figures 3.7a and 3.7a. Nevertheless, for $r_{\mathrm{on}} < 0.08\,\mu\mathrm{m}$, all the curves are stably under 1 well defining a region for that the feedback is weak, as figure 3.7b shows.

This simple model, despite its limitations such as not considering a maximum power value (the power can be infinite) and not considering the dynamics of the laser system, returns an intuitive description of what in intracavity trapping by helping to understand its operating principles.

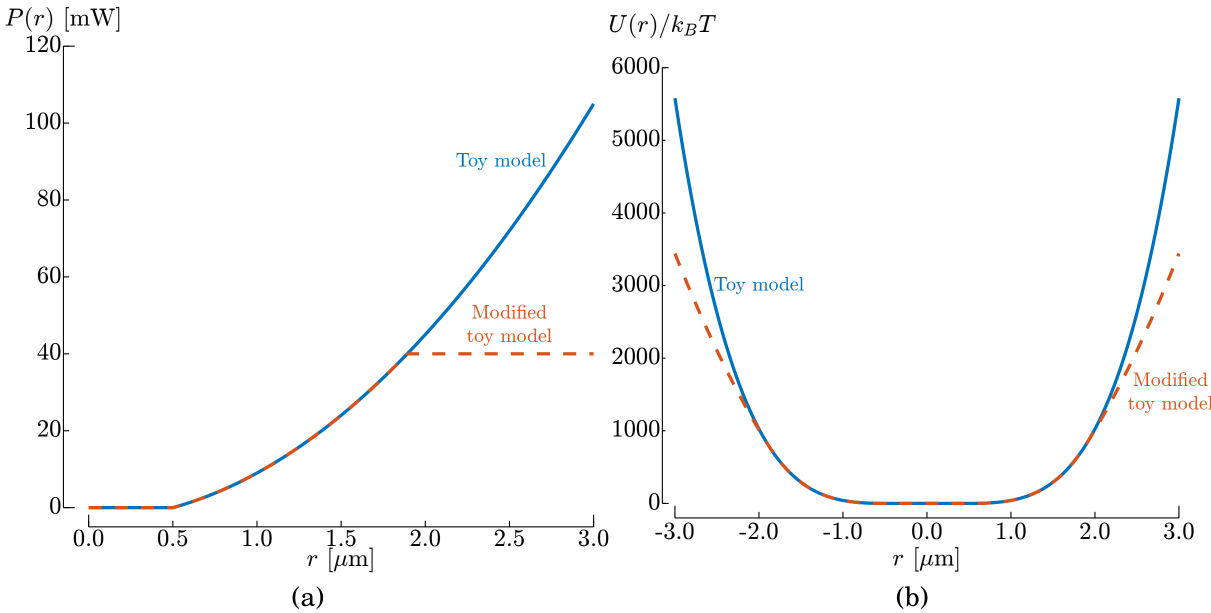

Figure 3.8: (a) power of the modified toy model (dashed orange line) as function of r compared to the toy model (blue solid line); (b) potential of the modified toy model (dashed orange line) as function of r compared to the toy model (blue solid line). For (a) and (b) $P_0 = 3\,\mathrm{mW}$, $P_{\max} = 40\,\mathrm{mW}$, and the temperature of the thermal bath is $298.15\,\mathrm{K}$, $\hbar = 1 \cdot 10^{-4}\,\mathrm{N/(m \cdot W)}$.

3.2.2 Modified toy model

In this section, a modified toy model is proposed to introduce the maximum power value of the system and, therefore, a maximum force value. For this purpose, the power of equation (3.19) is modified as

$$P(r) = \begin{cases} 0 & \text{if } |r| \leq r_{\text{on}} \\ P_0 \left(\dfrac{r^2}{r_{\text{on}}^2} - 1 \right) & \text{if } r_{\text{on}} < |r| \leq r_{\max} \\ P_0 \left(\dfrac{r_{\max}^2}{r_{\text{on}}^2} - 1 \right) & \text{if } |r| > r_{\max} \end{cases} \tag{3.30}$$

that can be written in a compact way with the indicator function, i.e.

$$P(r) = P_0 \left(\frac{r^2}{r_{\text{on}}^2} - 1 \right) \mathbb{I}_{r_{\text{on}} < |r| \leq r_{\max}} + P_{\max} \mathbb{I}_{|r| > r_{\max}} \tag{3.31}$$

with $P_{\max} = P_0 \left(\frac{r_{\max}^2}{r_{\text{on}}^2} - 1 \right)$ and $r_{\max} \geq r_{\text{on}}$. In this way, when the particle is sufficiently far away from the trapping region, the laser power saturates to the maximum value $P_{\max}$ defining a maximum distance $r_{\max}$ after that the feedback effect stops, as shown in figure 3.8a. Therefore, $r_{\max}$ depends on the particle properties (such as diameter, refractive index, geometrical shape) and on the trapping system properties (such as numerical aperture, focal distance, and working distance of the trapping lenses).

Assuming that $F_{\text{trap}} = -\bar{k}P(r)r(t)$ like in the toy model, the trapping force is

$$F_{\text{trap}}(t,r) = \begin{cases} 0 & \text{if } |r| \le r_{\text{on}} \\ -\bar{k}P_0 \left(\frac{r^2(t)}{r_{\text{on}}^2} - 1\right) r(t) & \text{if } r_{\text{on}} < |r| \le r_{\text{max}} \\ -\bar{k}P_{\text{max}} r(t) & \text{if } |r| > r_{\text{max}} \end{cases} \tag{3.32}$$

or

$$F_{\text{trap}} = -\bar{k}P_0 \left(\frac{r^2}{r_{\text{on}}^2} - 1\right) r\, \mathbb{I}_{r_{\text{on}}<|r|\le r_{\text{max}}} - k_{\text{max}} r\, \mathbb{I}_{|r|>r_{\text{max}}} \tag{3.33}$$

where all the functional dependencies are hidden, even if still present, and the maximum trapping force is given by $F_{\text{max}} = k_{\text{max}} r = \bar{k}P_{\text{max}} r$. The potential is related to the force by the relation $U(r) = -\int_0^r F_{\text{trap}}(r')\, dr'$, i.e.

$$\begin{aligned} U(r) &= \frac{\bar{k}P_0}{4r_{\text{on}}^2}\left(r^2 - r_{\text{on}}^2\right)^2 \mathbb{I}_{r_{\text{on}}<|r|\le r_{\text{max}}} + \left(\frac{1}{2}k_{\text{max}} r^2 - k_B T C_{\text{max}}\right) \mathbb{I}_{|r|>r_{\text{max}}} = \\ &= k_B T \left[\left(\frac{A}{4}r^4 - \frac{C}{2}r^2 + \frac{C_0}{4}\right) \mathbb{I}_{r_{\text{on}}<|r|\le r_{\text{max}}} + \left(\frac{1}{2}K_{\text{max}} r^2 - C_{\text{max}}\right) \mathbb{I}_{|r|>r_{\text{max}}}\right] \end{aligned} \tag{3.34}$$

where $C_{\text{max}} = \frac{1}{k_B T}\frac{\bar{k}P_0}{4r_{\text{on}}^2}\left(r_{\text{max}}^4 - r_{\text{on}}^4\right)$, $A = \frac{1}{k_B T}\frac{\bar{k}P_0}{r_{\text{on}}^2}$, $C = \frac{1}{k_B T}\bar{k}P_0$, $C_0 = \frac{1}{k_B T}\bar{k}P_0 r_{\text{on}}^2$, and $K_{\text{max}} = \frac{1}{k_B T}k_{\text{max}}$. This potential differs from the toy model potential of equation (3.21) because, when the particle displacement $|r| > r_{\text{max}}$, the trapping force is linear as in a standard optical tweezers with stiffness $\bar{k}P_{\text{max}}$ (figure 3.8b). Following the same procedure done for the toy model, the mean value of r^j is

$$\begin{aligned} &\int_{-\infty}^{+\infty} r^j \rho_r(r)\, dr = \rho_r(0)\int_{-\infty}^{+\infty} r^j e^{\left(-\frac{A}{4}r^4 + \frac{C}{2}r^2 - \frac{C_0}{4}\right)\mathbb{I}_{r_{\text{on}}<|r|\le r_{\text{max}}} - \left(\frac{1}{2}K_{\text{max}} r^2 - C_{\text{max}}\right)\mathbb{I}_{|r|>r_{\text{max}}}}\, dr = \\ &= \rho_r(0)\left[1 + (-1)^j\right]\left[\int_0^{r_{\text{on}}} r^j\, dr + e^{-\frac{C_0}{4}}\int_{r_{\text{on}}}^{r_{\text{max}}} r^j e^{-\frac{A}{4}r^4 + \frac{C}{2}r^2}\, dr + e^{C_{\text{max}}}\int_{r_{\text{max}}}^{+\infty} r^j e^{-\frac{1}{2}K_{\text{max}} r^2}\, dr\right] \end{aligned} \tag{3.35}$$

where the first and the third integrals are

$$\int_0^{r_{\text{on}}} r^j\, dr = \frac{r_{\text{on}}^{j+1}}{j+1} \tag{3.36}$$

$$e^{C_{\text{max}}}\int_{r_{\text{max}}}^{+\infty} r^j e^{-\frac{1}{2}K_{\text{max}} r^2}\, dr = \frac{1}{2}e^{C_{\text{max}}}\left(\frac{K_{\text{max}}}{2}\right)^{-\frac{j+1}{2}} \Gamma\left(\frac{j+1}{2}, \frac{K_{\text{max}} r_{\text{max}}^2}{2}\right) \tag{3.37}$$

The second integral is resolvable developing in Maclaurin series the exponential $\exp\left(\frac{C}{2}r^2\right)$ as done for (3.24), with the only difference that the integration interval is different, i.e.

$$\begin{aligned} e^{-\frac{C_0}{4}} \int_{r_{\text{on}}}^{r_{\max}} r^j e^{-\frac{A}{4}r^4+\frac{C}{2}r^2}\, dr &= e^{-\frac{C_0}{4}} \sum_{n=0}^{+\infty} \frac{2^{-n}C^n}{n!} \int_{r_{\text{on}}}^{r_{\max}} r^{2n+j} e^{-\frac{A}{4}r^4}\, dr = \\ &= e^{-\frac{C_0}{4}} \sum_{n=0}^{+\infty} \frac{2^{-n}C^n}{n!} \left[\int_{r_{\text{on}}}^{\infty} r^{2n+j} e^{-\frac{A}{4}r^4}\, dr - \int_{r_{\max}}^{\infty} r^{2n+j} e^{-\frac{A}{4}r^4}\, dr \right] \\ = e^{-\frac{C_0}{4}} \sum_{n=0}^{+\infty} \frac{2^{-n}C^n}{n!\,A} \left(\frac{4}{A}\right)^{\frac{j+2n-3}{4}} & \left[\Gamma\left(\frac{j+2n+1}{4}, \frac{Ar_{\text{on}}^4}{4}\right) - \Gamma\left(\frac{j+2n+1}{4}, \frac{Ar_{\max}^4}{4}\right) \right] \end{aligned} \tag{3.38}$$

Therefore, the mean value of r^j is

$$\begin{aligned} \int_{-\infty}^{+\infty} r^j \rho_r(r)\, dr =& \rho_r(0)\left[1+(-1)^j\right] \left\{ \frac{r_{\text{on}}^{j+1}}{j+1} + \right. \\ & + e^{-\frac{C_0}{4}} \sum_{n=0}^{+\infty} \frac{2^{-n}C^n}{n!\,A} \left(\frac{4}{A}\right)^{\frac{j+2n-3}{4}} \left[\Gamma\left(\frac{j+2n+1}{4}, \frac{Ar_{\text{on}}^4}{4}\right) - \Gamma\left(\frac{j+2n+1}{4}, \frac{Ar_{\max}^4}{4}\right) \right] + \\ & \left. + \frac{1}{2} e^{C_{\max}} \left(\frac{K_{\max}}{2}\right)^{-\frac{j+1}{2}} \Gamma\left(\frac{j+1}{2}, \frac{K_{\max} r_{\max}^2}{2}\right) \right\} \end{aligned} \tag{3.39}$$

where the first term depends only on r_{on} and the other two terms are dependent of r_{on}, $r_{\max}$, P_0, and $\bar{k}$ directly or through the definition of A, C, C_0, $C_{\max}$, and $K_{\max}$. This result for $j = 0$ can be used to obtain $\rho_r(0)$ from the normalization condition, i.e.

$$\begin{aligned} \rho_r(0) = \frac{1}{2} \left\{ \frac{r_{\text{on}}}{2} + e^{-\frac{C_0}{4}} \sum_{n=0}^{+\infty} \frac{2^{-n}C^n}{n!\,A} \left(\frac{4}{A}\right)^{\frac{2n-3}{4}} \left[\Gamma\left(\frac{2n+1}{4}, \frac{Ar_{\text{on}}^4}{4}\right) - \Gamma\left(\frac{2n+1}{4}, \frac{Ar_{\max}^4}{4}\right) \right] + \right. \\ \left. + \frac{1}{2} e^{C_{\max}} \left(\frac{K_{\max}}{2}\right)^{-\frac{j+1}{2}} \Gamma\left(\frac{j+1}{2}, \frac{K_{\max} r_{\max}^2}{2}\right) \right\}^{-1} \end{aligned} \tag{3.40}$$

From these relations, it follows that

$$E[r] = 0 \tag{3.41}$$

and that the variance is

$$\begin{aligned} \mathrm{Var}[r] = \int_{-\infty}^{+\infty} r^2 \rho_r(r)\, dr =& 2\rho_r(0) \left\{ \frac{r_{\text{on}}^3}{3} + \frac{1}{2} e^{C_{\max}} \left(\frac{K_{\max}}{2}\right)^{-\frac{3}{2}} \Gamma\left(\frac{3}{2}, \frac{K_{\max} r_{\max}^2}{2}\right) + \right. \\ & \left. + e^{-\frac{C_0}{4}} \sum_{n=0}^{+\infty} \frac{2^{-n}C^n}{n!\,A} \left(\frac{4}{A}\right)^{\frac{2n-1}{4}} \left[\Gamma\left(\frac{2n+3}{4}, \frac{Ar_{\text{on}}^4}{4}\right) - \Gamma\left(\frac{2n+3}{4}, \frac{Ar_{\max}^4}{4}\right) \right] \right\} \end{aligned} \tag{3.42}$$

The behaviour of the variance of the particle trajectory as function of r_{on} is shown in figure 3.9a and it is compared with the toy model variance of equation (3.27)

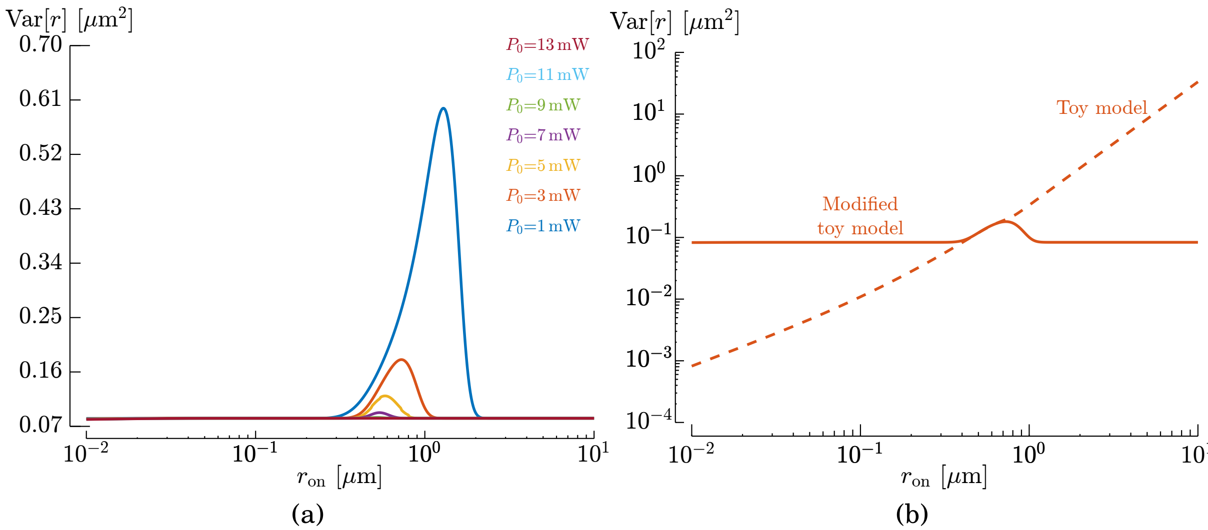

Figure 3.9: (a) trajectory variance $\mathrm{Var}[r]$ as function of $r_{\rm on}$ at different values of P_0 for $P_{\max} = 40\,\mathrm{mW}$, temperature of the thermal bath $298.15\,\mathrm{K}$, $\bar{k} = 1 \cdot 10^{-4}\,\mathrm{N/(m \cdot W)}$; (b) comparison between $\mathrm{Var}[r]$ of equation (3.27) (dashed line) and equation (3.42) (solid line) as function of $r_{\rm on}$ for $P_0 = 3\,\mathrm{mW}$.

in figure 3.9b. The variance is almost constant for $r_{\rm on} \in [1 \cdot 10^{-2}, 1.5 \cdot 10^{-1}]\,\mu\mathrm{m}$, subsequently presenting peaks that decrease as P_0 increases. The presence of a maximum power means that the variance does not grow as in the case of the toy model, although for $r_{\rm on}$ values between $0.42\,\mu\mathrm{m}$ and $0.62\,\mu\mathrm{m}$ the two curves grow equally, figure 3.9b.

The other quantity of interest is the mean power of the laser system $E[P(r)]$. In this case, the expression of $E[P(r)]$ is

$$
\begin{aligned}
E[P(r)] &= \int_{-\infty}^{+\infty} P(r)\rho_r(r)\,dr = 2P_0 \int_{r_{\rm on}}^{r_{\max}} \left(\frac{r^2}{r_{\rm on}^2} - 1\right) \rho_r(r)\,dr + 2P_{\max} \int_{r_{\max}}^{+\infty} \rho_r(r)\,dr = \\
&= 2\rho_r(0)P_0 \left[\frac{e^{-\frac{C_0}{4}}}{r_{\rm on}^2} \int_{r_{\rm on}}^{r_{\max}} r^2 e^{-\frac{A}{4}r^4 + \frac{C}{2}r^2}\,dr - e^{-\frac{C_0}{4}} \int_{r_{\rm on}}^{r_{\max}} e^{-\frac{A}{4}r^4 + \frac{C}{2}r^2}\,dr + \right. \\
&\left. + \frac{P_{\max} e^{C_{\max}}}{P_0} \int_{r_{\max}}^{+\infty} e^{-\frac{1}{2}K_{\max} r^2}\,dr \right]
\end{aligned}
\tag{3.43}
$$

and it can be evaluated using equation (3.37) for $j = 0$ and equation (3.38) for $j = 1, 2$. The mean value of the power is plotted as function $r_{\rm on}$ in figure 3.10a and, differently from the original toy model that for $r_{\rm on} \to 0$ the power tends to infinity, it reaches P_{max} for $r_{\rm on} \to 0$, as it can be seen in figure 3.10b. This prevents the model from producing infinite energy like the toy model of the previous section.

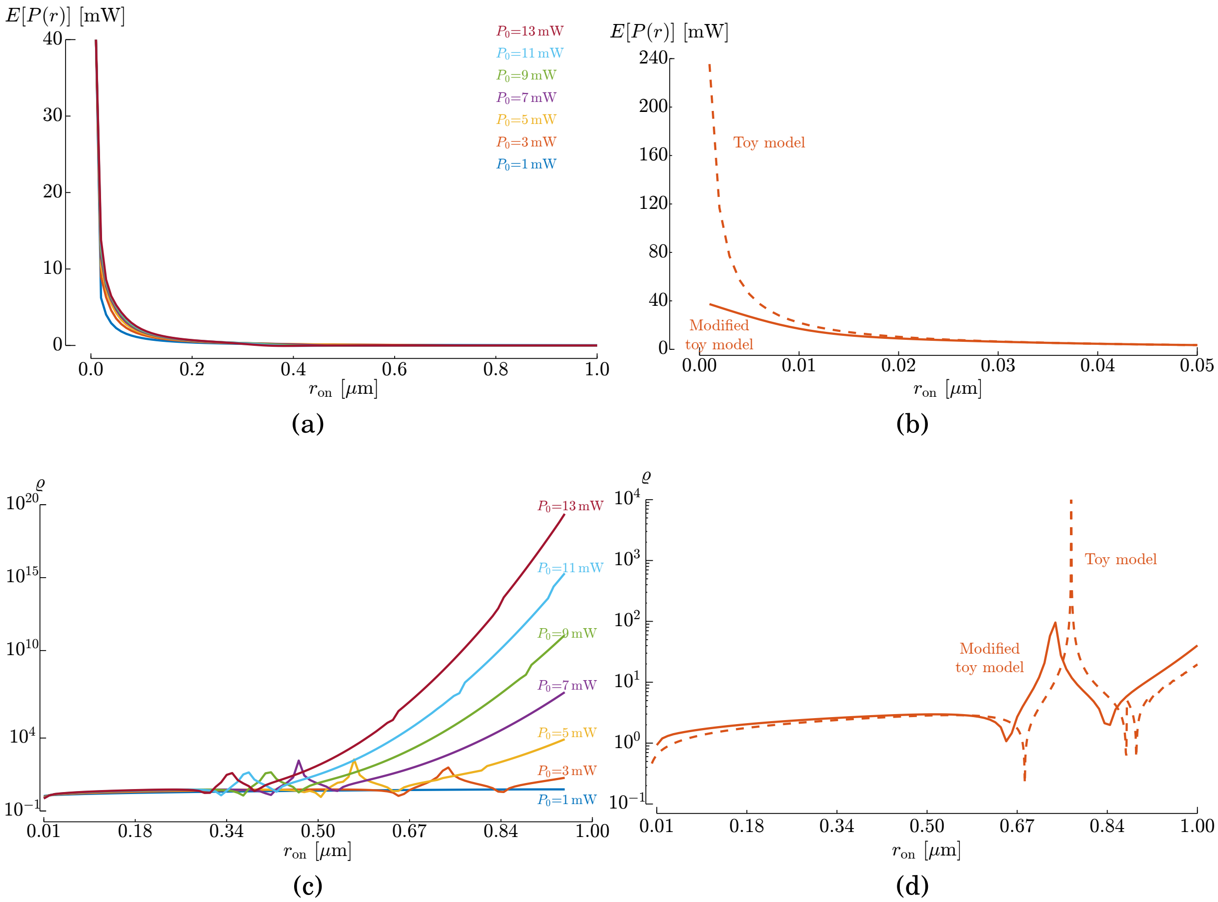

Figure 3.10: (a) mean power $E[P(r)]$ as function of r_{on} at different values of P_0 using the same parameters of figure 3.9a; (b) comparison between $E[P(r)]$ of equation (3.28) (dashed line) and (3.43) (solid line); (c) ratio ϱ as function of r_{on} at different values of P_0 using the same parameters of figure 3.9a; (d) comparison between ϱ obtained with toy model (dashed line) and with the modified toy model (solid line) for $P_0 = 3\,\text{mW}$.

To conclude this section, the variance of the power is

$$\begin{aligned}\text{Var}[P(r)] = E[P^2] - E[P]^2 = 2P_0^2 \Bigg[\int_{r_{\text{on}}}^{r_{\text{max}}} \frac{r^4}{r_{\text{on}}^4} \rho_r(r)\, dr - 2 \int_{r_{\text{on}}}^{r_{\text{max}}} \frac{r^2}{r_{\text{on}}^2} \rho_r(r)\, dr + \\ + \int_{r_{\text{on}}}^{r_{\text{max}}} \rho(r)\, dr + \frac{P_{\text{max}}^2}{P_0^2} \int_{r_{\text{max}}}^{+\infty} \rho_r(r) \Bigg] - E[P]^2\end{aligned} \tag{3.44}$$

and, as done for the toy model, the ratio ϱ between the standard deviation of the laser power and its mean value is calculated as function of r_{on} and it can be compared with the toy model. The behaviour of ϱ in function of r_{on} is shown in figure 3.10c and compared to the toy model of figure 3.10d. The ratio ϱ not changes drastically and, therefore, the same consideration can be done: for $r_{\text{on}} < 0.08\,\mu\text{m}$, all the curves are stably under 1 well defining a region for that the feedback is weak.

Chapter 4

Experimental setups

In this chapter, the optical trapping setups used in these experiments are described: a standard single-beam optical tweezers (SBOT), used mainly for preliminary experiments of particles trapping in water and in air, and an *intracavity optical tweezers* (IOT), employed for the intracavity trapping. The SBOT uses an infrared laser beam coupled with an optical homemade microscope that forms an optical trap thanks to a high numerical aperture NA objective lens. Instead the IOT consists of a fibre-air laser ring cavity in which it is built a trapping system. Thanks to a removable optical isolator [27], the IOT can trap particles in single-beam configuration (with the isolator) and in double-beam configuration (without the isolator). Both systems are homemade, i.e. designed and realized specifically for this work.

Furthermore, this chapter describes the homemade loading system realised for *particle loading* in air based on a piezoelectric transducer (PZT).

Hence, the first and the second sections of this chapter describe how the SBOT and the IOT are designed and realised respectively. The third section, instead, deals with the sample preparation for trapping particles in water and how to load them into the trap. The last section deals with how to trap particles in air and describes the loading homemade system, introducing also the van der Waals force and the basic principles of the piezoelectric effect.

4.1 Standard single-beam optical tweezers

The standard single-beam optical tweezers (SBOT) setup is made by coupling a laser beam with an optical homemade microscope that use high numerical aperture objective lenses ($\mathrm{NA} > 0.8$) in order to achieve the trapping condition. Building the SBOT, it is also very important to minimise all noise sources, like laser power instabilities, mechanical vibrations, temperature and humidity fluctuations, because they strongly affect the trapping performance.

The setup of SBOT is shown schematically in figure 4.1a and it is built following the guidelines provided by Pesce et al. [50] . The laser source is a single frequency

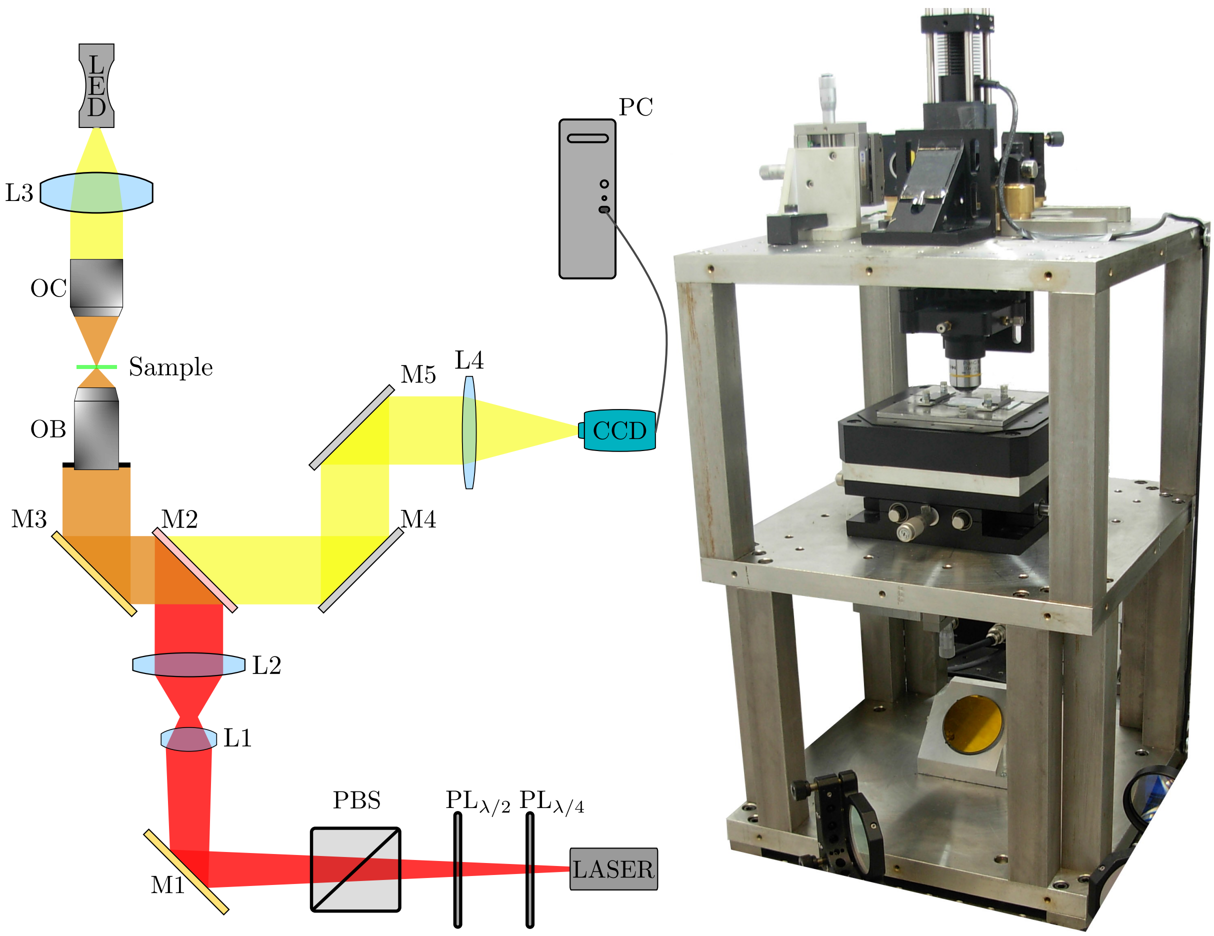

(a) (b)

Figure 4.1: (a) diagram of the single-beam optical tweezers experimental setup; (b) picture of the homemade microscope.

continuous-wave solid-state laser (*Innolight Mephisto 500*) based on a monolithic Nd:YAG crystal in non-planar ring oscillator configuration and it produces a TEM_{00} beam at $1064\,\mathrm{nm}$ with elliptical polarisation. Its polarisation is made linear by the zero-order quarter-wave plate $\mathrm{PL}_{\lambda/4}$ placed after the laser source. To control the laser power without affecting the laser beam quality[1], the zero-order half-wave plate $\mathrm{PL}_{\lambda/2}$ and the polarising beam splitter cube PBS are placed after $\mathrm{PL}_{\lambda/4}$. In this way, by varying the polarisation direction of the beam with $\mathrm{PL}_{\lambda/2}$, the power of the beam transmitted by the PBS can be finely tuning.

To maximise the trapping efficiency, the laser beam needs to be injected into the homemade microscope with a beam size larger than the back aperture of the

[1]This laser source is pumped by a laser diode and its output power is defined by the injection current of the pump diode laser. Thus, to change the output power, it is possible to change the injection current, but this can alter the laser beam quality, appreciably lowering the optical trapping efficiency.

trapping lens. In this way, the *focusing power*[2] is maximum and consequently the optical gradient is the most uneven possible increasing the gradient trapping force. Therefore, the laser beam is directed, thanks to the mirror $\mathrm{M1}$, into a $10\mathrm{X}$ telescope made by the lenses $\mathrm{L1}$ of focal length $f = 25\,\mathrm{mm}$ and $\mathrm{L2}$ of $f = 250\,\mathrm{mm}$.

Then, the laser beam is injected into the homemade microscope, see figure 4.1b, with the mirrors $\mathrm{M2}$ and $\mathrm{M3}$ (*Thorlabs PF20-03-M03*). The microscope is built on a stabilised optical table in AISI 316 stainless steel, characterised by low thermal expansion coefficients and great rigidity, to make it as stable as possible. This microscope has a three-level structure organised as follows:

- the first level is fixed on the optical table and contains the gold mirror $\mathrm{M3}$ (*Thorlabs PF20-03-M03*), arranged at $45°$ reflecting the laser beam into the second level;

- the second level is a breadboard fixed on eight columns and hosts the trapping lens OB mounted vertically on a high-stability linear translation stage (*Physik Instrumente M-105.10*), a two-axis manual translation stage (*Newport M406* with *HR-13* actuators) and a three-axis piezoelectric automatic stage (*PhysikInstrumente, PI-517.3CL*) both with a through-hole design to mount them around OB. In this way, it is possible to move micrometrically the sample. These two stages are joined together to form a single stage hosting the sample, that can be moved roughly with the manual micrometric stage and finely with the piezoelectric stage[3];

- the third level is placed above the second-level breadboard with four columns. It hosts the illumination LED (*Thorlabs MCWHL5* white led $6500\,\mathrm{K}$) with its collimation aspheric lens $\mathrm{L3}$, mounted together with modular optomechanics components (*Thorlabs cage system*). This level hosts also the condenser objective lens CB, mounted vertically opposite OB on a five-axis stage that allows fine alignment of CB with respect to OB.

The *imaging system* is formed by a LED light source and a CCD camera. The LED light is focused on the sample by its collimation lens $\mathrm{L3}$ and the condenser OC. Its light is transmitted by the sample and, thanks to the mirror $\mathrm{M3}$ and the dichroic mirror $\mathrm{M2}$ (*STANDA 14DM-2-HR15-45-1*)[4], is reflected to the tube lens $\mathrm{L4}$ by the silver mirrors $\mathrm{M4}$ and $\mathrm{M5}$ (*Thorlabs PF20-03-P01* mounted on precision kinematic mirror mounts *Thorlabs KS2*)[5]. This lens focuses on the CCD camera (*Mikrotron MotionBLITZ EoSens Mini 1*) the image of the sample[6]. In this way, images and videos of the sample can be acquired with the computer, PC, connected to the CCD.

[2]The focusing power is the degree to which an optical system converges or diverges light.

[3]The piezoelectric stage, if necessary, can move the sample automatically and, also, following movement patterns.

[4]The dichroic mirror reflects the 99.5% of the laser light and transmits almost completely the LED light

[5]The precision kinematic mirror mounts helps to proper align the tube lens and the CCD.

[6]The tube lens needs to be aligned and placed properly in order to overlap the focal plane of

The tube lens L4 determines, depending on its focal length, the magnification of the microscope: the shorter the focal length, the lower the magnification and in this setup it has a focal length of $500\,\mathrm{mm}$.

The entire setup is encapsulated in a protective box that insulates it from external light sources and air flows, helps to stabilise the temperature, and protects lab users from stray laser beams.

the imaging system with the trapping plane, i.e. the plane that contains the particle centre when trapped. In addition, the alignment of the camera and the tube lens is decisive for minimising the image distortions and, therefore, having a clear image.

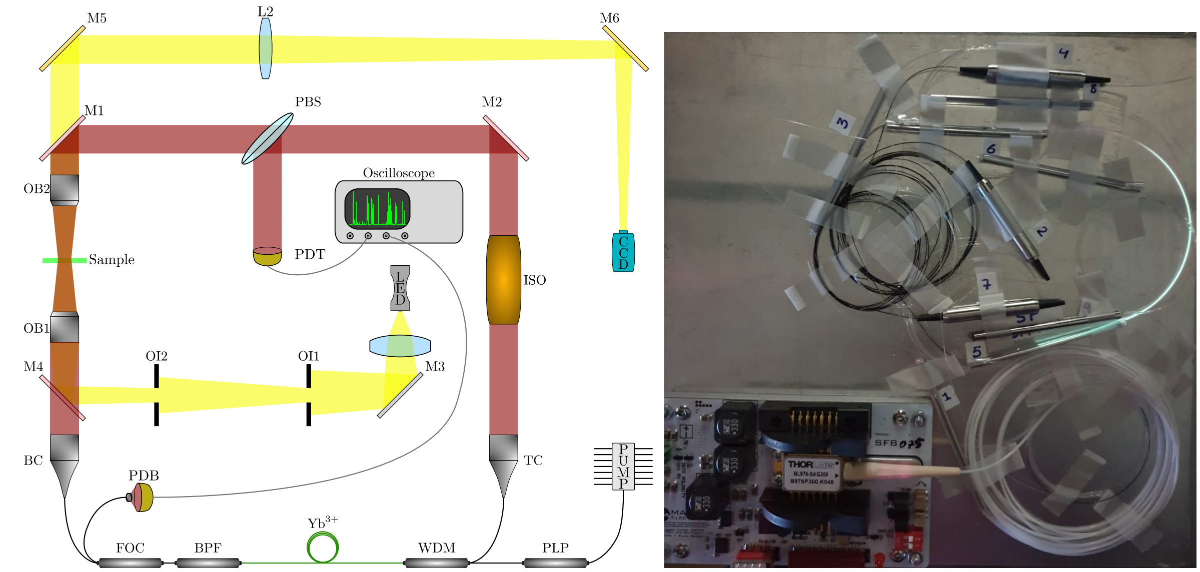

(a) (b)

Figure 4.2: (a) diagram of the experimental setup used to trap particles with intracavity optical tweezers both with single-beam and double-beam configurations thanks to the removable isolator ISO; (b) picture of the fibre path of the ring fibre laser where device number 1, 3, 5, 6, and 8 are splice protectors, device number 2 is the fibre pump laser protector PLP, device number 4 is the wavelength division multiplexing WDM, device number 7 is the fibre bandpass filter, BPF, and device number 9 is the fibre optical coupler FOC.

4.2 Intracavity optical tweezers

A intracavity optical tweezers (IOT) setup is realised by modifying a ring fibre laser in a hybrid laser cavity in which laser light travels both in fibre and in air. The air part (free-space) of the cavity allows the trapping system to be built inside the laser cavity. The setup diagram of the IOT used in this work is shown in figure 4.2a and allows to trap particle in both single-beam and double-beam configurations. The entire setup, which is encapsulated in a protective box, can be schematically divided into a laser system[7] and a trapping system [27].

Laser system The laser system consists of a Yb^{3+} ring fibre laser pumped by a $976\,\mathrm{nm}$ butterfly fibre Bragg grating stabilised laser (*Thorlabs BL976-SAG300*) coupled to a single mode fibre. To avoid damaging the pump with reversed laser light, the fibre pump laser protector PLP (*Optosun Pump Laser Protector* $976\,\mathrm{nm}$) is used. This fibre component, characterised by one input and one output fibre terminals, blocks the light directed towards the pump and it is spliced with the fibre of the laser pump using a fusion splicer (*Sumitomo TYPE-71C Direct Core*

[7]The fibre laser system was designed and realised in collaboration with professor Parviz Elahi

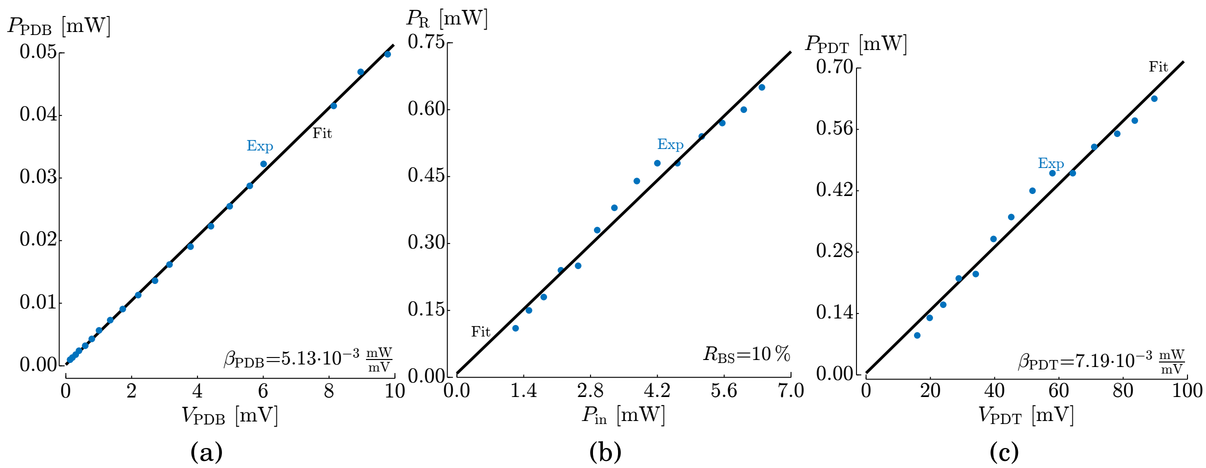

Figure 4.3: (a) calibration of PDB, where P_{PDB} is the power of the laser beam measured with the power meter, V_{PDB} is the voltage of the photodiode PDB measured with the oscilloscope, and $\beta_{\mathrm{PDB}} = 5.13 \cdot 10^{-3}\,\mathrm{mW/mV}$ is the measured calibration factor; (b) reflectance of BS, where P_{in} is the power of the laser light that impinges on BS, P_{R} is the power of the laser beam reflected in direction of the photodiode PDT, and $R_{\mathrm{BS}} = 10\%$ is the measured reflectance; (c) calibration of PDT, where P_{PDT} is the power of the laser beam, V_{PDT} is the voltage of the photodiode PDT, and $\beta_{\mathrm{PDT}} = 7.19 \cdot 10^{-3}\,\mathrm{mW/mV}$ is the measured calibration factor.

Monitoring Fusion Splicer).

The pump light is injected into the Yb^{3+} doped fibre (*Coractive YB 406*) splicing the output fibre terminal of PLP with one of the two input terminals of the wavelength division multiplexing WDM (*Optosun* WDM*,* $980\,\mathrm{nm}/1050\,\mathrm{nm}$ *non PM hi1060 fiber*). Indeed, the WDM is a fibre component with two input and one output fibre terminals, which mixes the light from the two inputs into the output fibre. As said, one input is spliced to the pump laser through PLP and the other to the fibre of the cavity. Instead, the output terminal is spliced with the doped fibre. This ensures that both the laser signal and the pump light are injected into the active medium (Yb^{3+} doped fibre) making the laser mechanism possible.

Then, the active medium is spliced with the input terminal of the fibre bandpass filter BPF (*Optosun bandpass filter* $1030 \pm 2\,\mathrm{nm}$) to prevent the light from the pump at $976\,\mathrm{nm}$ reaching the sample. In order to monitor the laser light inside the cavity, the output fibre terminal of BFP is spliced with the input fibre terminal of the fibre optical coupler FOC (*Optosun short wavelength coupler*).

The FOC split the light of its input fibre terminal into two fibre output terminals with a coupling ratio of $95\%/5\%$. The 5% fibre output terminal is spliced with a FC connector and connected with a photodiode PDB (*Thorlabs FD11A*), so that the laser power can be measured and the feedback effect quantified. Indeed, the PDB is connected to an oscilloscope and calibrated using a calibrated power meter (*Thorlabs PM100D* with the power sensor *Thorlabs S144C*), see figure 4.3a.

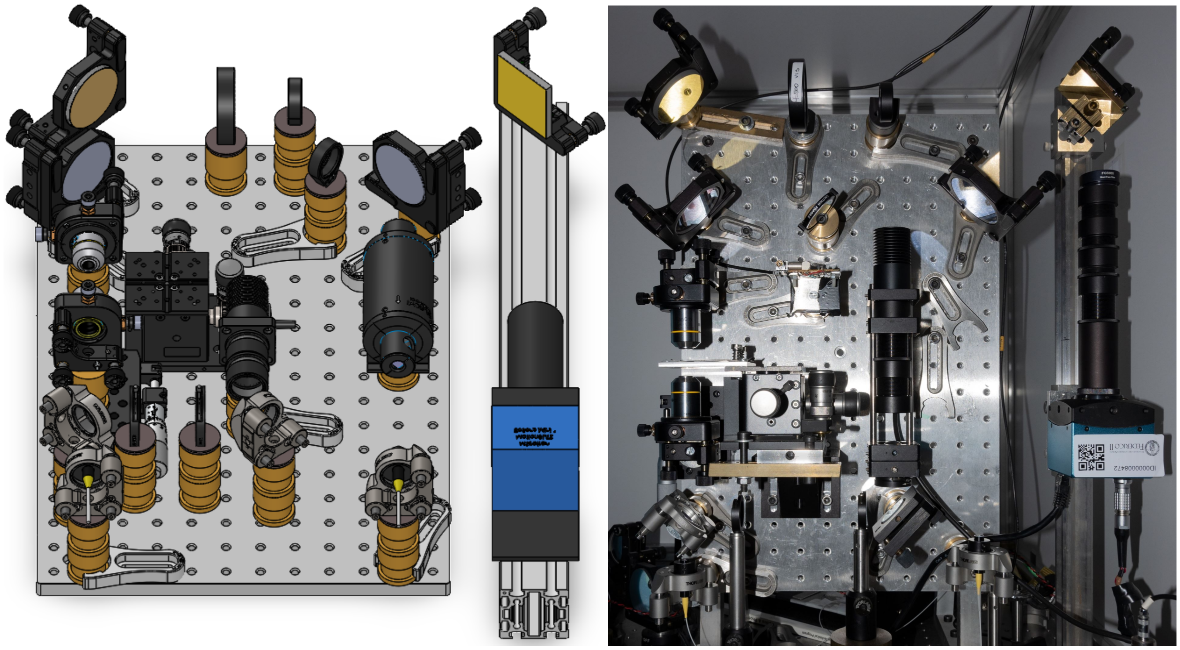

(a) (b)

Figure 4.4: (a) design and (b) realisation of trapping system for IOT.

The 95% fibre output terminal is spliced, instead, with the *bottom collimator* BC (*Oz optics LPC-04-1030-6/125-S-4.0-18AS-40-3S-1-1*) that expels the laser light from the fibre. This light is then recollected by a similar collimator that is spliced with the second input of the WDM closing the cavity. This collimator is called *top collimator* TC. Between the two collimators, a removable free-space optical isolator ISO (*Optics for Research IO-8-1064-VHP*) is placed to choose between single-beam IOT (SBIOT) or double-beam IOT (DBIOT). Without the ISO, two beams travel inside the laser cavity (see chapter 3.1): one travelling from the bottom collimator to the top collimator, called the *bottom beam*; the other travelling in the opposite direction and called the *top beam*. Instead, mounting the isolator that suppresses the top beam, the SBIOT is achieved.

Trapping system In the free-space part of the cavity, between the two collimators, the trapping system is mounted. The whole trapping system and part of the imaging system are mounted on a breadboard (*Thorlabs MB3045U/M*), figures 4.4a and 4.4b. This breadboard is mounted vertically on two L-shape rods and, if needed, the system can be mounted horizontally on the optical table. Before mounting the trapping and imaging system, the bottom collimator BC and the top collimator TC must be aligned with each other in order to close the cavity and, hence, to obtain the lasing condition. For this reason, the bottom collimator BC and the top one TC are mounted on kinematic mounts with tip, tilt, and optical axis adjustment (*Thorlabs POLARIS-K1T3*). In this way, thanks also to the dichroic mirrors M1 and M2 (*STANDA 14DM-2-HR15-45-1*), it is possible to align them together.

The trapping system consists of two objective lenses OB1 and OB2 (*Olympus PlanC N 10x* with $\mathrm{NA} = 0.25$ or *Thorlabs C060TMD-B* with $f = 9.6\,\mathrm{mm}$ and $NA = 0.3$) in confocal configuration, which form the optical trap by focusing the optical field between them. At the same time, the confocal configuration does not alter the laser beam properties outside them, allowing the laser beam to be completely re-injected into the fibre [8]. Therefore, the lenses are mounted on 5-axis locking kinematic mounts (*Thorlabs K5X1*). The objective lens OB1 is also mounted on a linear translation stage (*Thorlabs XRN25P/M*) that moves it precisely along the optical axis in order to obtain the confocal configuration.

On the breadboard, the sample is placed between the two objective lenses on a 3-axis compact flexure stage (*Thorlabs MBT616D/M*) to translate it micrometrically. The breadboard hosts also a pellicle beam splitter BS placed between M1 and M2. The BS reflects the 11% of the top beam power (see figure 4.3b for the measurement of BS reflectance, R_{BS}) on the photodiode PDT (*Thorlabs FD11A*), which is connected to the oscilloscope and calibrated in the same way of PDB, see figure 4.3c. This allows to monitor simultaneously the power of the two beams in double-beam configuration.

Instead, the imaging system is mounted partially on the breadboard and partially on a rail system (*Newport X26-512*) fixed on the optical table. The breadboard hosts the red light LED (*Thorlabs M625L4*) with its collimation lens L1, whose light is guided on the sample by the silver mirror M3 (*Thorlabs PF20-03-P01*) and the longpass dichroic mirror M4 (*Thorlabs DMLP1000*), that reflects more than the 95% of the light with wavelength $< 1000\,\mathrm{nm}$ and transmits about the 96% of the laser light at $1030\,\mathrm{nm}$. Between M3 and M4, there are two optical iris OI1 and OI2 (*Thorlabs ID25*) that decrease the size of the LED beam to avoid unwanted visible reflections in the experimental apparatus. The visible light, therefore, is focused on the sample by OB1 and defocused again by OB2. To have the best image of the sample, the LED light is not perfectly collimated, but reaches OB1 with a slight divergence. The transmitted light by the sample passes through the dichroic mirror M1 and it is guided by the mirror M5 on the lens L2 with focal length $500\,\mathrm{mm}$. This lens produces on the CCD camera (*Mikrotron MotionBLITZ EoSens Mini 1*) the image of the sample. Instead, the rail system host the gold mirror M6 (*Thorlabs PFSQ20-03-M03*) and the CCD camera. It is important to underline that, in order to synchronise the photodiodes signals and the CCD camera video, the CCD camera and the oscilloscope are connected both to the same function generator that works as clock. This allows to study correlation phenomena between the particle trajectory and the power of the two laser beams.

[8] As for the bottom and top collimators, the alignment between OB1 and OB2 is critical to close the cavity.

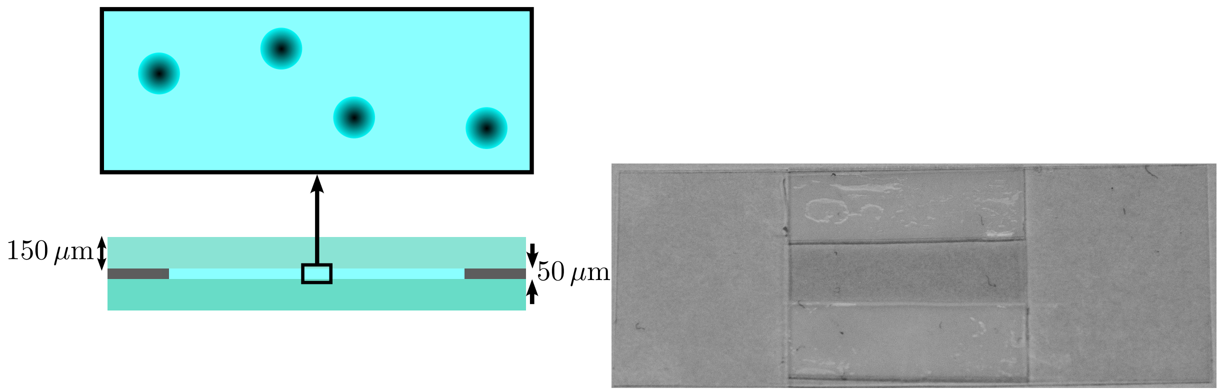

(a) (b)

Figure 4.5: (a) diagram of a sample to trap particles in water, in the inset (top of the image) there is a sketch of particles floating in water; (b) experimental realisation of a sample to trap particles in water.

4.3 Sample and loading in water

The sample chamber consists of two thin glass coverslips glued together to form a channel, into which a solution of water and particles is injected. The glass coverslips are approximately $150\,\mu\mathrm{m}$ thick and are glued together with UV glue using parafilm strips as a spacers. In this way, the chamber has an internal height that can be varied between $50\,\mu\mathrm{m}$ and $200\,\mu\mathrm{m}$. The solution of particles and water, on the other hand, is made using commercial monodisperse micrometric sphere (*microParticles GmbH*) diluted in milli-Q water that is not contaminated by unwanted particles or bacteria. If necessary, a small percentage of Triton-X surfactant ($0.01\,\%$ or less) can be added to the solution to increase the lifetime of the sample. Indeed, particles tend to stick to the surface a few hours after the sample production due to van der Waals and Coulomb forces and Triton-X reduces this phenomenon. The volume percentage of the particles diluted in water is crucial because: if it is too high, there will be too many particles in the sample and trapping a single particle can be very difficult (other particles are trapped unintentionally during the experiment); if it is too low, finding a particle is time-consuming and also frustrating. A good compromise is to use a volume percentage of micrometric particles in water of about $0.01\,\mu\mathrm{l/ml}$ or less depending on the chamber volume. A diagram of the sample and its experimental realisation are shown in figures 4.5a and 4.5b.

The particle loading, instead, is very simple. In water, micrometric particles float for quite a long time, hours if the particles are less dense than water (like polystyrene particles) and tens of minutes if denser (like silica particles). This time is sufficient to locate a particle in the sample, move the sample using the micrometer stages to get the particle into the trap region, and, therefore, trap the particle. Once trapped, the particle can virtually remain in the trap forever. It is important at this point to check that the particle is not unintentionally in contact with, or extremely close to, a chamber wall as this greatly alters the measurement results. This check can be carried out by moving the particle (i.e. the sample) and, via real-time video, verify whether the particle does not follow the trap as it should. For simplicity, consider the optical axis to be the vertical direction: if the particle is far from a wall, it always remains in the centre of the trap and in focus; if, on the other hand, the particle touches the bottom or top of the chamber, its image becomes blurry when the particle is moved vertically (along the optical axis); if the particle touches one of the sides of the chamber, its position relative to the centre of the trap changes when moving it horizontally (in the plane orthogonal to the optical axis).

4.4 Sample and loading in air

Trapping particle in air is not trivial because particles do not float like in water, but they are stuck on the chamber wall by the van der Waals force. To load the particle, three different methods can be employed based on lasers pulses, nebulisers, and piezoelectric transducer.

The first method is based on the high instantaneous power of nanoseconds pulsed lasers, which produces forces on the stuck particle greater than the van der Waals one. As a result, the particle is detached from the surface and can be trapped by optical tweezers. This method can not be implemented easily in a trapping system, in particular in an intracavity optical tweezer, because it requires an additional optical path for the pulsed laser that overcomplicates the experimental setup. In addition, it is an expensive method and, in general, much more complex than the others.

The second method allows to trap particles in air by nebulising a solution of a volatile fluid (such as propanol) and of the micrometric particles to trap near the optical trap. By chance, a droplet of the fluid in which there is a particle can be trapped by the optical tweezers and, after the fluid is completely evaporated, the particle only is trapped. This method presents some major issues: the particle diameter needs to be less than $2\,\mu\mathrm{m}$ otherwise the probability that a droplet contains a particle is very low; the nebulised solution settles on walls of the sample altering the trapping laser beam; the trapping rate is very low (1 trapped particle after hours of nebulisation); multiple particle can be trapped simultaneously.

The third method is based on the possibility to overcome the van der Waals force and launch a particle close to the focus of the trapping laser beam by vibrating the sample with a piezoelectric crystal. This method does not requires a complex modification of the trapping setups and is not characterised by the problems of nebulisation. For these reasons, the piezoelectric transducer loading method is used in this work. In this work, the loading of particle in air is achieved by powering with a high-frequency ($> 100\,\mathrm{kHz}$) and high-power ($> 500\,\mathrm{W}$) oscillating signal a piezoelectric crystal.

To explain the particle loading, it is useful to introduce the van der Waals force and the operating principles of piezoelectric crystals. Finally the homemade power supply designed and realised for this work is described.

4.4.1 Van der Waals force

The van der Waals force[51] is an electrical force that attracts neutral molecules towards each other and, therefore, it can be extended to the attraction between two different solids, such as a particle and a flat surface. When two neutral objects are close enough, an attractive interaction arises because of random fluctuations of electron density in the their electron clouds. Indeed, these fluctuation form non-zero temporary dipole moment into the two objects that are attracted together. This force is called the London-van der Waals force and sticks a micrometric particle in air with its supporting surface, such as a silica coverslip.

Without going into the details of the formulation of this force, the London-van der Waals force can be calculated for two spheres of radius R_1 and R_2 using the generalised Hamaker equation [52] for the energy U

$$U(d, R_1, R_2) = -\frac{A}{6}\left[\frac{2R_1R_2}{(2R_1+2R_2+d)d} + \frac{2R_1R_2}{(2R_1+d)(2R_2+d)} + \ln\frac{(2R_1+2R_2+d)d}{(2R_1+d)(2R_2+d)}\right] \quad (4.1)$$

that produces simply this force

$$F_{ad}(d, R_1, R_2) = -\left.\frac{dW}{dD}\right|_{D=d} = \frac{32}{3}A\frac{R_1^3R_2^3\,(d+R_1+R_2)}{d^2\,(d+2R_1)^{\,2}\,(d+2R_2)^{\,2}\,(d+2R_1+2R_2)^{\,2}} \quad (4.2)$$

where d is the distance between the two surfaces of the spheres and A is called Hamaker constant that depends on the materials of the surfaces and of the medium in which the spheres are located. To have the force between a plane surface and a sphere, consider that one of the two surfaces has infinite curvature ($R_1 \equiv a$ and $R_2 \to \infty$) so that:

$$F_{\mathrm{vdW}}(d, a) = \lim_{R_2\to\infty} F_{ad}(d, a, R_2) = \frac{2Aa^3}{3d^2(d+2a)^2} \quad (4.3)$$

where d is the distance between the surface of the particle and the supporting plane that for a micrometric particle placed on a coverslip is of the order of magnitude of some nanometres. nm.

To quantify the force $F_{ad}(d, R_1, R_2)$ in order to design a suitable loading system, the evaluation of Hamaker constant is significant. The best way to obtain the Hamaker constant, which depends on the material of the two surfaces (plane and sphere) and on the medium in which this two object are immersed (in this work air), is by experimental measurement, e.g. using an atomic force microscope [53]. However, it is not always possible to find measurements of this constant in the literature for every case study, but, without carrying out a complex measurement, it is possible to evaluate the Hamaker constant A using Lifshitz's theory [54]. If

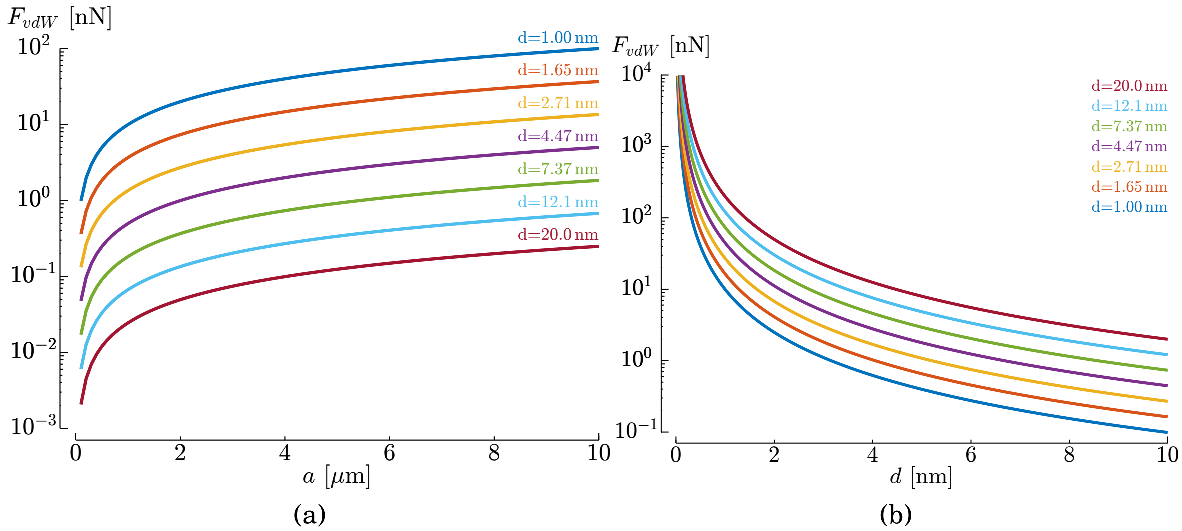

Figure 4.6: van der Waals force F_{vdW} of equation (4.3) as function of (a) the particle radius a, for different values of the distance d of the particle surface from the plane surface, and (b) of d, for different values of the particle radius a. For this evaluation, the Hamaker constant is $A = 5.98 \cdot 10^{-20}\,\mathrm{J}$.

two objects with dielectric permittivity ϵ_1 and ϵ_2 (i.e. with refractive indexes n_1 and n_2) are immersed in a medium with dielectric permittivity ϵ_3 (i.e. n_3), the Hamaker constant is

$$A \simeq \frac{3}{4} k_B T \frac{\epsilon_1 - \epsilon_3}{\epsilon_1 + \epsilon_3} \frac{\epsilon_2 - \epsilon_3}{\epsilon_2 + \epsilon_3} + \frac{3h}{4\pi} \int_{\nu_1}^{+\infty} \frac{\epsilon_1(i\nu) - \epsilon_3(i\nu)}{\epsilon_1(i\nu) + \epsilon_3(i\nu)} \frac{\epsilon_2(i\nu) - \epsilon_3(i\nu)}{\epsilon_2(i\nu) + \epsilon_3(i\nu)} d\nu \tag{4.4}$$

that can be rewritten in a simpler form [55, 56, 57]

$$A = \frac{3h}{8\sqrt{2}} \frac{(n_1^2 - n_3^2)\,(n_2^2 - n_3^2)\,\nu_e}{\sqrt{n_1^2 + n_3^2}\sqrt{n_2^2 + n_3^2}\left(\sqrt{n_1^2 + n_3^2} + \sqrt{n_2^2 + n_3^2}\right)} + \frac{3kT}{4} \frac{(\epsilon_1 - \epsilon_3)\,(\epsilon_2 - \epsilon_3)}{(\epsilon_1 + \epsilon_3)\,(\epsilon_2 + \epsilon_3)} \tag{4.5}$$

where h is the Plank constant, k is Boltzmann constant, and ν_e is the main electronic absorption frequency of the medium. For example, considering a $\mathrm{SiO_2}$ micrometric spherical particle and a $\mathrm{SiO_2}$ coverslip immersed in air, equation (4.5) gives

$$A = 5.98 \cdot 10^{-20}\,\mathrm{J} \tag{4.6}$$

because $v_e = 3.2\,\mathrm{PHz}$, $\epsilon_1 = 3.80$, $n_1 = 1.42$, $\epsilon_2 = 3.80$, and $n_2 = 1.45$. Instead, if the particle is made of polystyrene, equation (4.5) gives

$$A = 8.90 \cdot 10^{-20}\,\mathrm{J} \tag{4.7}$$

because $\epsilon_1 = 2.55$ and $n_1 = 1.68$.

Now, the force of equation (4.3) can be evaluated as function of the particle radius a for the case of interest: $\mathrm{SiO_2}$ or polystyrene micrometric spherical particle interacting with a $\mathrm{SiO_2}$ coverslip flat surface. In figure 4.6a, F_{vdW} is evaluated as a function of the particle radius a for different values of the distance of the particle surface from the plane surface d. This force increases increasing the particle radius, but decreases as the distance d increases, as shown in figure 4.6b. In addition, the order of magnitude of F_{vdW} varies between $10^{-3}\,\mathrm{nN}$ and $10^{4}\,\mathrm{nN}$ and, for the specific case of this work (d about $1\,\mathrm{nm}$ and a between $1\,\mu\mathrm{m}$ and $5\,\mu\mathrm{m}$), $10\,\mathrm{nN}$ and $100\,\mathrm{nN}$. The magnitude of this force is 3 orders of magnitude greater than the other forces involved in optical trapping: the trapping force is of the order of magnitude of $10\mathrm{pN}$, while the gravitational force of $1\mathrm{pN}$. Therefore, it is impossible to detach micrometric particle from a plane surface in air with an optical tweezers or the gravitational force, but this is possible by using piezoelectric crystals to vibrate the surface of the plane enough to produce a force comparable to F_{vdW}.

4.4.2 Piezoelectric crystals

Piezoelectric crystals consist of dielectric materials that can be polarised not only by an electric field, but also by a mechanical force. The piezoelectric effect [58, 59] is characterised by an interconnection between electrical and elastic phenomena: some materials deform when an electric potential difference is applied to them and, conversely, they exhibit macroscopic polarisation, i.e. the production of surface electrical charges, when a mechanical force acts on them.

This phenomena can be understood with a simple molecular model [60]. When a piezoelectric crystal is not exposed to an external force, the centres of the negative and positive charges of its molecules coincide so that the material is electrically neutral, figure 4.7a. Instead, in presence of an external mechanical force, the positive and negative centres of the molecule are separated, figure 4.7b, generating electric dipoles. Macroscopically, the crystal bulk is still neutral, while the external surfaces of the crystal are electrically charged: all the dipoles induced by the mechanical force are arranged in a lattice so that they annihilate each other except on the surface of the crystal, like figure 4.7c schematically shows. Conversely, when an external field is applied to the piezoelectric crystal, the molecules forms electric dipoles that change their shape inducing a deformation of the crystal.

Without going into the mathematical details of the piezoelectricity modelling, the application of an electric field $\vec{E}$ to a piezoelectric crystal makes it expand or contract along the axes x, y and z depending on the material properties [61]. For simplicity, assuming a linear deformation of the piezoelectric crystal, the second-rank strain tensor S_{ij} is related to the applied electric field through the relation [60, 61]

$$S_{ij} = \boldsymbol{d}_{kij} E_k \tag{4.8}$$

where $\boldsymbol{d}_{kij}$ is the third-rank piezoelectric tensor and E_k is the k-th component of the electric field vector $\vec{E}$.

In this work, to load the particle into the optical trap, a ring piezoelectric crystal is placed with its axis coincident to the optical axis z and a coverslip with particles

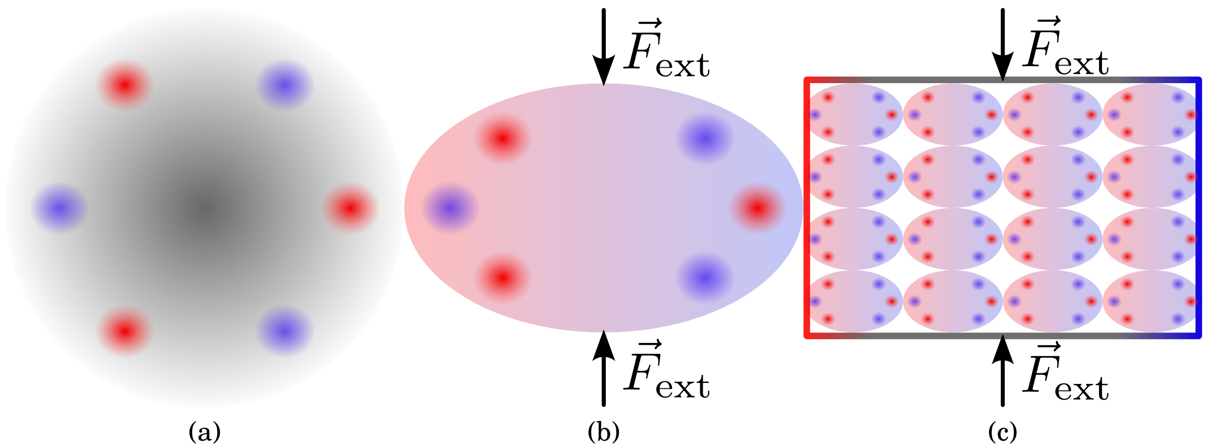

Figure 4.7: (a) sketch of a piezoelectric crystal molecule not exposed to an external force, where the grey shadow in the background indicates that the overall charge of the molecule is zero, the red circle indicates a positive charge, and the blue circle a negative charge; (b) sketch of a piezoelectric crystal molecule deformed by an external force and, therefore, characterised by a separation of the charge centres, where the shadow in the background fading from red to blue indicates the charge distribution along the molecule; (c) piezoelectric crystal sketch under external forces, where the solid line represents the outline of the crystal boundaries and it changes colour according to the net charge.

is fixed on it orthogonally to z. In this way, the elongations and the contractions of the ring height (along z) allows to detach the particle and lunch them into the trap. Therefore, the applied electric field $\vec{E}$ is directed only along z and, for simplicity, it is considered to be:

$$E = V \cdot l \tag{4.9}$$

with V the voltage applied to the piezoelectric ring crystal and l the height of the ring. Under these conditions, the displacement along z is

$$\Delta z = l \cdot S_{33} = \boldsymbol{d}_{33} V \tag{4.10}$$

Therefore, if the voltage $V \equiv V(t)$ oscillates periodically with frequency f, the particle on the coverslip are subjected to the mechanical force

$$F_m = m\frac{d^2 z}{dt^2} = \left(\frac{4}{3}\pi a^3 \rho\right) \Delta z\, \omega^2 \tag{4.11}$$

where m is the mass of the particle, a its radius, ρ its density, Δz and $\omega = 2\pi f$ the vibration amplitude and the angular frequency respectively. This force must be greater than the London-van der Waals force of equation (4.3) in order to detach the particle and load it in the trap, i.e.

$$F_m = \left(\frac{4}{3}\pi a^3 \rho\right) \Delta z\, \omega^2 > F_{\text{vdW}}(a) = \frac{2Aa^3}{3d^2(d+2a)^2} \tag{4.12}$$

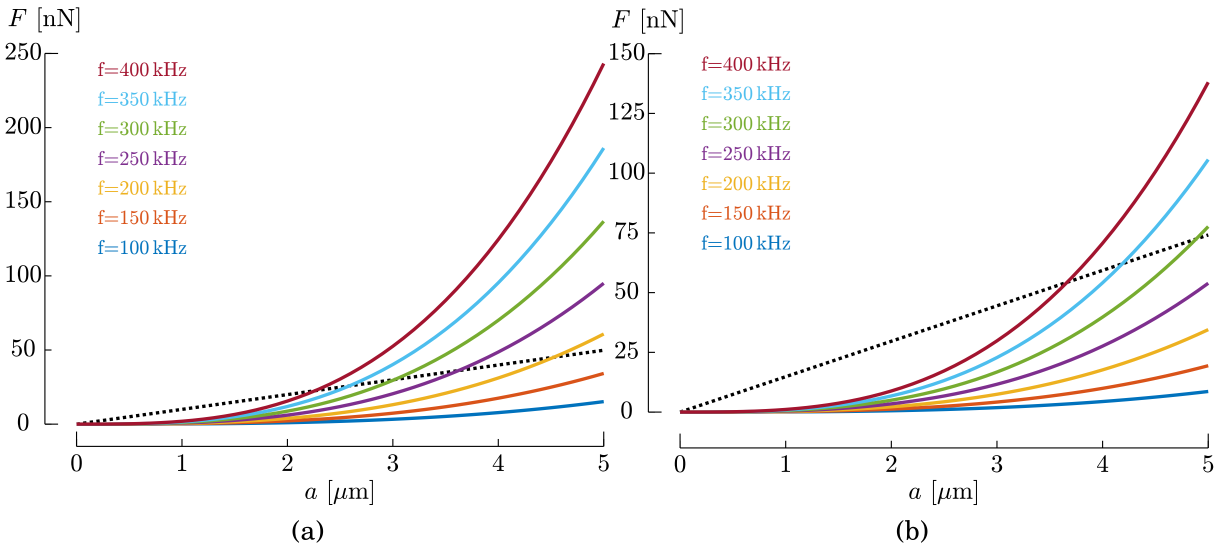

Figure 4.8: comparison of the mechanical force F_m (solid line) and the van der Waals force F_{vdW} (black dotted line) as function of the particle radius a and for different frequency f for (a) a $\mathrm{SiO_2}$ particle and (b) a polystyrene particle on a $\mathrm{SiO_2}$ surface.

and this condition shows that the two most effective parameters to detach the particle are its radius a, because $F_m \propto a^3$, and the oscillation frequency f, because $F_m \propto f^2$. Also the particle material is very important, as shown in figures 4.8a and 4.8b. Indeed, the Hamaker constant A and the particle density ρ can change drastically the detaching condition of equation (4.12). For example, a polystyrene particle has an higher Hamaker constant (higher F_{vdW}) and a lower density ρ (lower F_m) than a $\mathrm{SiO_2}$ particle and it is much more difficult to detach.

Experimentally, it is necessary to find the right compromise between these two parameters. The radius of the particle, for the purposes of this work, can be between $0.5\,\mu$m and $3.0\,\mu$m and, therefore, is not a limiting parameter. Instead, the frequency f needs to be of the order of 10^5 Hz and it is a stricter parameter. Indeed, the piezoelectric ring crystal needs to be chosen in such a way that its resonant frequency f_h is of the order of 10^5 Hz, its capacitance small enough to not integrate the oscillating signal ($C < 20\,\mathrm{nF}$), and its mechanical quality factor[9] high enough to produce a force sufficient to detach the particle ($Q > 1000$). While Q is determined by the material constituting the piezoelectric crystal, the resonant frequency f_h and the capacitance C depend on the geometrical properties of the piezoelectric ring crystal, being

$$\begin{cases} f_h = \frac{N_t}{h} \\ C = \epsilon_{33}\epsilon_0\pi\frac{d_o^2 - d_i^2}{h} \end{cases} \tag{4.13}$$

where ϵ_0 is the vacuum permittivity, ϵ_{33} is the relative permittivity in the polarisa-

[9]The mechanical quality factor Q is the amplification factor for strain and vibration in resonance conditions. Instead, its inverse quantifies the energy lost per cycle.

tion direction z of the piezoelectric ring crystal, N_t is the frequency coefficient, d_i, d_o and h the inner diameter, the outer diameter and the height of the ring, respectively.

To satisfy all these conditions, the chosen piezoelectric ring crystal (*Physik Instrumente* made of *PIC181*) has

$$\begin{cases} Q = 2000 \\ f_h = 351.7\,\mathrm{kHz} \\ C = 10.7\,\mathrm{nF} \end{cases} \tag{4.14}$$

being $h = 6\,\mathrm{mm}$, $d_i = 20\,\mathrm{mm}$, $d_o = 50\,\mathrm{mm}$, $N_t = 2110\,\mathrm{Hz}\cdot\mathrm{m}$, and $\epsilon_{33} = 1100$. To properly supply this piezoelectric ring crystal in order to detach the particle, the power supply must produce an electric signal oscillating at least at $350\,\mathrm{kHz}$ with a current of $4\,\mathrm{A}$ and a voltage of $150\,\mathrm{V}$, i.e. with a power of at least $600\,\mathrm{W}$.

4.4.3 Loading system

To supply the piezoelectric ring crystal, a homemade system is designed, simulated, and realised specifically for this work. This system is a low budget device to produce electric signals up to $150\,\mathrm{V}$ and $5\,\mathrm{A}$ at oscillating frequencies up to $500\,\mathrm{kHz}$. The system is designed in three blocks: a high-power voltage supply, a high-power periodic signal generator, and a piezoelectric transducer. Since this system has 3 “heads” and it is potentially dangerous (high power signals), it has been nicknamed *Cerbero* (schematics in figure 4.9a) even though, in reality, it is equipped with safety systems that minimise the danger of injury.

The high-power voltage supply, i.e. the first block, is designed to use two toroidal transformers, $\mathrm{TR1}$ and $\mathrm{TR2}$, with a nominal power of $800\,\mathrm{VA}$ (*RS PRO 2x115V ac, 2x55V ac Toroidal Transformer, 800VA 2 Output, 123-4050*). To have high current, the two output of a transformer are wired together in series so that each transformer generates a voltage of $110\,V$ and $50\,\mathrm{Hz}$. To have a current sufficient to supply the piezoelectric ring crystal, the two transformer are wired in parallel so as to supply twice as much current as the single transformer. The output of the two transformers is rectified by the Graetz bridge $\mathrm{B1}$ (*Fagor FB 5004*) and made DC by a $1000\,\mu\mathrm{F}$ capacitor $\mathrm{C1}$ (*BHC Aerovox 1000* μF, 415 VDC). In this way, the output voltage of the high-power voltage supply is about $150\,\mathrm{V}$. The schematics of this block is shown in figure 4.9a outlined by the blue dashed line and its realisation in figure 4.9b. For safety reasons, the system is designed to be completely unplugged from the $220\,\mathrm{VAC}$ main electricity when the key-switch $\mathrm{S1}$ and the rocker toggle switch $\mathrm{S2}$ are set to OFF: the relay $\mathrm{K1}$ disconnects completely the toroidal transformers, therefore the whole system, from both phase and neutral thanks to its poles $\mathrm{P2}$ and $\mathrm{P3}$. Switching $\mathrm{S1}$, a transformer $220\,\mathrm{VAC}$-$12\,\mathrm{VAC}$ is connected to the main electricity powering on only a voltmeter-amperemeter. Indeed, for additional safety, the two toroidal transformers are connected to the main power supply only if first $\mathrm{S1}$ and then $\mathrm{S2}$ are set to ON (*starting sequence*). After the starting sequence, the capacitor starts to charge absorbing a limited amount of current (about $0.15\,\mathrm{A}$) thanks to $\mathrm{R1}$.

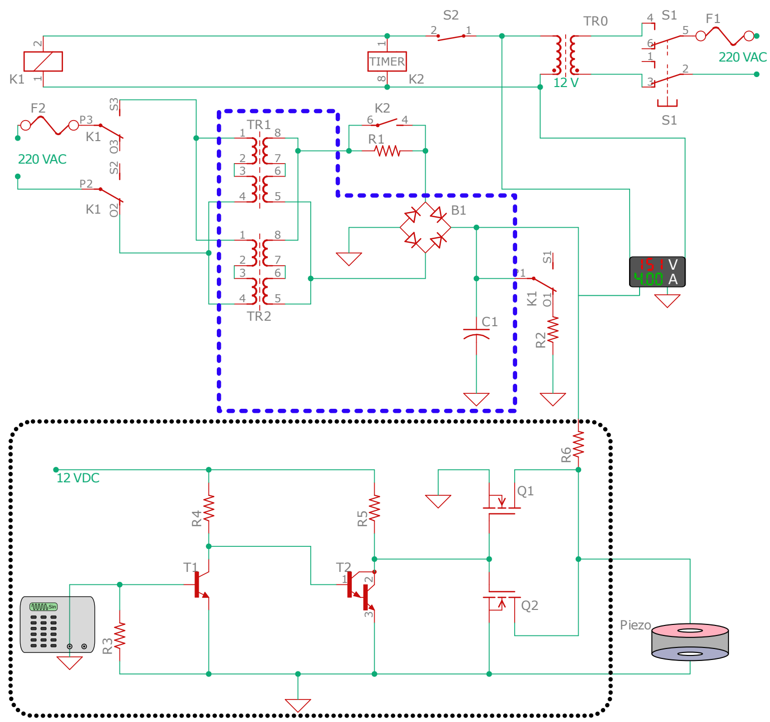

(a)

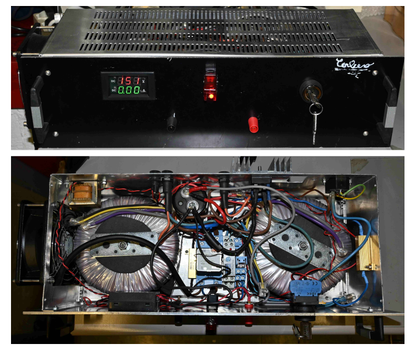

(b)

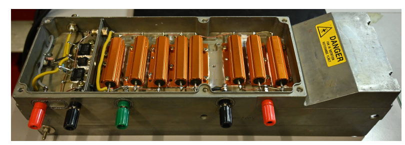

(c)

Figure 4.9: (a) schematics of *Cerbero* where F1 is a 0.5 A fuse, F2 is a 5 A fuse, S1 and S2 are switches, K1 is a relay with three poles (P1 P2, and P3), K2 is a temporised relay with one pole, R1 and R2 are $1\,\mathrm{k\Omega}$-$50\,\mathrm{W}$ resistors, B1 is the Graetz bridge, C1 the $1000\,\mu$F-$400\,$V capacitor, R3 is a $3.3\,\mathrm{k\Omega}$ resistor, R4 is a $1.5\,\mathrm{k\Omega}$ resistor, R5 is a $150\,\Omega$-$50\,$W, R6 is a series of 8 resistors of $4\,\Omega$-$100\,$W, T1 is a NPN transistor, T2 a NPN Darlington transistor, Q1 and Q2 power MOSFETs; (b) realisation of the high-power voltage supply (the schematic of this part is outlined by a blue dashed line); (c) realisation of the high-power periodic signal generator (the schematic of this part is outlined by a black dotted line).

Indeed, without R1, the capacitor charges itself absorbing a huge amount of current damaging the transformers. This problem only occurs in the initial transient as the high-capacity capacitor C1 is completely discharged, i.e. $5\,\mathrm{R1}\cdot\mathrm{C1} \simeq 5\,\mathrm{s}$ after the start sequence. Thus, after this initial transient, R1 is short circuited to have the full power of the system for supplying the piezoelectric transducer, thanks to the temporised relay K2. Furthermore, it is important to emphasise that the capacitor C1 stores a sufficiently large amount of energy to be dangerous and, for safety reasons, it is mandatory to discharge the capacitor whenever the device is switched OFF: the relay K1, in addition to disconnect completely the toroidal transformers from the main electricity, grounds the capacitor C1 (pole P1) through the resistor R2 ensuring the complete discharge about 5 seconds ($\mathrm{R2}\cdot\mathrm{C1} \sim 1\,\mathrm{s}$) after switching off.

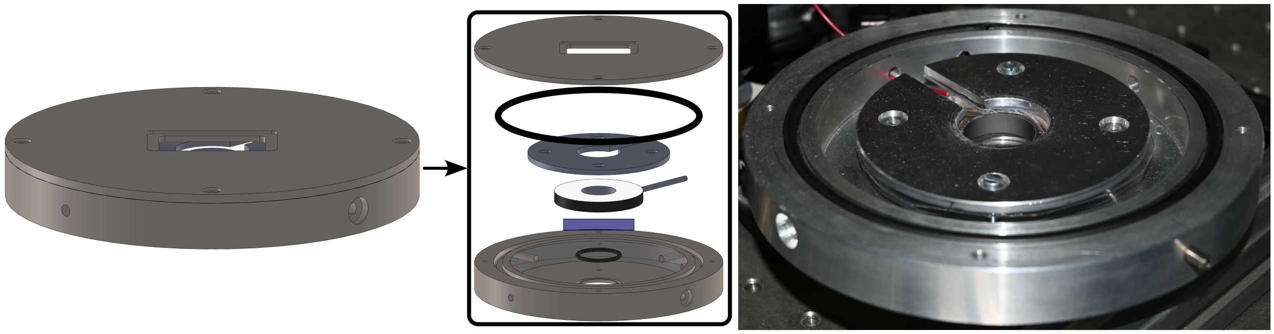

(a) (b)

Figure 4.10: piezoelectric transducer (a) design and (b) realisation.

The high-power periodic signal generator, i.e. the second block, has one input and one output. It supplies the first block with $150\,\mathrm{VDC}$, through the resistor $\mathrm{R6}$: the input is connected to a $10\,\mathrm{MHz}$ low-power commercial function generator (*Wavetek model 29*) that produces a low-voltage signal at frequency f; the output is connected to the piezoelectric transducer. The input enters in a two stage amplifier made with a NPN transistor $\mathrm{T1}$ (*STMicroelectronics BD139*) and a NPN Darlington transistor $\mathrm{T2}$ (*STMicroelectronics TIP 121*), which amplifies the signal in current[10] in order to drive two power MOSFETs (*STMicroelectronics IRFP450*), $\mathrm{Q1}$ and $\mathrm{Q2}$, in phase with the input. These MOSFETs, connected in parallel to handle the high power, open and close the circuit between the resistor $\mathrm{R6}$ and the ground with opposite phase with respect to the input. In this way they supplies the piezoelectric transducer with a square-wave of frequency f, voltage that oscillates from $0\,\mathrm{V}$ to about $150\,\mathrm{V}$ (the maximum voltage produced by the high-power voltage supply), and opposite phase to the input. Therefore, no electrical power is absorbed by the second block when no input signal is provided. The schematics of the high-power periodic signal generator is shown in figure 4.9a outlined by the black dotted line. Its realisation is shown in figure 4.9c.

The third block is the piezoelectric transducer, formed by a piezoelectric ring crystal and a homemade chamber. The piezoelectric ring crystal is connected to the output of the high-voltage periodic signal generator and, thanks to the piezoelectric effect (chapter 4.4.2), converts the electrical signal energy in mechanical energy by vibrating. To produce a piezoelectric transducer able to detach particles from their supporting surface and load them into the optical trap, a homemade chamber is needed to physically couple the piezoelectric ring crystal with the sample, see figures 4.10a and 4.10b. This chamber is a hollow disc with a through-hole in the centre allowing the optical trapping beam to illuminate the sample. The piezoelectric crystal is placed in the chamber on a solid rubber O-ring which electrically isolates the positive terminal of the high-power periodic signal generator from the chamber floor avoiding short circuit fault. On the other side of the piezoelectric

[10]The Darlington transistor allows to amplify the signal in current.

crystal, a coverslip is pressed onto it with a plate screwed into the chamber floor. The chamber is closed by a lid also perforated in the centre to allow the LED visible light to illuminate the sample.

The sample is made in a simple way: the coverslip is cleaned with a plasma cleaner and grains of dry particles are placed on it, avoiding large clusters (linear dimensions greater than $1\mathrm{mm}$). With this system, $\mathrm{SiO_2}$ particles with a diameter greater than $2\,\mu m$ are successfully loaded into the optical trap.

Chapter 5

Data analysis

This chapter is about the data analysis algorithms used to extract the trajectory of the studied particle from the videos acquired with the experimental setups described in the chapter 4, and to evaluate the physical quantities of interest. The first section deals with the particle tracking algorithms used to extract the $2\mathrm{D}$ or the $3\mathrm{D}$ trajectory from the videos in physical units. The $3\mathrm{D}$ tracking algorithm is based on holographic techniques that are computationally time-consuming. To reduce the computational time, the *convolutional neural network* described in the last part of the first section is developed specifically for this purpose. The second section describes the trajectory analysis used to evaluate the physical parameters of interest such as the trap stiffness, the fluid viscosity, the particle mass. These parameters are extracted measuring the quantities theoretically described in chapter 2 for different experimental conditions, i.e. the power spectral density (PSD), the mean squared displacement (MSD), the autocorrelation function (ACF), the potential, and the variance of the particle trajectory.

5.1 Particle tracking

In this work, the particle tracking is done in bright-field by recording a video of the trapped particle with a CCD camera. The position of the particle is determined analysing the video frame-by-frame with detection algorithms, which extract the particle position in terms of pixels, and the particle trajectory reconstructed using a linking algorithm. Consequently, the trajectory is measured in pixels and, performing a CCD calibration procedure that quantifies the pixel/length conversion factor β_{CCD}, converted in physical units.

5.1.1 Calibration

The CCD camera calibration is achieved by imaging a calibration ruler (*Pyser Optics PS12*) having a length of $100\,\mu\mathrm{m}$ and reflective tick marks $2\,\mu m$ spaced from each other. The tick marks have a line width of $1\,\mu m$ and are reflective so that they

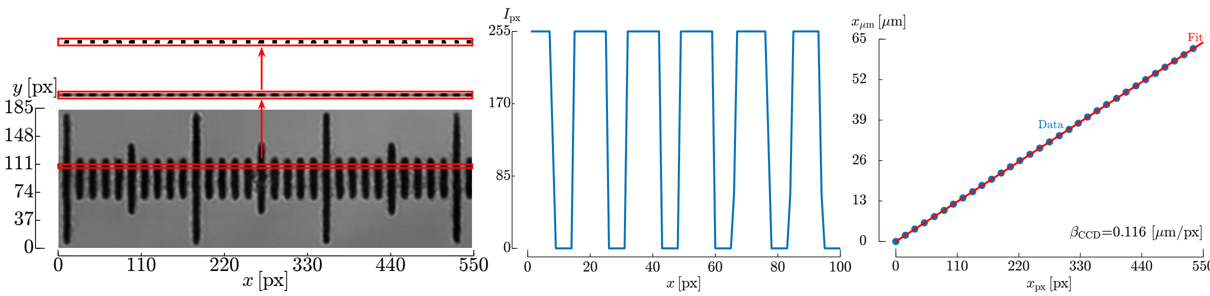

(a) (b) (c)

Figure 5.1: (a) acquired frame of the ruler with the SBOT setup where the cropping region is delimited by the red rectangle. The first inset (middle of the image, delimited by a red rectangle) contains the cropped frame and the second (the top one) the black and white version of the cropped frame; (b) pixel intensity of the black and white cropped frame $I_{\mathrm{px}}(\bar{n}, m)$ as function of the position x for the first $100\,\mathrm{px}$; (c) physical distance between the tick marks $x_{\mu\mathrm{m}}$ as function of the centre of tick marks measured in pixel x_{px} (blue circles) and its best fit line (red solid line) where $\beta_{\mathrm{CCD}} = 0.116\,\mu\mathrm{m/px}$.

appear black in bright-field acquisition (see figure 5.1a). The acquired frame is an 8-bit greyscale image $I_{\mathrm{px}}(n, m)$, i.e. a matrix of dimensionless integers between 0 (black) and 255 (white), where n and m are the pixel row and column indexes respectively. Therefore, the tick marks are represented by regions of the frame with $I_{\mathrm{px}} < I_{\mathrm{th}}$, where I_{th} is a threshold value. This threshold value, in proper illumination conditions, is the mean value of the black regions and it is used for locating the centre of each tick marks.

The calibration procedure is as follow: first, in order to enhance the accuracy of the calibration, the frame is cropped to a 1 row image containing only the most regular part of the tick marks, as shown in the inset (1) of figure 5.1a. Then the frame is converted into a black and white image according to this transformation

$$\tilde{I}_{\mathrm{px}} = \begin{cases} 0 & I_{\mathrm{px}} \leq I_{\mathrm{th}} \\ 255 & I_{\mathrm{px}} > I_{\mathrm{th}} \end{cases} \tag{5.1}$$

the result of which is shown in the second inset (2) of figure 5.1a.

The pixel intensity of this image $\tilde{I}_{\mathrm{px}}(\bar{n}, m)$ as function of the position x (see figure 5.1b) allows to extrapolate the centre of each tick marks x_{px} as the mean value of each region with $\tilde{I}_{\mathrm{px}} = 0$. All the values x_{px} are collected into a vector $\vec{x}_{\mathrm{px}}$, with dimension N equal to the number of tick marks in the frame, and then shifted to have $\vec{x}_{\mathrm{px}}(0) = 0$. Since the distance between the tick marks is $l = 2\,\mu\mathrm{m}$, the vector $\vec{x}_{\mu\mathrm{m}} = (0, l, ..., N \cdot l)$ is proportional to $\vec{x}_{\mathrm{px}}$. The conversion factor β_{CCD} is estimated as the slope of the best fit line of $x_{\mu\mathrm{m}}$ as function of x_{px}, see figure 5.1c.

In general, β_{CCD} depends on the pixel size of the CCD sensor, the tube lens used to focus the sample image on the sensor, and the objective lenses used to

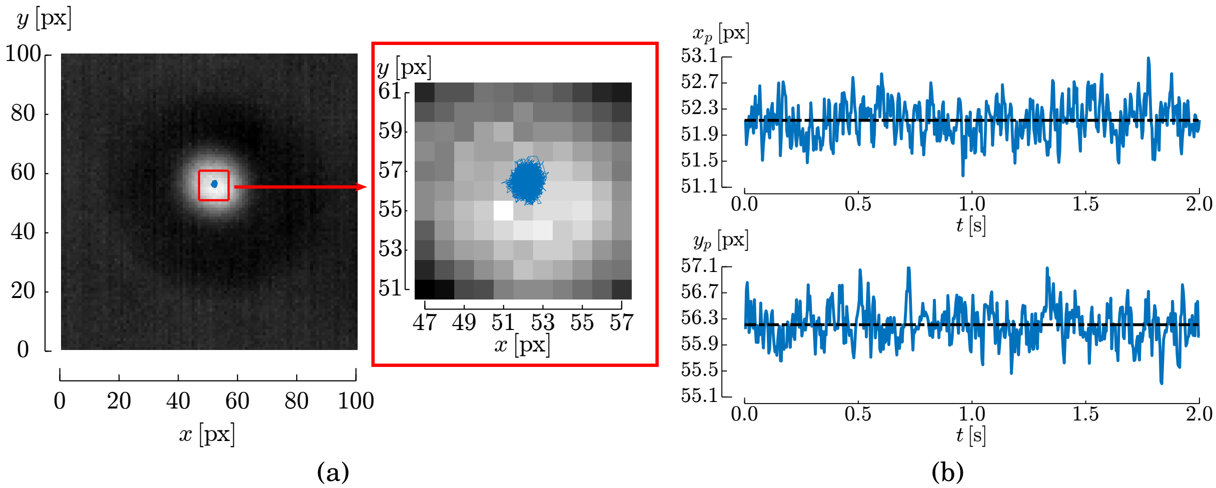

Figure 5.2: (a) frame of an acquired video of a trapped particle with a sampling rate of $1500\,\mathrm{Hz}$, where the blue solid line represents the particle trajectory and in the inset there is a magnification of the region delimited by the red square; (b) centre position of the particle x_p and y_p as function of the time t.

observe the sample. Therefore, the conversion factors of the different setups used in this work are: $\beta_{\mathrm{CCD}} = 0.116\,\mu\mathrm{m/px}$ for the single-beam optical tweezers (SBOT), $\beta_{\mathrm{CCD}} = 0.073\,\mu\mathrm{m/px}$ for the single-beam intracavity optical tweezers (SIOT) used for trapping in water, and $\beta_{\mathrm{CCD}} = 0.508\,\mu\mathrm{m/px}$ for the double-beam intracavity optical tweezers (BIOT) used for trapping in water and the SIOT used for trapped in air.

5.1.2 2D tracking

The digital video microscopy tracks particles taking advantage of the particle intensity profile that is Gaussian when the sample is illuminated with a proper light intensity and contrast. Indeed, the particle appears as a circle brighter than the background encircled by a dark ring 5.2a and its video is a set of frames acquired at constant sampling rate f_{fps} (i.e at sampling interval $\Delta t = 1/f_{\mathrm{fps}}$). In this work, the *feature point detection* technique [62] is used and implemented in MATLAB to measure the particle centre position frame-by-frame and to link these position forming particle trajectory, as shown in figure 5.2b. Then, the trajectory is converted into actual physical units of length thanks to the calibration procedure explained before.

5.1.3 3D holographic tracking

The *holographic video microscopy* technique tracks a particle 3-dimensionally through a 2-dimensional image taking advantage of the interference between the portion of the illumination beam scattered by the particle and the unscattered portion of the same beam. Since, this interference happens only if the illumination light has a proper coherence degree, a monochromatic LED is used in this work as

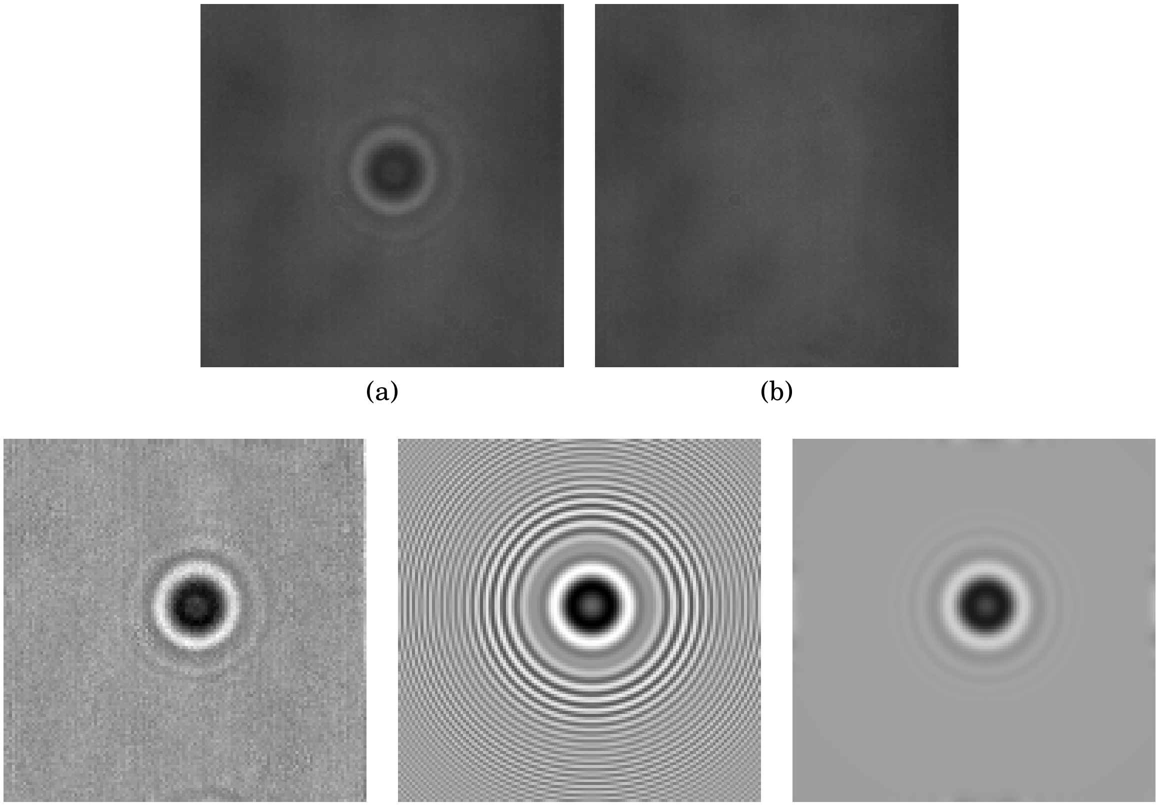

(a) (b) (c) (d) (e)

Figure 5.3: (a) holographic image of a polystyrene particle of diameter $2.82\,\mu\mathrm{m}$; (b) background image; (c) normalised holographic image obtained dividing the first image with the background image; (d) best fist holographic prediction; (e) best fit holographic prediction implementing a Gaussian filter in the fitting procedure.

light source of the imaging system. In this way, the interference pattern of figure 5.3a is obtained. A LED is used instead of a more coherent laser source to avoid unwanted effects such as high noise in the image due to other particles or dust. Following the method developed by [63, 64], the optical intensity $I(\vec{r})$ of a single particle on the CCD camera is given by

$$I(\vec{r}) \simeq u_0^2(\vec{r}) + 2\Re\left[u_0(\vec{r})E_s(\vec{r},0)\right] + \left|E_s(r,\vec{0})\right|^2 \tag{5.2}$$

with

$$E_s(\vec{r},0) = u_0(\vec{r}_p)f_s(k\vec{r} - k\vec{r}_p) \tag{5.3}$$

where $u_0(\vec{r})$ is the amplitude of the illumination plane-wave and $f_s(k\vec{r})$ defined by Mie's theory (see equations (A.11), (A.12) and (A.13)).

Equation (5.2) is valid if the height of the particle above the focal plane is greater then its size. This condition is experimentally achieved defocusing on purpose the image of the particle moving slightly the tube lens of the CCD. Often, the major

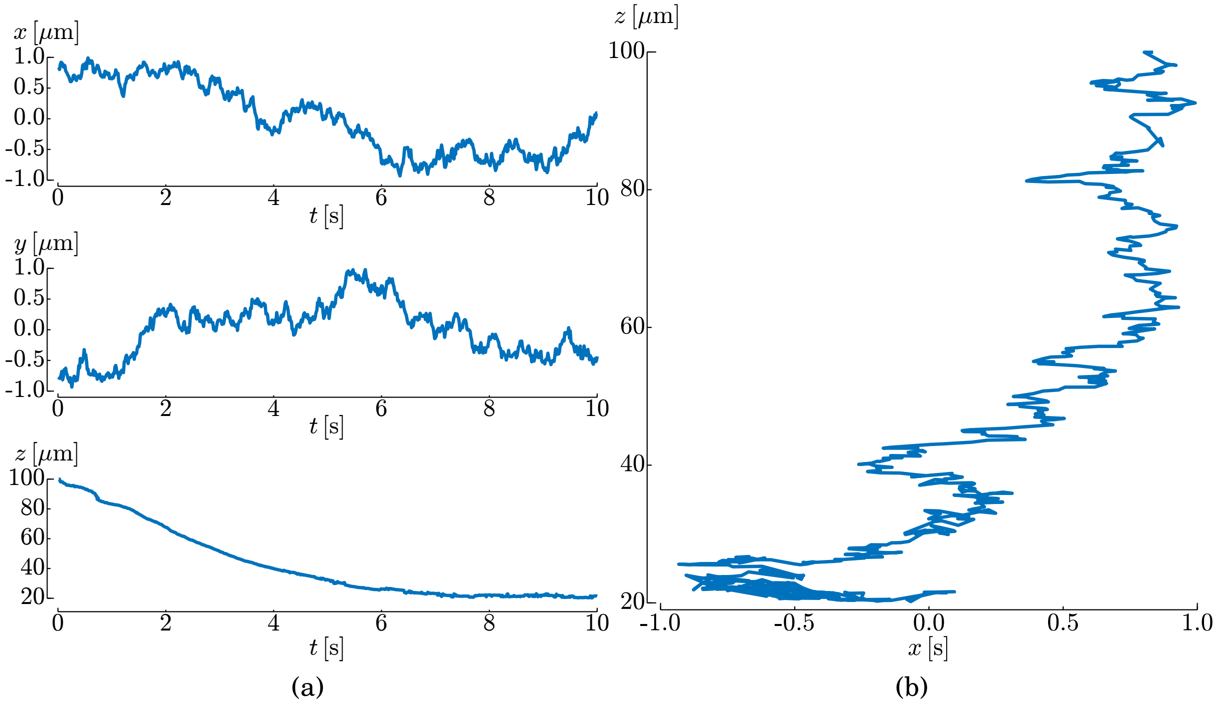

Figure 5.4: (a) x, y, and z position of the centre of a particle in water which is pushed by a laser beam as function of the time t; (b) z position as function of x position for the same particle. The trajectory is obtained with the holographic $3D$ tracking.

source of noise in this technique is due to a background interference pattern due to a non ideal illumination source, small imperfection of the imaging system, or dust on the sample. To avoid this problem, a background image is acquired without any particle in the field of view, as shown in figure 5.3b, and it is used to normalise the acquired images of the tracked particle, as shown in figure 5.3c.

Evaluating numerically equation (5.2), it is possible to generate the prediction images as function of $\vec{r}$. In this way, the acquired images can be fit using a best fit algorithm, like the Levenberg-Marquardt, thus obtaining the particle position $\vec{r}_p$. In this work, the prediction images are generated using DeepTrack [65] or HoloPy [66]. A prediction image, relative to the normalised acquired frame of 5.3c, is shown in 5.3d. The predicted image has a very detailed intensity pattern compared to the normalised image and, in order to help the fitting procedure, a Gaussian filter is implemented in the fitting algorithm. The Gaussian filter parameters are also used as fitting parameters and improving greatly the best fit image, see figure 5.3e.

Applying this procedure frame-by-frame, the 3D positions of the particle can be extrapolated and the trajectory is then obtained with the linking criterion described previously, see figure 5.4a. This fitting procedure is time-consuming due to the complexity of the function $f_s(k\vec{r} - k\vec{r}_p)$. To evaluate 10000 frames of $35\,\text{px} \times 35\,\text{px}$, the fitting procedure requires about 10 hours. The particle positions are then linked together forming the particle trajectory, figures 5.4b and 5.4a.

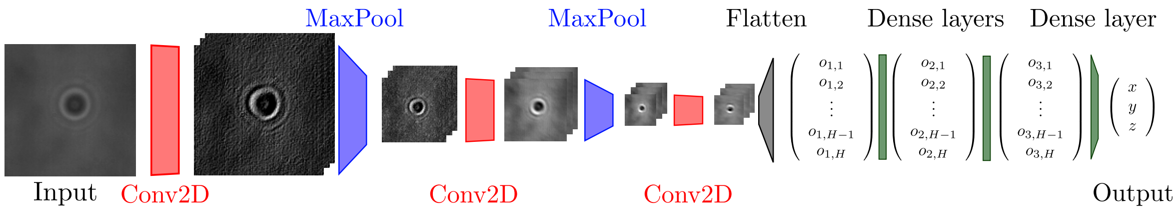

Figure 5.5: convolutional neural network realised for 3-D holographic tracking. It consists of a first 2D convolutional layer (red shape) that applies 32 filters 3×3, max pooling layers with pool size 2×2 (blue shapes), other 2 convolution layers applying 64 filters 3×3, a flatten layer (grey shape), two dense layers with 64 neurons, and the output dense layer.

5.1.4 Convolutional neural network for 3D tracking

To speed up the 3D tracking of a particle, the convolutional neural network (CNN) [67] of figure 5.5 is realised, that performs a regression having as input an $N \times M$ matrix representing an acquired holographic image of the particle and as output the array (x, y, z) of the 3D coordinates of its centre.

This result is achieved using 2D convolutional layers and maximum pooling layers. The 2D convolutional layer multiplies a $n \times m$ matrix of *weights*, called *filter*, to the input producing a new matrix of dimension $(N - n + 1) \times (M - m + 1)$, called *feature map*. The goal of the filter is to extract features from the input such as edges, shapes, high-intensity regions. To recognize different features, this layer applies many different filters producing a stack of feature maps. Then, the *activation function* is applied to the feature maps, i.e. the non-linear function $\mathrm{ReLu}(x) = \max(0, x)$. Instead, the maximum pooling layer extracts the maximum values of $n_p \times m_p$ sub-matrices of its input. The input is the stack of $n_c \times m_c$ feature maps and its output are matrices with dimension $n_o = n_c/n_p$ and $m_o = m_c/m_p$. This improves the analysis eliminating parts of the input that are not significative and reducing the data size while keeping the features. In this CNN, there are 3 convolutional layers followed by 2 pooling layers.

To extract the vector position from the last feature maps, a flatten layer reshapes its input in a 1-dimensional vector that is given in input to the two dense layers that follow. The *neurons* of the dense layers perform the scalar product between the input and a vector of *weights* and, then, applies the $\mathrm{ReLu}(x)$ *activation function*.

Finally, the output layer is a dense layer with a number of neurons equal to the dimension of the CNN output and a linear activation function. Its output (*prediction*) is the particle position.

This CNN is trained through *supervised learning*, that finds the set of weights solving the given problem. Because the training is supervised, the training dataset is manually labelled. Specifically, the training dataset is a set of 10000 selected frames from acquisitions characterised by different experimental conditions whose particle position (labels) is determined with HoloPy. Instead, the test dataset consists of 20000 frames from other experimental acquisitions than the training dataset

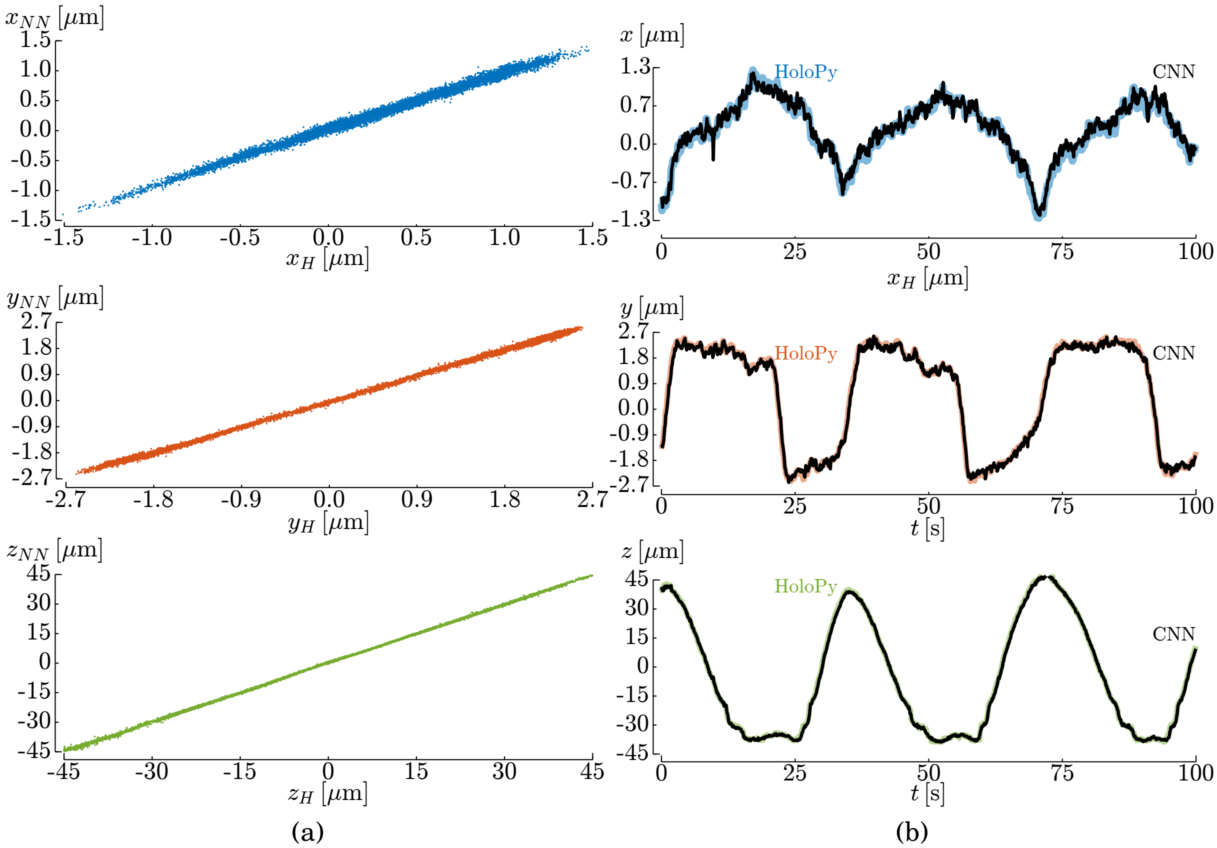

Figure 5.6: (a) neural network output (x_{NN}, y_{NN}, z_{NN}) as functions of the training dataset labels (x_H, y_H, z_H); (b) comparison between particle position (x, y, z) as function of time t measured with HoloPy (coloured semitransparent solid lines) and with the convolutional neural network after training (black solid lines), i.e. the application of the CNN on a subset of the test dataset.

and their corresponding particle positions $(x_\text{H}, y_\text{H}, z_\text{H})$. Training on this dataset requires about 3 hours, while the evaluation few seconds. To check the goodness of the prediction, the trained CCN is applied to the test dataset and its predictions $(x_\text{NN}, y_\text{NN}, z_\text{NN})$ studied as function of the labels $(x_\text{H}, y_\text{H}, z_\text{H})$, figure 5.6a. Good predictions depend linearly on the labels as a straight line passing through the origin with slope 1.

In this way, it is possible to measure the centre position of a particle frame-by-frame for an experimental acquisition in few seconds instead of dozens of hours with a good accuracy. Then, applying the linking algorithm, it is possible to obtain the trajectory, figure 5.6b.

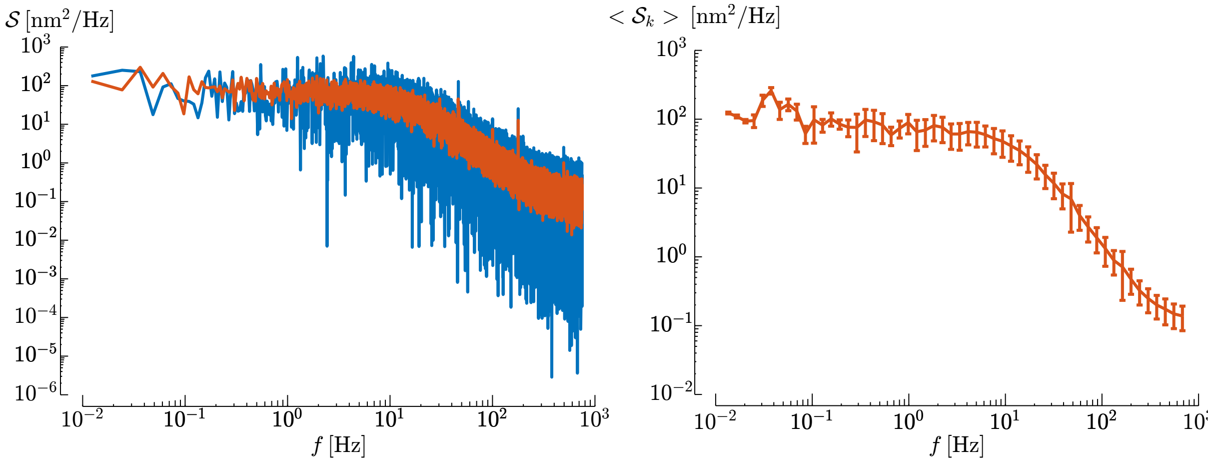

(a) (b)

Figure 5.7: (a) experimental power spectral density $\mathcal{S}$ (blue solid line) and the average $\mathcal{S}$ evaluated by repeating the same experiment (orange solid line) as function of the frequency f for a particle trapped in water by a SBOT; (b) $\mathcal{S}$ obtained by blocking the average of $\mathcal{S}$ of figure (a) as function of f.

5.2 Trajectory analysis

To measure the parameters characterising the optical trapping, the techniques described in chapter 2.2 are applied to the experimental particle trajectories. A trajectory is a discrete and finite set of positions $r_j = r(t_j)$ acquired at the sampling times $t_j = j\Delta t$ and, because these techniques deals with continuos trajectories, they needs to be discretised. For simplicity, the trajectory of the particle is assumed to be 1-dimensional being the 3-dimensional extension straightforward[1].

5.2.1 Power spectrum

The power spectrum analysis (chapter 2.2.1) is based on the Fourier transform (chapter 2.2.1) of the trajectory. Therefore, the *discrete* Fourier transform of the particle trajectory needs to be performed, defined as:

$$\tilde{r}_k = \sum_{j=1}^{N} r_j e^{-2\pi i f_k t_k} = \sum_{j=1}^{N} r_j e^{-2\pi i \frac{k}{N} j} \tag{5.4}$$

where $1 \leq k \leq N$ and $f_k = k/T_s$ with $T_s = N\Delta_t$ total acquisition time. The power spectral density (PSD) $\mathcal{S}_k$ is then obtained as

$$\mathcal{S}_k = \frac{\Delta t}{N} \left|\tilde{r}_k\right|^2 \tag{5.5}$$

[1]To extend these methods, the 1-dimensional results are simply applied on each direction of the particle trajectory.

and it requires strictly a time series of correlated particle positions (trajectory) at regular time intervals. Figure 5.7a shows the experimental PSD for a particle trapped in water with the single beam optical tweezers (SBOT).

To estimate the physical quantities of interest, $\mathcal{S}_k$ should be fitted to its theoretical expression by a least square fitting. Nevertheless, the best fit can not be performed because the values of $\mathcal{S}_k$ are drawn from an exponential distribution[2] [31]. Indeed, in order to apply a least square fitting procedure, the data points need to follow a Gaussian distribution and to be statistically independent from each other . To satisfy these conditions there are two possibilities: evaluate $\mathcal{S}_k$ by repeating the experiment K times and averaging the resulting PSDs, and/or replacing a block of n_b consecutive data points with their average value placed at their average position, called *blocking* procedure. When K and/or n_b are sufficiently large, the resulting data points have a Gaussian distribution (central limit theorem) and the least square fitting can be performed. Therefore, when possible, these two procedures are applied, figures 5.7a and 5.7b, and, then, least square fitting performed. These two procedures, in addition, decrease data noise improving the estimation accuracy.

5.2.2 Mean squared displacement and autocorrelation

The mean squared displacement and the autocorrelation procedure require a time series of correlated particle positions $r_j = r(t_j)$ at regular time intervals $t_j = j\Delta t$. As for the PSD, by performing these analyses multiple times on various repetitions of the same experiment, the MSD and the ACF can be better estimated as the mean value of the resulting MSDs and ACFs, while the uncertainty as their standard deviation.

Mean squared displacement The MSD is defined as $\mathrm{Var}[r(\tau)]$ (chapter 2) and, for a discrete trajectory, is given by

$$\mathrm{MSD}_{r,k} = \frac{1}{N-k} \sum_{j=1}^{N-k} [r_{j+k} - r_j]^2 \tag{5.6}$$

where $r_{j+k} = r(j\Delta t + k\Delta t)$ and, therefore, the *time lag* τ is $\tau_k = k\Delta t$. Performing this operation on a finite trajectory, the $\mathrm{MSD}_{r,k}$ becomes less reliable as the delay time τ_k is increased, because it is evaluated on a progressively smaller set of points, as shown in figure 5.8a. For this reason, the maximum delay time τ_K is typically smaller than 20% of the acquisition time, $\tau_K < 0.2 \cdot N\Delta t$, as indicated by the dashed vertical line of figure 5.8a. The MSD of equation (5.6) allows to estimate physical quantities of interest, such as the trap stiffness, with a least square fitting to its theoretical expression.

[2] The PSD is proportional to the square modulus of the Gaussian random force of the Langevin equation and, therefore, is distributed exponentially.

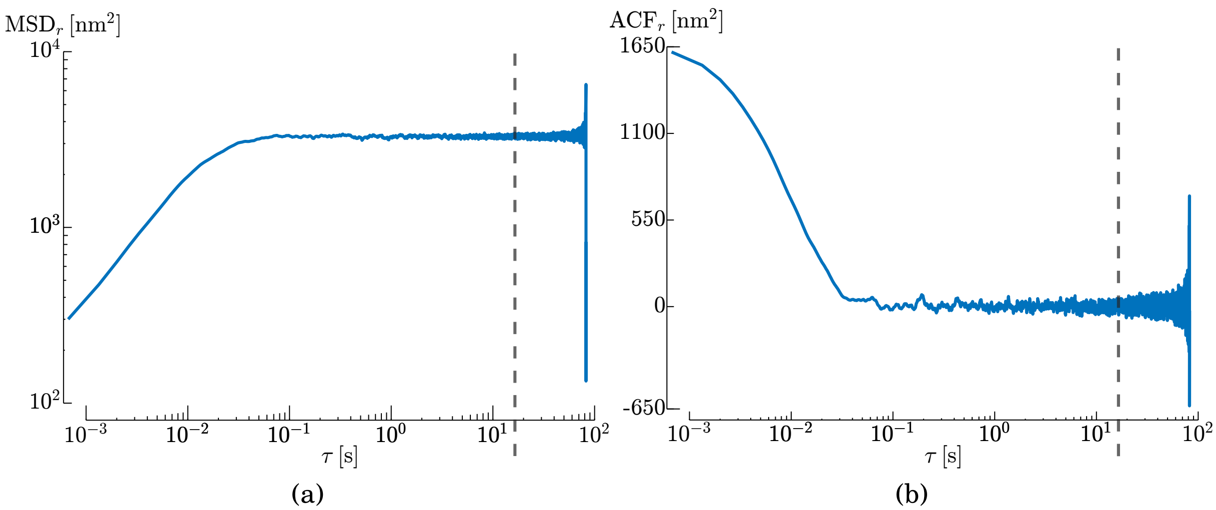

Figure 5.8: (a) mean squared displacement $\mathrm{MSD_r}$, and (b) autocorrelation function $\mathrm{ACF_r}$ as function of the lag time τ for a particle trapped in water by a SBOT. The vertical black dashed line indicates the maximum delay time $\tau_K = 0.2 \cdot N\Delta t$.

Autocorrelation function The ACF of a discrete trajectory is

$$\mathcal{C}_{r,k} = \frac{1}{N-k} \sum_{j=1}^{N-k} r_{j+k} r_j \tag{5.7}$$

and it can be fitted to its theoretical expression by a least square fitting. Also for ACF, the result of (5.7) becomes less reliable when the delay time τ_K is greater than $0.2 \cdot N\Delta t$. Figure 5.8b shows an experimental ACF for a particle trapped in water with a SBOT.

5.2.3 Potential and equipartition method

Potential analysis This analysis is quite general and can be used to measure even very complex potentials, not only harmonic ones. It does not require a time series of correlated particle position, like the previous methods, but it only needs a series of N independent particle positions r_i. It is based on equation (2.62) that relates the potential $U(r)$ with the probability distribution of the particle $\rho(r)$, i.e.

$$U(r) = -k_B T \log[\rho(r)] + U_0 \tag{5.8}$$

where r is the particle position, T is the temperature of the sample and U_0 is a constant.

To obtain $\rho(r)$ experimentally, the positions r_i are sorted into a series of equally spaced bin of width m and their counts ϕ_m are evaluated. Then, ρ_m is obtained as

$$\rho_m = \frac{\phi_m}{N \cdot m} \tag{5.9}$$

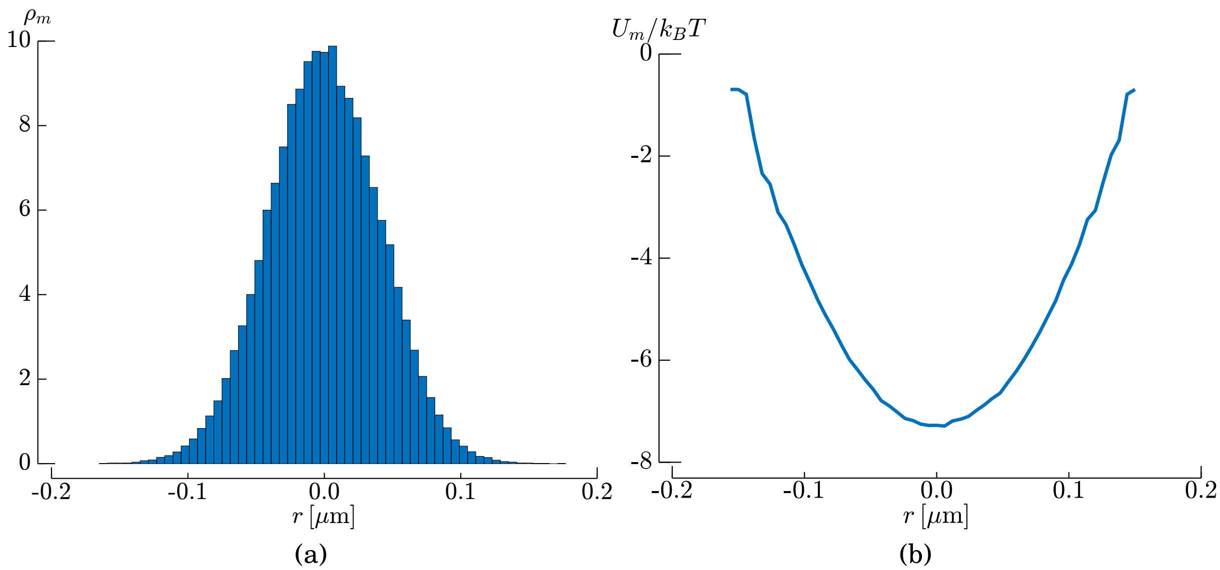

Figure 5.9: (a) experimental probability density function ρ_m and (b) the experimental potential U_m/k_BT as function of the particle position r.

that represents an approximation of $\rho(r)$ which becomes progressively better as the number of data N increases. An average value and a standard deviation of ϕ_m can be obtained repeating this operation several times on different datasets of the same experiment. Then, the logarithm of ϕ_m gives the potential through the relation

$$U_m = -k_BT \ln\left[\phi_m\right] + U_0 \tag{5.10}$$

This equation allows to estimate the physical parameters of the experimental potential by performing a least square fitting of U_m to its theoretical expression. Figure 5.9a shows the experimental $\rho(r)$ and figure 5.9b its associated potential for a trapped particle in water.

Equipartition method This method requires the evaluation of the position variance (chapter 2.2.4), that for a discrete trajectory is

$$\mathrm{Var}[r] = \frac{1}{N}\sum_{n=1}^{N}(x_n - x_{eq})^2 \tag{5.11}$$

with N the number of the trajectory elements and

$$x_{eq} = \frac{1}{N}\sum_{n=1}^{N} x_n \tag{5.12}$$

the mean position of the particle. Therefore, if the particle is trapped by an harmonic potential, the trap stiffness is

$$k_r = k_B T \left[\frac{1}{N} \sum_{n=1}^{N} (x_n - x_{eq})^2 \right]^{-1} \tag{5.13}$$

according to equation (2.66). By repeating the experiment N times, equation (5.11) can be used to estimate the variance of each repetition, $\mathrm{Var}[r]_n$. In this way, a better estimation of $\mathrm{Var}[r]$ is provided by the mean value of the set $\{\mathrm{Var}[r]_n\}_{n=1,\ldots,N}$, while its uncertainty as the standard deviation of $\{\mathrm{Var}[r]_n\}_{n=1,\ldots,N}$.

Chapter 6

Results and discussion

This chapter deals with the experimental results obtained by trapping particles with the setups described in chapter 4 and analysed by using the techniques described in chapter 5. In the first section, the standard single-beam optical tweezers (SBOT) is preliminary use to trap particles in water in order to optimise the functioning of the experimental setup. Then, the SBOT is used to fine tune the loading system for air trapping (chapter 4.4) to extend this techniques to the intracavity optical tweezers setup (IOT).

The second section discusses the results of particles trapped with the IOT and it is divided in five parts. The first part deals with the characterisation of the laser system when no particle is trapped. The second part concerns the trapping of particles in water with the single-beam IOT (SBIOT). The feedback effect is quantified and the results are compared with the theoretical models of chapter 3. The third part describes the novel double-beam IOT (DBIOT) characterised by two counter-propagating beams. Unlike the SBIOT, the DBIOT is characterised by a stronger confinement of the particle that reduces the feedback effect during trapping. The fourth part describes a novel DBIOT configuration in which the two counter-propagating beams are slightly misaligned forming a *double-trap* configuration: the two beams trigger a periodic motion of the particle between them producing regular periodic transitions that differ from the Kramers' transition described in chapter 2.3 because of the feedback effect. The last part deals with trapping particles in air with SBIOT comparing it with the analogous case in water and with the case of trapping in air with the standard optical tweezers.

6.1 Single-beam standard optical tweezers

In this section, the results obtained trapping particles with a SBOT are discussed. The first part deals with trapping in water, while the second part with trapping in air.

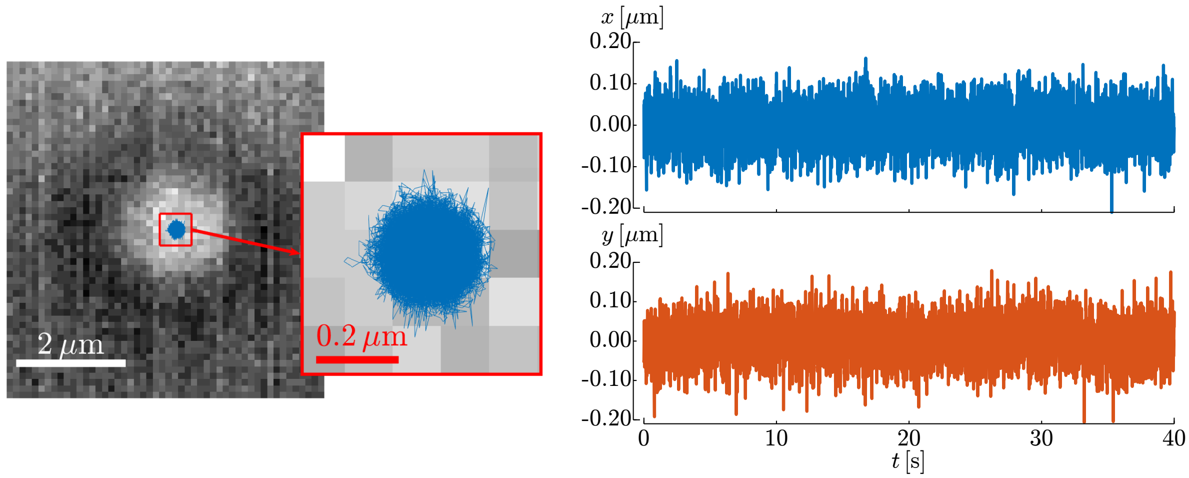

(a) (b)

Figure 6.1: (a) image of a silica particle of diameter $3.16\,\mu\mathrm{m}$ trapped in water with SBOT with its trajectory that is visible more clearly in the inset; (b) x and y component of the particle trajectory as function of time t.

6.1.1 Trapping in water

Trapping particles in water represents a preliminary step to check the performances of the SBOT. The experiments are performed using $3.16\,\mu m$ silica particles and a laser power of $P = 24.86\,\mathrm{mW}$.

The particle trajectory is obtained applying the $2\mathrm{D}$ tracking procedure described in chapter 5.1.2 to 30 videos of 60000 frames acquired at 1500 frames per second (fps). Figure 6.1a show a typical image of the trapped particle with its trajectory whose components are shown in figure 6.1b as function of the acquisition time t.

Firstly, the trap stiffness is evaluated by using the equipartition method, that gives

$$\begin{cases} k_x^{\mathrm{eq}} = (2.21 \pm 0.05) \cdot 10^{-6}\,\dfrac{\mathrm{N}}{\mathrm{m}} \\ k_y^{\mathrm{eq}} = (2.15 \pm 0.04) \cdot 10^{-6}\,\dfrac{\mathrm{N}}{\mathrm{m}} \end{cases} \tag{6.1}$$

where the temperature, measured during the whole experiments, is $298.1 \pm 0.5\,\mathrm{K}$. The stiffness along the x and the y directions are not discrepant denoting that the trap is symmetric in the trapping plane.

Then the power spectral density method is applied calculating the experimental PSDs (figure 6.2a). They present a Lorentzian shape according to the theoretical expression of equation (2.45), i.e.

$$\mathcal{S}_r(\omega) = \frac{2k_BT}{\gamma}\frac{1}{\omega^2 + (\frac{k}{\gamma})^2} \tag{6.2}$$

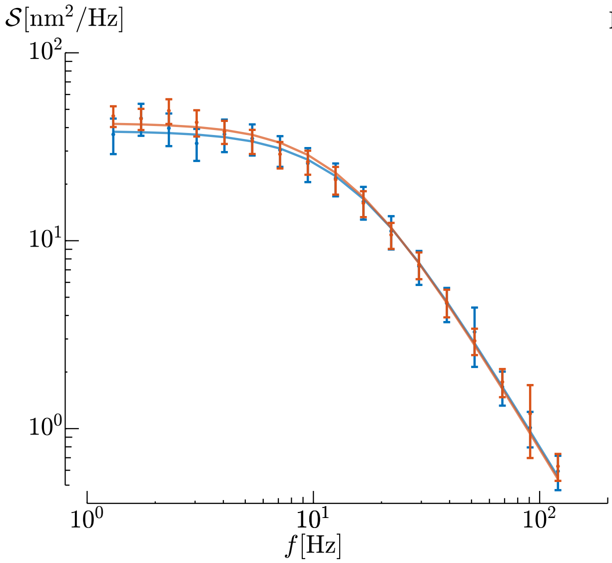

(a)

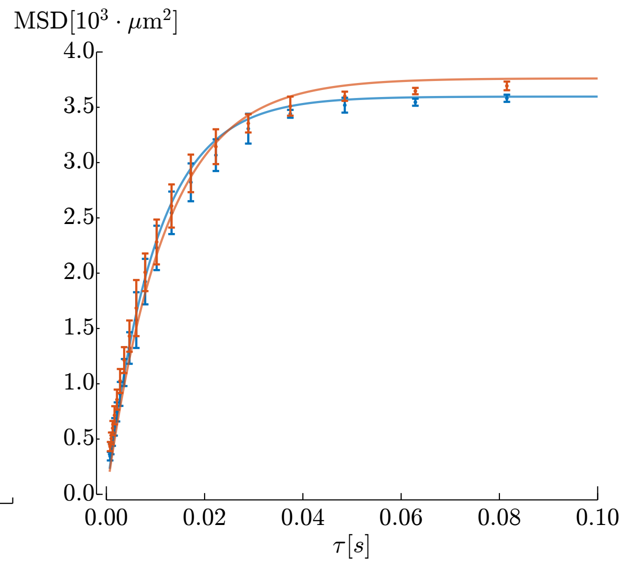

(b)

Figure 6.2: (a) experimental power spectral density $\mathcal{S}$ (dots with error bars) and its best fit curve (solid line) as function of the frequency f along the x direction (blue data) and the y direction (orange data); (b) experimental mean squared displacement MSD (dots with error bars) and its best fit curve (solid line) as function of the lag time τ along the x direction and the y direction.

This expression is used as fit function in order to estimate the stiffness k and the friction coefficient γ. The best fit stiffnesses are

$$\begin{cases} k_x^{\mathcal{S}} = (2.34 \pm 0.04) \cdot 10^{-6}\,\dfrac{\mathrm{N}}{\mathrm{m}}; \\ k_y^{\mathcal{S}} = (2.26 \pm 0.06) \cdot 10^{-6}\,\dfrac{\mathrm{N}}{\mathrm{m}}; \end{cases} \tag{6.3}$$

which are in not discrepant with the values obtained with the equipartition method, equation (6.1). The friction coefficient γ of the fluid is obtained as mean value of the two estimates along x and y directions resulting in

$$\gamma^{\mathcal{S}} = (2.59 \pm 0.07) \cdot 10^{-8}\,\frac{\mathrm{N} \cdot \mathrm{s}}{\mathrm{m}} \tag{6.4}$$

that is not discrepant with the expected value of $\gamma_{\mathrm{th}} = (2.65 \pm 0.06) \cdot 10^{-8}\,\frac{\mathrm{N \cdot s}}{\mathrm{m}}$ evaluated assuming known the water viscosity and the particle diameter.

Then the mean squared displacement is calculated following the procedure of chapter 5.2.2, obtaining the experimental MSDs of figure 6.2b. These curves reach the plateau value in about $0.15\,\mathrm{s}$ after a first exponential growth and follow the theoretical expression of equation (2.48), i.e.

$$\mathrm{MSD}(\tau) = \frac{2k_BT}{k}\left(1 - e^{-\frac{k}{\gamma}t}\right) \tag{6.5}$$

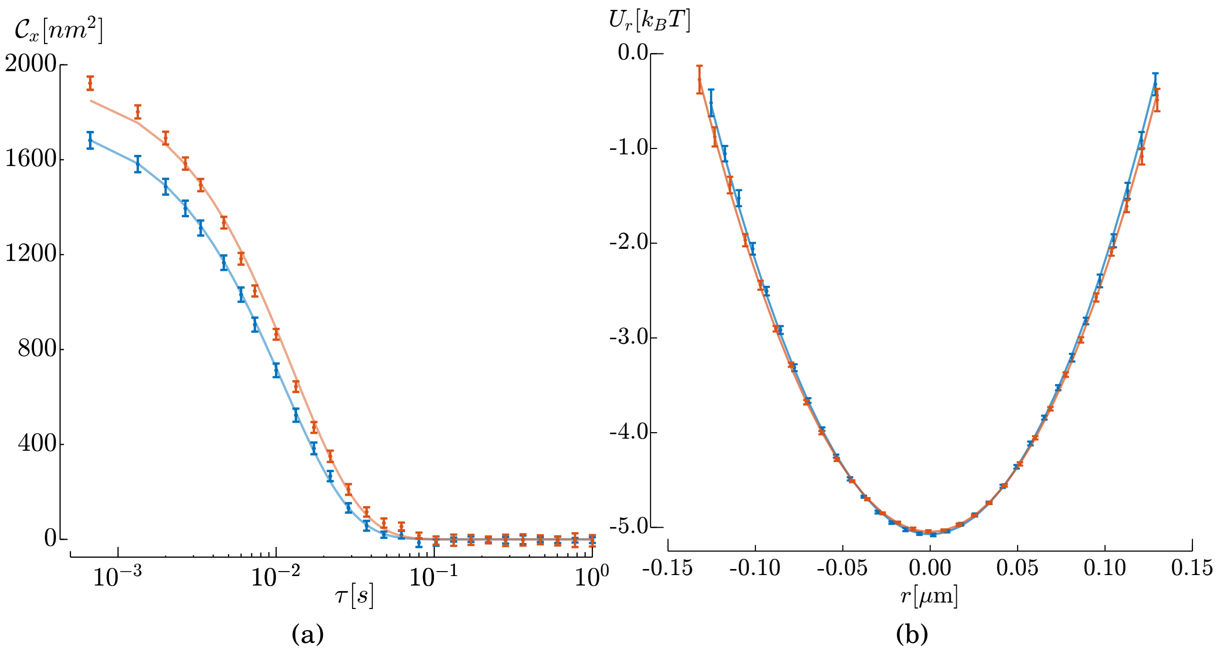

Figure 6.3: (a) experimental autocorrelation function ACF (dots with error bars) along the x direction (blue data) and the y direction (orange data) as function of the lag time τ. The solid lines indicate the best fit curves; (b) experimental potential U_r (dots with error bars) along the $r = x$ direction (blue data) and the $r = y$ direction (orange data) as function of the x and y position of the particle, respectively. Its best fit curve are indicates by the solid lines.

that is used as fit function with k and γ as fit parameters. The best fit curves are shown in figure 6.2b as solid lines and the best fit estimations of the stiffnesses are

$$\begin{cases} k_x^{\text{MSD},(1)} = (2.28 \pm 0.21) \cdot 10^{-6} \dfrac{\text{N}}{\text{m}} \\ k_y^{\text{MSD},(1)} = (2.19 \pm 0.22) \cdot 10^{-6} \dfrac{\text{N}}{\text{m}} \end{cases} \tag{6.6}$$

which agree, within their uncertainties, with the values shown above. Similarly, the estimated friction coefficient γ is

$$\gamma^{\text{MSD}} = (2.2 \pm 0.3) \cdot 10^{-10} \, \frac{\text{N} \cdot \text{s}}{\text{m}} \tag{6.7}$$

which agree, within the uncertainties, with the expected value γ_{th}.

A third approach to estimate these parameters is based on the autocorrelation function ACF. The experimental ACFs, obtained following the procedure of chapter 5.2.2, are shown in figure 6.3a, which reflect the theoretical behaviour of equation (2.52) that is used as fit function with k and γ as fitting parameters, i.e.

$$\mathcal{C}(\tau) = \frac{k_B T}{k} e^{-\frac{k}{\gamma}\tau} \tag{6.8}$$

The best fit estimations of these parameters are

$$\begin{cases} k_x^{\mathrm{ACF},(1)} = (2.30 \pm 0.03) \cdot 10^{-6}\,\dfrac{\mathrm{N}}{\mathrm{m}} \\ k_y^{\mathrm{ACF},(1)} = (2.11 \pm 0.05) \cdot 10^{-6}\,\dfrac{\mathrm{N}}{\mathrm{m}} \\ \gamma^{\mathrm{ACF}} = (2.61 \pm 0.05) \cdot 10^{-10}\,\dfrac{\mathrm{N}\cdot\mathrm{s}}{\mathrm{m}} \end{cases} \tag{6.9}$$

and that agree, within their uncertainties, with the other methods.

Finally, the potential method is applied following the procedure described in chapter 5.2.3. The experimental potential along the x and the y directions is extracted from the trajectories, see figure 6.3b, and it is fitted using equation (2.63), that is

$$\frac{U(r)}{k_B T} = \frac{1}{2}k(r - r_0)^2 + C \tag{6.10}$$

with $r = x, y$, the stiffness k and the arbitrary constant C as fitting parameters. The best fit curve are shown in figure 6.3b (solid lines) and they allows to extrapolate the stiffnesses that are

$$\begin{cases} k_x^{U,(1)} = (2.39 \pm 0.09) \cdot 10^{-6}\,\dfrac{\mathrm{N}}{\mathrm{m}}; \\ k_y^{U,(1)} = (2.25 \pm 0.07) \cdot 10^{-6}\,\dfrac{\mathrm{N}}{\mathrm{m}}; \end{cases} \tag{6.11}$$

not discrepant with estimates from other methods.

To conclude, it is useful to evaluate the trap efficiency

$$\varsigma^2 = \mathrm{Var}[r] \cdot P \tag{6.12}$$

with $r = x, y$. This quantity allows to compare the system trapping efficiency with other systems regardless the power used to trap, like the intracavity optical tweezers. For this SBOT, ς^2 is

$$\varsigma^2_{\mathrm{SBOT}} = (41.2 \pm 0.6)\,\mu\mathrm{m}^2 \cdot \mu\mathrm{W} \tag{6.13}$$

and it is evaluated as the mean value along x and y directions.

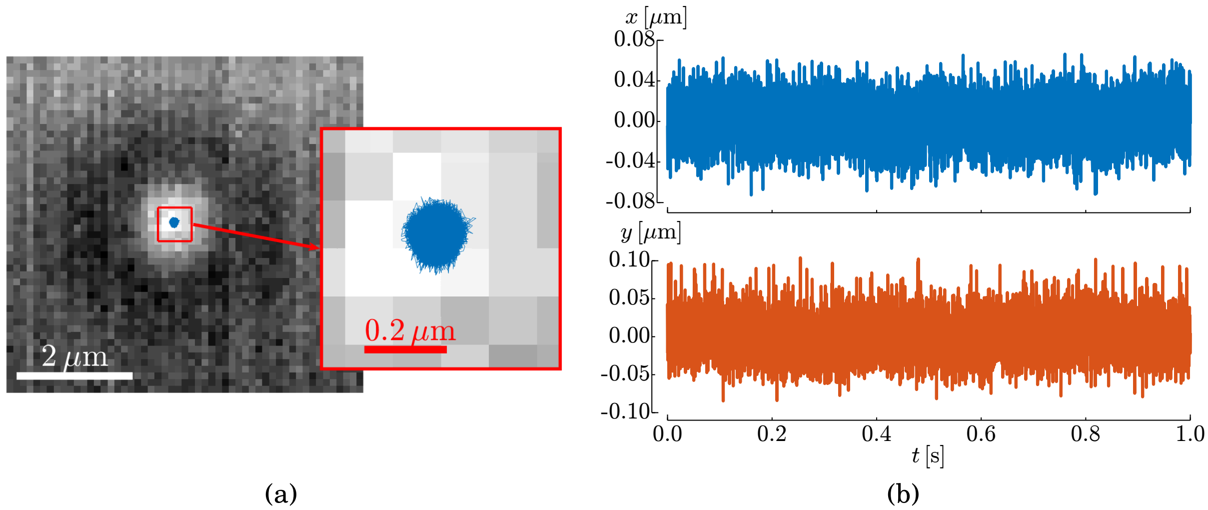

Figure 6.4: (a) image of a silica particle of diameter $3.16\,\mu\mathrm{m}$ trapped in air with SBOT with its trajectory that is visible more clearly in the inset; (b) x and y component of the particle trajectory as function of time t.

6.1.2 Trapping in air

When a particle is trapped in air the inertial effects are not negligible because the *relaxation time* ($\tau_m = m/\gamma$), which indicates the time scale at which the inertial effects decay, is

$$\tau_m^{\mathrm{air}} \sim 50\,\mu\mathrm{s} \tag{6.14}$$

while in water is

$$\tau_m^{\mathrm{water}} \sim 1\,\mu\mathrm{s} \tag{6.15}$$

Therefore, if the acquisition frequency is larger than $1/\tau_m^{\mathrm{water}}$, the experimental trajectory is describe by the complete Langevin equation (2.37), which gives place to different behaviours of the power spectral density, the mean squared displacement, and the autocorrelation function.

The air experiment is done trapping silica particles of $3.16\,\mu\mathrm{m}$ diameter using the loading system described in chapter 4.4 and, to study inertial effects, the acquisition frequency is increased to 30000 fps, i.e. the sampling time is $\Delta t \sim 33\mu\mathrm{s} < \tau_{\mathrm{m}}^{\mathrm{air}}$. The 400 acquired videos consist of 30000 frames for a duration of $1\,\mathrm{s}$. The experiments are done using three laser powers: $P_1 = 19.2\,\mathrm{mW}$, $P_2 = 20.5\,\mathrm{mW}$, and $P_3 = 23.7\,\mathrm{mW}$. The corresponding measured quantities are indicated by the superscripts (1), (2), and (3). A typical trajectory in the x-y plane is shown in figure 6.4a and its components as functions of time t are shown in figure 6.4b. From the analysis of the trajectories, it is possible to estimate the particle mass m, the particle diameter d, the fluid viscosity η, and the trap stiffness k.

The simplest way to evaluate the trap stiffness is based on the equipartition

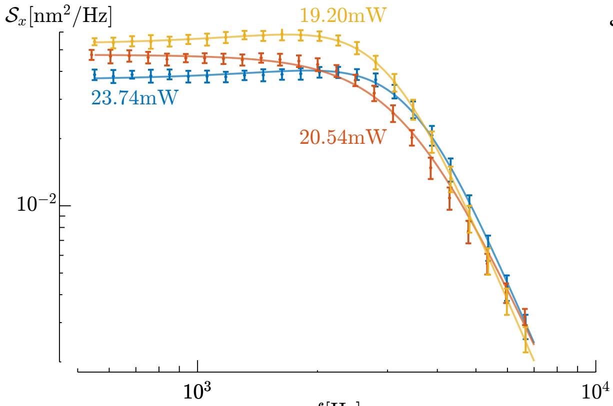

(a)

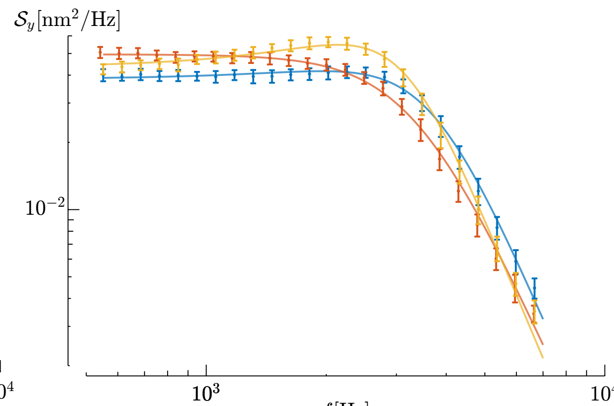

(b)

Figure 6.5: experimental power spectral density $\mathcal{S}$ (dots with error bars) and its best fit curve (solid line) as function of the frequency f for three different laser power and along (a) the x direction and (b) the y direction.

method that provides the following results:

$$\begin{cases} k_x^{\mathrm{eq},(1)} = (9.24 \pm 0.11) \cdot 10^{-6}\dfrac{\mathrm{N}}{\mathrm{m}}; & k_y^{\mathrm{eq},(1)} = (9.11 \pm 0.08) \cdot 10^{-6}\dfrac{\mathrm{N}}{\mathrm{m}}; \\ k_x^{\mathrm{eq},(2)} = (1.119 \pm 0.013) \cdot 10^{-5}\dfrac{\mathrm{N}}{\mathrm{m}} & k_y^{\mathrm{eq},(2)} = (1.136 \pm 0.020) \cdot 10^{-5}\dfrac{\mathrm{N}}{\mathrm{m}}; \\ k_x^{\mathrm{eq},(3)} = (1.125 \pm 0.011) \cdot 10^{-5}\dfrac{\mathrm{N}}{\mathrm{m}}; & k_y^{\mathrm{eq},(3)} = (1.051 \pm 0.007) \cdot 10^{-5}\dfrac{\mathrm{N}}{\mathrm{m}} \end{cases} \tag{6.16}$$

where the temperature is monitored during the whole experiments and remained stable to the value $298.1 \pm 0.5\,\mathrm{K}$.

Then, the PSD is calculated from the data and, unlike the case of trapping in water, presents a non-Lorentzian behaviour characterised by a central peak at around $2500\,\mathrm{Hz}$, see figures 6.5a and 6.5b. Therefore, the PSD expression of equation (2.42) is used as fit function, i.e.

$$\mathcal{S}(\omega) = \frac{2\gamma k_B T}{m^2}\frac{1}{\left(\frac{k}{m} - \omega^2\right)^2 + \frac{\gamma^2}{m^2}\omega^2} \tag{6.17}$$

where the fit parameters are the particle mass m, the friction coefficient γ, and the stiffness k. The estimated k from the fitting procedure are

$$\begin{cases} k_x^{\mathcal{S},(1)} = (9.6 \pm 0.3) \cdot 10^{-6}\dfrac{\mathrm{N}}{\mathrm{m}}; & k_y^{\mathcal{S},(1)} = (9.5 \pm 0.3) \cdot 10^{-6}\dfrac{\mathrm{N}}{\mathrm{m}}; \\ k_x^{\mathcal{S},(2)} = (1.191 \pm 0.020) \cdot 10^{-5}\dfrac{\mathrm{N}}{\mathrm{m}} & k_y^{\mathcal{S},(2)} = (1.120 \pm 0.018) \cdot 10^{-5}\dfrac{\mathrm{N}}{\mathrm{m}}; \\ k_x^{\mathcal{S},(3)} = (1.22 \pm 0.03) \cdot 10^{-5}\dfrac{\mathrm{N}}{\mathrm{m}}; & k_y^{\mathcal{S},(3)} = (1.109 \pm 0.020) \cdot 10^{-5}\dfrac{\mathrm{N}}{\mathrm{m}} \end{cases} \tag{6.18}$$

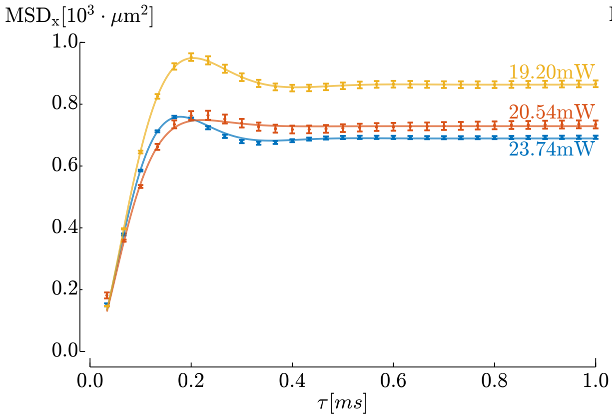

(a)

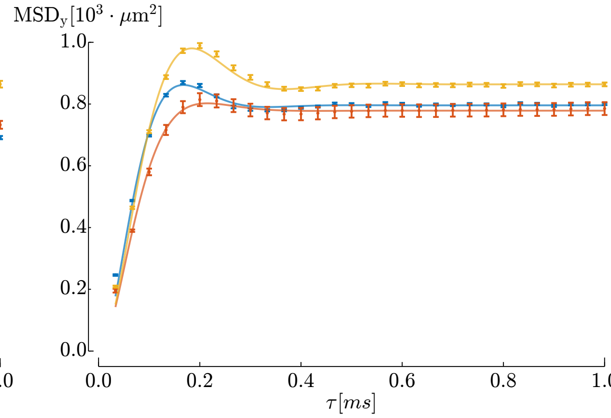

(b)

Figure 6.6: experimental mean square displacement MSD along (a) the x direction and (b) the y direction (dots with error bars) and its best fit curve (solid line) as function of the lag time τ for three different laser power.

in agreement with the equipartition method estimations. Instead the other parameters, mass m and friction coefficient γ, are estimated as the average of their best fit estimations obtained along x and y directions for each laser power, being them independent on the laser power. Therefore, the mass m of the particle is estimated to be

$$m^{\mathcal{S}} = (2.49 \pm 0.09) \cdot 10^{-14}\,\text{kg} \tag{6.19}$$

From this value of m, the particle diameter is estimated and compared with its nominal value assuming known the particle density, i.e. $\rho = 1800\,\text{kg/m}^3$, being

$$d^{\mathcal{S}} = 2\sqrt[3]{\frac{3}{4\pi\rho}m} = (2.98 \pm 0.03)\,\mu\text{m} \tag{6.20}$$

which shows discrepancy from the nominal value of $3.16\,\mu\text{m}$. Finally, the estimation of γ is

$$\gamma^{\mathcal{S}} = (6.54 \pm 0.17) \cdot 10^{-10}\,\frac{\text{N} \cdot \text{s}}{\text{m}} \tag{6.21}$$

from that, once estimated the particle diameter, the fluid viscosity η results to be

$$\eta^{\mathcal{S}} = \frac{\gamma}{3\pi d} = (2.33 \pm 0.06) \cdot 10^{-5}\,\text{Pa} \cdot \text{s} \tag{6.22}$$

that is discrepant with respect to the air viscosity measured at $1\,\text{atm}$ and $298.1 \pm 0.5\,\text{K}$ that is $1.84 \cdot 10^{-5}\,\text{Pa} \cdot \text{s}$.

Also the mean squared displacement analysis, figures 6.6a and 6.6b, shows the presence of inertial effects. Indeed, these curves reach a plateau value in about $0.6\,\text{ms}$ after a first exponential growth followed by some oscillations, as described in chapter 2.2.2. Therefore, the theoretical expression of equation (2.46),

$$
\begin{cases}
\mathrm{MSD}(\tau) = 2\dfrac{k_B T}{k} - 2\dfrac{k_B T}{k}\left[\cosh\left(\dfrac{\Omega_1}{2}\tau\right) + \dfrac{\Gamma_0}{\Omega_1}\sinh\left(\dfrac{\Omega_1}{2}\tau\right)\right]e^{-\Gamma_0\tau/2} \\
\Omega = \sqrt{k/m} \\
\Omega_1 = \sqrt{\dfrac{\gamma^2}{m^2} - 4\dfrac{k}{m}} = \sqrt{\Gamma_0^2 - 4\Omega^2} \\
\Gamma_0 = \dfrac{\gamma}{m}
\end{cases}
\tag{6.23}
$$

is used as fit function, shown in figure 6.6a as solid lines, and the estimated stiffnesses are

$$
\begin{cases}
k_x^{\mathrm{MSD},(1)} = (9.54 \pm 0.21)\cdot 10^{-6}\dfrac{\mathrm{N}}{\mathrm{m}}; & k_y^{\mathrm{MSD},(1)} = (9.53 \pm 0.18)\cdot 10^{-6}\dfrac{\mathrm{N}}{\mathrm{m}}; \\
k_x^{\mathrm{MSD},(2)} = (1.13 \pm 0.03)\cdot 10^{-5}\dfrac{\mathrm{N}}{\mathrm{m}} & k_y^{\mathrm{MSD},(2)} = (1.057 \pm 0.019)\cdot 10^{-5}\dfrac{\mathrm{N}}{\mathrm{m}}; \\
k_x^{\mathrm{MSD},(3)} = (1.195 \pm 0.016)\cdot 10^{-5}\dfrac{\mathrm{N}}{\mathrm{m}}; & k_y^{\mathrm{MSD},(3)} = (1.034 \pm 0.019)\cdot 10^{-5}\dfrac{\mathrm{N}}{\mathrm{m}}
\end{cases}
\tag{6.24}
$$

while the mass m and the friction coefficient γ are

$$
\begin{cases}
m^{\mathrm{MSD}} = (2.32 \pm 0.07)\cdot 10^{-14}\,\mathrm{kg} \\
\gamma^{\mathrm{MSD}} = (6.32 \pm 0.11)\cdot 10^{-10}\,\dfrac{\mathrm{N}\cdot\mathrm{s}}{\mathrm{m}}
\end{cases}
\tag{6.25}
$$

From these estimation, it follows that

$$
\begin{cases}
d^{\mathrm{MSD}} = (2.91 \pm 0.03)\,\mu\mathrm{m} \\
\eta^{\mathrm{MSD}} = (2.25 \pm 0.04)\cdot 10^{-5}\,\mathrm{Pa}\cdot\mathrm{s}
\end{cases}
\tag{6.26}
$$

in agreement with the measurement done with the PSD.

A third estimation of these parameters is done using the autocorrelation function method. The experimental ACF are shown in figure 6.7a and 6.7b and are characterised by the typical anti-correlations due to the inertia, for lag times between $0.12\,\mathrm{ms}$ and $0.31\,\mathrm{ms}$. Therefore, the experimental ACF is fitted with the theoretical expression of equation (2.51), solid lines in figure 6.7a, that is

$$
\mathcal{C}(\tau) = \frac{k_B T}{k}\left[\cosh\left(\frac{\sqrt{\frac{\gamma^2}{m^2} - 4\frac{k}{m}}}{2}\tau\right) + \frac{\gamma/m}{\sqrt{\frac{\gamma^2}{m^2} - 4\frac{k}{m}}}\sinh\left(\frac{\sqrt{\frac{\gamma^2}{m^2} - 4\frac{k}{m}}}{2}\tau\right)\right]e^{-\frac{\gamma}{2m}\tau}
\tag{6.27}
$$

The best fitting procedure gives the following stiffnesses:

$$
\begin{cases}
k_x^{\mathrm{ACF},(1)} = (9.41 \pm 0.18)\cdot 10^{-6}\dfrac{\mathrm{N}}{\mathrm{m}}; & k_y^{\mathrm{ACF},(1)} = (9.57 \pm 0.21)\cdot 10^{-6}\dfrac{\mathrm{N}}{\mathrm{m}}; \\
k_x^{\mathrm{ACF},(2)} = (1.131 \pm 0.017)\cdot 10^{-5}\dfrac{\mathrm{N}}{\mathrm{m}} & k_y^{\mathrm{ACF},(2)} = (1.023 \pm 0.016)\cdot 10^{-5}\dfrac{\mathrm{N}}{\mathrm{m}}; \\
k_x^{\mathrm{ACF},(3)} = (1.187 \pm 0.016)\cdot 10^{-5}\dfrac{\mathrm{N}}{\mathrm{m}}; & k_y^{\mathrm{ACF},(3)} = (1.062 \pm 0.014)\cdot 10^{-5}\dfrac{\mathrm{N}}{\mathrm{m}}
\end{cases}
\tag{6.28}
$$

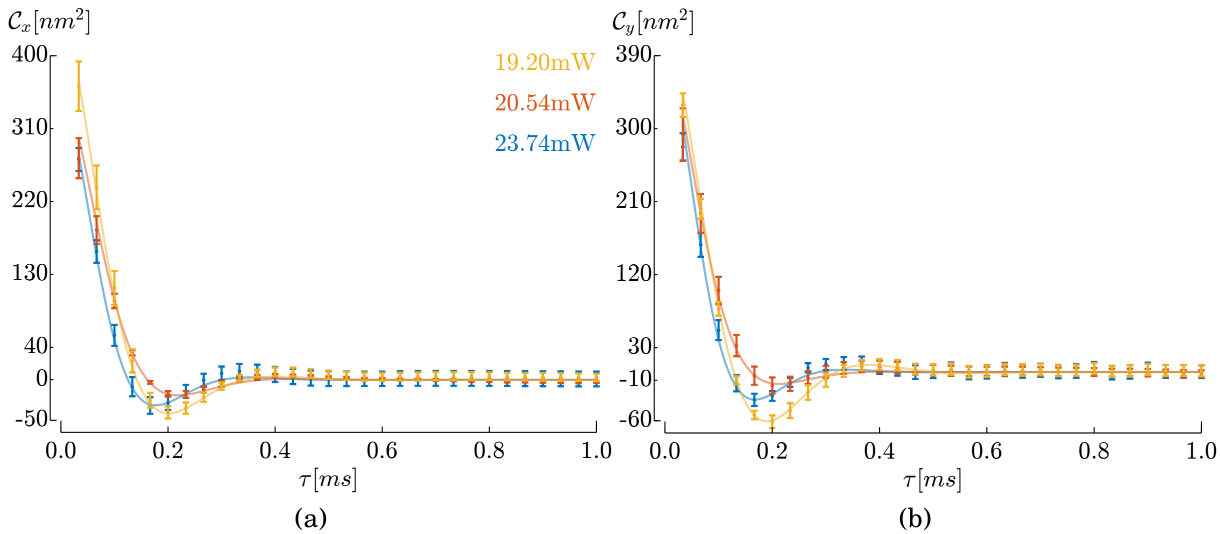

Figure 6.7: experimental autocorrelation function ACF along (a) the x direction and (b) the y direction (dots with error bars) and its best fit curve (solid line) as function of the lag time τ for three different laser powers.

Instead, m and γ are

$$\begin{cases} m^{\text{ACF}} = (2.34 \pm 0.45) \cdot 10^{-14}\,\text{kg} \\ \gamma^{\text{ACF}} = (6.4 \pm 0.4) \cdot 10^{-10}\,\dfrac{\text{N} \cdot \text{s}}{\text{m}} \end{cases} \tag{6.29}$$

From this it follows

$$\begin{cases} d^{\text{ACF}} = (2.92 \pm 0.20)\,\mu\text{m} \\ \eta^{\text{ACF}} = (2.29 \pm 0.16) \cdot 10^{-5}\,\text{Pa} \cdot \text{s} \end{cases} \tag{6.30}$$

in agreement with the measurement done with the other methods.

Finally, the potential method is applied resulting in the experimental potential of figures 6.8a and 6.8b. This method is not able to distinguish the presence of inertial effects, because it is based on the hypothesis that the particle is in thermal equilibrium with the surrounding medium and, therefore, the distribution of the particle position does not depend on the presence of inertial effects. The experimental potential along the x direction and the y direction is extracted from the trajectories, see figure 6.8a, and it is fitted using equation (2.63), that is

$$\frac{U(r)}{k_B T} = \frac{1}{2}k(r - r_0)^2 + C \tag{6.31}$$

with $r = x, y$. The stiffness k and the arbitrary constant C are used as fitting parameters. The best fit curve are shown in figure 6.8a and they allows to extrapolate

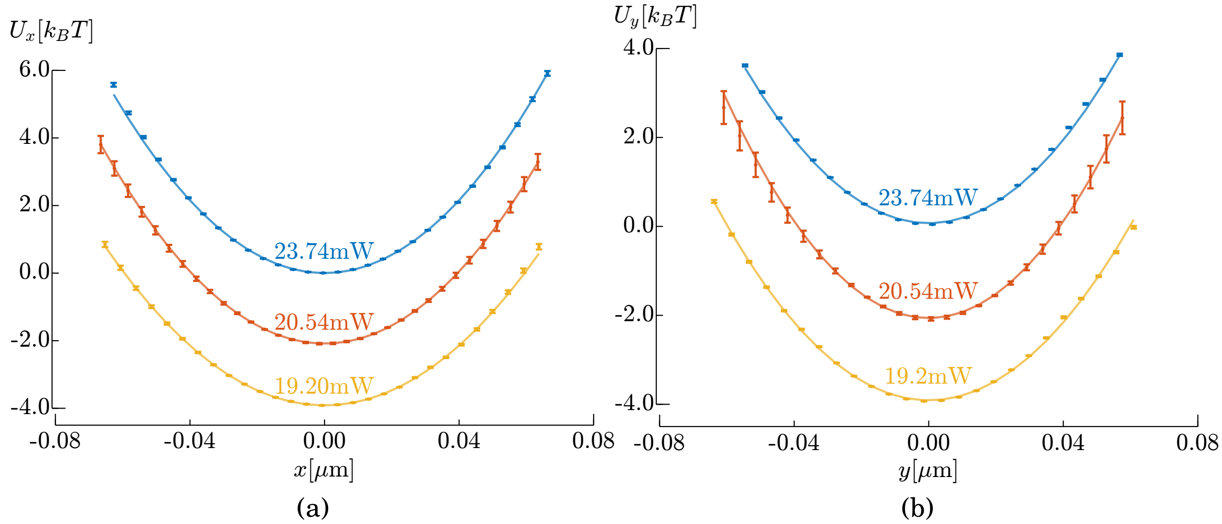

Figure 6.8: experimental potential U along (a) the x direction and (b) the y direction (dots with error bars) and its best fit curve (solid line) as function of the x and y position of the particle, respectively, for three different laser power. The potential are shifted of an arbitrary constant to make clearer the figure.

the stiffnesses that are

$$\begin{cases} k_x^{U,(1)} = (9.10 \pm 0.07) \cdot 10^{-6} \dfrac{\mathrm{N}}{\mathrm{m}}; & k_y^{U,(1)} = (9.01 \pm 0.16) \cdot 10^{-6} \dfrac{\mathrm{N}}{\mathrm{m}}; \\ k_x^{U,(2)} = (1.10 \pm 0.03) \cdot 10^{-5} \dfrac{\mathrm{N}}{\mathrm{m}} & k_y^{U,(2)} = (1.119 \pm 0.016) \cdot 10^{-5} \dfrac{\mathrm{N}}{\mathrm{m}}; \\ k_x^{U,(3)} = (1.108 \pm 0.005) \cdot 10^{-5} \dfrac{\mathrm{N}}{\mathrm{m}}; & k_y^{U,(3)} = (1.054 \pm 0.015) \cdot 10^{-5} \dfrac{\mathrm{N}}{\mathrm{m}} \end{cases} \tag{6.32}$$

in agreement with the previous measurements.

To conclude this section, it is useful to evaluate the quantity $\varsigma^2 = \mathrm{Var}[r] \cdot P$ ($r = x, y$) to compare the trapping efficiency of this system with the intracavity optical tweezers for air trapping. In this case, the estimation for each laser power of ς^2, evaluated as the average value of its estimation along x and y directions, are

$$\begin{cases} \varsigma^{2,(1)}_{\mathrm{SBOT,air}} = (8.93 \pm 0.8)\, \mu\mathrm{m}^2 \cdot \mu\mathrm{W} \\ \varsigma^{2,(2)}_{\mathrm{SBOT,air}} = (8.32 \pm 0.9)\, \mu\mathrm{m}^2 \cdot \mu\mathrm{W} \\ \varsigma^{2,(3)}_{\mathrm{SBOT,air}} = (8.76 \pm 0.6)\, \mu\mathrm{m}^2 \cdot \mu\mathrm{W} \end{cases} \tag{6.33}$$

Therefore, the estimation of $\varsigma^2_{\mathrm{SBOT,air}}$ is obtained as mean value of $\varsigma^{2,(j)}_{\mathrm{SBOT,air}}$ with $j = 1, 2, 3$ and it is

$$\varsigma^2_{\mathrm{SBOT,air}} = (8.7 \pm 0.6)\, \mu\mathrm{m}^2 \cdot \mu\mathrm{W} \tag{6.34}$$

All the stiffnesses obtained are summarised in the following table:

	$k_x^{(1)}$	$k_y^{(1)}$	$k_x^{(2)}$	$k_y^{(2)}$	$k_x^{(3)}$	$k_y^{(3)}$
Eq	0.924 ± 0.011	0.911 ± 0.008	1.119 ± 0.013	1.136 ± 0.020	1.125 ± 0.011	1.051 ± 0.007
PSD	0.96 ± 0.03	0.95 ± 0.03	1.191 ± 0.020	1.120 ± 0.018	1.22 ± 0.03	1.109 ± 0.020
MSD	0.954 ± 0.021	0.953 ± 0.018	1.13 ± 0.03	1.057 ± 0.019	1.195 ± 0.016	1.034 ± 0.019
ACF	0.941 ± 0.018	0.957 ± 0.021	1.131 ± 0.017	1.023 ± 0.016	1.187 ± 0.016	1.062 ± 0.014
U	0.910 ± 0.007	0.901 ± 0.016	1.10 ± 0.03	1.119 ± 0.016	1.108 ± 0.005	1.054 ± 0.015

where Eq indicates the equipartition method and the stiffnesses are indicated in $10^{-5}\mathrm{N/m}$.

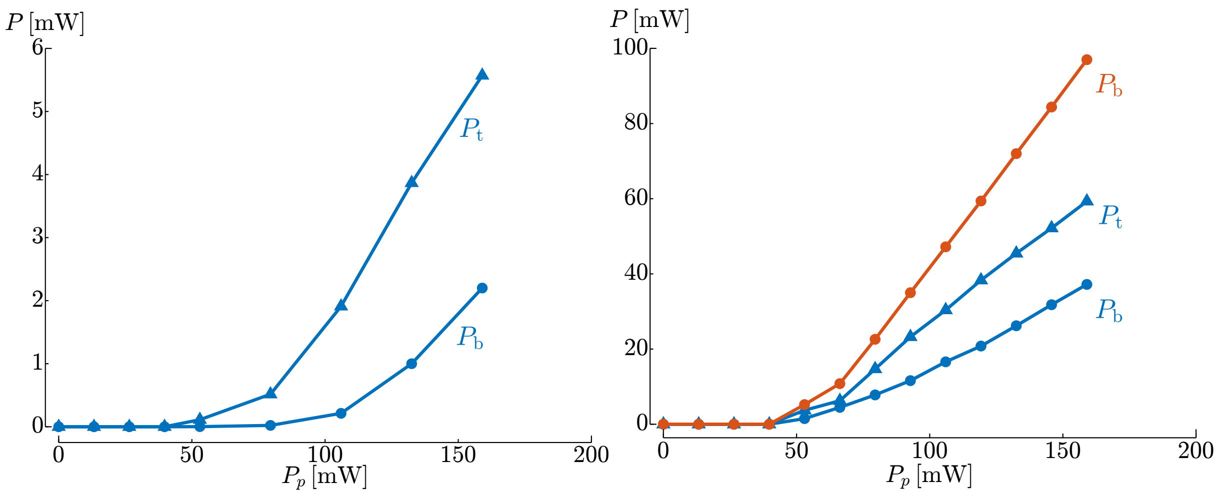

(a) (b)

Figure 6.9: (a) optical power P of the bottom beam (circles) and of the top beam (triangles) as function of the pump power P_p when the system is misaligned; (b) optical power P of the bottom beam (circles) and of the top beam (triangles) as function of the pump power P_p when the system is aligned in single-beam configuration (orange circles) and in double-beam configuration (blue circles and triangles).

6.2 Intracavity trapping

The intracavity optical trapping differs from conventional optical traps because the trapped particle is part of the laser cavity and, therefore, the laser power changes according to the particle position. Since the laser power is one of the key quantities, a preliminary characterisation of the laser system is needed. Then, the results concerning the trapping in water for both single-beam and double-beam configuration are reported for different types of particles. In addition, the results concerning the motion of a particle when a slight misalignment of the two beams is done on purpose are presented (*double-trap*). Finally, some preliminary results trapping particle with IOT air are discussed.

6.2.1 Characterisation of the laser system

The characterisation of the laser system is done measuring the optical power inside the cavity when no particle is trapped. To examine all the experimental conditions, the power is measured when the cavity is misaligned and aligned, with and without the isolator. When the cavity is completely misaligned, there is no laser effect in the cavity, but the optical power is not completely zero due to the spontaneous emission that in fibre lasers is guided by the fibre through the collimators: increasing the pumping power, the optical power increases according to figure 6.9a. Therefore, the laser can be considered powered off if the power inside the cavity is almost equal to the measured power in this condition. In addition, the beam exiting from the bottom collimator (*bottom beam*), that is the beam used in single-beam configuration, has an optical power P_b smaller than the beam exiting from the top collimator (*top beam*).

When the cavity is aligned, instead, the laser power of both beams increases due to the laser effect. In single-beam configuration, the optical isolator suppresses the top beam and constrains the stimulated emission only in the direction of the bottom beam[1]. Removing the isolator (double-beam configuration), the laser power is split almost equally between the two beams being their sum almost equal to the power of the bottom beam in single-beam configuration, see figure 6.9b[2].

Finally, the laser is characterised by a threshold pump power $P_{p,\mathrm{th}}$ under that the laser effect does not happen that is about $P_{p,\mathrm{th}} = 44.5 \pm 0.1\,\mathrm{mW}$.

6.2.2 Single-beam trapping in water

The IOT system, as described in chapter 3, is characterised by a correlation between the position of the trapped particle and the laser power inside the cavity. For this reason, the acquired video of the trapped particle is synchronised with an hardware clock with the measured optical power. Then, the trajectory of the particle is reconstructed from the video files applying the holographic tracking described in chapter 5.1.3.

According to the toy model discussed in chapters 3.2.1 and 3.2.2, the laser power P and the square of the distance of the particle from the centre of the trap r are proportional. However, the experimental particle coordinates x and y are measured in the reference frame having as origin the bottom-left corner of each acquired frame. Instead, the z direction is referred to the imaging plane that, in order to improve the 3D tracking, is on purpose shifted[3] from the focal plane of the trapping system, i.e. the *trap centre*. Therefore, the experimental particle coordinates $(x_\mathrm{exp}, y_\mathrm{exp}, z_\mathrm{exp})$ are studied in a reference frame different from the one in which the toy model is formulated. To compare the experimental data with the model, it is mandatory to estimate the position of the trap centre (x_c, y_c, z_c).

The estimation of (x_c, y_c, z_c) can be performed observing that the laser is switched off when the particle is near the trap position. Experimentally, the IOT can be considered switched off when the laser power is below a certain threshold value P_th, i.e. $P < P_\mathrm{th}$. In these experiments, the pump power is $P_p = 53.0\,\mathrm{mW}$ which corresponds, as figure 6.9a shows, to a laser power in misaligned condition of about $P_\mathrm{off} \simeq 2\,\mu\mathrm{W}$. Consequently, the threshold value is set to $P_\mathrm{th} \simeq 2\,\mu\mathrm{W}$. Thus, the centre (x_c, y_c, z_c) is measured as the average position of the particle for which $P < P_\mathrm{th}$. The typical

[1] In this condition, the pump power P_p is used by only one beam explaining why in single-beam configuration the laser beam power is higher.

[2] The laser power measured in this condition is the maximum laser power that the two beams can have at a fixed value of the pump power

[3] The shift of the imaging plane is done by moving the tube lens of the CCD camera.

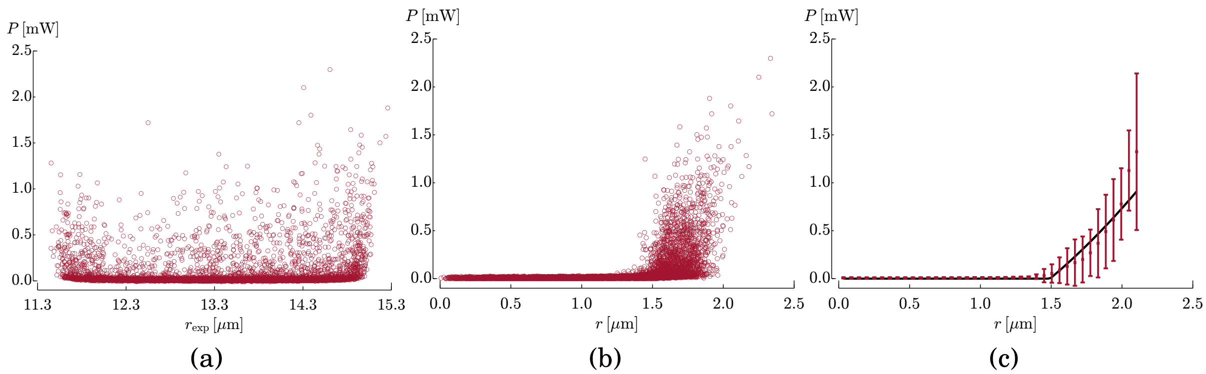

Figure 6.10: optical power P as function of the particle distance from (a) the experimental reference frame, r_{exp}, and (b) from the estimated trap centre, r, when a $1.98\,\mu\text{m}$ diameter polystyrene particle is trapped; (c) blocking of P as function of r (red squares with error bars) and its best fit function with the theoretical expression of equation (6.35).

uncertainties of (x_c, y_c, z_c) are less than $100\,\text{nm}$ and it does not appreciably affect the results obtained in this section. Then, the particle coordinates are translated according to the transformation $x = x_{\text{exp}} - x_c$, $y = y_{\text{exp}} - y_c$, and $z = z_{\text{exp}} - z_c$.

Having estimated (x_c, y_c, z_c), the power P as function of $r = \sqrt{x^2 + y^2 + z^2}$ follows the relation:

$$P(r) = \begin{cases} 0 & \text{if } |r| \leq r_{\text{on}} \\ P_0 \left(\frac{r^2}{r_{\text{on}}^2} - 1 \right) & \text{if } r_{\text{on}} < |r| \leq r_{\text{max}} \\ P_0 \left(\frac{r_{\text{max}}^2}{r_{\text{on}}^2} - 1 \right) & \text{if } |r| > r_{\text{max}} \end{cases} \tag{6.35}$$

with $P_0 \left(\frac{r_{\text{max}}^2}{r_{\text{on}}^2} - 1 \right) = P_{\text{max}}$ the maximum value of the laser power, i.e. without a trapped particle. To underline the importance of finding (x_c, y_c, z_c), figures 6.10a and 6.10b show the difference of studying P as function of r_{exp} or of r. As figure 6.10b shows, $P(r)$ is characterised by a statistical noise due to the Brownian motion of the particle inside the trap and, in order to improve the accuracy of the fitting parameters, a blocking procedure is applied to the data as shown in figure 6.10c. In this way, the parameters P_0, r_{on}, and r_{max} are estimated by fitting the data with the theoretical expression of equation (6.35) allowing a physical explanation of the behaviour of SBIOT. This preliminary analysis is done for all the three experiments, which involve particles of different materials and diameters.

Polystyrene particles of diameter $1.98\,\mu m$

The first experiment is done with polystyrene particles of diameter $1.98\,\mu m$ and the acquired data consists of 15 videos of 100 frames at $10\,\text{fps}$. The x, y, and z components of a typical trajectory and the relative laser power P are shown in figures 6.11a and 6.11b, respectively, as functions of time t. The particle trajectory is characterised by

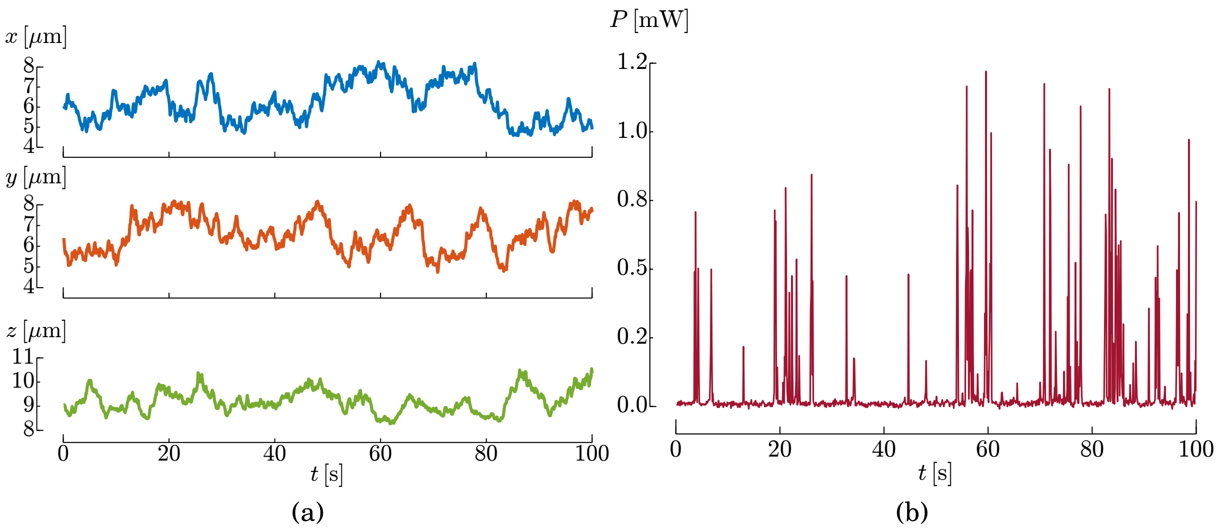

Figure 6.11: (a) x, y, and z components of the particle trajectory and (b) its corresponding power P as function of time t for a $1.98\,\mu\mathrm{m}$ polystyrene particle.

fluctuations of the order of some micrometers, while the power P is about zero, i.e. $P < P_{\mathrm{th}}$, for relatively long time intervals and suddenly it increases to high values. The time intervals with $P < P_{\mathrm{th}}$ indicate when the particle has a distance r from the trap centre less than r_{on}, $r \leq r_{\mathrm{on}}$, allowing the estimation of r_{on} as the mean of the maximum values of r in each of these time intervals, i.e.

$$\tilde{r}_{\mathrm{on}}^{\mathrm{PS}\,1.98} = (1.46 \pm 0.09)\,\mu\mathrm{m} \tag{6.36}$$

where its uncertainty is estimated by the standard deviation of all the maximum values. This parameter can also be estimated by the fitting the experimental power as function of r as explained before, which gives

$$r_{\mathrm{on}}^{\mathrm{PS}\,1.98} = (1.49 \pm 0.08)\,\mu\mathrm{m} \tag{6.37}$$

presenting no discrepancy with the previous estimation. This value is about 1.5 times the particle radius suggesting that the laser powers on only when the particle moves from the trap centre by a distance comparable to its diameter.

The fitting procedure allows also to estimate the other parameters, but, in this experiment, the laser power never reaches its maximum value $P_{\max} \simeq 5.23\,\mathrm{mW}$ (figure 6.9b for $P_p = 53.0\,\mathrm{mW}$) after the particle loading and $r_{\max}$ can not be estimated. Instead, the best fit estimation of P_0 is

$$P_0^{\mathrm{PS}\,1.98} = (0.92 \pm 0.18)\,\mathrm{mW} \tag{6.38}$$

where the larger uncertainty of about 20% is principally determined by the experimental points at higher power, which are less frequent than the others.

An additional proof of the feedback effect is given by the correlation coefficient between the laser power $P(t)$ and $r^2(t)$, which is

$$C_{P,r^2}^{\mathrm{PS}\,1.98} \simeq 0.73 \tag{6.39}$$

This value indicates that the relationship between $P(t)$ and $r^2(t)$ is not perfectly linear, as expected from equation (6.35). The linear relationship is expected to happen when the distance r is greater than r_{on} and, indeed, the correlation coefficient becomes

$$C_{P,r^2}^{\mathrm{PS}\,1.98} \simeq 0.95 \quad \text{if } r > r_{\mathrm{on}} \tag{6.40}$$

indicating an almost perfect linear correlation.

Thanks to the feedback effect, the particle confinement, quantified by the variance $\mathrm{Var}[r]$ of the particle as explained in chapter 3.2, is relatively high if compared to the mean optical power of the system $\bar{P}$. In this case, the mean power is

$$\bar{P} = 54 \pm 4\,\mu\mathrm{W} \tag{6.41}$$

and it is 6 times greater than the value evaluated by the toy model expression of equation (3.19)

$$\bar{P}_{\mathrm{toy}} \simeq 9.2\,\mu W \tag{6.42}$$

utilising the estimated value of $r_{\mathrm{on}}^{\mathrm{PS}\,1.98}$ and $P_0^{\mathrm{PS}\,1.98}$. Also the modified toy model of equation (3.31) gives a similar value:

$$\bar{P}_{\mathrm{toy}} \simeq 8.9\,\mu W \tag{6.43}$$

utilising as maximum power the value $P_{\mathrm{max}} \simeq 5.23\,\mathrm{mW}$. This indicates that the toy model describes well only qualitatively the IOT. On the other hand, the variance $\mathrm{Var}[r]$ is

$$\mathrm{Var}[r] = (0.186 \pm 0.002)\,\mu\mathrm{m}^2 \tag{6.44}$$

and it is 3.6 time less than the value obtained by applying the toy model expression of equation (3.27), which is

$$\mathrm{Var}[r]_{\mathrm{toy}} \simeq 0.663\,\mu\mathrm{m}^2 \tag{6.45}$$

and 2.2 times less than the value given by the modified toy model, which is

$$\mathrm{Var}[r]_{\mathrm{mod\ toy}} \simeq 0.402\,\mu\mathrm{m}^2 \tag{6.46}$$

obtained utilising equation (3.42) the estimated values of $r_{\mathrm{on}}^{\mathrm{PS}\,1.98}$ and $P_0^{\mathrm{PS}\,1.98}$, and for $P_{\mathrm{max}} \simeq 5.23\,\mathrm{mW}$. The modified toy model proposed in this work, therefore, improves the particle variance estimation compared to the standard toy model. In order to compare the IOT system with the SBOT, the parameter $\varsigma^2 = \mathrm{Var}[r] \cdot \bar{P}$ needs to be evaluated to deal with the different optical powers used in these different experiments. In this case, ς^2 is

$$\varsigma^2 = 10.1 \pm 0.7\,\mu\mathrm{m}^2 \cdot \mu\mathrm{W} \tag{6.47}$$

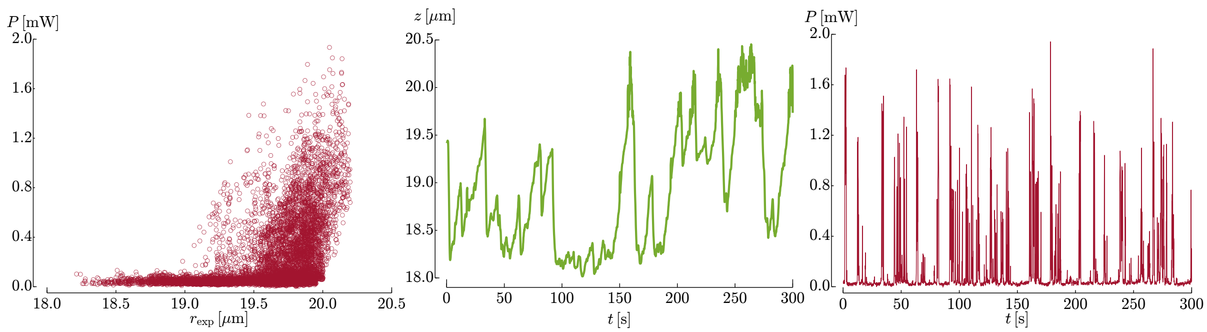

(a) (b) (c)

Figure 6.12: (a) optical power P as function of the particle distance r_{exp} from the experimental reference frame when trapping a $4.97\,\mu\mathrm{m}$ diameter polystyrene particle; (b) z component of the particle trajectory as function of time t; (c) power P as function of t.

and it is about 4 times smaller that the corresponding value for the SBOT of equation (6.13),

$$\varsigma^2_{\mathrm{SBOT}} = 41.2 \pm 0.6\,\mu\mathrm{m}^2 \cdot \mu\mathrm{W} \tag{6.48}$$

This indicates a higher trapping efficiency that arises from the feedback effect, which allows to trap particle with a very low mean power compared to SBOTs.

Polystyrene particles of diameter $4.97\,\mu m$

Other experiments are done with polystyrene particles of diameter $4.97\,\mu\mathrm{m}$ and the acquired dataset consists of 20 videos of 3000 frames at 10 frames per second. Trapping larger particles involves a different experimental behaviour. Indeed, the laser power $P(r_{\mathrm{exp}})$ shown in figure 6.12a is not symmetrical like for the smaller particles, figure 6.10a, suggesting that the motion of the particle with respect to the trap centre is asymmetric. Qualitatively, the particle is positioned *below* the trap centre and the trapping force pushes the particle towards it. However, the particle is so big as to turn off the laser before reaching the trap centre. Consequently, the particle starts to settle slowly with Brownian motion and, when far enough from the trap centre (some micrometers), the laser powers on trapping the particle again. This can be seen from the behaviour of the z trajectory(figure 6.12b) and of the laser power P (figure 6.12c): the particle is falling almost periodically of at most 3 μm about each $5\,\mathrm{s}$. The motion is not properly periodic due to its Brownian motion and because the laser power depends also on the x and/or y position of the particle. This explains why the particle motion in the trap is asymmetric along z and, therefore, why z_c can not be estimated. Therefore, the fit with the theoretical model can not be done.

Nevertheless, the correlation coefficient can be still evaluated and it is

$$C^{\mathrm{PS}\,4.97}_{P,r^2} \simeq 0.65 \tag{6.49}$$

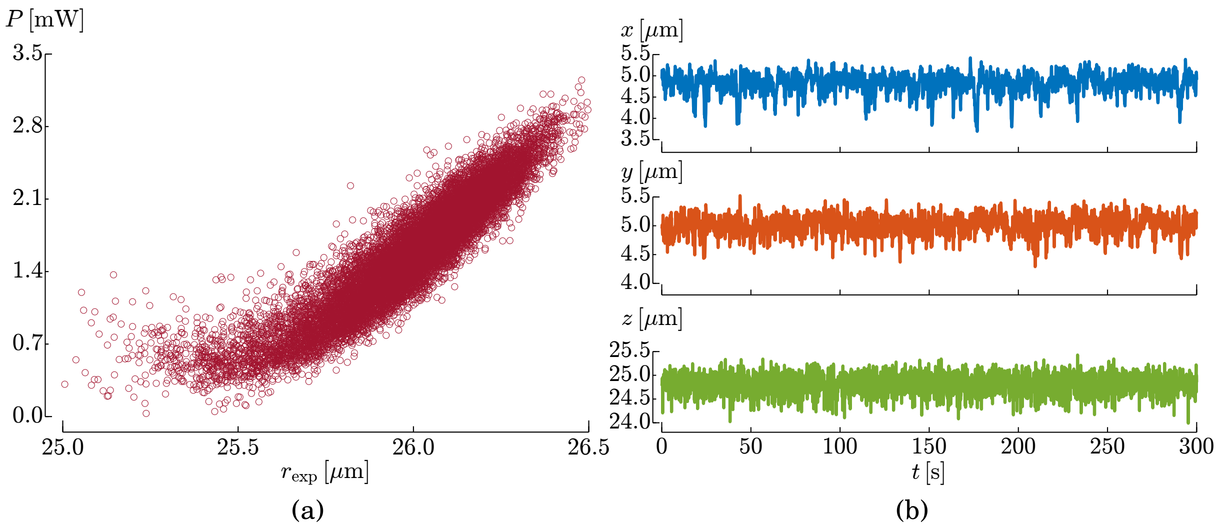

Figure 6.13: (a) optical power P as function of the particle distance r_{exp} from the experimental reference frame when trapping a $2.31\,\mu\text{m}$ diameter silica particle; (b) x, y, and z components of the particle trajectory as function of time t.

indicating a non-linear relationship between P and r. In this case, the region in which the linear relationship is expected can not be identified by using r_{on} as done for smaller particles, but observing that this region is also defined as the region in which the laser power is above the threshold P_{th}. Thus, the correlation coefficient evaluated for $P > P_{\text{th}}$ becomes:

$$C_{P,r^2}^{\text{PS}\,4.97} \simeq 0.87 \quad \text{if } P > P_{\text{th}} \tag{6.50}$$

Also $\text{Var}[r]$ can be still estimated and it is

$$\text{Var}[r] = 0.1615 \pm 0.0017\,\mu\text{m}^2 \tag{6.51}$$

while $\varsigma^2 = \text{Var}[r] \cdot \bar{P}$ is

$$\varsigma^2 = 22.3 \pm 0.4\,\mu\text{m}^2 \cdot \mu\text{W} \tag{6.52}$$

being $\bar{P} = 137.9 \pm 1.9\,\mu\text{W}$. Compared to the SBOT (equation (6.48)), ς^2 is about 2 times smaller. Therefore, the IOT is still more efficient with respect to SBOT, but its efficiency is decreased because the large size of the particle forces the laser to be powered on for longer time compared to a smaller particle.

Silica particles of diameter $2.31\,\mu m$

The last experiments are done using $2.31\mu m$ silica particles and the dataset consists of 20 videos of 1000 frames at 10 frames per second. Like for polystyrene particles of diameter $4.97\,\mu m$, the laser power P as function of r_{exp} (figure 6.13a) is not symmetrical and, in particular, the laser is always on. This can be explained observing that silica is denser than polystyrene and, for this reason, the equilibrium

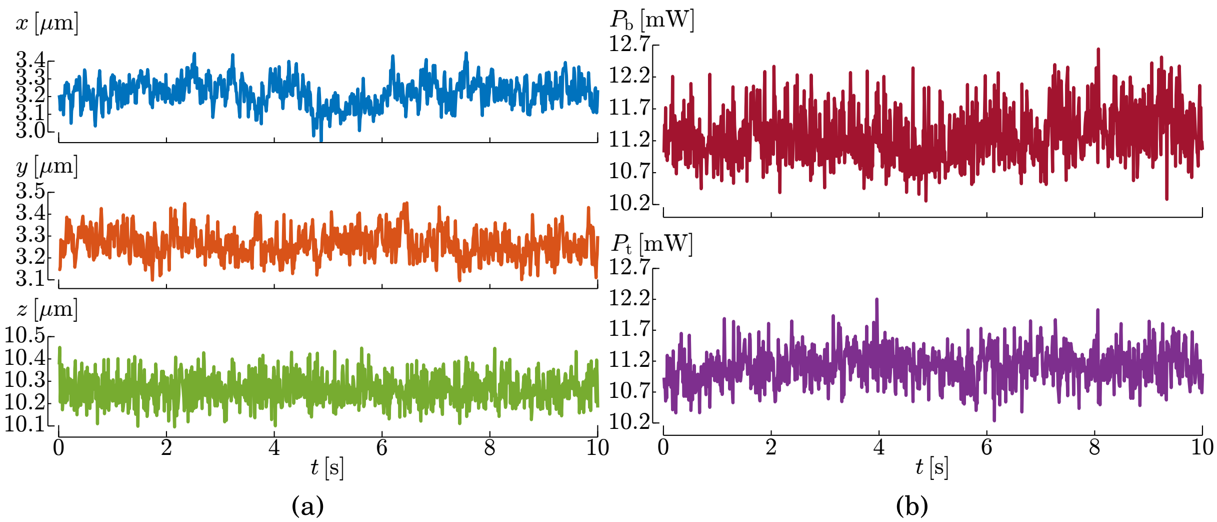

Figure 6.14: (a) x, y, and z components of the particle trajectory as function of time t and (b) optical power of the bottom beam P_b (red solid line) and of the top beam P_t (violet solid line) as function of t for a $2.31\,\mu\mathrm{m}$ diameter silica particle trapped with a double-beam intracavity optical tweezers.

position inside the trap is below the trap centre. In this position, the laser beam is larger than in the focus and the light scattered out by the particle is not sufficient to completely shut down the laser, i.e. the power never satisfies the condition $P \leq P_\mathrm{th}$. This is confirmed by the particle trajectory of figure 6.13b because, differently from the $4.97\,\mu m$ polystyrene particles, x, y, and z are oscillating around an equilibrium position (far from the particle centre) like in a standard SBOT. The feedback effect is still present and, because the laser is always on, the correlation coefficient is

$$C_{P,r^2}^{\mathrm{Si}\,2.31} \simeq 0.95 \tag{6.53}$$

without the need of any restriction on the data points. Even if the feedback effect is strongly present, this condition greatly decreases the trapping efficiency, because the mean power $\bar{P}$ is much higher than the other experiments, i.e. $\bar{P} = 1586 \pm 7\,\mu\mathrm{W}$, resulting in

$$\varsigma^2 = 71.2 \pm 1.2\,\mu\mathrm{m}^2 \cdot \mu\mathrm{W} \tag{6.54}$$

being $\mathrm{Var}[r] = (44.9 \pm 1.3 \cdot 10^{-3})\,\mu\mathrm{m}^2$. Therefore, the ς^2 is about 1.7 times greater than $\varsigma^2_\mathrm{SBOT}$ indicating that IOT is less efficient with respect to SBOT when trapping silica particles.

6.2.3 Double-beam trapping in water

By removing the optical isolator from the cavity, the IOT system traps particle with two counter-propagating beams, called *bottom beam* and *top beam*, as demonstrated in [27].

The experiment is done with silica particles of diameter $2.31\,\mu m$ with a pump power of $P_p = 75.6\,\mathrm{mW}$ and the acquired data consists of 50 videos of 1000 frames at 100 frames per second. The x, y, and z components of a typical trajectory and the relative laser power for the bottom beam, P_b, and for the top beam, P_t, are shown in figures 6.14a and 6.14b as functions of time t. The DBIOT confines the particle more than the single-beam configuration, as it can be seen from the particle trajectory: the particle oscillates around its equilibrium position by hundreds of nanometres and not by micrometers like in single-beam configuration. Quantitatively, this is confirmed by the measured variance, which is

$$\mathrm{Var}[r] = 3.9 \pm 0.4 \cdot 10^{-3}\,\mu\mathrm{m}^2 \tag{6.55}$$

i.e. about 10 times smaller than the value obtained trapping the same type of particles with the SBIOT. Thus, ς^2 is

$$\varsigma^2 = 88 \pm 8\,\mu\mathrm{m}^2 \cdot \mu\mathrm{W} \tag{6.56}$$

being the mean power inside the cavity equal to

$$\bar{P}_\mathrm{tot} = 22.4 \pm 0.4\,\mathrm{mW} \tag{6.57}$$

This inhibits the feedback effect that, as seen in single-beam configuration, arises only when the particles is far from the trap centre more than r_on. This is confirmed by the following correlation coefficients

$$\begin{cases} C_{xP_\mathrm{b}} \simeq 0.21 & C_{xP_\mathrm{t}} \simeq 0.19 \\ C_{yP_\mathrm{b}} \simeq -0.11 & C_{yP_\mathrm{t}} \simeq -0.12 \\ C_{zP_\mathrm{b}} \simeq -0.08 & C_{zP_\mathrm{t}} \simeq -0.03 \end{cases} \tag{6.58}$$

The interesting novelty of DBIOT is that the power of the two beams are correlated, being generated by the same active medium, unlike in standard counter-propagating optical tweezers. Therefore, the particle is trapped in the position that makes the two beams of equal power, which is the fundamental condition in counter-propagating optical tweezers for trapping. In this experiment, the correlation can be seen from the behaviour of P_b as function of P_t, figure 6.15a. Indeed, P_b and P_t change their power in an anti-correlated way when the particle tries to escape from the trap. This happens rarely (only few times in all the dataset) and figure 6.15b shows the power behaviour of the two beams when the particle moves more than some hundreds of nanometres from the equilibrium position.

This slight anti-correlation is also confirmed by the correlation coefficient

$$C_{P_\mathrm{b}P_\mathrm{t}} =\simeq -0.40 \tag{6.59}$$

In addition, the top beam, which travels in the same direction of the gravity, has a mean power $\bar{P}_\mathrm{t}$ slightly smaller than the bottom beam, which travels in the opposite

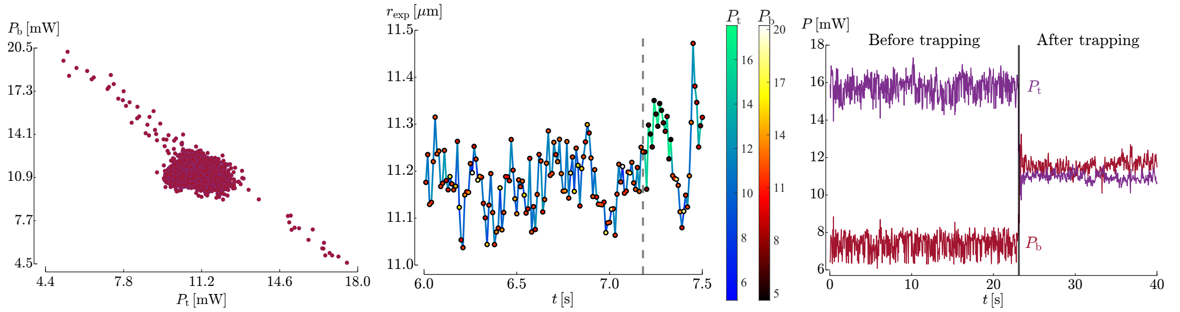

(a) (b) (c)

Figure 6.15: (a) optical power of the bottom beam P_b as function of the optical power of the top beam P_t; (b) distance r_exp of the particle from the centre of the experimental reference frame as function of time t when a particle tries to escape from the trap (dashed grey line $t \simeq 7.18\,\mathrm{s}$). The solid line changes its colour according to the power of the top beam P_t while the markers changes their face colour according to the power of the bottom beam P_b; (c) power of the top beam P_t (red solid line) and of the bottom beam P_b (violet solid line) as functions of time t before ($t \lesssim 23.1\,\mathrm{s}$) and after ($t \gtrsim 23.1\,\mathrm{s}$) trapping a particle.

direction, and both of them have a mean power that differs from their power when no particle is inside the cavity, $\bar{P}_\mathrm{no,t}$ and $\bar{P}_\mathrm{no,b}$, which are

$$\begin{cases} \bar{P}_\mathrm{no,t} \simeq 14.2\,\mathrm{mW} \\ \bar{P}_\mathrm{no,b} \simeq 7.4\,\mathrm{mW} \end{cases} \tag{6.60}$$

Instead, with a trapped particle, $\bar{P}_\mathrm{t}$ and $\bar{P}_\mathrm{b}$ are c

$$\begin{cases} \bar{P}_\mathrm{t} = 11.0 \pm 0.3\,\mathrm{mW} \\ \bar{P}_\mathrm{b} = 11.4 \pm 0.3\,\mathrm{mW} \end{cases} \tag{6.61}$$

i.e. the top beam is suppressed by the presence of the particle while the bottom beam is enhanced. This is confirmed by measuring these powers during a trapping event, as figure 6.15c shows.

Other experiments are performed using $2.82\,\mu\mathrm{m}$ diameter polystyrene particles acquiring 50 videos of 1000 frames at 100 frames per second. The x, y, and z components of a typical trajectory and the relative laser powers P_b and P_t, are shown in figures 6.16a and 6.16b. In this case the measured variance is

$$\mathrm{Var}[r] = 1.26 \pm 0.15 \cdot 10^{-3}\,\mu\mathrm{m}^2 \tag{6.62}$$

and $\varrho^2 = 29 \pm 3\,\mu\mathrm{m}^2 \cdot \mu\mathrm{W}$, being the mean power $\bar{P}_\mathrm{tot} = 23 \pm 0.2\,\mathrm{mW}$. As for the silica particle, the mean power of the two beams changes after trapping in a similar way being

$$\begin{cases} \bar{P}_\mathrm{b} = 11.3 \pm 0.12\,\mathrm{mW} \\ \bar{P}_\mathrm{t} = 11.2 \pm 0.16\,\mathrm{mW} \end{cases} \tag{6.63}$$

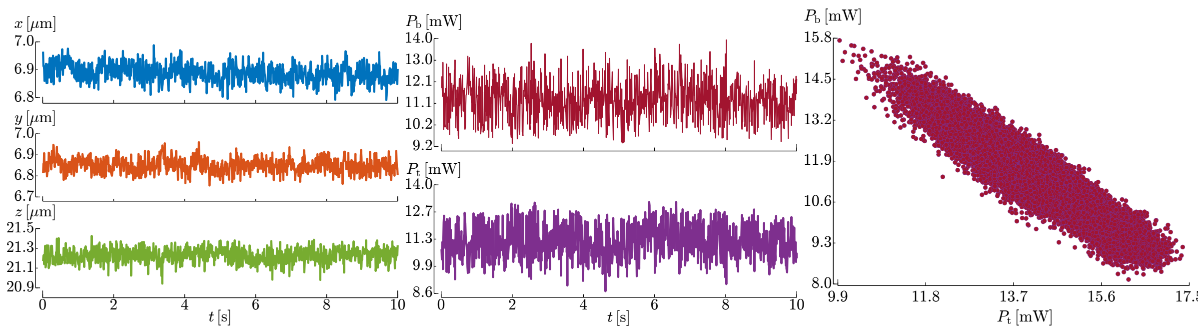

(a) (b) (c)

Figure 6.16: (a) x, y, and z components of the particle trajectory as functions of time t; (b) optical power of the bottom beam P_{b} (red solid line) and of the top beam P_{t} (violet solid line) as functions of t for a $2.82\,\mu\mathrm{m}$ diameter polystyrene particle trapped with a double-beam intracavity optical tweezers; (c) P_{b} as function of P_{t}.

The main difference with the previous case is that the power of the two beams is strongly anti-correlated being

$$C_{P_{\mathrm{b}}P_{\mathrm{t}}} = \simeq -0.98 \tag{6.64}$$

and this is also confirmed by the behaviour of P_{b} as function of P_{t} as figure 6.16c. This arises because this type of particles move along the z axis more than the silica ones (but less along x and y), see figure 6.16a, so as to involve the feedback effect. This larger motion of polystyrene can be explained observing that polystyrene scatters more light than silica (higher refractive index, $n_{PS} \simeq 1.59 > n_{Si} \simeq 1.42$) causing higher losses in the cavity and lowering the trap stiffness when the particle is in its equilibrium position.

In conclusion, the feedback effect of the DBIOT is fundamental to trap the particle, even if, during the trapping of silica particles, it is almost completely inhibited by the strong confinement of the particle. Indeed, it adjusts intrinsically and automatically the power of the two beams to be similar, so that the scattering forces of the two beams cancel each other out when the particle is in the trapping position, as figure 6.15c shows, allowing de facto the trapping itself.

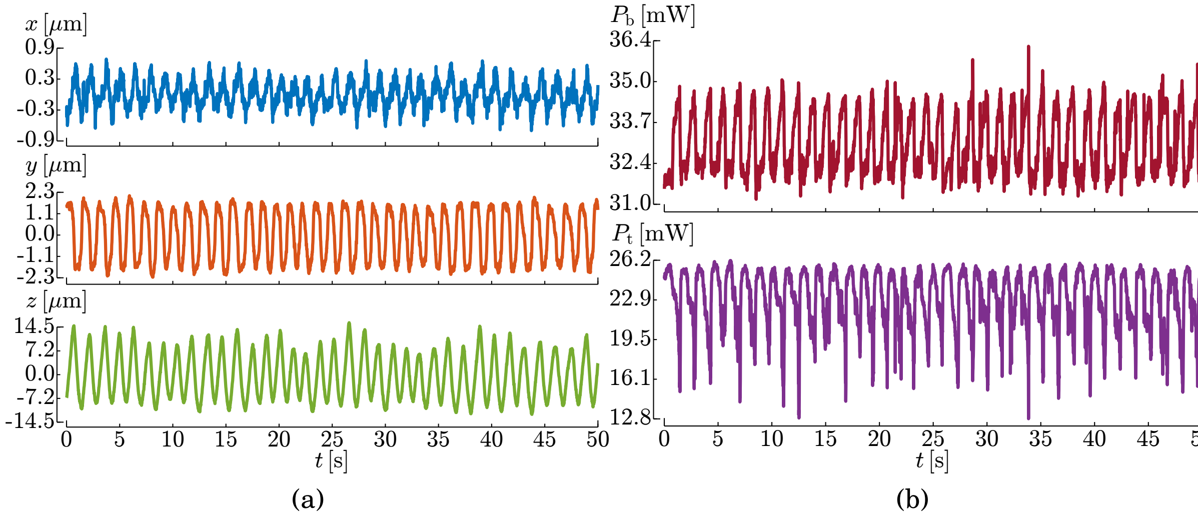

Figure 6.17: (a) x, y, and z components of the particle trajectory and (b) its corresponding power P as function of time t for a $2.82\,\mu\mathrm{m}$ polystyrene particle trapped with two slightly misaligned beams and considering only the first $50\,\mathrm{s}$ of the acquired data.

6.2.4 Double-trap

In double-beam configuration, two close optical traps can be produced if the two counter-propagating beams are slightly misaligned. In this experiment, the misalignment is produced by translating one of the two trapping objective lenses by only few micrometers along one direction (*misalignment distance*), assuring that the laser cavity is still closed and, therefore, the laser effect is still present. In this way, the two optical traps compete to capture the particle, producing two metastable states between which the particle transits. These transitions are mainly characterised by the feedback effect and, therefore, differ substantially from thermal *Kramers' transitions*.

Experimentally, polystyrene particles with diameter $2.82\,\mu m$ are trapped in this configuration changing the misalignment distance d_{mis} along the y direction, so that the top beam centre is shifted in the video frames to the left with respect to the bottom one. The phenomenon is studied parametrically by changing d_{mis} and the pump power P_p. For each value of d_{mis} and P_p, 10 videos of 10000 frames at 100 frames per second are acquired. The components of the trajectories, measured by means of the $3\mathrm{D}$ holographic tracking, are shifted so that their average value is zero, so that the bottom beam centre is located at positive y values and the top one at negative y values.

A typical trajectory of a trapped particle is shown in figure 6.17a for $d_{\mathrm{mis}} \simeq 4\mu m$ and $P_p = 174.9\,\mathrm{mW}$, while the power of the bottom beam P_{b} and the top one P_{t} are shown in figure 6.17b as functions of the time. Figure 6.17a shows that this phenomenon is different from the Kramers' transitions, which are random

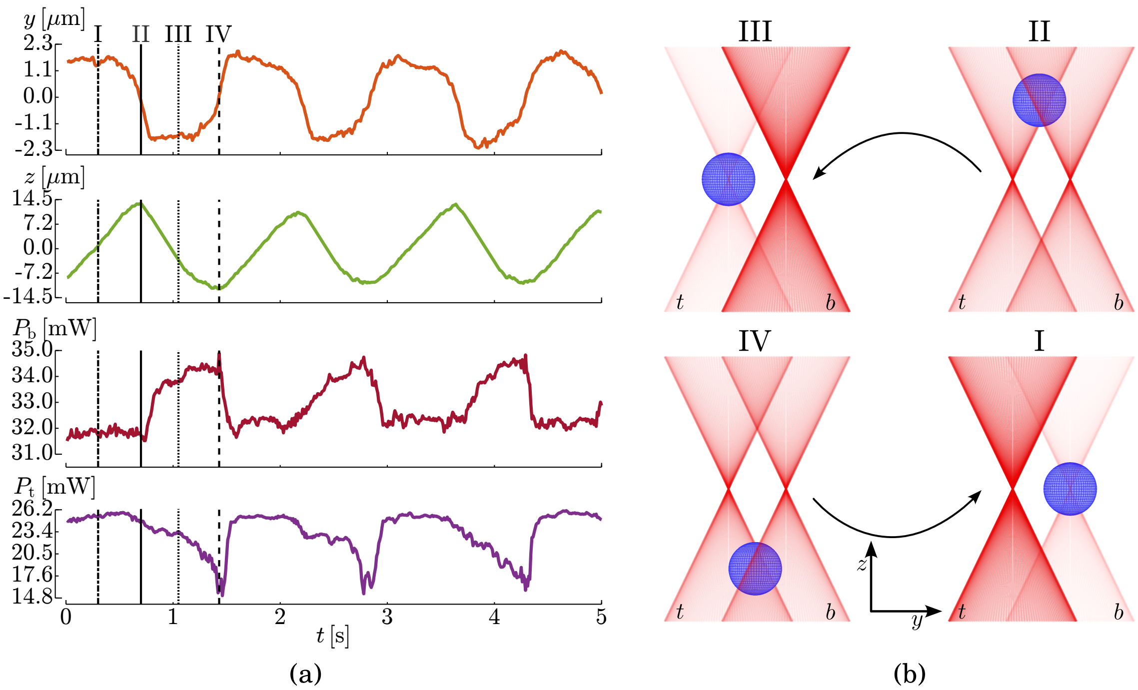

Figure 6.18: (a) y and z component of the particle trajectory, P_b, and P_t as functions of time t ; (b) sketch of the four positions configuration where the transparency of the beams changes according to their laser power.

transitions, being the coordinates of the particle trajectory regular and periodic. In addition, the peak-peak amplitude of the oscillations along the y is comparable to d_{mis} ($\sim 4\,\mu$m), the one along z is larger than along y ($\sim 28\,\mu$m), while along x is less than $1\,\mu$m. In other words, the particle motion happens principally in the y-z plane. In addition, during the transitions from the bottom beam to the top one, the laser power of the two beams changes according to the particle position as shown in figure 6.17b. Indeed, the power of the bottom beam P_{b} is low when the particle is in the bottom beam centre, while the power of the top one P_{t} is high and vice versa.

To well describe how the laser power of the two beams changes, it is useful to study only few seconds of the particle trajectory referring in particular to figures 6.18a and 6.18b. In position I, the particle is located in the bottom beam ($y \simeq +2\,\mu$m and $z \simeq 0\,\mu$m) that tends to push the particle upwards, but it is depleted by the particle scattering. Consequently, its power P_b is minimum while the top beam power P_t is maximum.

Therefore, the particle begins to be trapped by the top beam passing thorough the position II ($y \simeq -\,\mu$m and $z \simeq 0\,\mu$m), while P_b increases and P_t decreases. From position II, the particle transits to the top beam pushed downwards (position III, $y \simeq -2\,\mu$m and $z \simeq 0\,\mu$m), while P_t continues to decrease due to the scattering of the particle and P_b increases. Finally, the particle transits to position IV ($y \simeq -\,\mu$m and $z \simeq 0\,\mu$m) faster than the transition I-II because the particle is pushed downwards

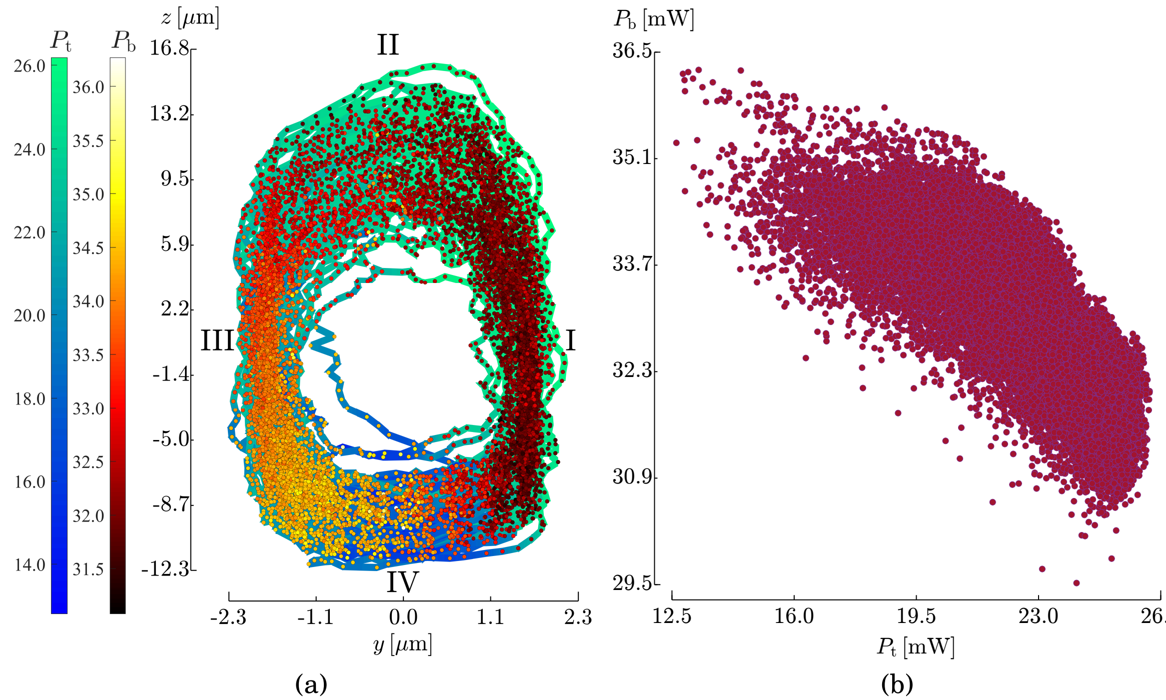

Figure 6.19: (a) z component of the particle trajectory as function of its y component. The solid line changes its colour according to the power of the top beam P_t and the markers change their face colour according to the power of the bottom beam P_b; (b) bottom beam power P_b as function of the top beam power P_t.

by the scattering force of the top beam and, also, the gravity. In position IV, P_t is minimum and P_b is maximum and the particle is trapped again by the bottom beam starting a new cycle. This behaviour can also be visualised in figure 6.19a, which shows the y-z trajectory of the particle whose colours that change according to the power of the two beams.

The strong dependency between the particle position and the laser power of the two beams is measured with the correlation coefficients, that are

$$\begin{cases} C_{yP_\mathrm{b}} = -0.79 \pm 0.013 & C_{yP_\mathrm{t}} = 0.608 \pm 0.008 \\ C_{zP_\mathrm{b}} = -0.301 \pm 0.007 & C_{zP_\mathrm{t}} = 0.454 \pm 0.011 \end{cases} \tag{6.65}$$

showing that the two beams are correlated mainly with the y position of the particle, as described before. Similarly, the power of the two beams is strongly anti-correlated being

$$C_{P_\mathrm{b}P_\mathrm{t}} = -0.864 \pm 0.012 \tag{6.66}$$

as shown also by the behaviour of P_b as function of P_t, figure 6.19b. This demonstrates that the particle is acts like a *micro-isolator*, which suppresses the laser beam in which is trapped enhancing the other beam.

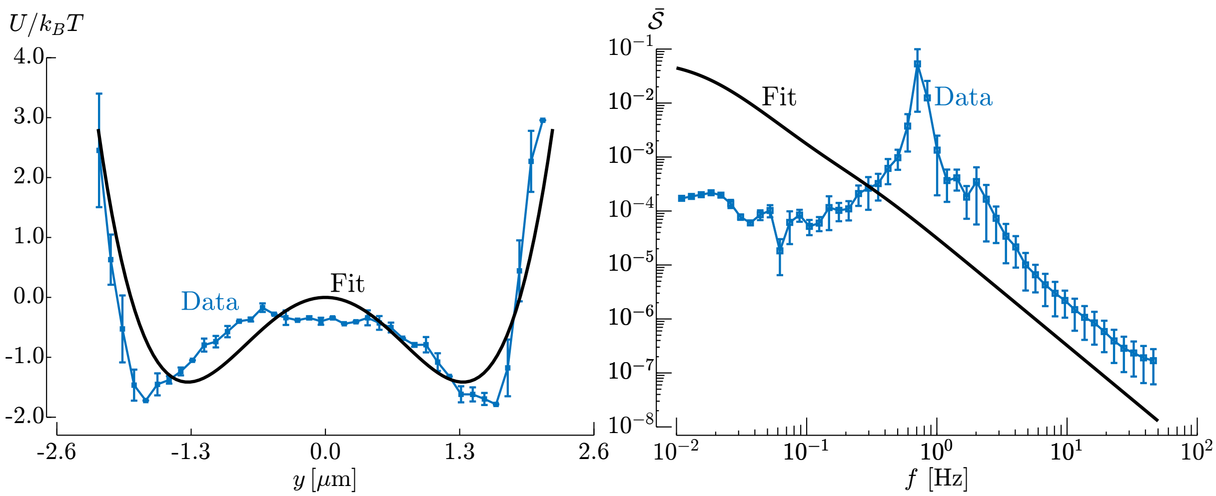

(a) (b)

Figure 6.20: (a) experimental potential U as function of y (blue squares) and its best fit function (black solid line) assuming that the potential is a double-well potential; (b) normalised PSD, $\bar{\mathcal{S}}$, as function of the frequency f (blue squares) and the PSD relative to the double-well potential $\bar{\mathcal{S}}_{\mathrm{DW}}$ as function of f (black solid line).

This process remembers the thermal activated Kramers' transitions, that are characterised by a double-well potential. As said, the dynamics of Kramers' thermal transitions totally differ from those observed in this experiment. In fact, thermal transitions from one trap to another occur stochastically, while in a double-trap intracavity, the interconnection between the powers of the two beams and the particle position causes regular transitions. However, to further highlight these differences, the experimental potential is extrapolated following the procedure described in chapter 5.2.3. The potential is not properly a double-well potential, figure 6.20a, mainly because it is the temporal average of the instantaneous potentials produced by the two beams being their power changing in time. Nevertheless, to numerically show that this transitions are not thermal activated because of the feedback effect, the potential is assumed to be a double-well potential in order to fit it with the theoretical expression of equation (2.68), which gives

$$\begin{cases} U(y) = \dfrac{a_{\mathrm{exp}}}{4} y^4 - \dfrac{b_{\mathrm{exp}}}{3} y^3 - \dfrac{c_{\mathrm{exp}}}{2} y^2 + d_{\mathrm{exp}} \\ a_{\mathrm{exp}} = 1.8 \pm 0.3 \, \dfrac{k_B T}{\mu\mathrm{m}^4} \\ b_{\mathrm{exp}} = (2.46 \pm 0.14) \cdot 10^{-8} \, \dfrac{k_B T}{\mu\mathrm{m}^3} \\ c_{\mathrm{exp}} = 3.2 \pm 0.4 \, \dfrac{k_B T}{\mu\mathrm{m}^2} \\ d_{\mathrm{exp}} = 2.32 \pm 0.05 \, k_B T \end{cases} \tag{6.67}$$

shown as solid line in figure 6.20a. From this best fit, the physical quantities predicted by Kramers' theory are compared with the experimental ones. It is important to observe that, practically, the potential has $b = 0$ and, therefore, all the results of chapter 2.3 can be used being the potential symmetric.

The physical quantities to compare are the transition times, which are defined by equation (2.71) according to Kramers' theory. Using the best fit potential parameters obtained before, they are

$$\begin{cases} T_{+} = 26 \pm 2\,\mathrm{s} \\ T_{-} = 26 \pm 2\,\mathrm{s} \end{cases} \tag{6.68}$$

Instead, the experimental transition times [4] are

$$\begin{cases} T_{+,\mathrm{exp}} = 0.70 \pm 0.06\,\mathrm{s} \\ T_{-,\mathrm{exp}} = 0.69 \pm 0.06\,\mathrm{s} \end{cases} \tag{6.69}$$

Therefore, the experimental values are completely different from the values predicted by Kramers' theory, confirming that this transition are not thermally activated, but feedback activated.

Another quantity that confirms this hypothesis is the normalised power spectral density $\mathcal{S}$, that, for a double-well potential with $b = 0$, is given by the sum of two Lorentzian curves as shown in equation (2.79), i.e.

$$\begin{cases} \bar{\mathcal{S}}_{\mathrm{DW}}(\omega) = \dfrac{\Delta_1 \lambda_1}{\lambda_1^2 + \omega^2} + (1 - \Delta_1)\dfrac{\tau_W}{1 + \tau_W^2 \omega^2} \\ \Delta_1 \simeq 0.93 \\ \lambda_1 \simeq 0.097\,\mathrm{Hz} \\ \tau_W = 0.67\,\mathrm{s} \end{cases} \tag{6.70}$$

where λ_1, Δ_1, and τ_W are numerically evaluated with equations (2.74), (2.75), (2.76), and (2.77) using the best fit potential parameters. To compare the experimental $\mathcal{S}$ with the theoretical one, they are normalised and plotted in figure 6.20b. The experimental $\mathcal{S}$ does not follow the theoretical expression and, in particular, is characterised by a large peak for $f \simeq 0.71\,\mathrm{Hz}$ that corresponds to the period of the y component of the trajectory. The presence of only one peak in this function confirms that the transition rates between the two beams is the same. Therefore, the transition time can be also estimated by

$$T_{\pm,\mathrm{exp}} = \frac{1}{2f} \simeq 0.7\,\mathrm{s} \tag{6.71}$$

that confirms the previous estimates.

[4] The transition times are measured as the difference between the local maxima and the local minima of the y component of the trajectory

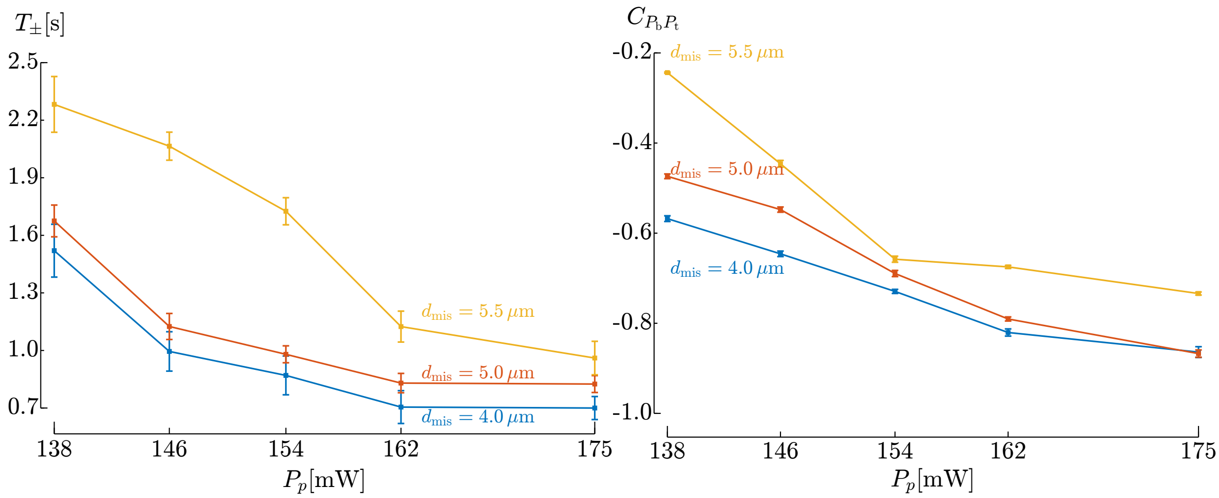

(a) (b)

Figure 6.21: (a) transition times $T_{\pm}$ and (b) correlation coefficient $C_{P_{\rm b}P_{\rm t}}$ as functions of the pump power P_p for different misalignment distances $d_{\rm mis}$.

To conclude this section, the behaviour of this periodic motion is studied for several values of $d_{\rm mis}$ and P_p, analysing the transition times $T_{\pm}$ and the correlation coefficient $C_{P_{\rm b}P_{\rm t}}$. The transition times $T_{\pm,\rm exp}$ increase as the pump power P_p decreases (figure 6.21a) because, when P_p increases, the trapping force of the two beams is higher and the particle is trapped quickly. Moreover, $T_{\pm,\rm exp}$ increase as $d_{\rm mis}$ increases, because the particle needs to move more to enter in the beam centre.

Similarly, $C_{P_{\rm b}P_{\rm t}}$ increases as the pump power P_p decreases: when the laser effect is weak because of a low pump power P_p, the micro-isolator effect is almost ineffective reducing substantially the anti-correlation. For the same reason, the correlation $C_{P_{\rm b}P_{\rm t}}$ increases as the distance $d_{\rm mis}$ decreases because high misalignment implies higher losses being the laser power of the two beams not properly reinjected in the active medium. The behaviour of $C_{P_{\rm b}P_{\rm t}}$ as functions of P_p for each $d_{\rm mis}$ is shown in figure 6.21b.

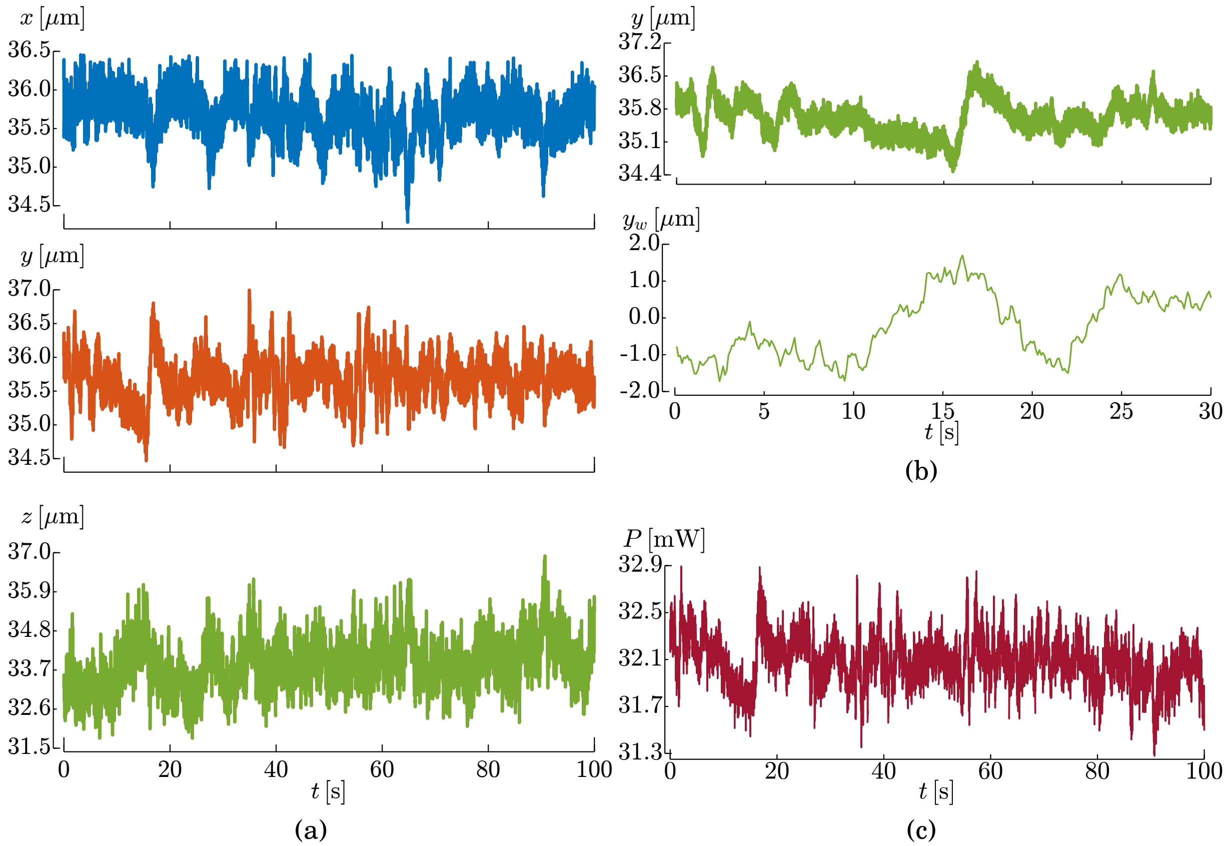

Figure 6.22: (a) x, y, and z components of the particle trajectory as functions of the time t for a $4.80\,\mu\mathrm{m}$ diameter silica particle trapped with a single-beam intracavity optical tweezers in air; (b) zoom of the y component as function of t and y_w component for a particle trapped in water with the same system; (c) optical power of the trapping beam P as function of t.

6.2.5 Intracavity trapping in air

In the last part of this work, the IOT is used in single-beam configuration to trap particles in air using the loading system described in chapter 4.4. As said before, particles in air are characterised by relaxation times ($\sim 50\,\mu\mathrm{s}$) greater than in water ($\sim 1\,\mu\mathrm{s}$) that make the inertial effects not negligible. Therefore, particles trapped in air are affected by strong and almost instantaneous changes in momentum, which are suppressed by the fluid's viscosity in the case of particles trapped in water. To deal with these sudden accelerations, the dataset is acquired at $500\,\mathrm{fps}$ and it consists of 10 videos of 50000 frames of a silica $4.80\,\mu\mathrm{m}$ particle is trapped using a pump power of $P_p = 124.5\,\mathrm{mW}$.

A typical time evolution of the x, y and z coordinates of a particle trapped by IOT in air is shown in figure 6.22a, which has structured fluctuations unlike the one obtained trapping with conventional optical trap in air (see figure 6.4b). Figure 6.22b shows that the particle along the y direction moves by $3\,\mu\mathrm{m}$ in $\sim 1.5\,\mathrm{s}$, while in

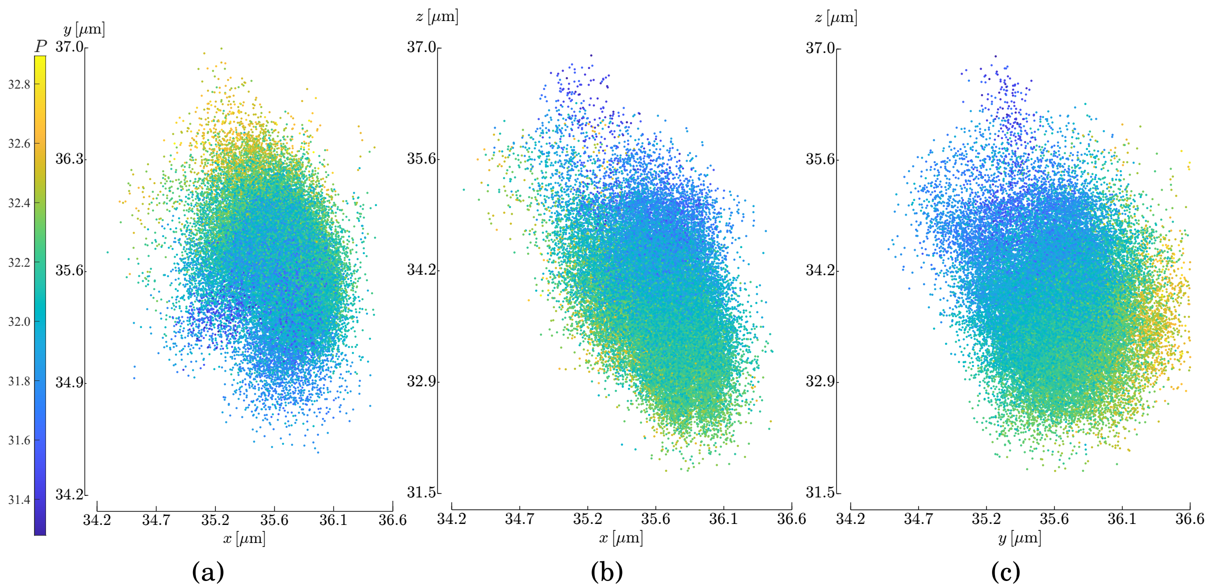

Figure 6.23: trajectory of the particle in (a) x-y, (b) x-z, and (c) y-z plane for a $4.80\,\mu\text{m}$ diameter silica particle trapped in air with a SBIOT. The dots change their colour according to the laser power P.

water the coordinate y_m varies by $3\,\mu\text{m}$ in $\sim 7\,\text{s}$. This behaviour indicates that, even in air, the particle is trapped thanks to the optical feedback mechanisms observed trapping in water. Indeed, the time-dependent laser power shown in figure 6.22c confirms the correlation between the particle position and the laser power.

Despite these similarities with trapping in water, a major difference is that the buoyancy is negligible in air (air density is 1000 times less than that of water) and, therefore, the particle falls downwards rapidly when the laser power decreases making all the dynamics faster. Indeed, when the particle is close to the trapping position the scattering losses increase leading to a decrease of the beam power. Therefore, the particle falls along the beam direction due to gravity, moving away from the trapping position. Hence, the scattering losses decrease and the laser power increases pulling again the particle close to the trapping position. This explains why the particle trajectory is characterised by oscillations, which are also influenced by the Brownian motion of the particle, and indicates that the dynamics is mainly determined by the z position of the particle. To visualise this behaviour, the particle position in the planes x-y, x-z, and y-z are shown taking into account the laser power P variations. Figures 6.23a, 6.23b, and 6.23c show that the beam power increases when the particle is at low z-values (measured from the imaging plane located above the trap centre) and decreases when z increases, which indicates that the particle fluctuates below the trap centre. In addition, the laser power increases when the y component (measured from the bottom left edge of frame) has high values indicating a small tilt of the optical axis of the imaging system with respect to the direction of the laser beam.

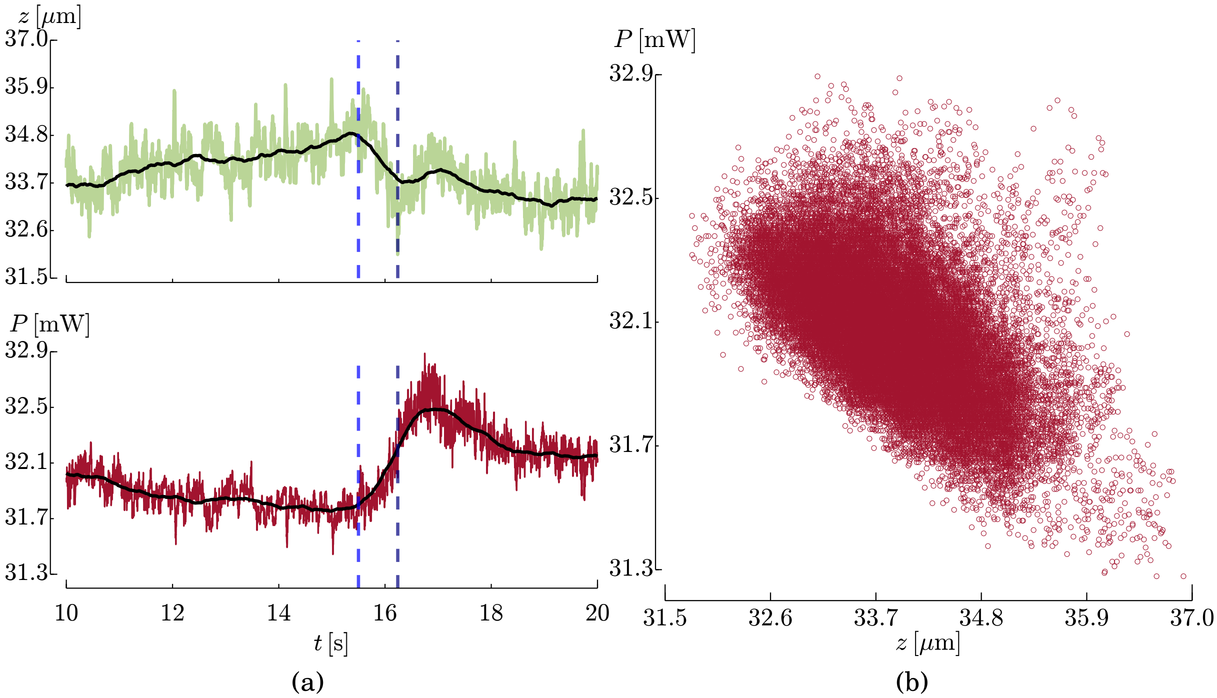

Figure 6.24: (a) z components of the particle trajectory and laser power P as functions of time t with their corresponding moving mean curves (black solid line); (b) optical power of the trapping beam P as function of z for a $4.80\,\mu\text{m}$ diameter silica particle trapped in air with the single-beam intracavity optical tweezers.

To clarify the correlation between the z position of the particle and the laser power, the 10 seconds interval of the z position and the laser power P shown in figure 6.24a is analysed. Due to the presence of Brownian motion, the trend of the z position and the power P of figure 6.24a are extrapolated applying a moving mean procedure (solid black lines). In figure 6.24a, the particle is initially attracted by the trap along z towards its centre: the z component increases slowly, while the laser power decreases. Then, at about $15.5\,\text{s}$, the laser power becomes insufficient to trap the particle, which falls very rapidly moving about $2\,\mu\text{m}$ in about $1\,\text{s}$. Consequently, the laser power increases just as quickly and the trapping force is again able to trap the particle. Since the viscosity of air is low, the trapping is very fast pushing suddenly the particle towards the trap centre and, after $1\,\text{s}$, the particle is in a new position that inhibits the laser beam and, so, it starts to fall again. This behaviour of the particle trajectory occurs throughout the optical trapping and it confirms the presence of the feedback effect, which is also confirmed by the correlation coefficient between the power P and the z position, that is

$$C_{zP_{\text{b}}} = -0.77 \pm 0.01 \tag{6.72}$$

and also by the behaviour of P as function of z of figure 6.24b.

This behaviour of the IOT in air explains why the variance of the particle trajectory is higher than in water, i.e.

$$\mathrm{Var}[r] = 0.225 \pm 0.013\,\mu\mathrm{m}^2 \tag{6.73}$$

while the mean power $\bar{P}$ is

$$\bar{P} = 32.2 \pm 1.2\,\mathrm{mW} \tag{6.74}$$

being the laser always on, like trapping silica particles with IOT in water. This decreases the trap efficiency being

$$\varsigma^2 = 7.2 \pm 0.5\,\mu\mathrm{m}^2 \cdot \mathrm{mW} \tag{6.75}$$

which indicates this system is less efficient than standard optical tweezers when particles are trapped in air.

Conclusions

In this thesis, *intracavity optical tweezers* (IOT) are realised using a ring cavity Yb^{3+} fibre laser. The experimental setup here proposed allows to trap particles in single-beam configuration (SBIOT) and in double counter-propagating beams configuration (DBIOT). The switch between these two configuration is obtained by means of a removable optical isolator in the laser cavity.

The experiments done by trapping particles in water with the SBIOT demonstrate the presence of a non-linear *intrinsic feedback effect*, which improves the trapping efficiency with respect to that of a standard optical tweezers (OT). However, the efficiency of SBIOT decreases as the diameter and density of the particle increase, because of the effects that these parameters have on the trapping dynamics. For this reason, three different types of particles have been studied: polystyrene particle of diameter $1.98\,\mu\mathrm{m}$ and $4.97\,\mu\mathrm{m}$, and silica particle of diameter $2.31\,\mu\mathrm{m}$. When a polystyrene particle of diameter $1.98\,\mu\mathrm{m}$ is trapped, its trajectory is isotropic around the trap centre and the laser power increases quadratically with the displacement of the particle from this position. Moreover, when the particle is close enough to the centre, the laser power is almost zero as predicted by the toy model. In addition, this experiment demonstrates that the modified toy model predicts the variance of the trajectory of the particle better than the original toy model.
On the contrary, the experiments done with polystyrene particles of diameter $4.97\,\mu\mathrm{m}$ show a different laser-particle dynamics. The particle is pulled by laser towards the centre of the trap. However, the large scattering losses due to the particle size turns off the laser before the particle reaches the trap centre explaining why the particle remains mainly above this position. This implies that, unlike for smaller particles, the trap centre can not be estimated and, consequently, the toy model can not be applied being it formulated in terms of the distance of the particle from the trap centre. Although the feedback effect is reduced, it still makes the SBIOT more efficient than a similar conventional trap, but less than for smaller particles like the previous case.
Similarly, silica particles (diameter $2.31\,\mu\mathrm{m}$) mainly remain above the trap centre, but due to their larger density. The equilibrium position is located in such a way that the particle never switches off the laser, reducing the feedback effect and therefore the trapping efficiency.

Regarding the DBIOT, the trapped particle is much more confined than the case of SBIOT and, consequently, the feedback effect is practically negligible. Nevertheless, the study of the dynamics of particle loading shows that the feedback effect is still fundamental in the trapping mechanism and that the laser powers of the two beams are anti-correlated. Indeed, the powers of the two beams adjust automatically to be very similar to each other when the particle enters the trap, so that the scattering forces of the two beams cancel each other out guaranteeing the trapping condition.

The DBIOT is also used to produce two close optical traps by slightly misaligning the two beams along one direction. The trapped particle exhibits periodic transitions between the two traps characterised by the feedback effect. Indeed, the laser power of the two beams changes periodically as the particle trajectory. Therefore, the particle acts as a *micro-isolator* that suppresses the beam in which it is trapped enhancing the other beam thanks to their anti-correlation interconnection. These transitions are then feedback activated as also confirmed by the comparison with Kramers' theory, in particular comparing the experimental transitions times with the Kramers' one. Finally, this phenomenon has been studied parametrically changing the misalignment distance and the laser pump power. The transition times increase as the pump power decreases: indeed, when the pump power increases, the trapping force of the two beams is higher and the particle is trapped quickly. Similarly, the anti-correlation between the two beams vanishes as the pump power decreases: when the laser effect is weak because of a low pump power, the micro-isolator effect is almost ineffective thereby reducing substantially the anti-correlation of the two beams.

Then, the SBIOT is used for trapping in air. Trapping in air is not trivial because particles do not float like in water, but they are stuck on the chamber wall due to the van der Waals force. To push the particle in the trap centre, a special system based on a piezoelectric transducer is developed for this thesis, which detaches the particles by vibrating the chamber wall. To fine tune the loading system, a standard single-beam optical tweezers is used to trap particles in air, from which inertial effects on the particle motion are observed.

After this preliminary step, SBIOT is used to trap particles in air. Due to inertial effects and a negligible buoyancy, the particle is characterised by faster dynamics than in water. When the particle is near the trap centre, the laser power is low (due to scattering losses) and the particle falls along the beam direction faster than in water. Hence, the laser power increases pulling again the particle close to the trapping position producing oscillations in the particle motion that are totally absent when trapping with a standard optical tweezers. In addition, the particle never powers off the laser reducing the IOT efficiency.

This work demonstrates that is possible to use IOT to trap particles in air keeping the intrinsic feedback effect. In these conditions, the laser is always in its steady-state because the timescale for the displacement of the particle (milliseconds) is much greater than the response time of the laser (nanoseconds). In vacuum, on the other hand, these timescales are comparable and, therefore, the feedback dynamics changes completely, also leading to possible chaotic effects. Future experiments about IOT trapping in vacuum, therefore, will lead to more intriguing physics, such as the study of chaotic effects and, thanks to the feedback effect, the cooling of the trapped particles with the consequent possibility of observing quantum effects on mesoscale.

Appendix A

Mie theory

To give an explicit expression of the optical force in the intermediate regime, it is necessary to use the multipole expansion and the Mie theory, named after the German physicist Gustav Mie [68], which provides an analytical solution for the scattering problem of an electromagnetic wave on a sphere or cylinder. In this discussion, it is essential to use the Helmholtz equation for the electric field (similarly for the magnetic field)

$$\left(\nabla^2 + k^2\right)\vec{\mathscr{E}}(\vec{r}) = 0 \tag{A.1}$$

whose general solution is given ([31], chapter 5.2.3), for the case of a field regular in the origin of the reference system[1], by the following multipole expansion:

$$\vec{E}_i(\vec{r}) = E_i \sum_{p=1,2} \sum_{l=0}^{\infty} \sum_{m=-l}^{l} W_{i,lm}^{(p)} \vec{J}_{lm}^{(p)}(kr, \hat{r}) \tag{A.2}$$

where:

- $E = \left|\vec{E}\right|$;
- the superscript $p = 1$ ($p = 2$) refers to the multipolar components of the magnetic (electric) kind;
- the vectors $\vec{J}_{lm}^{(j)}(kr, \hat{r})$ are

$$\begin{cases} \vec{J}_{lm}^{(1)}(kr, \hat{r}) = j_l(kr)\vec{Z}_{lm}^{(1)}(\hat{r}) \\ \vec{J}_{lm}^{(2)}(kr, \hat{r}) = i\dfrac{\sqrt{l(l+1)}}{kr} j_l(kr)\vec{Y}_{lm}(\hat{r}) - \dfrac{1}{kr}\left[j_l(kr) + r\dfrac{dj_l}{dr}(kr)\right]\vec{Z}_{lm}^{(2)}(\hat{r}) \end{cases} \tag{A.3}$$

  where $j_l(kr)$ indicates a spherical Bessel function, and $\vec{Y}_{lm}(\hat{r})$ and $\vec{Z}_{lm}^{(1,2)}(\hat{r})$ indicate the *radial* and the *transversal* vector spherical harmonics, defined

[1] The field is supposed to be regular in the centre of the reference frame, which is chosen coincident with the centre of the sphere.

respectively as ([31], chapter 5.2.3):

$$\vec{Y}_{lm} = Y_{lm}\vec{\boldsymbol{r}} \tag{A.4}$$

$$\vec{Z}^{(1)}_{lm} = -\frac{i}{\sqrt{l(l+1)}}\vec{\boldsymbol{r}} \wedge \vec{\nabla} Y_{lm} \tag{A.5}$$

$$\vec{Z}^{(2)}_{lm} = -\vec{Z}^{(1)}_{lm} \wedge \vec{\boldsymbol{r}} \tag{A.6}$$

if Y_{lm} is a *spherical harmonic* ([31], chapter 5.2.1);

- $W^{p}_{i,lm}$ is a numerical coefficient ([31], chapter 5.2).

Instead, the general solution of equation (A.1) for a field satisfying the radiation condition at infinity, i.e. the scattered electric field by the particle, is

$$\vec{E}_s(\vec{r}) = E_s \sum_{p=1,2} \sum_{l=0}^{\infty} \sum_{m=-l}^{l} A^{(p)}_{s,lm} \vec{H}^{(p)}_{lm}(kr, \vec{\boldsymbol{r}}) \tag{A.7}$$

where $A^{(p)}_{s,lm}$ is a numerical coefficient and

$$\begin{cases} \vec{H}^{(1)}_{lm}(kr, \vec{\boldsymbol{r}}) = h_l(kr)\vec{Z}^{(1)}_{lm}(\vec{\boldsymbol{r}}) \\ \vec{H}^{(2)}_{lm}(kr, \vec{\boldsymbol{r}}) = i\frac{\sqrt{l(l+1)}}{kr} h_l(kr)\vec{Y}_{lm}(\vec{\boldsymbol{r}}) - \frac{1}{kr}\left[h_l(kr) + r\frac{dh_l}{dr}(kr)\right]\vec{Z}^{(2)}_{lm}(\vec{\boldsymbol{r}}) \end{cases} \tag{A.8}$$

and $h_l(kr)$ spherical Hankel functions of the first kind.

Equations (A.2) and (A.7), indeed, allow to derive the phasor of equation (1.48), which by exploiting the superposition principle is

$$\vec{E} = \vec{E}_i + \vec{E}_s \tag{A.9}$$

being the total electric field $\vec{\mathscr{E}}$ the sum of the incident field, $\vec{\mathscr{E}}_i$, and of the scattered one, $\vec{\mathscr{E}}_s$ (similarly for the magnetic field). These two phasor, $\vec{E}_i$ and $\vec{E}_s$ in far field condition, using the asymptotic behaviour of the Bessel functions, are (the same for the magnetic field)

$$\vec{E}_i \sim E_i \sum_{p=1,2} \sum_{l=0}^{\infty} \sum_{m=-l}^{l} W^{(p)}_{i,lm} \vec{Z}^{(p)}_{lm}(\vec{\boldsymbol{r}}) \frac{(-1)^{p-1}}{kr} \sin\left(kr - (l+1-p)\frac{\pi}{2}\right) \tag{A.10}$$

$$\vec{E}_s \sim E_i \sum_{p=1,2} \sum_{l=0}^{\infty} \sum_{m=-l}^{l} A^{(p)}_{s,lm} \vec{Z}^{(p)}_{lm}(\vec{\boldsymbol{r}}) \frac{e^{ikr}}{kr} i^{-l-p} \tag{A.11}$$

where $k = 2\pi n_i/\lambda_0$ and λ_0 is the wavelength of the incident radiation. The expression of $A^{(1,2)}_{s,lm}$ can be analytically evaluated for a sphere of refractive index n_p

and radius a. According to this theory, $A_{s,lm}^{(1,2)}$ is related to $W_{i,lm}^{(1,2)}$ through the Mie's coefficients a_l and b_l given by

$$\begin{cases} a_l = -\dfrac{A_{s,lm}^{(2)}}{W_{i,lm}^{(2)}} = \dfrac{n_i u_l'(k_p a) u_l(ka) - n_p u_l(k_p a) u_l'(ka)}{n_i u_l'(k_p a) w_l(ka) - n_p u_l(k_p a) w_l'(ka)} \\ b_l = -\dfrac{A_{s,lm}^{(1)}}{W_{i,lm}^{(1)}} = \dfrac{n_p u_l'(k_p a) u_l(ka) - n_i u_l(k_p a) u_l'(ka)}{n_p u_l'(k_p a) w_l(ka) - n_i u_l(k_p a) w_l'(ka)} \end{cases} \tag{A.12}$$

where k_p is the wavenumber of the electromagnetic field in the sphere, the superscript $'$ denotes the total derivative, $u_l(x)$ is $u_l(x) = xj_l(x)$, and $w_l(x)$ is $w_l(x) = xh_l(x)$. For a plane wave propagating along the z-direction, it is possible to demonstrate that [31]

$$W_{i,lm}^{(1)} = \begin{cases} i^l \sqrt{\pi(2l+1)} & \text{if} m = \pm 1 \\ 0 & \text{if} m \neq \pm 1 \end{cases} \tag{A.13}$$

$$W_{i,lm}^{(2)} = \begin{cases} m i^l \sqrt{\pi(2l+1)} & \text{if} m = \pm 1 \\ 0 & \text{if} m \neq \pm 1 \end{cases} \tag{A.14}$$

Appendix B

About the Langevin equation of a free particle

In the simple 1-D case, the *Langevin equation* is given by adding a random force $\xi(t)$ to Newton's equation for a particle in a viscous fluid, i.e.

$$\begin{cases} \dfrac{dr(t)}{dt} = v(t) \\ \dfrac{dv(t)}{dt} = -\dfrac{\gamma}{m}v(t) + \dfrac{1}{m}\xi(t) \end{cases} \tag{B.1}$$

where m is the mass of the particle, η the viscosity coefficient of the fluid in which the particle moves, and $\gamma = 6\pi\eta a$ is the *particle friction coefficient* defined by Stokes' law assuming the particle to be spherical with radius a.

The random force $\xi(t)$ is fundamental to explain the equilibrium properties of the system because, as expected from the equipartition theorem, the expected value of v^2 is

$$E[v^2(t)]_{eq} = \frac{k_B T}{m} \tag{B.2}$$

This expression is found if $\xi(t) \neq 0$, since equation (B.1) with $\xi(t) = 0$ has the solution

$$v(t) = e^{-t/\tau_B}v(0) \Rightarrow E[v^2(t)]_{eq} = e^{-2t/\tau_B}E[v^2(0)]_{eq} \xrightarrow[t\to\infty]{} 0 \tag{B.3}$$

where $\tau_B = m/\gamma$.

The random force $\xi(t)$ has two important properties that are useful to evaluate the solution of the Langevin equation.

1. The average value over all possible realisations of the noise, defined as $E[\xi(t)]_\xi$, is zero due to the homogeneity and isotropy of the fluid.

2. $E[\xi(t_1)\xi(t_2)]_\xi = g\delta(t_1 - t_2)$ with $g \equiv E[\xi(t)^2]_\xi$ with g called. This property is true because the particle has a very large mass with respect to the mass of the fluid constituents and, therefore, the collisions at time t_1 are independent of those at time t_2, i.e. there are no memory effects in this stochastic process.

To write g in terms of physical quantities, it is necessary to evaluate the autocorrelation function of the velocity $E[v(t_1)v(t_2)]_\xi$ and, consequently, the expression of the velocity $v(t)$. The velocity can be obtained with the differential form of equation (2.2):

$$dv(t) = -\frac{\gamma}{m}v(t)dt + \frac{1}{m}d\mathfrak{U} \tag{B.4}$$

with $d\mathfrak{U} \equiv \xi(t)dt$, that gives

$$v(t) - v(0) = -\frac{\gamma}{m}\left[x(t) - x(0)\right] + \frac{1}{m}\left[\mathfrak{U}(t) - \mathfrak{U}(0)\right] \tag{B.5}$$

Before evaluating g, it is important to observe that the Langevin equation respects all the properties of Brownian motion is a Wiener process, because the random variable $\mathfrak{U}(t)$, which introduces the stochastic process $\mathfrak{U} = \{\mathfrak{U}(t), t \geq 0\}$, is defined by:

$$\mathfrak{U}(t) = \sum_{k=1}^{n} \mathfrak{U}(t_k) - \mathfrak{U}(t_{k-1}) \tag{B.6}$$

where the interval time $[0, t]$ is partitioned in the partition $\{0 = t_0 < t_1 < ... < t_n = t\}$. Indeed:

- $\mathfrak{U}(0) = 0$, choosing properly the time origin;
- as explained above, the increments are independent;
- since the collisions are very frequent, by an application of the central limit theorem the increments are found to be normally distributed;
- this process is almost surely continuous due to the continuity of the integral function, being defined by

$$\mathfrak{U}(t) = \int_0^t \xi(t)dt \tag{B.7}$$

Having verified that the Langevin equations describe the correct stochastic process, the expression of the velocity can be obtained from equation (B.4), which has the solution

$$v(t) = e^{-\frac{t}{\tau_B}}v(0) + \frac{1}{m}\int_0^t e^{-\frac{t-s}{\tau_B}}dW(s) = e^{-\frac{t}{\tau_B}}v(0) + \frac{1}{m}\int_0^t e^{-\frac{t-s}{\tau_B}}\xi(s)ds \tag{B.8}$$

with $\tau_B = m/\gamma$. Consequently, the autocorrelation function of the velocity is

$$\begin{aligned}
E[v(t_1)v(t_2)]_\xi &= E\left[\left(e^{-\frac{t_1}{\tau_B}}v(0) + \frac{1}{m}\int_0^{t_1} e^{-\frac{t_1-s}{\tau_B}}\xi(s)ds\right)\left(e^{-\frac{t_2}{\tau_B}}v(0) + \frac{1}{m}\int_0^{t_2} e^{-\frac{t_2-s}{\tau_B}}\xi(s)ds\right)\right]_\xi = \\
&= v(0)^2 e^{-\frac{t_1+t_2}{t_B}} + \frac{1}{m^2}\int_0^{t_1}\int_0^{t_2} e^{-\frac{t_1-s_1}{t_B}} e^{-\frac{t_2-s_2}{t_B}} E\left[\xi(s_1)\xi(s_2)\right]_\xi ds_2 ds_1 = \\
&= v(0)^2 e^{-\frac{t_1+t_2}{t_B}} + \frac{g t_B}{2m^2}\left(e^{-\frac{|t_2-t_1|}{t_B}} - e^{-\frac{t_2+t_1}{t_B}}\right)
\end{aligned} \tag{B.9}$$

where Fubini's theorem is applied to change the order of integration between $E[\cdot]_\xi$ and $\int \cdot\, ds$ and the terms with $E[\xi(t)]_\xi$ are not shown due to the property $E[\xi(t)]_\xi = 0$. From this expression, g can be evaluated observing that

$$E[v(t)v(t)]_\xi = E[v(t)^2]_\xi = v(0)^2 e^{-\frac{2t}{t_B}} + \frac{g t_B}{2m^2}\left(1 - e^{-\frac{2t}{t_B}}\right) \xrightarrow[t\to\infty]{} \frac{g t_B}{2m^2} = \frac{k_B T}{m} \tag{B.10}$$

and, therefore,

$$g = 2k_B T\gamma \tag{B.11}$$

where the last equality of equation (B.10) arises from the thermal equilibrium that the particle reaches at long times ($t \to \infty$) and, therefore, $\lim_{t\to\infty} E[v(t)^2]_\xi = \frac{k_B T}{m}$.

Having obtained the noise properties, $\xi(t)$ can be rewritten as

$$\xi(t) = \sqrt{2\gamma k_B T}\,\Xi(t) \tag{B.12}$$

with $\Xi(t)$ a white noise random variable that satisfies the relations $E[\Xi(t)]_\Xi = 0$ and $E[\Xi(t_1)\Xi(t_2)]_\Xi = \delta(t_1 - t_2)$.

Now, the Langevin equation can be solved using the method of the variation of the constants. Applying this method, the solution is

$$r(t) = a_1(t) r_1(t) + a_2(t) r_2(t) \tag{B.13}$$

with r_n ($n = 1, 2$) a solution of the associated homogeneous equation of equation (2.2), that is

$$\frac{d^2 r_n}{dt^2} = -\frac{\gamma}{m}\frac{dr_n}{dt} \Rightarrow \begin{cases} r_1(t) = c_0 + \frac{m v_0}{\gamma} \\ r_2(t) = -\frac{m v_0}{\gamma} e^{-\frac{\gamma}{m}t} \end{cases} \tag{B.14}$$

with c_0 and v_0 constants defined by the initial conditions. To identify the analytical form of $a_1(t)$ and $a_2(t)$, the following system of equations needs to be solved

$$\begin{cases} \frac{da_1}{dt}\frac{dr_1}{dt} + \frac{da_2}{dt}\frac{dr_2}{dt} = \frac{\sqrt{2\gamma k_B T}}{m}\Xi \\ \frac{da_1}{dt} r_1 + \frac{da_2}{dt} r_2 = 0 \end{cases} \Rightarrow \begin{cases} a_1(t) = \frac{1}{c_0 + \frac{m v_0}{\gamma}}\sqrt{\frac{2k_B T}{\gamma}}\int_0^t \Xi(\tau)\, d\tau + a_{10} \\ a_2(t) = \frac{\sqrt{2\gamma k_B T}}{m}\int_0^t \Xi(\tau) e^{\frac{\gamma}{m}\tau}\, d\tau + a_{20} \end{cases} \tag{B.15}$$

from which it follows that the solution and its derivative (the velocity) are

$$r(t) = C_1 e^{-\frac{\gamma}{m}t} + C_2 + \sqrt{\frac{2k_B T}{\gamma}}\left(\int_0^t \Xi(\tau)\, d\tau - \int_0^t \Xi(\tau) e^{\frac{\gamma}{m}\tau}\, d\tau e^{-\frac{\gamma}{m}t}\right) \tag{B.16}$$

$$v(t) = -\frac{\gamma}{m} C_1 e^{-\frac{\gamma}{m}t} + \frac{\gamma}{m}\sqrt{\frac{2k_B T}{\gamma}}\int_0^t \Xi(\tau) e^{\frac{\gamma}{m}\tau}\, d\tau e^{-\frac{\gamma}{m}t} \tag{B.17}$$

with C_1 and C_2 given by the initial conditions $r_0 = r(t = 0)$ and $v_0 = v(t = 0)$, i.e.

$$\begin{cases} r_0 = C_1 + C_2 \\ v_0 = -\frac{\gamma}{m} C_1 \end{cases} \Rightarrow \begin{cases} C_1 = -\frac{m v_0}{\gamma} \\ C_2 = r_0 + \frac{m v_0}{\gamma} \end{cases} \tag{B.18}$$

As a result, it follows that

$$r(t) = r_0 + \frac{mv_0}{\gamma}\left(1 - e^{-\frac{\gamma}{m}t}\right) + \sqrt{\frac{2k_BT}{\gamma}}\left(\int_0^t \Xi(\tau)\,d\tau - \int_0^t \Xi(\tau)e^{\frac{\gamma}{m}\tau}\,d\tau e^{-\frac{\gamma}{m}t}\right) \quad \text{(B.19)}$$

$$v(t) = v_0 e^{-\frac{\gamma}{m}t} + \frac{\gamma}{m}\sqrt{\frac{2k_BT}{\gamma}}\int_0^t \Xi(\tau)e^{\frac{\gamma}{m}\tau}\,d\tau e^{-\frac{\gamma}{m}t} \quad \text{(B.20)}$$

It is useful to evaluate the expected value $E[r(t)]$ on all the realisations of the noise Ξ and $\mathrm{Var}[\Delta r(t)]$, which is called *mean squared displacement* (MSD). The expected value of $r(t)$, applying Fubini's theorem, is

$$E[r(t)]_\Xi = r_0 + \frac{mv_0}{\gamma}\left(1 - e^{-\frac{\gamma}{m}t}\right) \quad \text{(B.21)}$$

which implies

$$r(t) = E[r(t)]_\Xi + \sqrt{\frac{2k_BT}{\gamma}}\left(\int_0^t \Xi(\tau)\,d\tau - \int_0^t \Xi(\tau)e^{\frac{\gamma}{m}\tau}\,d\tau e^{-\frac{\gamma}{m}t}\right) \quad \text{(B.22)}$$

Instead, to evaluate the MSD it is useful to explicate the quantity $E[r(t_1)r(t_2)]_\Xi$, being the $\mathrm{MSD} = E[r(t)r(t)]_\Xi$. Applying Fubini's theorem and observing that all the terms containing Ξ (and not $\Xi(\tau)\Xi(\tau')$) are zero because $E[\Xi]_\Xi = 0$, the MSD is evaluated by direct calculation from (B.22), i.e.

$$\begin{aligned}
E[r(t_1)r(t_2)]_\Xi = E[r(t_1)]_\Xi E[r(t_2)]_\Xi + \frac{2k_BT}{\gamma}\Bigg[\int_0^{t_1}\int_0^{t_2} E[\Xi(\tau)\Xi(\tau')]\,d\tau\,d\tau' + \\
-\int_0^{t_1}\int_0^{t_2} E[\Xi(\tau)\Xi(\tau')]e^{\frac{\gamma}{m}\tau'}\,d\tau\,d\tau' e^{-\frac{\gamma}{m}t_2} - \int_0^{t_1}\int_0^{t_2} E[\Xi(\tau)\Xi(\tau')]e^{\frac{\gamma}{m}\tau}\,d\tau\,d\tau' e^{-\frac{\gamma}{m}t_1} + \\
+\int_0^{t_1}\int_0^{t_2} E[\Xi(\tau)\Xi(\tau')]e^{\frac{\gamma}{m}(\tau+\tau')}\,d\tau\,d\tau' e^{-\frac{\gamma}{m}(t_1+t_2)}\Bigg]
\end{aligned} \quad \text{(B.23)}$$

The integrals in this equation can be resolved using $E[\Xi(t_1)\Xi(t_2)]_\Xi = \delta(t_1 - t_2)$ and they are

$$\begin{cases}
\int_0^{t_1}\int_0^{t_2} E[\Xi(\tau)\Xi(\tau')]\,d\tau\,d\tau' = t_2 \\
\int_0^{t_1}\int_0^{t_2} E[\Xi(\tau)\Xi(\tau')]e^{\frac{\gamma}{m}(\tau')}\,d\tau\,d\tau' = \frac{m}{\gamma}\left(e^{\frac{\gamma}{m}t_2} - 1\right) \\
\int_0^{t_1}\int_0^{t_2} E[\Xi(\tau)\Xi(\tau')]e^{\frac{\gamma}{m}(\tau+\tau')}\,d\tau\,d\tau' = \frac{m}{2\gamma}\left(e^{\frac{2\gamma}{m}t_2} - 1\right)
\end{cases} \quad \text{(B.24)}$$

assuming $t_2 \leq t_1$. In addition, the initial velocity of the particle v_0 is usually unknown and, in order to have useful results, the average value over all the possible initial velocities is needed. Applying the equipartition theorem, this average gives $v_0 = \frac{k_bT}{m}$. Using these results and performing the calculations, $E[r(t_1)r(t_2)]_\Xi$ is

$$E[r(t_1)r(t_2)]_\Xi = \frac{2k_BT}{\gamma}t_2 + \frac{k_BTm}{\gamma^2}\left[e^{-\frac{\gamma}{m}t_1} + e^{-\frac{\gamma}{m}t_2} - e^{-\frac{\gamma}{m}(t_1-t_2)} - 1\right] \quad \text{(B.25)}$$

Equation (B.25) gives the MSD:

$$\mathrm{MSD}(\tau) = E[r^2(\tau)]_\Xi - 2E[r(\tau)r(0)]_\Xi + E[r^2(0)]_\Xi = \frac{2k_BT}{\gamma}\tau + \frac{2k_BTm}{\gamma^2}\left[e^{-\frac{\gamma}{m}\tau} - 1\right] \quad \text{(B.26)}$$

Following similar calculations, it is possible to demonstrate that for the overdamped Langevin equation the MSD is

$$E[r^2(t)]_\Xi = \frac{2k_BT}{\gamma}t \quad \text{(B.27)}$$

Appendix C

Langevin equation of a trapped particle

The Langevin equation of a trapped particle is given by the following expression:

$$\frac{d^2r}{dt^2}(t) = -\frac{\gamma}{m}\frac{dr}{dt}(t) - \frac{k}{m}r(t) + \frac{\sqrt{2\gamma k_B T}}{m}\Xi(t) \tag{C.1}$$

The solution of this equation can be obtained using the method of the variation of the constants:

$$r(t) = a_1(t)r_1(t) + a_2(t)r_2(t) \tag{C.2}$$

with r_n $(n = 1, 2)$ being a solution of the associated homogeneous equation of equation (C.1). The solution of the homogeneous equation is

$$\frac{d^2r_n}{dt^2} + \frac{\gamma}{m}\frac{dr_n}{dt} + \frac{k}{m}r_n = 0 \Rightarrow r_n(t) = C_n e^{\mu_n t} \tag{C.3}$$

with $\mu_{\frac{1}{2}} = -\frac{1}{2}\frac{\gamma}{m} \pm \frac{1}{2}\sqrt{\left(\frac{\gamma}{m}\right)^2 - 4\frac{k}{m}}$ and C_n a constant defined by the initial conditions. The variation of constants method gives the following system of equations to determine $a_1(t)$ and $a_2(t)$:

$$\begin{cases} \frac{da_1}{dt}\frac{dr_1}{dt} + \frac{da_2}{dt}\frac{dr_2}{dt} = \frac{\sqrt{2\gamma k_B T}}{m}\Xi \\ \frac{da_1}{dt}r_1 + \frac{da_2}{dt}r_2 = 0 \end{cases} \Rightarrow \begin{cases} a_1(t) = \frac{1}{C_1}\frac{\sqrt{2\gamma k_B T}}{m}\frac{1}{\mu_1-\mu_2}\int_0^t \Xi(\tau)e^{-\mu_1\tau}\,d\tau + a_{10} \\ a_2(t) = -\frac{1}{C_2}\frac{\sqrt{2\gamma k_B T}}{m}\frac{1}{\mu_1-\mu_2}\int_0^t \Xi(\tau)e^{-\mu_2\tau}\,d\tau + a_{20} \end{cases} \tag{C.4}$$

From these equations, the solution and its derivative (the velocity) are

$$r(t) = C_1 e^{-\mu_1 t} + C_2 e^{-\mu_2 t} + \frac{\sqrt{2\gamma k_B T}}{m}\frac{1}{\mu_1-\mu_2}\left(\int_0^t \Xi(\tau)e^{-\mu_1\tau}\,d\tau - \int_0^t \Xi(\tau)e^{-\mu_2\tau}\,d\tau\right) \tag{C.5}$$

and

$$v(t) = \mu_1 C_1 e^{-\mu_1 t} + \mu_2 C_2 e^{-\mu_2 t} + \frac{\sqrt{2\gamma k_B T}}{m}\frac{1}{\mu_1-\mu_2}\left(\mu_1\int_0^t \Xi(\tau)e^{-\mu_1\tau}\,d\tau - \mu_2\int_0^t \Xi(\tau)e^{-\mu_2\tau}\,d\tau\right) \tag{C.6}$$

with $C_n = c_n a_{n0}$ ($n = 1, 2$) defined by

$$\begin{cases} r_0 = C_1 + C_2 \\ v_0 = \mu_1 C_1 + \mu_2 C_2 \end{cases} \Rightarrow \begin{cases} C_1 = -\frac{\mu_2 r_0 - v_0}{\mu_1 - \mu_2} \\ C_2 = \frac{\mu_1 r_0 - v_0}{\mu_1 - \mu_2} \end{cases} \tag{C.7}$$

assuming $r_0 = r(t = 0)$ and $v_0 = v(t = 0)$. Averaging over all the possible noise realisations, these equations give the following expected position value $E[r(t)]_\Xi$

$$E[r(t)]_\Xi = C_1 e^{-\mu_1 t} + C_2 e^{-\mu_2 t} = \frac{\mu_1 r_0 e^{-\mu_2 t} - \mu_2 r_0 e^{-\mu_1 t} + v_0 e^{-\mu_1 t} - v_0 e^{-\mu_2 t}}{\mu_1 - \mu_2} \tag{C.8}$$

and the following expected velocity value $E[v(t)]_\Xi$

$$E[v(t)]_\Xi = \mu_1 C_1 e^{-\mu_1 t} + \mu_2 C_2 e^{-\mu_2 t} \tag{C.9}$$

where, for both the expected values, the second integral term of equations (C.5) and (C.6) is zero because the hypothesis of Fubini's theorem are satisfied in this analysis $\left(E\left[\int_0^t f(\tau)\, d\tau\right]_\Xi = \int_0^t E\left[f(\tau)\right]_\Xi\, d\tau\right)$ and, therefore, $E\left[\int_0^t \Xi(\tau) e^{-\mu_{1,2}\tau}\, d\tau\right]_\Xi = 0$, being $E[\Xi]_\Xi = 0$.

In order to evaluate the MSD, the average of $r(t_1)r(t_2)$ for $t_1 = t_2 = t$ needs to be obtained and, to evaluate $r(t_1)r(t_2)$ in a simple way, some important consideration are needed:

- $r(t)$ can be rewritten in terms of its average $E[r(t)]_\Xi$, i.e.

$$r(t) = E[r(t)]_\Xi + \frac{\sqrt{2\gamma k_B T}}{m} \frac{1}{\mu_1 - \mu_2} \left(\int_0^t \Xi(\tau) e^{-\mu_1 \tau}\, d\tau - \int_0^t \Xi(\tau) e^{-\mu_2 \tau}\, d\tau \right) \tag{C.10}$$

- all the terms obtained as product of the first term and the second one of the previous equation are zero, because they contain $E\left[\int_0^t \Xi(\tau) e^{-\mu_{1,2}\tau}\, d\tau\right]_\Xi$ that has zero average;

- all the terms obtained as product of the second term and itself (at different times t_1 and t_2) have an integral like $E\left[\int_0^{t_2}\int_0^{t_1} \Xi(\tau)\Xi(\tau') e^{-\mu_1\tau - \mu_2\tau'}\, d\tau d\tau'\right]_\Xi$ that is equal to

$$\int_0^{t_2}\int_0^{t_1} E\left[\Xi(\tau)\Xi(\tau')\right]_\Xi e^{-\mu_1\tau - \mu_2\tau'}\, d\tau d\tau' = \frac{1}{\mu_1 + \mu_2}\left(1 - e^{-(\mu_1+\mu_2)t_2}\right) \tag{C.11}$$

  where $E\left[\Xi(\tau)\Xi(\tau')\right]_\Xi = \delta(\tau - \tau')$ and $t_2 < t_1$ is assumed.

Using all these considerations, $E[r(t_1)r(t_2)]_\Xi$ is

$$\begin{aligned} E[r(t_1)r(t_2)]_\Xi = E[r(t_1)]_\Xi E[r(t_2)]_\Xi + \frac{2k_B T\gamma}{m^2(\mu_1-\mu_2)^2}\left[\frac{1}{2\mu_1}\left(1 - e^{-2\mu_1 t_2}\right)e^{\mu_1(t_1+t_2)} + \right. \\ \left. + \frac{1}{2\mu_2}\left(1 - e^{-2\mu_2 t_2}\right)e^{\mu_2(t_1+t_2)} - \frac{1}{\mu_1+\mu_2}\left(1 - e^{-(\mu_1+\mu_2)t_2}\right)\left(e^{\mu_1 t_1 + \mu_2 t_2} + e^{\mu_1 t_2 + \mu_2 t_1}\right)\right] \end{aligned} \tag{C.12}$$

that, for $t_1 = t_2 \equiv t$, gives

$$E[r(t)^2]_\Xi = (E[r(t)]_\Xi)^2 + \frac{2k_BT\gamma}{m^2(\mu_1-\mu_2)^2}\left[\frac{1}{2\mu_1}\left(e^{2\mu_1 t}-1\right)+\frac{1}{2\mu_2}\left(e^{2\mu_2 t}-1\right)-\frac{2}{\mu_1+\mu_2}\left(e^{(\mu_1+\mu_2)t}-1\right)\right] \quad \text{(C.13)}$$

To understand the physical meaning of this expression, this equation needs to be reduced to the terms of equation (2.37) only. Firstly, the term $(E[r(t)]_\Xi)^2$ can be rewritten observing that

$$\begin{aligned} E[r(t)]_\Xi = r_0 &\left[\cosh\left(\frac{\sqrt{\frac{\gamma^2}{m^2}-4\frac{k}{m}}}{2}t\right)+\frac{\gamma/m}{\sqrt{\frac{\gamma^2}{m^2}-4\frac{k}{m}}}\sinh\left(\frac{\sqrt{\frac{\gamma^2}{m^2}-4\frac{k}{m}}}{2}t\right)\right]e^{-\frac{\gamma}{2m}t}+ \\ &+\frac{2v_0}{\sqrt{\frac{\gamma^2}{m^2}-4\frac{k}{m}}}\sinh\left(\frac{\sqrt{\frac{\gamma^2}{m^2}-4\frac{k}{m}}}{2}t\right)e^{-\frac{\gamma}{2m}t} \end{aligned} \quad \text{(C.14)}$$

obtained adding and subtracting the terms $\mu_1 e^{\mu_1 t}$ and $\mu_1 e^{\mu_1 t}$ in equation (C.8), using the definition of $\cosh$ and $\sinh$, and substituting the definition of $\mu_{1,2}$. Secondly, the second term of equation (C.13), manipulating it in a similar way, is

$$\frac{k_BT}{k}\left[1-\left(2\frac{\gamma^2}{\gamma^2-4mk}\sinh^2\left(\frac{\sqrt{\frac{\gamma^2}{m^2}-4\frac{k}{m}}}{2}t\right)+\frac{\gamma/m}{\sqrt{\frac{\gamma^2}{m^2}-4\frac{k}{m}}}\sinh\left(\sqrt{\frac{\gamma^2}{m^2}-4\frac{k}{m}}t\right)+1\right)e^{-\frac{\gamma}{m}t}\right] \quad \text{(C.15)}$$

In typical experiments, the initial position r_0 is known, but not the velocity v_0 and, therefore, the useful expression of the MSD is obtained averaging over all the possible values of v_0, $E[(E[r(t)]_\Xi)^2]_{v_0}$. From the equipartition theorem, the initial condition $E[v_0^2]_{v_0} = \frac{k_BT}{m}$ allows to write

$$\begin{aligned} E[r(t)^2]_\Xi = \frac{k_BT}{k} + \left(r_0^2-\frac{k_BT}{k}\right)&\left[\cosh\left(\frac{\sqrt{\frac{\gamma^2}{m^2}-4\frac{k}{m}}}{2}t\right)+\frac{\gamma/m}{\sqrt{(\frac{\gamma}{m})^2-4\frac{k}{m}}}\sinh\left(\frac{\sqrt{\frac{\gamma^2}{m^2}-4\frac{k}{m}}}{2}t\right)\right]^2 e^{-\frac{\gamma}{m}t}+ \\ +\frac{2k_BTr_0}{k\sqrt{\frac{\gamma^2}{m^2}-4\frac{k}{m}}}\sinh\left(\frac{\sqrt{\frac{\gamma^2}{m^2}-4\frac{k}{m}}}{2}t\right)&\left[\cosh\left(\frac{\sqrt{\frac{\gamma^2}{m^2}-4\frac{k}{m}}}{2}t\right)+\frac{\gamma/m}{\sqrt{(\frac{\gamma}{m})^2-4\frac{k}{m}}}\sinh\left(\frac{\sqrt{\frac{\gamma^2}{m^2}-4\frac{k}{m}}}{2}t\right)\right]e^{-\frac{\gamma}{m}t} \end{aligned} \quad \text{(C.16)}$$

In this expression (for alternative approaches see [43, 44]), there are two angular frequencies contributions: $\Omega = \sqrt{k/m}$, that is the angular frequency of the trapped particle without damping, and $\Omega_1 = \sqrt{\frac{\gamma^2}{m^2}-4\frac{k}{m}} = \sqrt{\Gamma_0^2-4\Omega^2}$, that is the cyclic frequency of the damped oscillator in which $\Gamma_0 = \frac{\gamma}{m}$ is the damping coefficient. Therefore, assuming $r_0 = 0$, the $\mathrm{MSD} = E[r(t)^2]_\Xi - 2E[r(t)r(0)]_\Xi + E[r(0)^2]_\Xi$, obtained combining allt he previous results together, is

$$\mathrm{MSD(t)} = 2\frac{k_BT}{k} - 2\frac{k_BT}{k}\left[\cosh\left(\frac{\Omega_1}{2}t\right)+\frac{\Gamma_0}{\Omega_1}\sinh\left(\frac{\Omega_1}{2}t\right)\right]e^{-\Gamma_0 t/2} \quad \text{(C.17)}$$

The MSD, for $t\to\infty$, has the limit value of $\lim_{t\to\infty} E[r(t)^2]_\Xi = 2\frac{k_BT}{k}$.

Following a similar procedure, the MSD in the low Reynolds number regime si

$$E[r(t)^2]_\Xi = \frac{2k_BT}{k}\left(1-e^{-\frac{k}{\gamma}t}\right) \quad \text{(C.18)}$$

Bibliography

[1] Johannes Kepler. 1619. de cometis libelli tres.

[2] John Henry Poynting. Xv. on the transfer of energy in the electromagnetic field. *Philosophical Transactions of the Royal Society of London*, (175):343–361, 1884.

[3] Peter Lebedew. Untersuchungen über die druckkräfte des lichtes. *Annalen der Physik*, 311(11):433–458, 1901.

[4] Ernest Fox Nichols and Gordon Ferrie Hull. A preliminary communication on the pressure of heat and light radiation. *Physical Review (Series I)*, 13(5):307, 1901.

[5] Arthur Ashkin. Acceleration and trapping of particles by radiation pressure. *Physical review letters*, 24(4):156, 1970.

[6] A Ashkin, Karin Schütze, JM Dziedzic, Ursula Euteneuer, and Manfred Schliwa. Force generation of organelle transport measured in vivo by an infrared laser trap. *Nature*, 348:346–348, 1990.

[7] Carlos Bustamante, Zev Bryant, and Steven B Smith. Ten years of tension: single-molecule dna mechanics. *Nature*, 421(6921):423–427, 2003.

[8] Keir C Neuman and Attila Nagy. Single-molecule force spectroscopy: optical tweezers, magnetic tweezers and atomic force microscopy. *Nature methods*, 5(6):491–505, 2008.

[9] Michael M Burns, Jean-Marc Fournier, and Jene A Golovchenko. Optical matter: crystallization and binding in intense optical fields. *Science*, 249(4970):749–754, 1990.

[10] Yael Roichman and David G Grier. Holographic assembly of quasicrystalline photonic heterostructures. *Optics express*, 13(14):5434–5439, 2005.

[11] Lowell I McCann, Mark Dykman, and Brage Golding. Thermally activated transitions in a bistable three-dimensional optical trap. *Nature*, 402(6763):785–787, 1999.

[12] Adam M Kaufman, Brian J Lester, and Cindy A Regal. Cooling a single atom in an optical tweezer to its quantum ground state. *Physical Review X*, 2(4):041014, 2012.

[13] AM Kaufman, BJ Lester, CM Reynolds, ML Wall, M Foss-Feig, KRA Hazzard, AM Rey, and CA Regal. Two-particle quantum interference in tunnel-coupled optical tweezers. *Science*, 345(6194):306–309, 2014.

[14] Lucien P Ghislain and Watt W Webb. Scanning-force microscope based on an optical trap. *Optics Letters*, 18(19):1678–1680, 1993.

[15] Ernst-Ludwig Florin, Arnd Pralle, JK Heinrich Hörber, and Ernst HK Stelzer. Photonic force microscope based on optical tweezers and two-photon excitation for biological applications. *Journal of structural biology*, 119(2):202–211, 1997.

[16] Eric R Dufresne and David G Grier. Optical tweezer arrays and optical substrates created with diffractive optics. *Review of scientific instruments*, 69(5):1974–1977, 1998.

[17] Dmitri V Petrov. Raman spectroscopy of optically trapped particles. *Journal of Optics A: Pure and Applied Optics*, 9(8):S139, 2007.

[18] Alessandro Magazzu, D Bronte Ciriza, P Polimeno, Anna Musolino, Maria Grazia Donato, Antonino Foti, Pietro Giuseppe Gucciardi, Maria Antonia Iatì, Rosalba Saija, Luigi Folco, et al. Cosmic dust investigation by optical tweezers for space exploration. In *Optical Manipulation and Its Applications*, pages AF2D–5. Optica Publishing Group, 2021.

[19] Satoshi Kawata and Tadao Sugiura. Movement of micrometer-sized particles in the evanescent field of a laser beam. *Optics letters*, 17(11):772–774, 1992.

[20] Satoshi Kawata and T Tani. Optically driven mie particles in an evanescent field along a channeled waveguide. *Optics letters*, 21(21):1768–1770, 1996.

[21] Anders E Wallin, Heikki Ojala, Edward Hæggström, and Roman Tuma. Stiffer optical tweezers through real-time feedback control. *Applied Physics Letters*, 92(22):224104, 2008.

[22] Cécile Pacoret, Richard Bowman, Graham Gibson, Sinan Haliyo, David Carberry, Arvid Bergander, Stéphane Régnier, and Miles Padgett. Touching the microworld with force-feedback optical tweezers. *Optics express*, 17(12):10259–10264, 2009.

[23] Markus Koch, Christian Sames, Alexander Kubanek, Matthias Apel, Maximilian Balbach, Alexei Ourjoumtsev, Pepijn WH Pinkse, and Gerhard Rempe. Feedback cooling of a single neutral atom. *Physical review letters*, 105(17):173003, 2010.

[24] Markus Aspelmeyer, Tobias J Kippenberg, and Florian Marquardt. Cavity optomechanics. *Reviews of Modern Physics*, 86(4):1391, 2014.

[25] Mathieu L Juan, Reuven Gordon, Yuanjie Pang, Fatima Eftekhari, and Romain Quidant. Self-induced back-action optical trapping of dielectric nanoparticles. *Nature Physics*, 5(12):915–919, 2009.

[26] Fatemeh Kalantarifard, Parviz Elahi, Ghaith Makey, Onofrio M Maragò, F Ömer Ilday, and Giovanni Volpe. Intracavity optical trapping of microscopic particles in a ring-cavity fiber laser. *Nature communications*, 10(1):1–11, 2019.

[27] Antonio Ciarlo, Giuseppe Pesce, Fatemeh Kalantarifard, Parviz Elahi, Giovanni Volpe, and Antonio Sasso. Intracavity feedback optical trapping. *Il nuovo cimento C*, 45(6):1–4, 2022.

[28] Bahaa EA Saleh and Malvin Carl Teich. *Fundamentals of photonics*. John Wiley & Sons, 2019.

[29] Arthur Ashkin. Forces of a single-beam gradient laser trap on a dielectric sphere in the ray optics regime. *Biophysical journal*, 61(2):569–582, 1992.

[30] Agnese Callegari, Mite Mijalkov, A Burak Gököz, and Giovanni Volpe. Computational toolbox for optical tweezers in geometrical optics. *JOSA B*, 32(5):B11–B19, 2015.

[31] Philip H Jones, Onofrio M Maragò, and Giovanni Volpe. *Optical tweezers: Principles and applications*. Cambridge University Press, 2015.

[32] John David Jackson. Classical electrodynamics, 1999.

[33] L Bachelier. Theorie de la speculation, gauthier-villars, paris, w: P. cootner, the random character of stock market prices, 1900.

[34] Albert Einstein et al. On the motion of small particles suspended in liquids at rest required by the molecular-kinetic theory of heat. *Annalen der physik*, 17:549–560, 1905.

[35] M. Paul Langevin. Sur la théorie du mouvement brownien. *C. R. Acad. Sci. (Paris)*, 146:530–533, 1908.

[36] Marian V Smoluchowski. Über brownsche molekularbewegung unter einwirkung äußerer kräfte und deren zusammenhang mit der verallgemeinerten diffusionsgleichung. *Annalen der Physik*, 353(24):1103–1112, 1916.

[37] Norbert Wiener. Differential-space. *Journal of Mathematics and Physics*, 2(1-4):131–174, 1923.

[38] Adriaan Daniël Fokker. Die mittlere energie rotierender elektrischer dipole im strahlungsfeld. *Annalen der Physik*, 348(5):810–820, 1914.

[39] George Gabriel Stokes et al. On the effect of the internal friction of fluids on the motion of pendulums. 1851.

[40] Frank WJ Olver, Daniel W Lozier, Ronald F Boisvert, and Charles W Clark. *NIST handbook of mathematical functions hardback and CD-ROM*. Cambridge university press, 2010.

[41] VM Planck. Über einen satz der statistischen dynamik und seine erweiterung in der quantentheorie. *Sitzungberichte der*, 1917.

[42] Hannes Risken. Fokker-planck equation. In *The Fokker-Planck Equation*, pages 63–95. Springer, 1996.

[43] Subrahmanyan Chandrasekhar. Stochastic problems in physics and astronomy. *Reviews of modern physics*, 15(1):1, 1943.

[44] Ming Chen Wang and George Eugene Uhlenbeck. On the theory of the brownian motion ii. *Reviews of modern physics*, 17(2-3):323, 1945.

[45] Peter Hänggi, Peter Talkner, and Michal Borkovec. Reaction-rate theory: fifty years after kramers. *Reviews of modern physics*, 62(2):251, 1990.

[46] WT Coffey, Yu P Kalmykov, and JT Waldron. *The Langevin equation: With applications to stochastic problems in physics, chemistry and electrical*. World Scientific Publishing Company, 2004.

[47] Amos Hardy and R Oron. Signal amplification in strongly pumped fiber amplifiers. *IEEE Journal of Quantum electronics*, 33(3):307–313, 1997.

[48] Ido Kelson and Amos A Hardy. Strongly pumped fiber lasers. *IEEE Journal of Quantum Electronics*, 34(9):1570–1577, 1998.

[49] H Haken. Synergetics: Introduction and advanced topics (physics and astronomy online library), 2004.

[50] Giuseppe Pesce, Giorgio Volpe, Onofrio M Maragó, Philip H Jones, Sylvain Gigan, Antonio Sasso, and Giovanni Volpe. Step-by-step guide to the realization of advanced optical tweezers. *JOSA B*, 32(5):B84–B98, 2015.

[51] Johannes Diderik Van Der Waals and John Shipley Rowlinson. *On the continuity of the gaseous and liquid states*. Courier Corporation, 2004.

[52] H.C. Hamaker. The london—van der waals attraction between spherical particles. *Physica*, 4(10):1058–1072, 1937.

[53] Sean G. Fronczak, Christopher A. Browne, Elizabeth C. Krenek, Stephen P. Beaudoin, and David S. Corti. Non-contact afm measurement of the hamaker constants of solids: Calibrating cantilever geometries. *Journal of Colloid and Interface Science*, 517:213–220, 2018.

[54] Evgenni Mikhailovich Lifshitz. The theory of molecular attractive forces between solids. *Soviet Physics JETP*, 2:73–83, 1956.

[55] B-W_ Ninham and VA Parsegian. van der waals forces across triple-layer films. *The Journal of chemical physics*, 52(9):4578–4587, 1970.

[56] David B. Hough and Lee R. White. The calculation of hamaker constants from liftshitz theory with applications to wetting phenomena. *Advances in Colloid and Interface Science*, 14(1):3–41, 1980.

[57] Fabio L Leite, Carolina C Bueno, Alessandra L Da Róz, Ervino C Ziemath, and Osvaldo N Oliveira Jr. Theoretical models for surface forces and adhesion and their measurement using atomic force microscopy. *International journal of molecular sciences*, 13(10):12773–12856, 2012.

[58] Jacques Curie and Pierre Curie. Développement par compression de l'électricité polaire dans les cristaux hémièdres à faces inclinées. *Bulletin de minéralogie*, 3(4):90–93, 1880.

[59] G Lippmann. Sur le principe de la conservation de l'électricité. *Ann. de chim. at phys*, 24:145–178, 1881.

[60] Ravinder S Dahiya and Maurizio Valle. *Robotic tactile sensing: technologies and system*. Springer, 2013.

[61] Jing-Feng Li. *Lead-Free Piezoelectric Materials*. John Wiley & Sons, 2020.

[62] Ivo F Sbalzarini and Petros Koumoutsakos. Feature point tracking and trajectory analysis for video imaging in cell biology. *Journal of structural biology*, 151(2):182–195, 2005.

[63] Sang-Hyuk Lee, Yohai Roichman, Gi-Ra Yi, Shin-Hyun Kim, Seung-Man Yang, Alfons van Blaaderen, Peter van Oostrum, and David G. Grier. Characterizing and tracking single colloidal particles with video holographic microscopy. *Opt. Express*, 15(26):18275–18282, Dec 2007.

[64] Fook Chiong Cheong, Bhaskar Jyoti Krishnatreya, and David G. Grier. Strategies for three-dimensional particle tracking with holographic video microscopy. *Opt. Express*, 18(13):13563–13573, Jun 2010.

[65] Benjamin Midtvedt, Saga Helgadottir, Aykut Argun, Jesús Pineda, Daniel Midtvedt, and Giovanni Volpe. Quantitative digital microscopy with deep learning. *Applied Physics Reviews*, 8(1):011310, 2021.

[66] Solomon Barkley, Thomas G Dimiduk, Jerome Fung, David M Kaz, Vinothan N Manoharan, Ryan McGorty, Rebecca W Perry, and Anna Wang. Holographic microscopy with python and holopy. *Computing in Science & Engineering*, 22(5):72–82, 2019.

[67] Ethem Alpaydin. *Introduction to Machine Learning*. The MIT Press, 2004.

[68] Gustav Mie. Beiträge zur optik trüber medien, speziell kolloidaler metallösungen. *Annalen der physik*, 330(3):377–445, 1908.